Doctorate Dissertation

博士論文

Cosmology and Cluster Astrophysics with Weak Gravitational Lensing and the Sunyaev–Zel'dovich Effect

(重力レンズとスニヤエフーゼルドビッチ効果を用いた銀河団宇宙論)

A Dissertation Submitted for Degree of Doctor of Philosophy
December 2018

平成30年12月博士（理学）申請

Department of Physics, Graduate School of Science,
The University of Tokyo

東京大学大学院理学系研究科物理学専攻

Ken Osato

大里　健

Abstract

Cosmology has experienced tremendous progresses in the last decade, and the concordance model of the Universe has been established. In order to verify the theoretical model or find phenomena beyond the standard model, various cosmological observations have been conducted so far. One of major cosmological probes which have played a crucial role in observational cosmology is galaxy clusters. Since the abundance of galaxy clusters is sensitive to the underlying cosmological models, one can use the mass function of galaxy clusters to constrain cosmological parameters, which is called as cluster cosmology. One of the ways to observe galaxy clusters is weak gravitational lensing (WL), which represents the weak deformation of images of distant galaxies. Through WL, we can reconstruct the gravitational field of clusters, and then the density distribution. Another important probe into galaxy clusters is the thermal Sunyaev–Zel'dovich (tSZ) effect. The tSZ effect denotes the secondary temperature anisotropy of cosmic microwave background (CMB) induced by inverse Compton scattering between CMB photons and hot free electrons in galaxy clusters. The advantage of tSZ is that since the observable of the tSZ effect is the projected pressure field, we can directly probe the thermodynamic properties of intra-cluster medium (ICM).

In cluster cosmology, the mass of galaxy clusters is the most fundamental physical quantity, but it is not the direct observable in X-ray or SZ observations. In order to relate the observed flux to the mass, hydrostatic equilibrium, where thermal pressure balances the self-gravity of galaxy clusters, is widely assumed. However, mass calibration measurements suggest that 10–30% of the mass is supported by physical processes other than thermal pressure. Such processes are called as non-thermal pressure and the dominant source is thought to be turbulent motion in galaxy clusters. The existence of the non-thermal pressure directly affects the mass estimate. Thus, precise evaluation of the amplitude of the non-thermal pressure is essential for cluster cosmology. In this dissertation, with WL and tSZ, we aim for scrutinizing the non-thermal pressure support in galaxy clusters for the wide ranges of redshift and mass. In addition to auto-correlations of tSZ, we employ the cross-correlation of tSZ and WL. One of the advantages of the cross-correlations is that we can preferentially extract the information of ICM at the redshift $z \sim 0.5$–1 where cluster formation and merger events actively occur, because WL probes the large-scale structures at this range. Furthermore, the cross-correlation is complementary to the tSZ auto-correlation, which is sensitive to the structures at higher redshifts ($z \gtrsim 1$). In addition, the cross-correlations measured based on maps contain the signals from low-mass halos ($\lesssim 10^{14}\,\mathrm{M}_\odot$), which are unresolved in the SZ survey due

to the small signal.

We carry out the analysis of the cross-correlation measurement from Red Cluster Sequence Lensing Survey (RCSLenS) and *Planck* to constrain two parameters: the amplitude of the non-thermal pressure α_0 and the amplitude of matter power spectrum σ_8. Only with tSZ auto-power spectrum, the large $\sigma_8 \sim 0.85$ and high non-thermal pressure $\alpha_0 \sim 0.2$–0.3 are preferred. In contrast, with tSZ-WL cross-correlations, smaller $\sigma_8 \sim 0.6$ and lower non-thermal pressure $\alpha_0 \sim 0.05$ are estimated. The difference arises from the different range of probed mass and redshift between tSZ auto-power spectrum and tSZ-WL cross-correlations, which have not been considered in previous studies. It implies the redshift or mass evolution of the non-thermal pressure.

In order to address the redshift evolution of the non-thermal pressure, we employ Subaru Hyper Suprime-Cam (HSC) data, which is deeper than that of RCSLenS. With the similar methodology in our previous analysis, we constrain hydrostatic bias parameter, which represents fraction of mass supported by non-thermal pressure, along with cosmological parameters. With the prior from *Planck* CMB measurements, which is widely adopted in previous studies, we find the bias parameter as $b = 0.394^{+0.046}_{-0.052}$. The estimated hydrostatic bias is consistent with the result with the analyses with tSZ auto-power spectrum or tSZ-WL cross-correlations with RCSLenS. This implies no significant redshift evolution in hydrostatic bias parameter. On the other hand, mass calibration measurements suggest that the hydrostatic bias is 10–30%, and the discrepancy indicates that the non-thermal pressure support is more predominant in low-mass halos, which cannot be detected in mass calibration measurements.

Acknowledgement

First of all, I would like to express my deepest gratitude to my supervisor Prof. Naoki Yoshida who introduced me to the research of observational cosmology for his continuous encouragement and advice. I also acknowledge my collaborators: Dr. Masato Shirasaki, Dr. Samuel Flender, Prof. Daisuke Nagai, and Dr. Hironao Miyatake for their supports and advice.

I would like to thank my collaborators: Prof. Masamune Oguri, Dr. Takahiro Nishimichi, Prof. Masahiro Takada, Dr. Teppei Okumura, Prof. Atsushi Taruya, Prof. Francis Bernardeau, and Prof. Ryuichi Takahashi. In addition, I also thank Prof. Eiichiro Komatsu, Dr. Boris Bolliet, and Dr. Chiaki Hikage for fruitful discussions about our studies and gave me precious insights into cosmology and astrophysics.

Numerical simulations in this dissertation were carried out on Cray XC50 at the Center for Computational Astrophysics, National Astronomical Observatory of Japan and on XC40 at Yukawa Institute for Theoretical Physics, Kyoto University.

The Hyper Suprime-Cam (HSC) collaboration includes the astronomical communities of Japan and Taiwan, and Princeton University. The HSC instrumentation and software were developed by the National Astronomical Observatory of Japan (NAOJ), the Kavli Institute for the Physics and Mathematics of the Universe (Kavli IPMU), the University of Tokyo, the High Energy Accelerator Research Organization (KEK), the Academia Sinica Institute for Astronomy and Astrophysics in Taiwan (ASIAA), and Princeton University. Funding was contributed by the FIRST program from Japanese Cabinet Office, the Ministry of Education, Culture, Sports, Science and Technology (MEXT), the Japan Society for the Promotion of Science (JSPS), Japan Science and Technology Agency (JST), the Toray Science Foundation, NAOJ, Kavli IPMU, KEK, ASIAA, and Princeton University.

The Pan-STARRS1 Surveys (PS1) have been made possible through contributions of the Institute for Astronomy, the University of Hawaii, the Pan-STARRS Project Office, the Max-Planck Society and its participating institutes, the Max Planck Institute for Astronomy, Heidelberg and the Max Planck Institute for Extraterrestrial Physics, Garching, The Johns Hopkins University, Durham University, the University of Edinburgh, Queen's University Belfast, the Harvard-Smithsonian Center for Astrophysics, the Las Cumbres Observatory Global Telescope Network Incorporated, the National Central University of Taiwan, the Space Telescope Science Institute, the National Aeronautics and Space Administration under Grant No. NNX08AR22G issued through the Planetary Science Division of the NASA Science Mission Directorate, the National Science Foundation un-

der Grant No. AST-1238877, the University of Maryland, and Eotvos Lorand University (ELTE).

Contents

Chapter 1

Introduction

Contents

1.1 Cosmology: The Accelerating Universe

The mysteries about the origin, evolution, and fate of our Universe and how rich structures in the sky such as stars and galaxies form have been attracting curiosities from ancient eras. The research area which gives an answer to such fundamental questions about the Universe is called as *cosmology*. In 1916, Einstein proposed a theory (Einstein, 1916), which is currently known as general relativity, and revolutionized the paradigm about the Universe. Beginning with the discovery of general relativity, the standard picture of cosmology have been established in the last decade. The Universe initiates from the singular point (*big-bang*), undergoes the exponential expansion (*inflation*), and becomes filled with the mixture of elementary particles with high temperature (*reheating*). Then, as the Universe expands, the hot plasma cools and hydrogen and helium nuclei form. Finally, various structures such as stars and galaxies form in the late-time Universe. The Universe continues to expand, but the expansion accelerates in the late-time, which is one of critical mysteries in cosmology.

For contents of the Universe, the ordinary matter, e.g., hydrogen or helium, accounts only for 5% of the energy budget of the Universe. The rest of the energy is occupied by the so-called dark sector: *dark matter* and *dark energy*. Dark matter is material which exerts gravity but does not interact via electro-magnetic field. Accordingly, dark matter

cannot be detected by light, which makes it impossible to observe dark matter through telescopes. The first indication of dark matter is proposed by Zwicky (1933). Applying the virial theorem to dynamics of galaxies in Coma cluster, he found that the mass of luminous component was not enough for the estimated self-gravity of the cluster. He concluded that there should be missing source of gravity and coined the name "dark matter". After forty years of the discovery, Rubin and collaborators (Rubin & Ford, 1970; Rubin et al., 1980) measured the rotation curves of galaxies using hydrogen 21cm emission line. The rotation curves remain flat even at the outskirts where no luminous matter was observed. This fact also indicates there exists dark gravitational source.

If the Universe were composed of ordinary and dark matter, since only gravity works at long distance, the Universe would end up with collapse into a point. However, this picture completely contradicts the observational fact that the Universe is expanding acceleratedly. It is dark energy that induces this acceleration. Although physicists have proposed various hypotheses to explain dark matter and candidates of dark matter particle, the physical property of dark energy is quite enigmatic. It works as repulsive force, or equivalently negative pressure, and the energy density is invariant even if the Universe expands. Some models based on string theory predict the existence of dark energy, but most of models fail to give observed magnitude of dark energy.

1.2 Observations: Shedding Light on The Dark Universe

The progresses of our understanding of the Universe are realized by precise and accurate *observations*. One of the most striking examples is the observation of cosmic microwave background (CMB), whose detection was first reported in 1960s (Penzias & Wilson, 1965). Furthermore, it has been predicted that CMB temperature has the anisotropy. The pattern imprinted in anisotropy provides us with rich information of the early Universe. In order to measure the anisotropy, several missions were proposed and yielded excellent results, for example, *COBE* (Boggess et al., 1992), *WMAP* (Bennett et al., 2003), and *Planck* (Planck Collaboration, 2016a). Another important observation is galaxy redshift surveys, i.e., three-dimensional mapping of galaxies, for example, CfA survey (Tonry & Davis, 1979; Davis et al., 1982; Davis & Huchra, 1982), 6dFGS (Jones et al., 2009), 2MASS (Huchra et al., 2012) and Sloan Digital Sky Survey (SDSS Collaboration, 2000; Dawson et al., 2013). The state-of-the-art telescopes can measure accurate redshifts with spectroscopy and detect faint galaxies. The distribution of galaxies is the tracer of dark matter distribution and one can infer dynamics of dark matter from the galaxy distribution.

One of major probes which have played a crucial role in modern observational cosmology is *gravitational lensing*. In Newton's theory, light always propagate along the straight line in vacuum. However, in general relativity, the path of light is subject to gravitational field, and as a result, bent path is realized. This effect is referred to as gravitational lensing. When we consider the propagation of light from distant sources such as galaxies,

images of the galaxies are distorted. This distortion is caused by the gravitational field of intervening matter in the Universe. At the location of the strongly distorted image, more matter exists. Generally, the distortion is very weak and thus it is specifically called as weak gravitational lensing (WL). Analyzing statistically a lot of shapes of galaxies, we can measure the weak lensing signal at significant level. WL has played a crucial role in observational cosmology because WL is a unique observable which can directly map the distribution of matter in the Universe. For other observables, it is necessary to take an assumption about relation between visible and dark matter, e.g., galaxy bias. On the other hand, WL probes into the distribution without such assumptions. That is why WL has important meaning in modern observational cosmology. However, the detection of WL is quite challenging due to the small signal. The modern observational technique and progress in image analysis enables one to measure the effect with a few percent accuracy. The precise measurements of WL provide us a useful way to discern cosmological models. On the other hand, as the accuracy of measurements increases, the discrepancy of results between CMB and WL has been reported. The CMB measurement estimates the higher amplitude of the matter power spectrum, i.e., σ_8, than those estimated from WL (see, e.g., Battye et al., 2015). Since these observables probe into matter distribution at different epochs, the tension can be reconciled if some physical processes suppress the growth of structures only at low redshift, where WL probes into large-scale structures.

Another important probe in observational cosmology is *galaxy clusters*. Galaxy clusters are the assembly of thousands of galaxies and the most massive bound objects in the Universe. The formation and evolution of galaxy clusters is sensitive to the underlying physics or law of gravity. For example, the abundance of galaxy clusters with respect to mass is employed to test or falsify the theory of gravity, i.e., general relativity or modified gravity. This approach in cosmology with galaxy clusters is referred to as *cluster cosmology*. In addition to cosmology, galaxy clusters are important also in astrophysics. The intra-cluster medium (ICM), which corresponds to hot and diffuse gas in galaxy clusters, is heated during infall through the deep gravitational potential and emits energetic radiation via free-free emission. The thermodynamic properties of ICM reflect complex physical processes: violent feedback from supernovae and active galactic nuclei, turbulence, and magnetic field. Thus, galaxy clusters are regarded as the laboratories of extreme (astro)physics and one of main targets in X-ray astronomy. Furthermore, the thermal Sunyaev–Zel'dovich effect (tSZ), which was proposed Sunyaev and Zel'dovich in their seminal works (Sunyaev & Zel'dovich, 1972, 1980), also provides a novel way to observe galaxy clusters. This effect denotes the anisotropy of CMB temperature created after last scattering. When CMB photons pass through galaxy clusters, energetic electrons transfer their energy to the photons via inverse Compton scattering. The tSZ effect probes the distribution of ICM. Although we have to assume the relation between gas and matter distributions, from tSZ we can reconstruct the large-scale structures and, at the same time, address the thermal properties of gas in galaxy clusters.

1.3 Hydrostatic Mass Bias of Galaxy Clusters

In cluster cosmology, the mass function of galaxy clusters plays a key role. Thus, the mass of galaxy clusters is the most fundamental quantity which characterizes the galaxy clusters. WL can directly reconstruct mass of galaxy clusters, but the samples detected by WL are limited to very massive clusters. Therefore, X-ray or tSZ observations are employed to explore the larger samples of galaxy clusters. However, for these probes, the mass is not a direct observable, and we need to convert the observed flux to the mass. In many applications, galaxy clusters are assumed to be in hydrostatic equilibrium (HSE), where the thermal pressure balances the self-gravity of galaxy clusters. For example, in X-ray observations, we can measure the pressure and under the hydrostatic equilibrium, the mass is reconstructed by radially integrating pressure. The reconstructed mass is referred to as *hydrostatic mass*. For several galaxy clusters which can be detected both through WL and X-ray or tSZ observations, the hydrostatic mass and true mass can be estimated, and this type of the measurements is called as mass calibration measurements. The deviation from unity of the ratio between the true mass and hydrostatic mass is defined as the hydrostatic bias $b \equiv 1 - M_{\rm HSE}/M_{\rm true}$. The measured hydrostatic mass is 10–30% less than the true mass, which indicates the deviation from HSE, i.e., the existence of physical processes which support the self-gravity other than the thermal pressure. Such processes are called as *non-thermal pressure*. The amplitude of non-thermal pressure directly affects the mass estimate of galaxy clusters and may cause the bias in cosmological parameters from cluster counts. Thus, for accurate determination of cosmological parameters with cluster counts, the evaluation of non-thermal pressure contribution is essential. The origin of non-thermal pressure is still uncertain, but the dominant source is thought to be turbulent motion in galaxy clusters. From hydrodynamical simulations, the contribution due to the non-thermal pressure is estimated as $\sim 20\%$ (Suto et al., 2013; Shi et al., 2016), which is consistent with the mass calibration measurements. However, in the simulations and measurements, the samples are limited to massive clusters ($> 10^{14}\,{\rm M}_\odot$), and the contribution in low-mass galaxy clusters has not clearly been addressed yet. Interestingly, the analyses with tSZ auto-power spectrum or cluster counts of SZ detected sources suggest larger non-thermal contribution $\sim 40\%$ (Planck Collaboration, 2016d,e).

1.4 The Cross-Correlation of The Thermal Sunyaev–Zel'dovich Effect and Weak Lensing

As we have seen, WL and the tSZ effect are effective ways in cosmology because both are sensitive to density fluctuation in the Universe and probe the structures at different epochs. Furthermore, the tSZ effect reflects the gas distribution, and we can probe the ICM through the tSZ effect, which is a key to figure out the source of the discrepancy of the hydrostatic bias. However, there are several difficulties in the tSZ effect. The measurement of the tSZ effect is quite noisy because the amplitude is much lower than the foreground and primary anisotropy of CMB temperature. Another difficulty in tSZ is that the observable for tSZ is a projected statistics and has no information in time

domain, i.e., redshifts. In order to evade these problems, we employ the *cross-correlation* of tSZ and WL in this dissertation. Since both of WL and tSZ trace the large-scale structures, the significant cross-correlation is expected. One of the advantages of the cross-correlations is that we can preferentially extract the information of ICM at the redshift $z \simeq 0.5$–1, where cluster formation and merger events actively occur, because WL probes the large-scale structures at this range. The cross-correlations yield significant gain of information compared with the case only with power spectra (in the case of WL and galaxy clustering, Miyatake et al. (2015); More et al. (2015); DES Collaboration (2017), and tSZ and galaxy clustering, Makiya et al. (2018)). Furthermore, the cross-correlation is complementary to the tSZ auto-correlation, which is sensitive to the structures at higher redshifts ($z \gtrsim 1$). In addition, the cross-correlations measured based on maps contain the signals from low-mass halos, which are unresolved in the SZ survey due to the small signal. In this dissertation, we present the analysis of the recent measurement of the cross-correlation with Red Cluster Sequence Lensing Survey (RCSLenS) and *Planck* (Hojjati et al., 2017) to constrain the σ_8 parameter and the contribution of the non-thermal pressure support with the analytical modeling of ICM. Subsequently, we present the results of the measurement with the Hyper Suprime-Cam (HSC) survey and *Planck*. Due to the deep observations by HSC, we can probe into structures at higher redshifts.

1.5 Organization of the Dissertation

The dissertation is organized as follows. In Chapter 2, we review the modern picture of the Universe, which has been established in the last decade and is now regarded as the standard model in cosmology, and basics of cosmological statistics which characterize the Universe. In Chapter 3, we review basics of gravitational lensing both in theoretical and observational aspects. In Chapter 4, we review astrophysical and cosmological aspects related with galaxy clusters with particular emphasis on the tSZ effect. Numerical methods in astrophysics and cosmology are discussed in Chapter 5. We present two studies on the cross-correlations of WL and tSZ. In Chapter 6, the analysis of measurements of cross-correlations from RCSLenS and *Planck* is presented, and in Chapter 7, we present measurements of the cross-correlations with the data from the HSC survey and *Planck*. Finally, we present concluding remarks in Chapter 8.

Chapter 2

Concordance Paradigm of Cosmology

Contents

In this Chapter, we review the standard and modern picture of cosmology. First we discuss the homogeneous and isotropic Universe, and then we extend it to the anisotropic and inhomogeneous Universe, which is the main target of modern observational cosmology. The topics we will cover have been established by previous works in these decades. We owe it to many pedagogical books and review articles, e.g., Weinberg (1972); Peebles (1980, 1993); Dodelson (2003); Weinberg (2008).

2.1 Homogeneous and Isotropic Universe

2.1.1 General Relativity

The theory of general relativity (GR) (Einstein, 1916) describes the gravity as consequence of curvature of the space-time. This distortion of the space-time is mathematically described by the *metric* $g_{\mu\nu}$. The metric is determined by a set of covariant equations, i.e., *Einstein equation*,

$$R_{\mu\nu} - \frac{1}{2}Rg_{\mu\nu} + \Lambda g_{\mu\nu} = \frac{8\pi G}{c^4}T_{\mu\nu}\,, \tag{2.1}$$

where $R_{\mu\nu}$ is the Riemann tensor, $R = R^{\mu}{}_{\mu}$ is the Ricci scalar, Λ is the cosmological constant, and $T_{\mu\nu}$ is the energy-momentum tensor. The structure of space-time is coupled with matter or energy via Einstein equation. For a perfect fluid at rest, $T^{\mu}{}_{\nu}$ takes a diagonal form,

$$T^{\mu}{}_{\nu} = \begin{pmatrix} -\rho & & & \\ & p & & \\ & & p & \\ & & & p \end{pmatrix}, \tag{2.2}$$

where ρ is the energy density of the fluid, p is the pressure, and off-diagonal terms are zero. Einstein equation is a set of partial differential equations, and intractable to solve in general cases. However, in the case of the Universe, the following two conditions simplify the situation.

1. When observables are averaged over large scales ($\gtrsim 100\,\mathrm{Mpc}$), there exists a frame where all properties are seen isotropic.

2. In such a frame, all fundamental observers experience the same history of the Universe.

These two postulations are referred to as *cosmological principles*, which are grounded on observational facts. In other words, there is no special location and direction in the

Universe. According to these assumptions, the form of the line element of the space-time can be simplified as

$$ds^2 = g_{\mu\nu}dx^\mu dx^\nu = -c^2dt^2 + a^2(t)[d\chi^2 + f_K^2(\chi)(d\phi^2 + \sin^2\theta d\theta^2)], \tag{2.3}$$

where

$$f_K(\chi) = \begin{cases} K^{-1/2}\sin(K^{1/2}\chi) & (K > 0) \\ \chi & (K = 0) \\ (-K)^{-1/2}\sinh[(-K)^{1/2}\chi] & (K < 0), \end{cases} \tag{2.4}$$

where K is the spatial curvature, which determines the global geometry of the Universe. The negative curvature ($K < 0$) corresponds to closed Universe, where the space can be described as sphere. On the other hand, the Universe with the positive curvature ($K > 0$) is called as open Universe, where the space is hyperbolic. Here, we introduced the *scale factor* $a(t)$, which represents the homogeneous expansion of space[1]. This isotropic metric is called as *Friedmann–Lemaître–Robertson–Walker metric*. By plugging the metric into the Einstein equation (Eq. 2.1), the evolution of the scale factor is obtained,

$$\left(\frac{\dot{a}}{a}\right)^2 = \frac{8\pi G}{3c^2}\rho - \frac{Kc^2}{a^2} + \frac{c^2\Lambda}{3}, \tag{2.5}$$

$$\frac{\ddot{a}}{a} = -\frac{4\pi G}{3c^2}(\rho + 3p) + \frac{c^2\Lambda}{3}. \tag{2.6}$$

The first equation is known as *Friedmann equation* (Friedmann, 1922, 1924). Combining these two equations, the following equation can be yielded,

$$\frac{d}{dt}(\rho a^3) + p\frac{da^3}{dt} = 0. \tag{2.7}$$

This is called as the adiabatic equation, which corresponds to energy conservation for an adiabatic fluid. We also need the equation of state (EoS), i.e., the relation between energy density ρ and pressure p, to close this set of equations. The EoS for representative components are listed below.

Radiation Relativistic species (photons and massless neutrinos) have non-negligible pressure. Assuming they are in thermal equilibrium, the EoS is expressed as

$$p = \frac{1}{3}\rho. \tag{2.8}$$

Matter The baryons and cold dark matter are non-relativistic even in the early Universe. In the late-time Universe, massive neutrinos also become non-relativistic as they lose momentum in the expanding Universe. Their pressure is sufficiently small with respect to energy density. We can ignore the contribution, i.e.,

$$p \ll \rho. \tag{2.9}$$

[1]The normalization of the scale factor is arbitrary, but usually the present value is set to be unity, $a(t_0) = 1$.

Dark energy There is no definite form of EoS for dark energy. Some theoretical models predict the functional form of equation of state. Thus, it is convenient to parametrize EoS as

$$p = w\rho, \tag{2.10}$$

where w is called as EoS parameter, and it can be an arbitrary function. The cosmological constant works as the dark energy which exerts repulsive force. From the Friedmann equation (Eq. 2.5), the energy density ρ_Λ and the pressure p_Λ are

$$\rho_\Lambda = \frac{c^4\Lambda}{8\pi G},\ p_\Lambda = -\frac{c^4\Lambda}{8\pi G}. \tag{2.11}$$

Therefore, the EoS becomes

$$p_\Lambda = -\rho_\Lambda. \tag{2.12}$$

For cosmological constant, the pressure becomes negative.

To summarize, the EoS for each component is

$$p = w\rho,\ w = \begin{cases} \frac{1}{3} & \text{(Radiation)} \\ 0 & \text{(Matter)} \\ -1 & \text{(Cosmological constant).} \end{cases} \tag{2.13}$$

Some dark energy models, e.g., quintessence (Tsujikawa, 2013), permit w varying with time.

So far, we deal with the single component fluid, but in reality, the Universe is mixture of multiple components. When the interaction between different components is inefficient, each component can be regarded as isolated and the energy-momentum tensor is the sum of the tensors for each component,

$$T^\mu{}_\nu = \sum_A (T_A)^\mu{}_\nu, \tag{2.14}$$

where A is the label of a component. Therefore, the density and pressure are also can be the sum of each component,

$$\rho = \sum_A \rho_A,\ p = \sum_A p_A. \tag{2.15}$$

When there exists an interaction between different components, we have to consider the energy transfer. However, in the late epoch, each component evolves adiabatically due to little interactions. In such a case, the time evolution of the density ρ_A can be determined from the adiabatic equation (Eq. 2.7),

$$\rho_A = \rho_{A0} a^{-3(1+w_A)}, \tag{2.16}$$

where ρ_{A0} is the density at present.

2.1.2 Cosmological Parameters and Initial Conditions of the Universe

The cosmological models contain parameters to characterize the Universe, which cannot be given by first principles. Here, we introduce commonly used parameters, which are called as *cosmological parameters*.

The first one is *Hubble constant* of the present value H_0, which represents the expansion rate of the present Universe. The expansion rate varies with time and it is defined as

$$H = \frac{\dot{a}}{a}. \tag{2.17}$$

This quantity is called as *Hubble parameter*. Edwin Hubble found that galaxies recede from us and the velocity is proportional to the distance from the observer d (Hubble, 1929),

$$v = H_0 d. \tag{2.18}$$

Observationally, it has been difficult to precisely determine the Hubble constant. There has been a long argument about the precise value of the Hubble constant. Among cosmological parameters, Hubble constant has large uncertainty. Conventionally, H_0 is parametrized as

$$H_0 = 100h\,\mathrm{km\,s^{-1}\,Mpc^{-1}}. \tag{2.19}$$

In cosmological studies, we leave Hubble constant undetermined as all resultant quantities have h in their units, like $h^{-1}\,\mathrm{M_\odot}$ or $h^{-1}\,\mathrm{kpc}$.

From the Friedmann equation (Eq. 2.5),

$$H_0^2 = \frac{8\pi G}{3c^2}\rho_0 - c^2 K, \tag{2.20}$$

ρ_0 is the sum of the present energy densities,

$$\rho_0 = \sum_A \rho_{A0}. \tag{2.21}$$

We can define the *critical density* ρ_{cr} as

$$\rho_{\mathrm{cr}} = \frac{3c^2 H_0^2}{8\pi G} = 1.878 \times 10^{-26}\,h^2\,\mathrm{kg\,m^{-3}} = 2.775 \times 10^{11} h^2\,\mathrm{M_\odot\,Mpc^{-3}}. \tag{2.22}$$

This density corresponds to the density in the no curvature Universe.

First, let us consider the energy density of the relativistic particles. The most important relativistic particle is photon. Since photons are bosons, from Bose–Einstein distribution, the energy density of photons are given as

$$\rho_\gamma = \frac{\pi^2}{15}\frac{k_{\mathrm{B}}^4}{\hbar^3 c^3} T_\gamma^4, \tag{2.23}$$

where T_γ is the temperature and its present value is $T_\gamma = 2.725\,\mathrm{K}$. Another relativistic particle is (massless) neutrino. Neutrinos decouple from other particles earlier than photons, because neutrinos interact only via weak interaction. At the neutrino decoupling,

electrons and anti-electrons are in thermal equilibrium, and they decay into photons as the cosmic plasma cools down. Thus, photons have higher temperature than neutrinos, and the temperature of neutrinos T_ν can be computed from entropy conservation,

$$T_\nu = \left(\frac{4}{11}\right)^{\frac{1}{3}} T_\gamma. \tag{2.24}$$

Hence, the total energy density of the radiation component in the present Universe is

$$\rho_{\rm r} = \frac{\pi^2}{30}\frac{k_{\rm B}^4}{\hbar^3 c^3} g_* T_\gamma^4, \tag{2.25}$$

where g_* is the effective degree of freedom:

$$g_* = 2 + \frac{7}{8} \times 3 \times 2 \times \left(\frac{4}{11}\right)^{\frac{4}{3}} \simeq 3.363. \tag{2.26}$$

The energy density is frequently parametrized with respect to the critical density as

$$\Omega_{\rm r} = \frac{\rho_{\rm r}}{\rho_{\rm cr}}. \tag{2.27}$$

The densities of baryon, dark matter, and massive neutrinos are not given ab initio. Similarly to photons, it is useful to define the energy density with respect to the critical density,

$$\Omega_{\rm b} = \frac{\rho_{\rm b}}{\rho_{\rm cr}},\ \Omega_{\rm cdm} = \frac{\rho_{\rm cdm}}{\rho_{\rm cr}},\ \Omega_\nu = \frac{\rho_\nu}{\rho_{\rm cr}}. \tag{2.28}$$

The energy density of massive neutrinos can be given with respect to the total mass of massive neutrinos M_ν,

$$\Omega_\nu = \frac{M_\nu}{93.14\, h^2\, {\rm eV}}. \tag{2.29}$$

Similarly, the total matter density can be written as

$$\Omega_{\rm m} = \Omega_{\rm b} + \Omega_{\rm cdm} + \Omega_\nu. \tag{2.30}$$

The curvature energy density becomes

$$\Omega_K = -\frac{c^2 K}{H_0^2}. \tag{2.31}$$

As a result, the following identity holds,

$$\sum_A \Omega_A + \Omega_K = 1. \tag{2.32}$$

The current observational facts show our Universe is mainly composed of dark matter and cosmological constant, and indicate no curvature, i.e., flat Universe. The cosmological model, where the Universe is made of baryons, (cold) dark matter, and cosmological constant without curvature, is called as the flat ΛCDM model.

If the Universe is homogeneous from the beginning, the homogeneity is kept until present. This clearly contradicts the observation, which shows complex structures of galaxies in the sky. In order to explain it, we need a seed of fluctuations of density or metric. In the modern paradigm, the fluctuations are thought to be generated through the exponential expansion in the very early Universe, which is called as *inflation* (Starobinsky, 1980; Sato, 1981; Guth, 1981). During the inflation era, the quantum fluctuation is stretched and become classical fluctuation. There are two types of production of initial perturbation. One is called as *adiabatic perturbation*, where the entropy is conserved by the condition,

$$\frac{\delta\rho_{\rm r}}{\rho_{\rm r}} = \frac{4}{3}\frac{\delta\rho_{\rm m}}{\rho_{\rm m}}. \tag{2.33}$$

This type of initial condition also generates the perturbation of spatial curvature, and the power spectrum of curvature perturbation is parametrised as

$$\frac{k^3}{2\pi^2}P_\zeta(k) = A_{\rm s}\left(\frac{k}{k_0}\right)^{n_{\rm s}-1}, \tag{2.34}$$

where $A_{\rm s}$ is the amplitude, $n_{\rm s}$ is the power-law index and k_0 is the pivot scale, which is usually fixed at the large scale. Then, the initial power spectrum of matter fluctuation is given as (Takada et al., 2006)

$$P_{\rm m}(k) = \left(\frac{2k^2}{5H_0^2\Omega_{\rm m}}\right)^2 P_\zeta(k). \tag{2.35}$$

The other type of initial condition is called as *isocurvature perturbation*, where there is no density perturbation but the fluctuation of entropy perturbation gives rise to fluctuation of density. Even before the discovery of the inflation, the shape of power spectrum was predicted as the power-law by Harrison (1970); Zel'dovich (1972) and the power-law index is close to the unity. Furthermore, the theory of inflation predicts $n_{\rm s}$ should be close to the unity but slightly less than the unity. Therefore, the deviation of $n_{\rm s}$ from unity would be the smoking gun of the inflation.

There is another commonly used parameter which determines the amplitude of the power spectrum, which is more connected with observations. The parameter is σ_8, which is the standard deviation of the mass variance smoothed with the top-hat filter of the radius $R = 8\,h^{-1}$ Mpc. We will give the definition in Eq. (2.102).

These parameters are quite accurately and precisely determined by the modern cosmological observations, e.g., measurements of the anisotropy and polarization of cosmic microwave background. Figure 2.1 shows constraints on cosmological parameters utilizing the result of the *Planck* survey (Planck Collaboration, 2016c).

2.1.3 Cosmological Redshift and Distance Measures

Since the Universe is expanding, every two objects recede each other. When we observe a light emitting object, the observed frequency can be different from the one at the rest

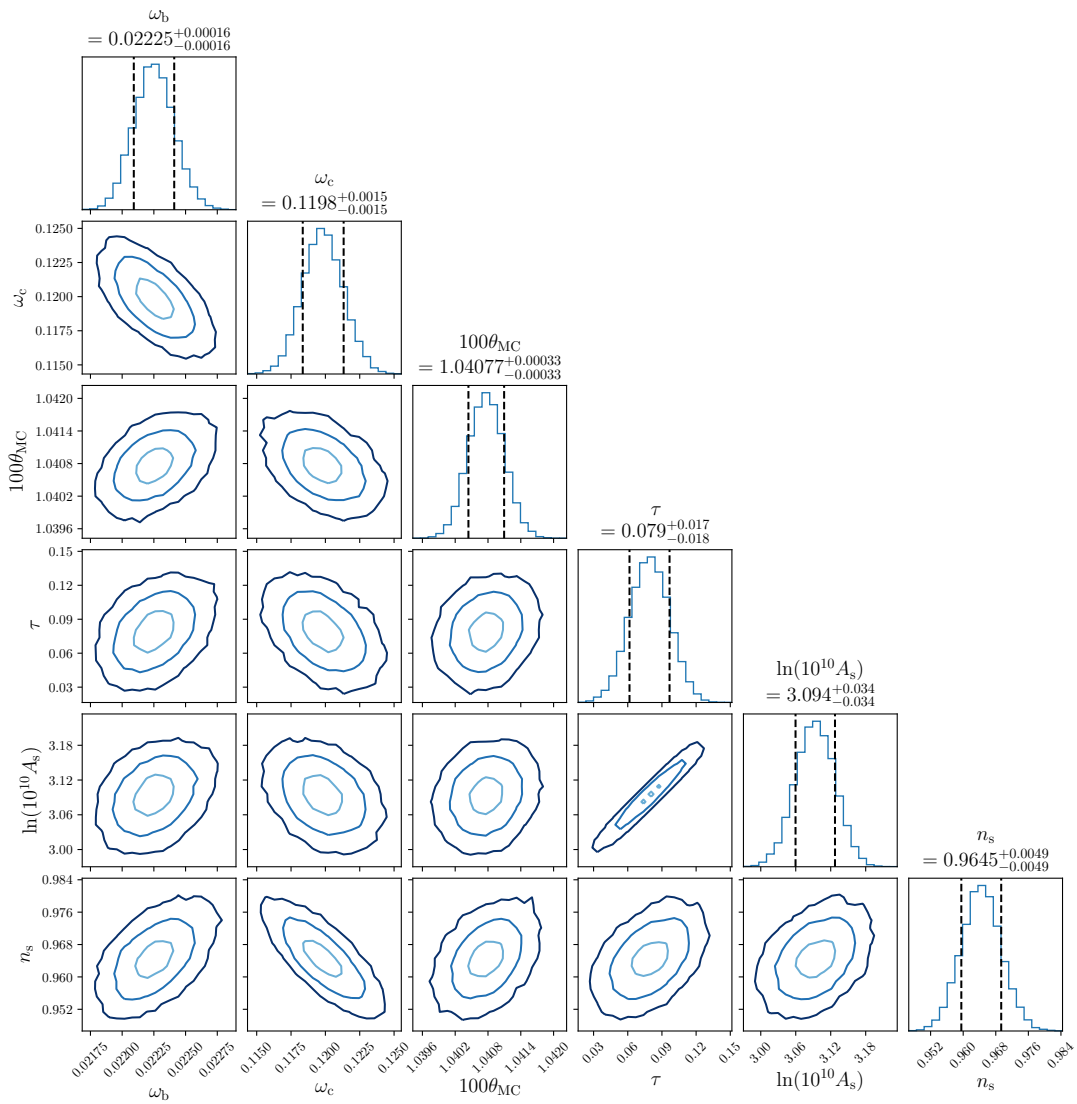

Figure 2.1: 2D posterior distribution of six standard cosmological parameters. The light, normal, and dark circles correspond to 1-σ, 2-σ, and 3-σ confidence levels, respectively. This results are based on TT,TE,EE+lowP dataset of *Planck* 2015 measurements (Planck Collaboration, 2016b,c).

frame, which corresponds to Doppler effect. Consider the situation that light travels from the distant place to us. Due to the cosmic expansion, the wavelength is stretched and as a result the frequency of the photon decreases. This phenomenon is called as *cosmological redshift* or simply *redshift*. Suppose that light is emitted at $t = t_{\rm e}$ and observed at $t = t_{\rm o}$. Then, the light of the same phase is emitted again at $t = t_{\rm e} + \Delta t_{\rm e}$ and reaches at $t = t_{\rm o} + \Delta t_{\rm o}$. From the geodesic equation for light $ds^2 = 0$, the comoving distance between the source and observer is

$$\chi = \int_{\rm e}^{\rm o} d\chi = \int_{t_{\rm e}}^{t_{\rm o}} \frac{c}{a} dt = \int_{t_{\rm e}+\Delta t_{\rm e}}^{t_{\rm o}+\Delta t_{\rm o}} \frac{c}{a} dt. \tag{2.36}$$

Assuming the period is short compared with the cosmic expansion, we can ignore the variation of the scale factor with time,

$$\int_{t_{\rm e}+\Delta t_{\rm e}}^{t_{\rm o}+\Delta t_{\rm o}} \frac{c}{a} dt - \int_{t_{\rm e}}^{t_{\rm o}} \frac{c}{a} dt \simeq \frac{c\Delta t_{\rm e}}{a(t_{\rm e})} - \frac{c\Delta t_{\rm o}}{a(t_{\rm o})} = 0, \tag{2.37}$$

and by converting the period to the wavelength,

$$\frac{\lambda_{\rm o} - \lambda_{\rm e}}{\lambda_{\rm e}} = \frac{a(t_{\rm o})}{a(t_{\rm e})} - 1, \tag{2.38}$$

where $\lambda_{\rm e}$ ($\lambda_{\rm o}$) is the wavelength at the source (observer) frame. Accordingly, if we observe light from the distant source, the wavelength is stretched due to cosmic expansion. The fractional expansion of wavelength is defined as redshift z,

$$z \equiv \frac{\lambda_{\rm o} - \lambda_{\rm e}}{\lambda_{\rm e}} = \frac{a(t_{\rm o})}{a(t_{\rm e})} - 1. \tag{2.39}$$

As we have seen, the space-time is not static nor flat. Hence, the idea of distance is not unique, and there are different definitions depending on the situation where the distance is measured. We introduce several distance measures frequently used in astronomy and cosmology.

Hubble distance The Hubble distance represents the characteristic length scale in the expanding Universe,

$$D_H = \frac{c}{H_0} = 9.26 \times 10^{27}\, h^{-1}\,\mathrm{cm}. \tag{2.40}$$

Radial comoving distance This distance represents the comoving distance which light travels from the observer to the event. From the geodesic equation of light $ds^2 = 0$ and Friedmann equation, line-of-sight comoving distance D_C should become

$$D_C = \int d\chi = \int \frac{c}{a} dt = D_H \int \frac{1}{a^2 E(a)} da. \tag{2.41}$$

Here we have introduced the expansion factor $E(a)$,

$$E(a) = \frac{H}{H_0} = \left(\frac{\Omega_{\rm r}}{a^4} + \frac{\Omega_{\rm m}}{a^3} + \frac{\Omega_K}{a^2} + \frac{\Omega_{\rm de}}{a^{3(1+w_{\rm de})}} \right)^{\frac{1}{2}} \tag{2.42}$$

In the standard flat ΛCDM Universe, Ω_K is zero, $\Omega_{\rm r}$ is negligible, and $w_{\rm de} = -1$. The following form of the expansion factor is commonly used,

$$E(a) = \left(\frac{\Omega_{\rm m}}{a^3} + \Omega_\Lambda\right)^{\frac{1}{2}}. \tag{2.43}$$

Transverse comoving distance The comoving distance between two points of the same redshift but separated with the small angle $d\theta$ is written as $D_M d\theta$, where D_M is the transverse comoving distance,

$$D_M = \begin{cases} D_H(\Omega_K)^{-1/2}\sinh\left(\sqrt{\Omega_K}D_C/D_H\right) & (K<0) \\ D_C & (K=0) \\ D_H(-\Omega_K)^{-1/2}\sin\left(\sqrt{-\Omega_K}D_C/D_H\right) & (K>0). \end{cases} \tag{2.44}$$

When the Universe is spatially flat, the transverse comoving distance coincides with the radial comoving distance.

Angular diameter distance Angular diameter distance is similar to the transverse comoving distance but differs in that the angular diameter distance corresponds to the proper distance. The angular diameter distance D_A is expressed as

$$D_A = aD_M = \frac{D_M}{1+z}. \tag{2.45}$$

Luminosity distance The luminosity distance is defined from the inverse power-law between the bolometric flux f and the bolometric luminosity L,

$$f = \frac{L}{4\pi D_L^2},\ D_L = \sqrt{\frac{L}{4\pi f}}. \tag{2.46}$$

The luminosity distance is related with the transverse comoving distance and angular diameter distance as follows,

$$D_L = (1+z)D_M = (1+z)^2 D_A, \tag{2.47}$$

which reflects the effect of the variation of angular sizes and frequency diminishing.

Figure 2.2 shows the comparison of three distance measures in two different cosmologies. Refer to Hogg (1999) for a thorough review about distance measures.

2.2 Growth of Structures in the Inhomogeneous Universe

Even at the glance of the sky, we learn the Universe is not actually homogeneous because there exists rich structures, such as stars and galaxies. As the next step from the previous Sections, we deal with inhomogeneity of the Universe and consider the growth of structures due to gravity.

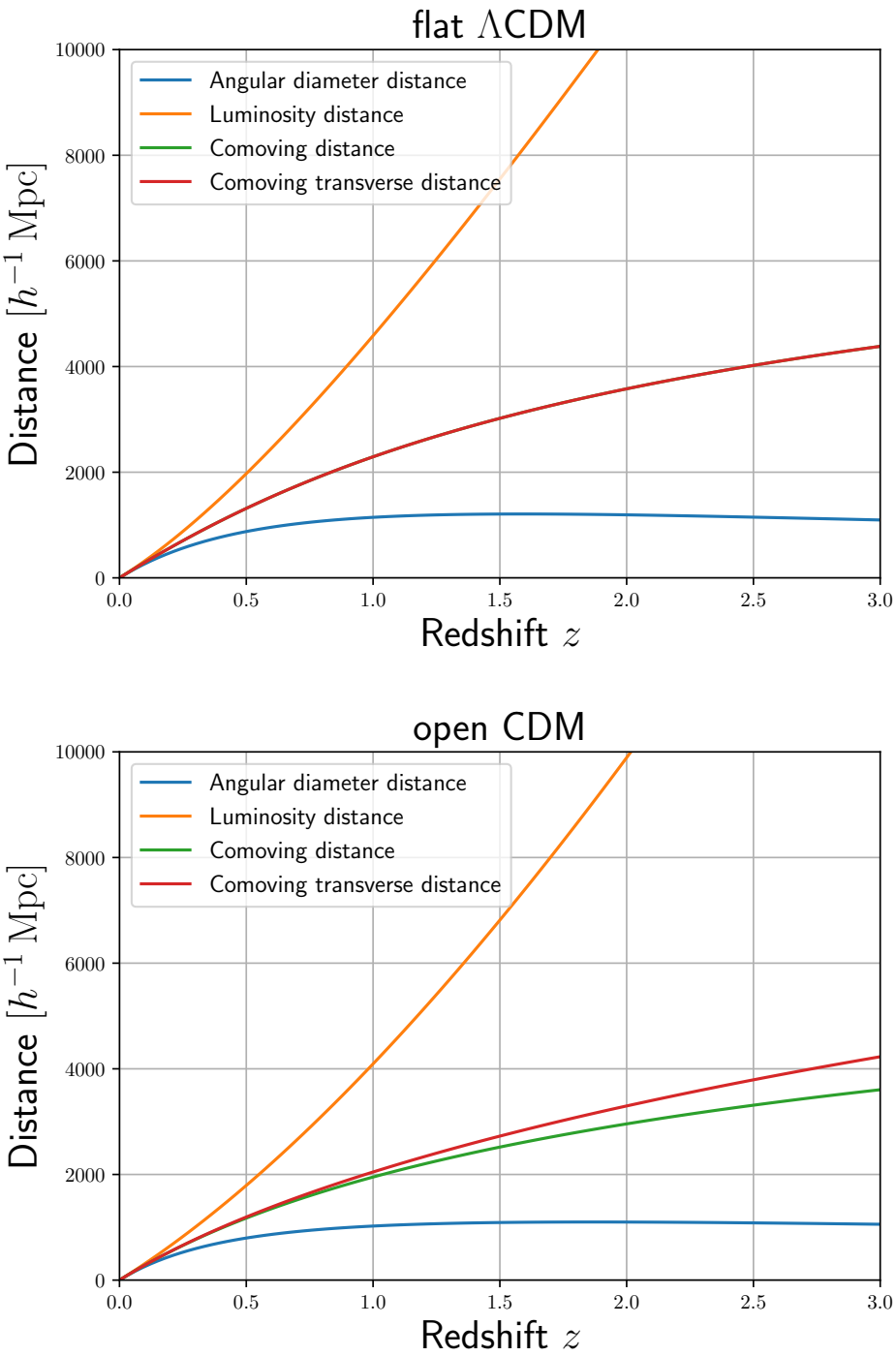

Figure 2.2: Comoving distance, angular diameter distance, and luminosity distance for a given cosmology. We adopt flat ΛCDM cosmology with $\Omega_{\mathrm{m}} = 0.3156$, $h = 0.6727$ and $\Omega_\Lambda = 1 - \Omega_{\mathrm{m}} = 0.6844$.

2.2.1 Linear Evolution of Density Fluctuation

We consider the case where the density field depends on the location. It is useful to introduce the deviation from the mean, i.e., *density contrast* δ,

$$\delta = \frac{\rho - \bar{\rho}}{\bar{\rho}}, \tag{2.48}$$

where $\bar{\rho}$ is a mean density[2]. The mean density follows equations in the homogeneous Universe like Friedmann equation.

Next we derive basic equations for δ. The matter in the inhomogeneous Universe can be regarded as a fluid on large scales. Thus, the basic equations are continuity equation, Euler equation, and Poisson equation for gravity,

$$\frac{\partial \rho}{\partial t} + \nabla \cdot (\rho \boldsymbol{v}) = 0, \tag{2.49}$$

$$\frac{\partial \boldsymbol{v}}{\partial t} + (\boldsymbol{v} \cdot \nabla)\boldsymbol{v} = -\frac{1}{\rho}\nabla p - \nabla \Phi, \tag{2.50}$$

$$\nabla^2 \Phi = 4\pi G \rho. \tag{2.51}$$

These equations can be modified using δ. Since the Universe is expanding, the velocity can decomposed into Hubble flow $H\boldsymbol{x}$ and the one caused by external force. The latter is called as *peculiar velocity* $\boldsymbol{u}$, i.e.,

$$\boldsymbol{u} = \frac{1}{a}\boldsymbol{v} - H\boldsymbol{x} \tag{2.52}$$

In other words, the peculiar velocity corresponds to the velocity in the comoving frame. Hereafter, we work on the comoving frame, and spatial derivatives are with respect to this frame. We rewrite these basic equations,

$$\frac{\partial \delta}{\partial t} + \frac{1}{a}\nabla \cdot [(1+\delta)\boldsymbol{u}] = 0, \tag{2.53}$$

$$\frac{\partial \boldsymbol{u}}{\partial t} + \frac{\dot{a}}{a}\boldsymbol{u} + \frac{1}{a}(\boldsymbol{u} \cdot \nabla)\boldsymbol{u} = -\frac{1}{a\bar{\rho}(1+\delta)}\nabla p - \nabla\left(\frac{\phi}{a}\right), \tag{2.54}$$

$$\nabla^2 \phi = 4\pi G \bar{\rho} a^2 \delta, \tag{2.55}$$

$$\phi = \Phi + \frac{a\ddot{a}}{2}x^2. \tag{2.56}$$

We redefined the gravitational potential ϕ, from which the contribution from inertial force by expansion is added. It is quite difficult to solve the set of equations because gravity works nonlinearly. As the first approximation, we consider the regime where δ and $\boldsymbol{u}$ are sufficiently small and linearize these equations with respect to these two variables. In addition, when matter is dominant in the Universe, pressure is negligible. Accordingly,

[2]Hereafter, the symbol ρ denotes the matter density, though in previous sections ρ denoted the energy density.

we can ignore the term which contains pressure in the Euler equation. The linearized continuity and Euler equations are

$$\frac{\partial \delta}{\partial t} + \frac{1}{a}\nabla \cdot \boldsymbol{u} = 0, \tag{2.57}$$

$$\frac{\partial \boldsymbol{u}}{\partial t} + \frac{\dot{a}}{a}\boldsymbol{u} = -\nabla\left(\frac{\phi}{a}\right). \tag{2.58}$$

Dropping out $\boldsymbol{u}$,

$$\ddot{\delta} + 2\frac{\dot{a}}{a}\dot{\delta} - 4\pi G\bar{\rho}\delta = 0. \tag{2.59}$$

Since we know the evolution of the scale factor and the mean density from the Friedmann equation, this equation can be solved analytically. Introducing a new variable $y = a\delta$ and substituting this, we get

$$\ddot{y} - \left(\frac{\ddot{a}}{a} + 4\pi G\bar{\rho}\right) y = 0. \tag{2.60}$$

From the Friedmann equation,

$$\dddot{a} - \frac{\ddot{a}\dot{a}}{a} - 4\pi G\dot{a}\bar{\rho} = 0 \tag{2.61}$$

Therefore $y = \delta$ is a special solution. Replacing y with $y = \dot{a}w$,

$$\dot{a}\ddot{w} + 2\ddot{a}\dot{w} = 0 \tag{2.62}$$

The solution of this equation is

$$w \propto \int \frac{dt}{\dot{a}^2} = \int \frac{da}{\dot{a}^3}. \tag{2.63}$$

Finally, two independent solutions without constant are found,

$$D_+ = H\int_0^a \frac{da}{a^3H^3}, \tag{2.64}$$

$$D_- = H. \tag{2.65}$$

Since Hubble parameter decreases with time, the second solution $\delta \propto D_-$ corresponds to the decaying mode. The first one $\delta \propto D_+$ grows with time and called as *linear growth factor*. As an important case, in Einstein–de Sitter Universe ($\Omega_\mathrm{m} = 1, \Omega_\Lambda = 0$),

$$D_+ \propto a, \tag{2.66}$$

$$D_- \propto a^{-3/2}. \tag{2.67}$$

In the case of the ΛCDM model, dark energy dominates at the late epoch. The acceleration prevents matter fluctuation from growing. As a result, the growth factor is smaller than one in the Einstein–de Sitter Universe.

2.2.2 Spherical Collapse Model

Since the initial fluctuations just after inflation are very tiny $\delta \sim \mathcal{O}(10^{-5})$, the linear theory discussed above is valid in an early epoch and on large scales. However, once the fluctuation grows up to $\delta \sim \mathcal{O}(1)$, the linear theory breaks down. As gravity is attractive force, ambient matter falls into such high density regions, which results in formation of halos. Here, we introduce the *spherical collapse* model proposed by Gunn & Gott (1972), which describes the formation of halos in an analytical and phenomenological manner. Suppose that there is spherical matter around a certain point in the Universe and initial density contrast is denoted as $\delta_i \ll 1$. The equation of motion of the shell which radius is R is

$$\frac{d^2R}{dt^2} = -\frac{GM(<R)}{R^2}, \tag{2.68}$$

where $M(<R)$ is enclosed mass within R. Multiplying dR/dt and integrate with t,

$$\left(\frac{dR}{dt}\right)^2 = \frac{2GM}{R} + 2E. \tag{2.69}$$

Here, E corresponds to the energy and $E < 0$ represents a bound state. We can obtain the parametrized expression of $R(t)$ in terms of θ:

$$\begin{cases} R = (GM)^{1/3}A^2(1-\cos\theta), \\ t = A^3(\theta - \sin\theta), \end{cases} \tag{2.70}$$

where A is an integration constant. Hereafter, we assume the Universe is dominated by matter, i.e., Einstein–de Sitter Universe. In this case, the mean density is expressed as $\bar{\rho} = (6\pi G t^2)^{-1}$. The density contrast within the shell is

$$1 + \delta = \frac{\rho}{\bar{\rho}} = \frac{9}{2}\frac{(\theta - \sin\theta)^2}{(1-\cos\theta)^3}. \tag{2.71}$$

At first, the cosmic expansion surpasses the gravity. For later time, the shell turns around by gravity. This time corresponds to $\theta = \pi$ and corresponding quantities are

$$R_{\rm ta} = 2(GM)^{1/3}A^2,\ t_{\rm ta} = \pi A^3. \tag{2.72}$$

And the density contrast at $t_{\rm ta}$ is

$$\delta_{\rm ta} = \frac{9\pi^2}{16} - 1 \simeq 4.55 \tag{2.73}$$

At $t = t_{\rm coll} = 2t_{\rm ta}$, the spherical matter collapses into the center $R = 0$ and the density contrast diverges $\delta \to \infty$. But this picture does not capture the real situation correctly. In practice, the collapse is halted by virial motion in the middle of the collapse. We assume the shell is virialized at the half radius of $R_{\rm ta}$ at $t = t_{\rm coll}$. As $\bar{\rho} \propto t^{-2}$, the mean

density at the virialization is 1/4 of the one at the turning around. The density contrast should be

$$\delta_{\rm vir} = \frac{9\pi^2}{16} \times 4 \times 2^3 = 18\pi^2 \tag{2.74}$$

There is another important point in the spherical collapse model. In the early epoch ($\theta \ll 1$), the fluctuation is small and the linear theory can be used. If we expand R and t with θ,

$$\delta = \frac{3}{20}\theta^2 + \mathcal{O}(\theta^4),\ t = \frac{A^3}{6}\theta^3 + \mathcal{O}(\theta^5). \tag{2.75}$$

This gives $\delta \propto t^{2/3}$ at the lowest order, which is consistent with the linear theory. $\delta_{\rm L}$ is denoted as this linear fluctuation,

$$\delta_{\rm L}(t) = \frac{3(6t)^{2/3}}{20A^2}. \tag{2.76}$$

When we substitute $t = t_{\rm ta}$ and $t_{\rm coll}$,

$$\delta_{\rm L}(t_{\rm ta}) = \frac{3(6\pi)^{2/3}}{20} \simeq 1.06,\ \delta_{\rm L}(t_{\rm vir}) = \frac{3(12\pi)^{2/3}}{20} \simeq 1.69. \tag{2.77}$$

This means if the density fluctuation interpolated to the present exceeds 1.69, the fluctuation collapses and then forms a bound object which is referred to as a *halo*. Furthermore, the density profile of halos is of great importance, and we will discuss it in Section 2.4.3.

2.3 Statistics of the Large-Scale Structure

2.3.1 Correlation Function and Power Spectrum

So far, we have treated the evolution of the density of matter. Since the density field itself is a stochastic field, the value at a specific point has almost no meaning. We have to rely on statistical measures to extract properties of the density field.

We begin with the discussion for a general random field $g(\boldsymbol{x})$, where $\boldsymbol{x}$ denotes n-dimensional position[3]. We assume that the ensemble mean of $g(\boldsymbol{x})$ vanishes. For a field which has non-zero ensemble mean $\langle g(\boldsymbol{x})\rangle$, we can redefine $g(\boldsymbol{x})$ as $g(\boldsymbol{x}) - \langle g(\boldsymbol{x})\rangle$. If the translated field $g(\boldsymbol{x}+\boldsymbol{y})$ has no statistical difference from the original field $g(\boldsymbol{x})$, the field is *homogeneous*. Similarly, if the statistical properties do not change when we apply rotation to the field, the field is *isotropic*. We restrict ourselves to homogeneous and isotropic fields. The density field δ which we deal with satisfies these two properties. First, we introduce the *two-point correlation function*,

$$\langle g(\boldsymbol{x})g^*(\boldsymbol{y})\rangle = C_{gg}(|\boldsymbol{x}-\boldsymbol{y}|). \tag{2.78}$$

It depends only on the separation distance due to homogeneity and isotropy. Next, we apply Fourier transform to the field as

$$\hat{g}(\boldsymbol{k}) = \int d^n x\, g(\boldsymbol{x}) e^{-i\boldsymbol{k}\cdot\boldsymbol{x}},\ g(\boldsymbol{x}) = \int \frac{d^n k}{(2\pi)^n}\, \hat{g}(\boldsymbol{k}) e^{i\boldsymbol{k}\cdot\boldsymbol{x}}. \tag{2.79}$$

[3]This field of course depends on time. But we omit it for a simplicity.

The correlation function in Fourier space is given by

$$\langle g(\boldsymbol{k})g^*(\boldsymbol{k}')\rangle = \int d^n x\, e^{-i\boldsymbol{k}\cdot\boldsymbol{x}} \int d^n x'\, e^{i\boldsymbol{k}'\cdot\boldsymbol{x}'} \langle g(\boldsymbol{x})g^*(\boldsymbol{x}')\rangle. \tag{2.80}$$

Using two-point correlation function and substituting $\boldsymbol{x} = \boldsymbol{x}' + \boldsymbol{y}$, we get

$$\begin{aligned} \langle g(\boldsymbol{k})g^*(\boldsymbol{k}')\rangle &= \int d^n y\, e^{-i\boldsymbol{k}\cdot(\boldsymbol{x}'+\boldsymbol{y})} \int d^n x'\, e^{i\boldsymbol{k}'\cdot\boldsymbol{x}'} C_{gg}(y) \\ &= (2\pi)^n \delta_{\rm D}(\boldsymbol{k}-\boldsymbol{k}') \int d^n y\, e^{-i\boldsymbol{k}\cdot\boldsymbol{y}} C_{gg}(y) \\ &\equiv (2\pi)^n \delta_{\rm D}(\boldsymbol{k}-\boldsymbol{k}') P_g(k), \end{aligned} \tag{2.81}$$

where $\delta_{\rm D}$ is the Dirac delta function. In Eq. 2.81, we defined *power spectrum* as Fourier transform of two-point correlation function:

$$P_g(k) \equiv \int d^n x\, e^{-i\boldsymbol{k}\cdot\boldsymbol{x}} C_{gg}(x). \tag{2.82}$$

When the field is the density field, we usually call it as (3D) matter power spectrum, which is the most fundamental statistic for large-scale structures:

$$P_\delta(k) \equiv \int d^3 x\, e^{-i\boldsymbol{k}\cdot\boldsymbol{x}} C_{\delta\delta}(x). \tag{2.83}$$

Finally, we explain a *Gaussian random field* (GRF). The probability distribution of a GRF at a given point follows a Gaussian distribution. In addition, any linear combination of GRFs also becomes a GRF. In an early epoch, the probability distribution function of the density contrast δ follows a Gaussian distribution. It is known that power spectrum suffices to characterize a GRF and higher-order statistics like three-point correlation vanish. The detailed discussion of statistics of GRF is presented in Bardeen et al. (1986).

2.3.2 Two Dimensional Statistics: Limber Equation

In the above discussions, the dimension of the field is arbitrary. In this Section, we explore two-dimensional statistics. Typically, the fundamental observables are functions of the angular positions in the sky. Two dimensional statistics can connect the theory to observations in the simplest way.

We work on a random field defined on the angular position $\boldsymbol{\theta}$. We consider two different fields $g_i(\boldsymbol{\theta})$ $(i = 1, 2)$ which are projected density fields with weight functions $q_i(\chi)$ $(i = 1, 2)$. The explicit form is

$$g_i(\boldsymbol{\theta}) = \int d\chi\, q_i(\chi) \delta[f_K(\chi), \boldsymbol{\theta}], \tag{2.84}$$

where χ is a comoving distance from the observer. Though we have omitted, all integrations extend from the observer $\chi = 0$ to the horizon $\chi = \chi_{\rm H}$. The correlation function of $g_1(\boldsymbol{\theta})$ and $g_2(\boldsymbol{\theta})$ is

$$C_{12} = \langle g_1(\boldsymbol{\theta}) g_2(\boldsymbol{\theta}')\rangle \tag{2.85}$$

$$= \int d\chi\, q_1(\chi) \int d\chi'\, q_2(\chi') \langle \delta[f_K(\chi'), \boldsymbol{\theta}] \delta[f_K(\chi'), \boldsymbol{\theta}']\rangle. \tag{2.86}$$

Over the long range there is no longer correlation because $P_\delta(k)$ is proportional to k^{-1} for small wavenumbers. We assume that the power vanishes when the comoving separation $\Delta\chi \equiv |\chi - \chi'|$ exceeds the coherence scale $L_{\rm coh}$. If the weight functions $q_i(\chi)$ do not vary considerably over the separation scale, we can approximate $f_K(\chi) \simeq f_K(\chi')$ and $q_2(\chi') \simeq q_2(\chi')$:

$$C_{12}(\theta) = \int d\chi\, q_1(\chi) q_2(\chi) \int d(\Delta\chi)\, C_{\delta\delta}\left(\sqrt{f_K^2(\chi)\theta^2 + \Delta\chi^2}; \chi\right). \tag{2.87}$$

The equation is called as the *Limber equation* (Limber, 1953; LoVerde & Afshordi, 2008). Thus, we can relate the three dimensional correlation function $C_{\delta\delta}$ with two dimensional correlation function $C_{12}(\theta)$, once the weight functions are known.

It is useful to derive the correlation function in Fourier space. We can write this Fourier transform as

$$\begin{aligned} C_{12}(\theta) &= \int d\chi\, q_1(\chi) \int d\chi'\, q_2(\chi') \int \frac{d^3k}{(2\pi)^3} \int \frac{d^3k'}{(2\pi)^3} \\ &\quad \times \langle \hat{\delta}(\boldsymbol{k}, \chi) \hat{\delta}^*(\boldsymbol{k}', \chi') \rangle e^{-i\boldsymbol{k}_\perp \cdot f_K(\chi)\boldsymbol{\theta}} e^{i\boldsymbol{k}'_\perp \cdot f_K(\chi')\boldsymbol{\theta}'} e^{-ik_3 \cdot \chi} e^{ik'_3 \cdot \chi'}, \end{aligned} \tag{2.88}$$

where $\boldsymbol{k}_\perp$ is wavevector perpendicular to the line-of-sight direction. By substituting the power spectrum $P_\delta(k, \chi)$ with the ensemble mean under the same assumptions as before $f_K(\chi) \simeq f_K(\chi')$ and $q_2(\chi) \simeq q_2(\chi')$,

$$C_{12}(\theta) = \int d\chi\, q_1(\chi) q_2(\chi) \int \frac{d^3k}{(2\pi)^3} P_\delta(k; \chi) e^{-if_K(\chi)\boldsymbol{k}_\perp \cdot (\boldsymbol{\theta} - \boldsymbol{\theta}')} e^{-ik_3\chi} \int d\chi'\, e^{ik_3\chi'}. \tag{2.89}$$

The last integral becomes $2\pi\delta_{\rm D}(k_3)$ and carrying out this integration,

$$\begin{aligned} C_{12}(\theta) &= \int d\chi\, q_1(\chi) q_2(\chi) \int \frac{d^2k_\perp}{(2\pi)^2} P_\delta(k_\perp; \chi) e^{-if_K(\chi)\boldsymbol{k}_\perp \cdot \boldsymbol{\theta}} \\ &= \int d\chi\, q_1(\chi) q_2(\chi) \int \frac{kdk}{2\pi} P_\delta(k_\perp; \chi) J_0[(f_K(\chi)\theta)k], \end{aligned} \tag{2.90}$$

where J_0 is the first kind Bessel function of the zeroth order. Finally, we can derive the two dimensional angular power spectrum by Fourier transform of the two point correlation function:

$$\begin{aligned} P_{12}(\ell) &= \int d^2\theta\, C_{12}(\theta) e^{-i\boldsymbol{\ell}\cdot\boldsymbol{\theta}} \\ &= \int d\chi\, q_1(\chi) q_2(\chi) \int \frac{d^2k_\perp}{(2\pi)^2} P_\delta(k_\perp; \chi) (2\pi)^2 \delta_{\rm D}[\boldsymbol{\ell} - f_K(\chi)\boldsymbol{k}_\perp] \\ &= \int d\chi\, \frac{q_1(\chi) q_2(\chi)}{f_K^2(\chi)} P_\delta\left(\frac{\ell}{f_K(\chi)}; \chi\right). \end{aligned} \tag{2.91}$$

This is the Limber equation in Fourier space (Kaiser, 1992, 1998).

2.4 Properties of Dark Halos

2.4.1 Mass Function of Halos

2.4.1.1 Press–Schechter Theory

Counting numbers of galaxies, clusters, or dark halos which host them is the most fundamental measurement and has great importance because the abundances directly reflect the structure formation in the Universe. Since the formation of these structures is a completely nonlinear process, we cannot directly apply the linear theory to predict the abundance of them. However, when we combine the linear theory and nonlinear treatment, we can predict the mass function of halos analytically. Here, we introduce the pioneering attempt of *Press–Schechter theory* (Press & Schechter, 1974).

Let us consider the density field which follows Gaussian distribution at each position. The probability distribution function is

$$P(\delta)d\delta = \frac{1}{\sqrt{2\pi\sigma^2}} \exp\left(-\frac{\delta^2}{2\sigma^2}\right) d\delta, \tag{2.92}$$

where σ^2 is a variance of the density field.

Supposed that the sphere with the radius R in Lagrangian coordinates. The mass included in this sphere is

$$M = \frac{4\pi}{3}\bar{\rho}_0 R^3, \tag{2.93}$$

where $\bar{\rho}_0$ is the mean matter density. We define the fluctuation in this scale as

$$\delta_M(\boldsymbol{q}, t) = \frac{3}{4\pi R^2} \int_{|\boldsymbol{q}'-\boldsymbol{q}|\leq R} d^3q' \, \delta_{\rm L}(\boldsymbol{q}', t) \tag{2.94}$$

This fluctuation $\delta_M(\boldsymbol{q}, t)$ follows also Gaussian distribution. Hence, the probability distribution function is

$$P(\delta_M) = \frac{1}{\sqrt{2\pi\sigma^2(M)}} \exp\left(-\frac{\delta_M^2}{2\sigma^2(M)}\right). \tag{2.95}$$

If δ_M exceeds a critical value $\delta_c = 1.69$, the Lagrangian region forms a halo. The fraction of Lagrangian region which are taken in halos is

$$P_{>\delta_c}(M) = \int_{\delta_c}^{\infty} P(\delta_M) d\delta_M = \frac{1}{\sqrt{2\pi}} \int_{\delta_c/\sigma(M)}^{\infty} e^{-x^2/2} dx \tag{2.96}$$

From this, mass which forms dark halo with more than M can be expressed as $\bar{\rho}_0 P_{>\delta_c}(M)$. $n(M)dM$ denotes the number of halos in the unit comoving volume which has a mass in the range between M and $M + dM$. At a first glimpse, the difference between $\bar{\rho}_0 P_{>\delta_c}(M)$ and $\bar{\rho}_0 P_{>\delta_c}(M + dM)$ gives the mass density $Mn(M)dM$. But in this calculation, merging of halos has been ignored. In Press–Schechter theory, we simply double the above expression to incorporate the effect of mergers,

$$n(M)MdM = 2\bar{\rho}_0 |P_{>\delta_c}(M + dM) - P_{>\delta_c}(M)| = 2\bar{\rho}_0 \left|\frac{P_{>\delta_c}}{d\sigma(M)}\right| \left|\frac{d\sigma(M)}{dM}\right| dM. \tag{2.97}$$

Substituting $P_{>\delta_c}(M)$,

$$n(M) = \sqrt{\frac{2}{\pi}}\frac{\bar{\rho}_0}{M^2}\left|\frac{d\ln\sigma(M)}{d\ln M}\right|\frac{\delta_c}{\sigma(M)}\exp\left(-\frac{\delta_c^2}{2\sigma^2(M)}\right). \tag{2.98}$$

This formula is called as *Press–Schechter mass function*.

Finally, we consider the variance $\sigma^2(M)$ at the mass scale M. We define the same sphere as before and mass fluctuation δM as follows,

$$M = \frac{4\pi}{3}\bar{\rho}_0 R^3,\ \delta M = \int_{x<R} d^3x\,\bar{\rho}\delta(\boldsymbol{x}). \tag{2.99}$$

Thus the normalized mass fluctuation $\delta M/M$ is

$$\frac{\delta M}{M} = \frac{3}{4\pi R^3}\int_{x<R} d^3x\,\delta(\boldsymbol{x}) = \int d^3x\,W_R(x)\delta(\boldsymbol{x}), \tag{2.100}$$

where $W_R(x)$ is the top-hat window function,

$$W_R(x) = \frac{3}{4\pi R^3}\Theta(R-x), \tag{2.101}$$

where Θ is the step function. This window function extracts the fluctuation smaller than the scale R. Then, we can compute mass variance,

$$\sigma^2(M) \equiv \left\langle\left(\frac{\delta M}{M}\right)^2\right\rangle = \int\frac{k^2dk}{2\pi^2}W^2(kR)P(k), \tag{2.102}$$

where $P(k)$ is matter power spectrum and $W(kR)$ is a Fourier transform of the tophat window function,

$$\begin{aligned} W(kR) &= \int d^3x\,e^{-i\boldsymbol{k}\cdot\boldsymbol{x}}W_R(x) \\ &= 4\pi\int x^2dx\,\frac{\sin(kx)}{kx}W_R(x) \\ &= \frac{3}{(kR)^3}[\sin(kR) - kR\cos(kR)]. \end{aligned} \tag{2.103}$$

Thus, we can construct the Press–Schechter mass function only from matter power spectrum.

2.4.1.2 Beyond Press–Schechter and Fitting Formulae with Numerical Simulations

In Press–Schechter theory, halo forms spherically based on spherical collapse scenario. In reality, matter collapses into halos non-spherically, which is observed in numerical simulations (Jing & Suto, 2002). One of the extension of Press–Schechter theory is the ellipsoidal collapse model (Sheth et al., 2001). Fitting formulae of the mass function are

well calibrated with numerical simulations. The following form of the fitting function is often used,

$$\frac{dn(M,z)}{dM} = \frac{\bar{\rho}_0}{M^2} f(\nu) \left| \frac{d\log\sigma}{dM} \right|, \tag{2.104}$$

where $\nu = \delta_c/\sigma(M)$ and $\delta_c = 1.686$ is the critical overdensity for spherical collapse. The function $f(\nu)$ defines the shape of the halo mass function. In the Press–Schechter theory, the corresponding function $f_{\rm PS}$ is

$$f_{\rm PS}(\nu) = \frac{2}{\pi}\nu \exp\left(-\frac{\nu^2}{2}\right). \tag{2.105}$$

Several works focus on determining the function $f(\nu)$ with a massive set of numerical simulations. Especially, Bocquet et al. (2016) utilized hydrodynamical simulations which incorporate baryonic feedback. Due to energetic feedback of supernovae and active galactic nuclei, some fractions of baryons are removed, and resultant halo masses are reduced. We summarize some of these fitting functions in Figures 2.3 and 2.4. For a complete comparison, refer to Murray et al. (2013).

2.4.2 Halo Bias

It is important to know how halos are distributed with respect to the background matter. The relation between matter overdensity δ and halo overdensity δ_h is referred to as *halo bias* or *bias*. We define halo overdensity in terms of number density,

$$\delta_h(\boldsymbol{x}) = \frac{n_h(\boldsymbol{x}) - \bar{n}_h}{\bar{n}_h}, \tag{2.106}$$

where $n_h(\boldsymbol{x})$ is the halo number density and $\bar{n}_h$ is the mean of the number density in the Universe. We naturally expect that there are more halos in the region where more matter exists. This is partially true, but in fact it depends on halo mass. In addition, this relation is not necessarily linear but takes a complex form. This makes it difficult to probe the underlying matter distribution from halos or galaxies. On the other hand, the galaxy bias is difficult to model because the nature of galaxy formation is highly nonlinear. The galaxy bias is determined from observations individually.

Mo & White (1996) combined the Press–Schechter theory and the spherical collapse model to derive the analytical form of linear bias factor, which is defined as

$$b_h(M,z) \equiv \frac{\delta_h(M,z)}{\delta(z)}, \tag{2.107}$$

where $\delta_h(M,z)$ is the halo overdensity at redshift z and with mass M. In the lowest order, they derived the linear bias,

$$b_h(M,z) = 1 + \frac{\nu(M,z)^2 - 1}{\delta_c}. \tag{2.108}$$

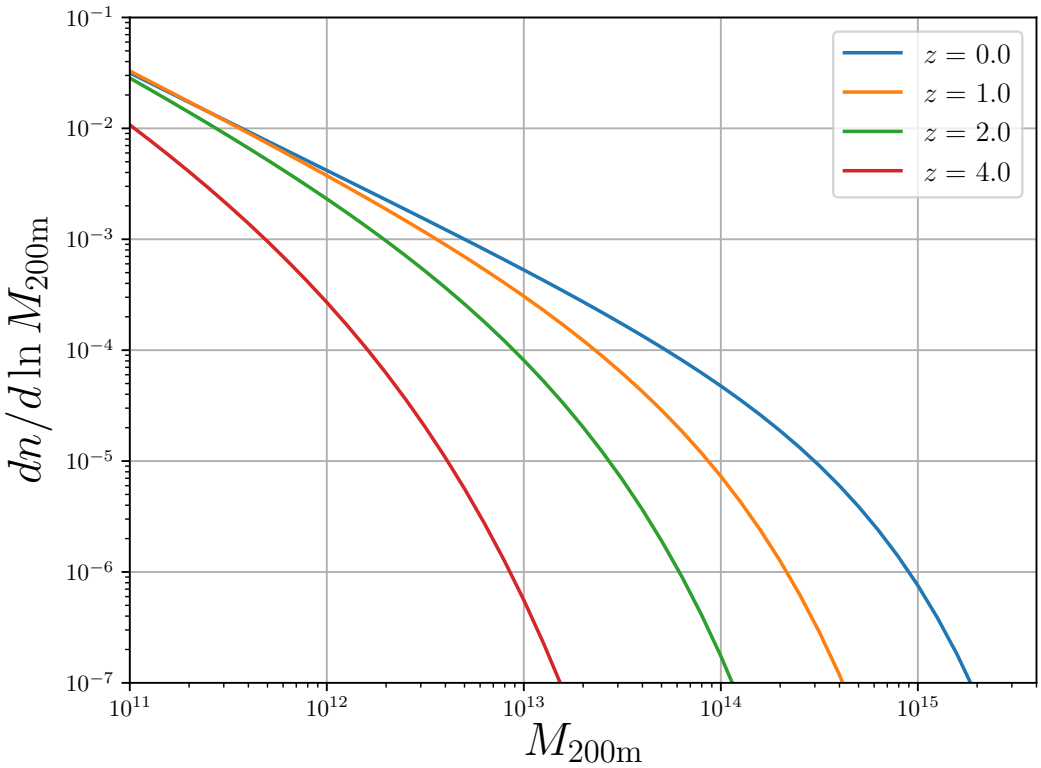

Figure 2.3: Redshift dependence of halo mass function of Tinker et al. (2008). We adopt halo overdensity $\Delta_{\mathrm{m}} = 200$.

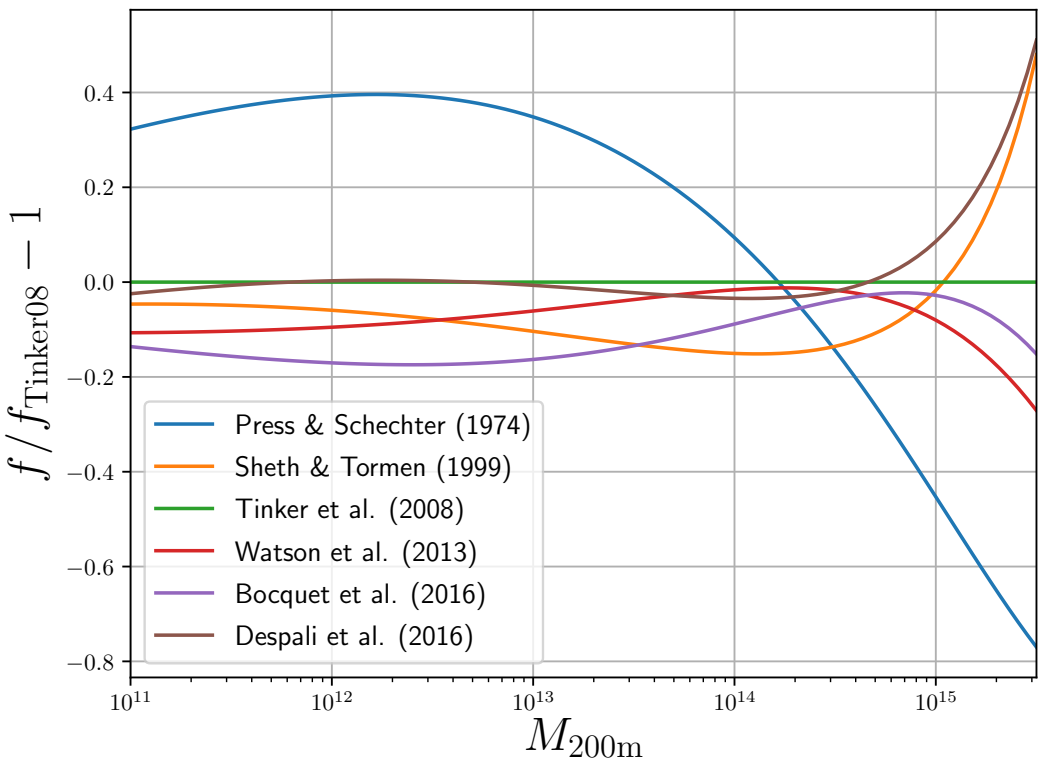

Figure 2.4: Halo mass functions with different fitting functions (Press & Schechter, 1974; Sheth & Tormen, 1999; Tinker et al., 2008; Watson et al., 2013; Bocquet et al., 2016; Despali et al., 2016). We adopt halo overdensity $\Delta_{\mathrm{m}} = 200$. In order to calculate the mass functions, we utilize the `COLOSSUS` package (Diemer, 2018).

It is useful to define the non-linear mass M_* as

$$\frac{\delta_c}{\sigma(M_*)} = 1. \tag{2.109}$$

When $M > M_*$, halos are biased with respect to matter ($b_h(M) > 1$). In the opposite case, when $M < M_*$, halos are said to be anti-biased. Sheth et al. (2001) extended the above formula using the ellipsoidal collapse model. They calibrated parameters with N-body simulations, and finally derived as

$$b_h(M, z) = 1 + \frac{1}{\sqrt{a}\delta_c}\left[\sqrt{a}(a\nu^2) + \sqrt{a}b(a\nu^2)^{1-c} - \frac{(a\nu^2)^c}{(a\nu)^c + b(1-c)(1-c/2)}\right], \tag{2.110}$$

where $a = 0.707$, $b = 0.5$, and $c = 0.6$. Figure 2.5 shows the comparison of fitting formulas of halo bias.

2.4.3 Density Profile of Halo

In the analysis so far, dark halos form as a result of collapse into the high density peak. Hereafter, we address the density profile of halos. However, since halos undergo nonlinear gravitational evolution, it is hard to analytically compute the density structure of halos. In this case, numerical simulations which solve the gravitational evolution are useful tool for investigating structure and clustering properties of halos. Navarro et al. (1996, 1997) found that halos have universal and spherical density profile, which is commonly referred to as Navarro–Frenk–White (NFW) profile. The NFW profile is the power-law profile

$$\rho_{\rm NFW}(r) = \frac{\rho_s}{(r/r_s)((r/r_s)+1)^2}, \tag{2.111}$$

where ρ_s is the scale density, and r_s is the scale radius. At inner radii, the profile has the core structure $\rho_{\rm NFW}(r) \propto r^{-1}$. On the other hand, at outskirt regions, the profile asymptotically damps as $\rho_{\rm NFW}(r) \propto r^{-3}$. There is a caveat that the enclosed mass is not well-defined for NFW profile because the mass $\int dr\, 4\pi r^2 \rho_{\rm NFW}(r)$ diverges. Accordingly, there is a need to truncate the density profile at an appropriate radius, which determines the boundary of halos[4]. Among several definitions of boundaries, the virial radius is commonly used. The virial radius $r_{\rm vir}$ is defined as radius where the mean density is equal to the overdensity predicted by spherical collapse, i.e.,

$$\bar{\rho}(r_{\rm vir}) = \Delta_{\rm vir}\rho_{\rm cr}, \tag{2.112}$$

where

$$\bar{\rho}(r_{\rm vir}) \equiv M(< r_{\rm vir}) \Big/ \left(\frac{4}{3}\pi r_{\rm vir}^3\right) = \int_0^{r_{\rm vir}} dr\, 4\pi r^2 \rho_{\rm NFW}(r) \Big/ \left(\frac{4}{3}\pi r_{\rm vir}^3\right). \tag{2.113}$$

[4] Another solution to the divergence of the enclosed mass is introducing tampering function which makes steeper damping at outer radii (Baltz et al., 2009).

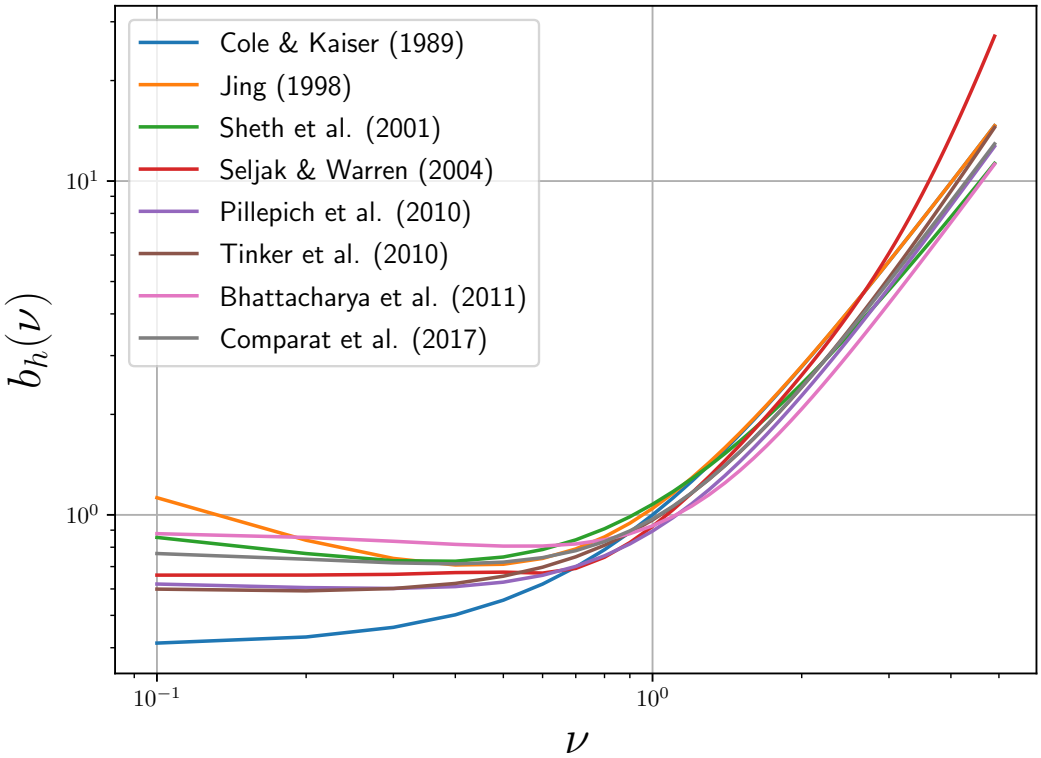

Figure 2.5: Halo bias as a function of the peak height ν for different fitting formulas (Cole & Kaiser, 1989; Jing, 1998; Sheth et al., 2001; Seljak & Warren, 2004; Pillepich et al., 2010; Tinker et al., 2010; Bhattacharya et al., 2011; Comparat et al., 2017). In order to calculate the bias relations, we utilize the `COLOSSUS` package (Diemer, 2018).

The critical overdensity $\Delta_{\rm vir} = 18\pi^2$ is computed based on the spherical collapse model in the Einstein–de-Sitter Universe, but for general cosmologies, there is a useful formula by Bryan & Norman (1998),

$$\Delta_{\rm vir} = 18\pi^2 - 82(1-\Omega_{\rm m}(z)) - 39(1-\Omega_{\rm m}(z))^2, \tag{2.114}$$

where $\Omega_{\rm m}(z) = \Omega_{\rm m}(1+z)^3 E^{-2}(z)$. Instead of virial overdensity, constant overdensity with respect to the critical density $\rho_{\rm cr}$ or $\rho_{\rm m}$ is also widely used. For example, $r_{\rm 200c}$ corresponds to the radius where mean enclosed density is 200 times critical density. After specifying the boundary, the profile is truncated at the boundary (Takada & Jain, 2003a,b), and then one can compute the halo mass as (see, e.g., Oguri & Hamana (2011)),

$$M_{\rm vir} = 4\pi r_s^3 \rho_s m(c_{\rm vir}), \tag{2.115}$$

with

$$m(c) \equiv \int_0^c \frac{x}{(1+x)^2} dx = \ln(1+c) - \frac{c}{1+c}. \tag{2.116}$$

Then, the scale density ρ_s can be determined once the scale radius r_s is specified. For the scale radius, numerical simulations also clarify that the scale radius strongly correlates with the mass. Instead of the scale radius r_s, it is useful to define the concentration parameter,

$$c_{\rm vir} \equiv \frac{r_{\rm vir}}{r_s}. \tag{2.117}$$

The fitting formula of the concentration parameter as a function of halo mass, or peak height, and redshift is well studied by works utilizing numerical simulations. Figure 2.6 shows the fitting formulas from several previous works. Eventually, NFW profile is characterized only by the mass.

It is useful to have expressions of Fourier transform of density profile. The expression for Fourier transform of the scaled density profile $u(r) = \rho(r)/M_{\rm vir}$ is given as

$$\begin{aligned} u(k) \quad = \quad & \frac{4\pi\rho_s r_s^3}{M_{\rm vir}} \{\sin(kr_s)[{\rm Si}([1+c_{\rm vir}]kr_s) - {\rm Si}(kr_s)] \\ & -\frac{\sin(c_{\rm vir}kr_s)}{(1+c_{\rm vir})kr_s} + \cos(kr_s)[{\rm Ci}([1+c_{\rm vir}]kr_s) - {\rm Ci}(kr_s)]\Big\}. \end{aligned} \tag{2.118}$$

The NFW profile is widely used due to its simple self-similar form, but other density profiles have been proposed by other works. The profile in Einasto (1965) is parametrized by three parameters,

$$\ln\left(\frac{\rho_{\rm Einasto}(r)}{\rho_{-2}}\right) = -\frac{2}{\alpha}\left[\left(\frac{r}{r_{-2}}\right)^{\alpha} - 1\right], \tag{2.119}$$

where ρ_{-2} and r_{-2} are characteristic density and radius, and α is the shape parameter. The shape parameter weakly depends on the peak height (Gao et al., 2008),

$$\alpha(\nu) = 0.155 + 0.0095\nu^2. \tag{2.120}$$

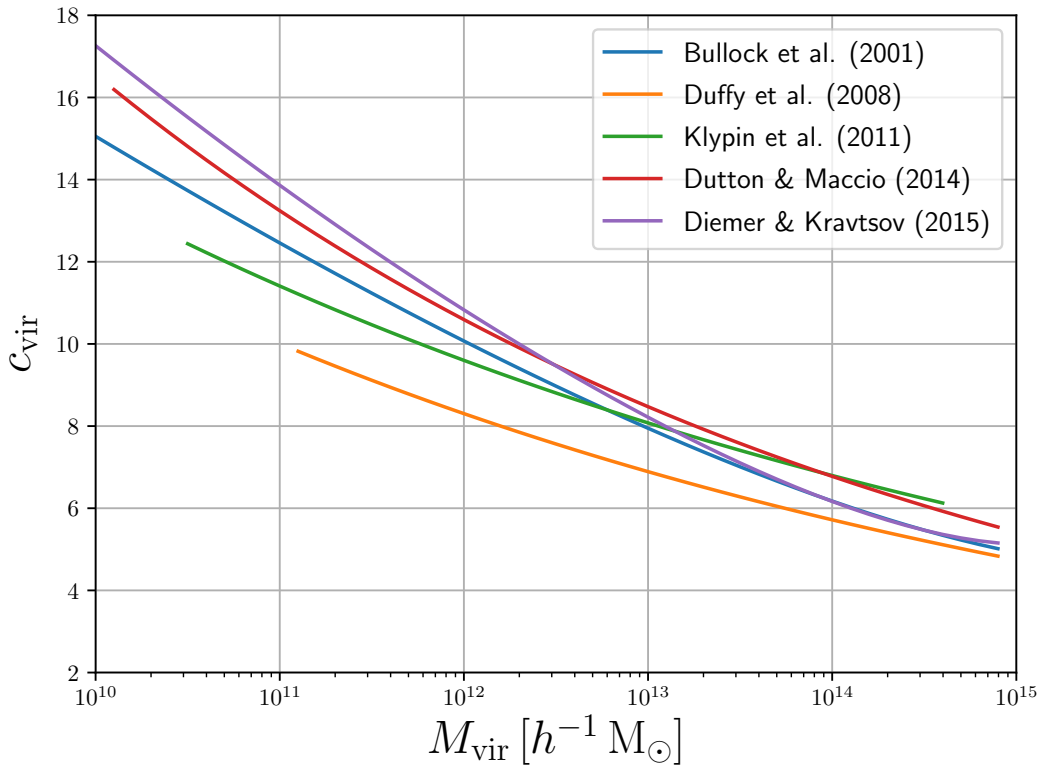

Figure 2.6: The mass-concentration relation for different fitting formulas (Bullock et al., 2001; Duffy et al., 2008; Klypin et al., 2011; Dutton & Macciò, 2014; Diemer & Kravtsov, 2015). In order to calculate the relation, we utilize the `COLOSSUS` package (Diemer, 2018).

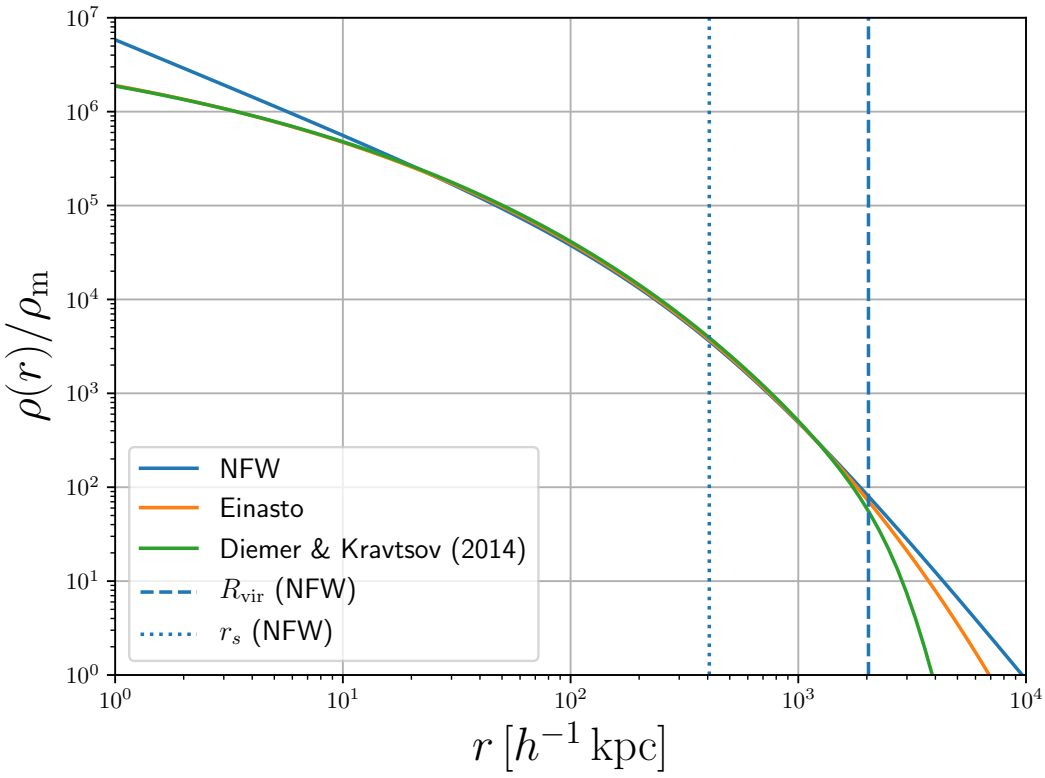

Figure 2.7: Density profiles of dark halos normalized by the mean density. For the NFW profile, the scale radius and virial radius are also shown as dotted and dashed lines, respectively. In addition to the NFW and Einasto profiles, Diemer & Kravtsov profile (Diemer & Kravtsov, 2014) is also shown. In order to compute the density profiles, we utilize the `COLOSSUS` package (Diemer, 2018).

Figure 2.7 shows density profiles of halos with $M_{\rm vir} = 10^{15}\,h^{-1}\,{\rm M}_\odot$ and $z = 0$. For NFW profile, the concentration parameter is $c_{\rm vir} = 5$, and scale radius and virial radius are also shown.

So far, we have considered only spherical profiles. The state-of-the-art simulations show that individual halo exhibits strong deviation from spherical symmetry due to merging events and violent relaxation. Oguri et al. (2003) have proposed the triaxial density profile, which explain the observed the weak lensing signals (Oguri et al., 2010, 2012). Precise modeling of halo density profiles is of great importance for further studies.

2.5 Matter Clustering Based on the Halo Model

Now we have formulae for halo abundance, halo bias, and density profile of halos. Thus, we can compute statistics based on halo model approach, where all matter and associated gas reside in halos. As an illustrative example, we will derive correlation function and power spectrum of matter based on this method.

2.5.1 The Two-Point Correlation Function

In this prescription, all matter is associated with halos which have finite spatial extent and variation of mass. The density field is described as the sum of contributions for all halos,

$$\rho(\boldsymbol{x}) = \sum_i \rho(\boldsymbol{x} - \boldsymbol{x}_i|M_i) = \sum_i \int dM d^3x'\, \delta_{\rm D}(M - M_i)\delta^3_{\rm D}(\boldsymbol{x}' - \boldsymbol{x}_i) M u(\boldsymbol{x} - \boldsymbol{x}'|M), \quad (2.121)$$

where $u(\boldsymbol{x}|M) \equiv \rho(\boldsymbol{x}|M)/M$ is the scaled density profile. The number density of halos is given as

$$\left\langle \sum_i \delta_{\rm D}(M - M_i)\delta^3_{\rm D}(\boldsymbol{x} - \boldsymbol{x}_i) \right\rangle \equiv n(M). \quad (2.122)$$

The mean density is given as the ensemble average,

$$\bar{\rho} \equiv \langle \rho(\boldsymbol{x}) \rangle = \int dM n(M) M \int d^3x\, u(\boldsymbol{x}|M) = \int dM\, n(M) M. \quad (2.123)$$

Let us consider the two-point correlation function of density field. The two-point correlation function is defined as

$$\xi(\boldsymbol{x} - \boldsymbol{x}') \equiv \langle \delta(\boldsymbol{x})\delta(\boldsymbol{x}') \rangle. \quad (2.124)$$

The correlation function can be decomposed as

$$\xi(\boldsymbol{x} - \boldsymbol{x}') = \xi^{1h}(\boldsymbol{x} - \boldsymbol{x}') + \xi^{2h}(\boldsymbol{x} - \boldsymbol{x}'), \quad (2.125)$$

where 1-halo and 2-halo terms are

$$\xi^{1h}(\boldsymbol{x}-\boldsymbol{x}') = \int dM \frac{M^2 n(M)}{\bar{\rho}^2} \int d^3y\, u(\boldsymbol{y}|M) u(\boldsymbol{y}+\boldsymbol{x}-\boldsymbol{x}'|M), \tag{2.126}$$

$$\begin{aligned}\xi^{2h}(\boldsymbol{x}-\boldsymbol{x}') &= \int dM_1 \frac{M_1 n(M_1)}{\bar{\rho}} \int dM_2 \frac{M_2 n(M_2)}{\bar{\rho}} \int d^3x_1 d^3x_2 \\ &\quad \times u(\boldsymbol{x}-\boldsymbol{x}_1|M_1) u(\boldsymbol{x}'-\boldsymbol{x}_2|M_2) \xi_{hh}(\boldsymbol{x}_1-\boldsymbol{x}_2|M_1, M_2),\end{aligned} \tag{2.127}$$

where correlation function halos is defined as

$$\left\langle \sum_{i\neq j} \delta_{\rm D}(M_1-M_i)\delta_{\rm D}(M_2-M_j)\delta^3_{\rm D}(\boldsymbol{x}_1-\boldsymbol{x}_i)\delta^3_{\rm D}(\boldsymbol{x}_2-\boldsymbol{x}_j) \right\rangle \equiv n(M_1)n(M_2)(1+\xi_{hh}(\boldsymbol{x}_1-\boldsymbol{x}_2)). \tag{2.128}$$

This correlation function at large scales can be approximated as

$$\xi_{hh}(\boldsymbol{x}) \approx b_h(M_1) b_h(M_2) \xi_{\rm m}(\boldsymbol{x}). \tag{2.129}$$

Towards smaller scales, the correlation function of halos drops sharply because two distinct halos cannot exist within close separation. This effect is called as exclusion effect.

2.5.2 Power Spectrum

The correlation function is expressed as convolution of profiles of halos. Therefore, in Fourier space, the formulae can be simplified as

$$P(k) = P^{1h}(k) + P^{2h}(k), \tag{2.130}$$

$$P^{1h}(k) = \int dM\, n(M) \left(\frac{M}{\bar{\rho}}\right)^2 |u(k|M)|^2, \tag{2.131}$$

$$P^{2h}(k) = \int dM_1 dM_2\, n(M_1) \frac{M_1}{\bar{\rho}} u(k|M_1) n(M_2) \frac{M_2}{\bar{\rho}} u(k|M_2) P_{hh}(k|M_1, M_2), \tag{2.132}$$

where $P_{hh}(k|M_1, M_2)$ is the power spectrum of halos with masses M_1 and M_2. Again, the halo power spectrum at large scales can be approximated with halo bias,

$$P_{hh}(k) \approx b_h(M_1) b_h(M_2) P_{\rm m}(k). \tag{2.133}$$

2.6 Observational Probes for Cosmology

We have discussed how the primordial fluctuation grows into large-scale structures with theoretical approaches. Here, we overview the observational probes into the large-scale structures in the Universe. Since large-scale structures are literally huge for us, we have to carry out wide and deep observations to map the whole structures. In addition, as we have already seen, dark matter plays a central role, which cannot be seen directly by optical telescopes. To overcome these problems, many observational techniques and ideas are developed. Refer to Weinberg et al. (2013) for more discussions on cosmological probes.

2.6.1 Cosmic Microwave Background

According to the big-bang scenario, the early Universe is full of hot cosmic plasma. After 38 Myrs from the birth of the Universe, photons can freely propagate without interacting baryons. This afterglow can be observed even today in radio (or microwave) wavelength, which we call *cosmic microwave background* (CMB). The intensity of the microwave is nearly isotropic over the sky, but there are tiny anisotropies ($\sim \mu$K). Since photons and baryons are tightly coupled in the early Universe, the anisotropic pattern reflects the primordial fluctuation of cosmic plasma, which contains rich information about the properties of contents of the Universe. The temperature anisotropy is well approximated by Gaussian distribution, and thus angular power spectrum is a useful statistic to extract the information. In addition to temperature anisotropy, the polarization of CMB photons provide independent information, especially about the reionization era. In Figures 2.8 and 2.9, we show the angular power spectrum of temperature and polarization anisotropy observed by the *Planck* satellite. The complex feature of these spectra are well explained by linear theory of cosmological perturbations.

2.6.2 Type Ia Supernovae as Standard Candles

After massive stars use up fuels, they end up with violent explosions, which are called as supernova explosion. Supernovae type Ia (SNe Ia) are standard candles in the Universe, which means we can estimate the absolute luminosity of the supernova. Observationally type Ia supernovae are defined as supernovae without hydrogen emission line and with silicon emission line. They are thought to be produced from thermo-nuclear burning of a white dwarf accreted from the companion star. There is a limiting mass for a white dwarf, that is *Chandrasekhar limit* $M \sim 1.38\,\mathrm{M}_\odot$. Due to this upper limit, the mass of exploding white dwarf is nearly constant. This results in similar luminosity among SNe Ia. Furthermore, it is known that the maximum brightness of supernovae is correlated with the decline of light curve during the period from the peak to a certain duration. This relation is called as Phillips relation (Phillips, 1993). When the redshift of type Ia supernovae is determined by spectroscopy or photometric imaging, we can probe the relation between the luminosity distance and the redshift. This distance-redshift relation reflects the geometry of the Universe, and through this relation, we can constrain cosmological models and Hubble parameter. For example, the SH0ES program (Riess et al., 2011) observed 253 SNe Ia with Wide Field Camera of *Hubble Space Telescope* and determined Hubble parameter with 3.3% precision,

$$H_0 = 73.8 \pm 2.4\,\mathrm{km\,s^{-1}\,Mpc^{-1}}. \tag{2.134}$$

2.6.3 Clustering of Galaxies and Baryon Acoustic Oscillation

Even if dark matter itself cannot be observed directly, we can see luminous galaxies in the sky. It is expected that the distribution of galaxies roughly follows dark matter, which accounts for massive components. We can map large-scale structures by observing the galaxy distribution. But the most important issue is that the distributions of galaxy and

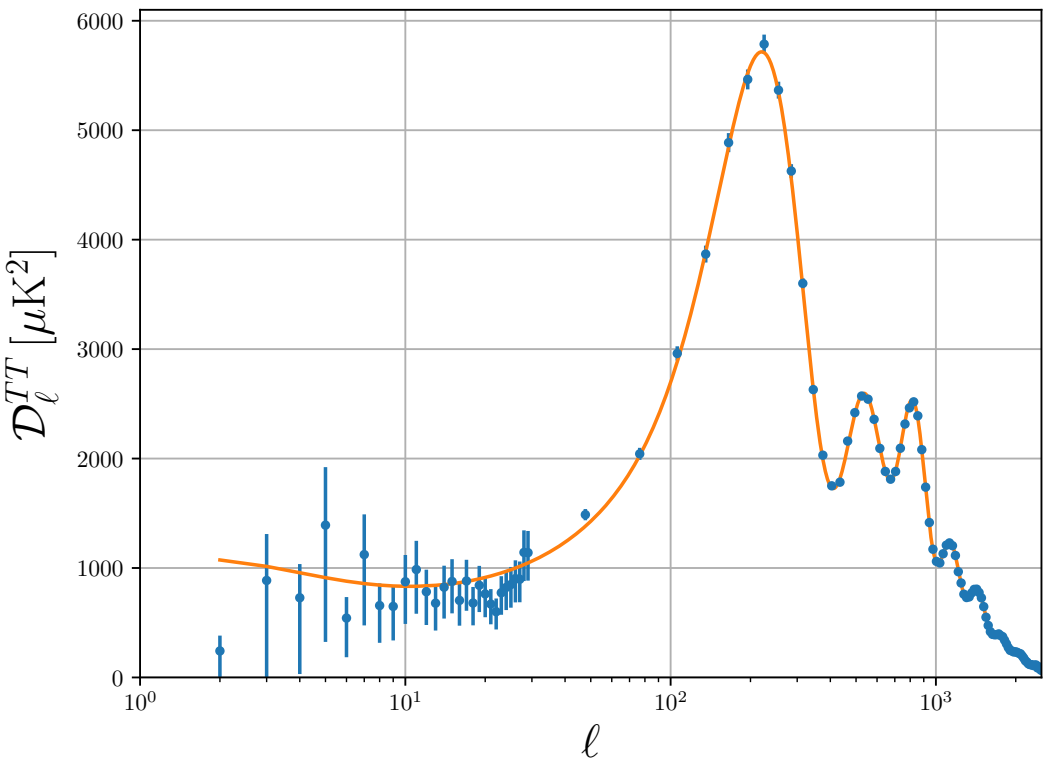

Figure 2.8: Angular power spectrum of temperature anisotropy from the *Planck* satellite (Planck Collaboration, 2016b). The best-fitting power spectrum is also shown as the solid line. The scaled spectrum $\mathcal{D}_\ell^{TT}$ is related with the power spectrum C_ℓ^{TT} as $\mathcal{D}_\ell^{TT} = \ell(\ell+1)/2\pi C_\ell^{TT}$.

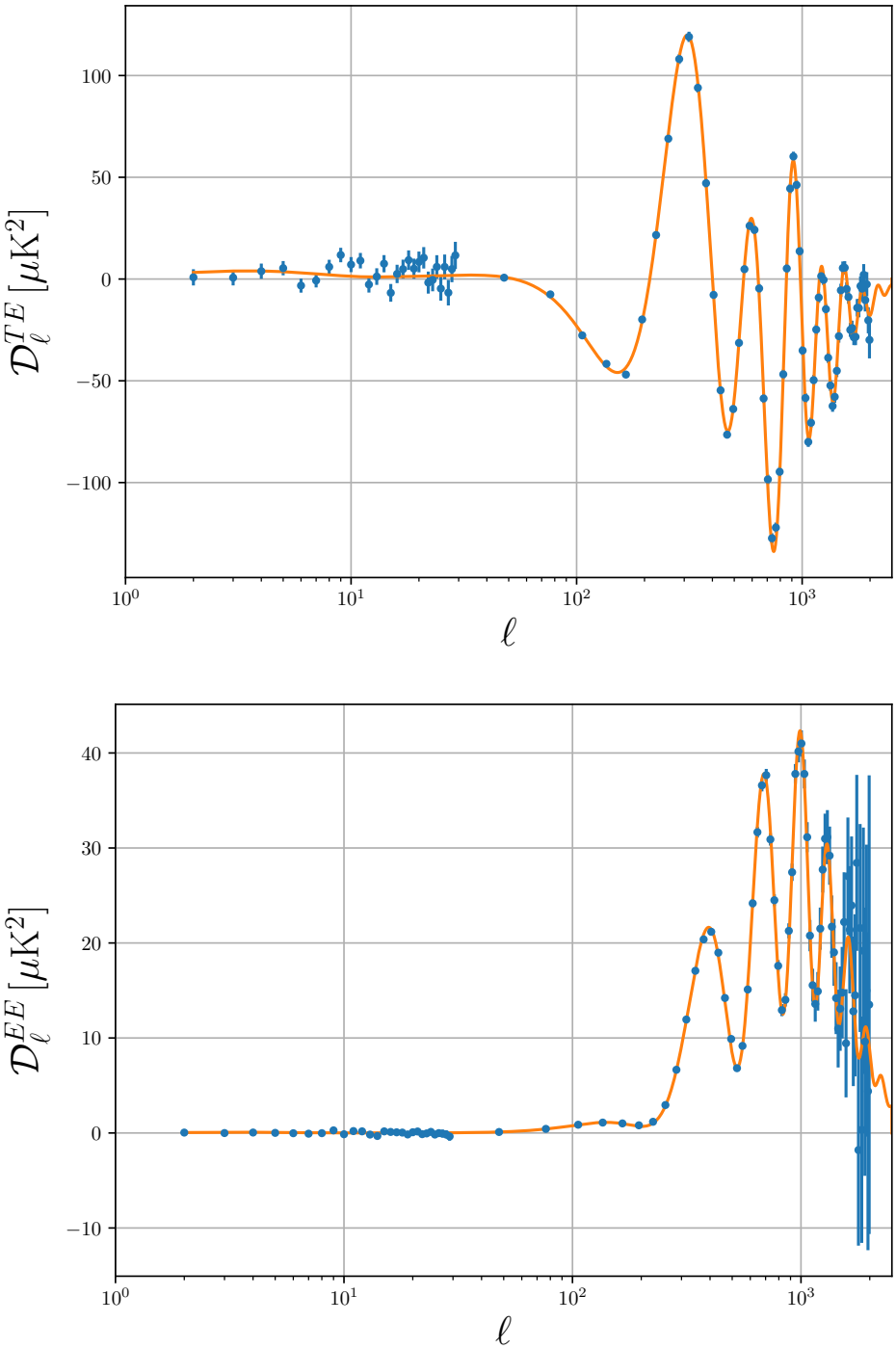

Figure 2.9: Angular power spectrum of E-mode polarization and cross-spectrum of E-mode polarization and temperature from the *Planck* satellite (Planck Collaboration, 2016b). The best-fitting power spectrum is also shown as the solid line. The scaled spectrum $\mathcal{D}_\ell^{TE,EE}$ is related with the power spectrum $C_\ell^{TE,EE}$ as $\mathcal{D}_\ell^{TE,EE} = \ell(\ell+1)/2\pi C_\ell^{TE,EE}$.

matter are not identical but biased. As we have defined the number density contrast for halo δ_h, we can also define the galaxy number density contrast δ_g,

$$\delta_g = \frac{n_g - \bar{n}_g}{\bar{n}_g}, \tag{2.135}$$

where n_g is number density of galaxy at a certain location and $\bar{n}_g$ denotes the mean of the number density in the Universe. Note that a galaxy is regarded as a discrete point and so we used the number density. Usually, the number density contrast is parametrized as

$$\delta_g = b_g \delta, \tag{2.136}$$

where b_g is galaxy bias, which is a still uncertain quantity.

The correlation function of galaxies has important feature, which is known as *baryon acoustic oscillation* (BAO). In the early Universe, since photons and baryons are tightly coupled, the sound wave can propagate in the cosmic fluid. But the interaction between photons and baryons becomes inefficient as the Universe is expanding, and the sound wave cannot propagate through the fluid anymore. As a result, the characteristic scale is imprinted onto the fluctuation of baryons and photons. In reality, the oscillatory feature appears in the power spectrum of temperature anisotropy of CMB (see Figure 2.8). The same feature can appear in the correlation function of galaxy distribution, which traces baryon and matter density field. This feature is BAO, and can be detected as a peak in the correlation function (Eisenstein et al., 2005; BOSS Collaboration, 2015). In practice, the position of BAO can be measured more precisely than the overall shape of the correlation function. The distance scale of BAO is accurately determined by linear theory of cosmological perturbations, and it can be used as the *standard ruler*. In Figures 2.10 and 2.11, we show the correlation function and power spectrum of galaxy distributions measured by Baryonic Oscillations Spectroscopic Survey (Anderson et al., 2014).

2.6.4 Weak Gravitational Lensing

Weak gravitational lensing is a unique observable among cosmological probes. Though other probes employ luminous objects as a tracer of matter distribution in principle, weak lensing probes it in a different way. In weak lensing observation, intervening matter distribution can be explored through coherent distortion of images of distant galaxies. It differs from other observations in that weak lensing is an *unbiased* tracer. This fact makes weak lensing important for cosmological studies. However, it was not until quite recently that weak lensing observations was made possible. For a precise measurement, we need accurate estimation of the shape of galaxies. To reduce statistical errors, many galaxies have to be observed, i.e., a deep and wide survey is essential for weak lensing. We will discuss how we can make use of weak lensing for cosmological studies in Chapter 3.

2.6.5 Clusters of Galaxies

Clusters of galaxies are the most massive objects in the Universe, which contain 100–10000 galaxies and have 10^{13}–$10^{15}\,\mathrm{M}_\odot$. The mass content of galaxy clusters is composed of

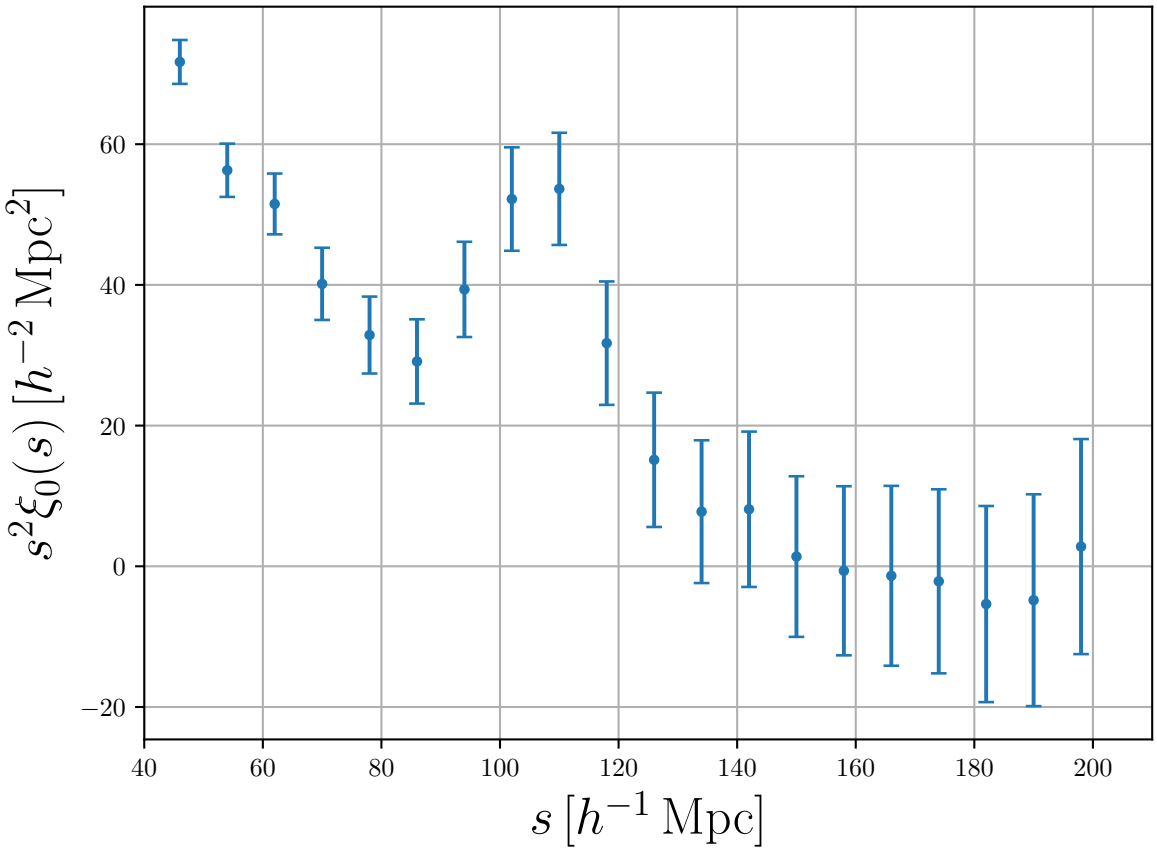

Figure 2.10: The monopole correlation function measured from BOSS DR11 (Anderson et al., 2014). The peak around $100\,h^{-1}$ Mpc corresponds to BAO scale.

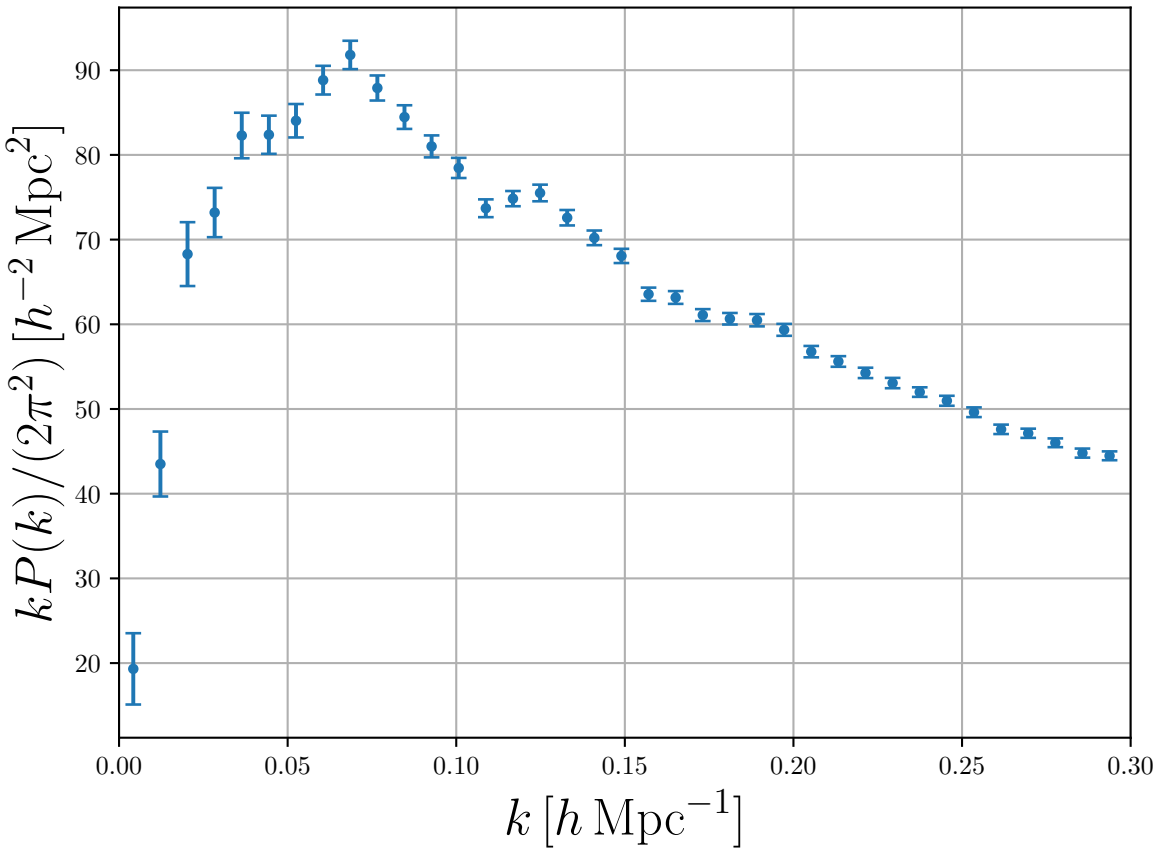

Figure 2.11: The power spectrum measured from BOSS DR11 (Anderson et al., 2014). The wiggle feature occurs due to acoustic oscillations.

dark matter and hot plasma emitting energetic X-ray and the shape is close to sphere with many substructures. The abundance of clusters, or halos, is an excellent probe for cosmology because it is sensitive to the structure formation and underlying physics. However, the cosmological models predict the abundance of clusters as the function of their mass, which is hard to infer from X-ray or optical observations. The challenging point is that quantities we can directly observe, e.g., X-ray luminosity or optical richness, have to be converted into mass. There are several methods to construct a mass-observable relation. One method is to use nearby clusters which mass can be measured with relatively high accuracy by strong lensing and so on. We can measure X-ray flux or optical richness of these clusters and finally we can construct the observable-mass relation. Meanwhile this method has limitations. Clusters whose mass can be measured safely is limited to nearby ones. In contrast, since weak gravitational lensing is sensitive only to mass content of galaxy clusters, we can directly measure the mass of galaxy clusters. With weak lensing measurements, we can calibrate X-ray or optical observations, which is *mass calibration*. These measurements are still limited to nearby clusters, and thus we need deeper observations to probe into the redshift dependence of the mass-observable relation.

Another method used for studies on galaxy clusters is numerical simulations. In simulations, it is easy to measure mass and observables and also to investigate the redshift evolution. On the other hand, complex baryonic physics is hard to implement and validate with real data. In the end, the observable-mass relation contains large uncertainty and is a target for an intensive study.

We have introduced the X-ray, optical observations, and weak lensing to probe the structures of galaxy clusters. There is another important probe proposed by Sunyaev & Zel'dovich (1972, 1980), which is the *Sunyaev–Zel'dovich effect* (SZ). The SZ effect represents the secondary anisotropy of temperature of CMB induced mainly by hot plasma in galaxy clusters. The advantage of SZ effect is that the selection function is flat with respect to redshift, though X-ray luminosity decreases as $(1+z)^{-3}$. In this dissertation, we focus on the thermal Sunyaev–Zel'dovich effect among the observables of clusters and give detailed discussions in Chapter 4.

2.6.6 Lyman-α Forest

Since primordial gas is mainly composed of hydrogen, Lyman-α emission is ubiquitous in the Universe. Similarly to the emission, absorption occurs frequently. At higher redshifts, neutral hydrogens are abundant, and photons at Lyman-α wavelength is absorbed. When we observe continuous emissions from quasar at high redshift, many spikes are observed at spectra, each of which corresponds to signs of Lyman-α absorptions. This feature is called as Gunn–Peterson troughs (Gunn & Peterson, 1965) or *Lyman-α forest* (LAF). This effect traces the distribution of gas, i.e., large-scale structures. Currently, LAF is the unique probe of BAO at high redshift ($z > 3$). The shortcoming of LAF is that we can observe the LAF only at the position of quasars and galaxies, which work as background light. We need to rely on statistical technique when reproducing three-dimensional structures of neutral gas (McQuinn & White, 2011; Font-Ribera et al., 2018). The power spectrum of LAF has already been measured by SDSS (Slosar et al., 2011), and constraints on mass

of warm dark matter or massive neutrinos are addressed (Viel et al., 2013; Yèche et al., 2017).

Chapter 3

Gravitational Lensing

Contents

3.1 Gravitaional Lensing: Strong, Weak, and Micro Lensing

One of the most important outcomes from general relativity is that the path of rays is deflected by gravity, which is now referred to as *gravitational lensing*. Originally, the deflection of light has already been predicted by Newton and Laplace using Newtonian gravity. However, the complete explanation of light deflection necessitates general relativity.

Eddington argued that the multiple images were observed by a single source under certain configurations, and such event was first observed as a pair of quasar (Walsh et al., 1979). This phenomenon is called as *strong lensing*. Strong lensing gives us rich information about the distribution of foreground matter. We can estimate the projected matter distribution in detail.

Paczynski (1986) noted that the image of a star is suddenly magnified by gravitational lensing when another star lines up straight between the star and the observer. This type of gravitational lensing is called as *micro lensing*. Micro lensing is a quite rare event for one object but if we can monitor the light of many stars in the Milky Way or in nearby galaxies, e.g., Large Magellanic Cloud, at the same time, we can detect the sudden magnification. This provides us the insight into distribution of massive objects in the Milky Way. Furthermore, the interesting feature of micro lensing is that we can use it to search for exoplanets. The sudden magnification can occur also by planets as well as stars.

Finally, the last type of gravitational lensing is *weak lensing*, which is one of main targets in this dissertation. In contrast to strong lensing, weak lensing denotes the weak deformation or distortion of images of distant galaxies or quasars due to the gravitational potential by large-scale structures. Apart from the other two types, weak lensing occurs universally, but literally, the signal of weak lensing is very small. In order to detect the signal at significant level, we need to rely on the statistical analysis. As we have already discussed, we can use weak lensing to probe the matter distribution in the Universe.

In this Chapter, we review the theory of gravitational lensing with emphasis on weak lensing in the cosmological context. For thorough reviews, refer to Schneider et al. (1992) for a general overview, to Bartelmann & Schneider (2001); Munshi et al. (2008); Kilbinger (2015); Mandelbaum (2018) for weak lensing and to Treu (2010) for strong lensing.

3.2 Deflection of Light

3.2.1 Schwarzshild Lens

The simplest case of gravitational lensing is the situation with a point source and a point mass (*lens* object), which is depicted in Figure 3.1. We will derive this deflection angle with the analogy of optics. We assume the weak gravitational field ($|\Phi| \ll c^2$) and no

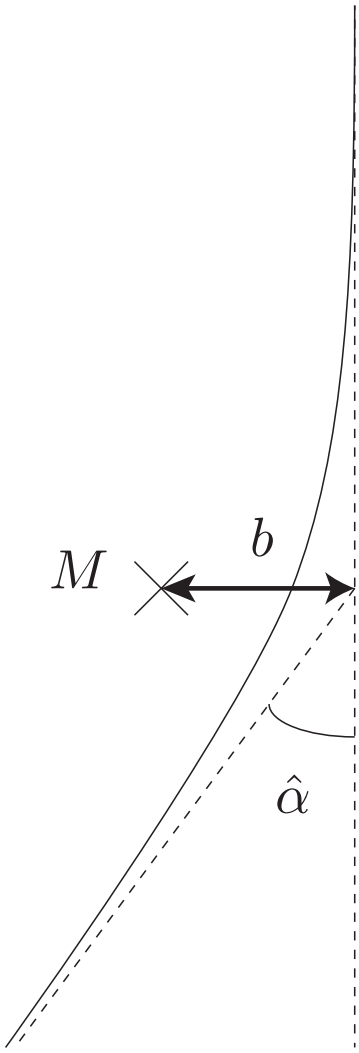

Figure 3.1: Deflection by a point mass. If there is no point mass, light travels straight. If there exists a point mass, the path of light with the impact parameter b is deflected by the angle $\hat{\alpha}$.

cosmological expansion. The metric can be expressed as

$$ds^2 = -\left(1 + \frac{2}{c^2}\Phi\right) c^2 dt^2 + \left(1 - \frac{2}{c^2}\Phi\right) dx^2, \tag{3.1}$$

where Φ corresponds to the gravitational potential. The refractive index n is

$$n = c \Big/ \left(\frac{dx}{dt}\right) = \sqrt{\frac{1 - 2\Phi/c^2}{1 + 2\Phi/c^2}} \simeq 1 - 2\Phi. \tag{3.2}$$

From the Fermat's principle, the deflection angular position $\hat{\boldsymbol{\alpha}}$ is given by

$$\hat{\boldsymbol{\alpha}} = -\int \nabla_\perp n \, dl = \frac{2}{c^2} \int \nabla_\perp \Phi \, dl, \tag{3.3}$$

where $\nabla_\perp$ denotes the differential operator in the direction perpendicular to the path of light. In general, we have to integrate along the path of light, but in many cases the deflection angle is small and we can integrate along the unperturbed path. Consider the situation that light comes toward us with the impact factor b and is deflected by the point mass which mass is M. The system is referred to as *Schwarzshild lens*. The gravitational potential Φ is

$$\Phi(b, z) = -\frac{GM}{(b^2 + z^2)^{1/2}}. \tag{3.4}$$

And the differentiation of it is

$$\nabla_\perp \Phi(b, z) = -\frac{GM}{(b^2 + z^2)^{3/2}} \boldsymbol{b}. \tag{3.5}$$

Using Eq. (3.3), we can obtain the deflection angle,

$$\hat{\boldsymbol{\alpha}} = \frac{4GM}{c^2 b} \boldsymbol{e}_b = \frac{2R_s}{b} \boldsymbol{e}_b, \tag{3.6}$$

where $\boldsymbol{e}_b$ is the unit vector in the direction of $\boldsymbol{b}$ and $R_s \equiv 2GM/c^2$ is the Schwarzshild radius.

3.2.2 Thin Lens Approximation and Lens Equation

In astrophysically interested cases, the spatial extent of the lens object is sufficiently small compared with the distance between the lens and the observer. The mass distribution of the lens is projected in the line-of-sight direction and treated as mass sheet. This sheet is called as *lens plane*. The lens plane is characterized by surface density,

$$\Sigma(\boldsymbol{\xi}) = \int \rho(\boldsymbol{\xi}, z) dz, \tag{3.7}$$

where $\boldsymbol{\xi}$ is a two-dimensional vector in the lens plane. The deflection angle at the position $\boldsymbol{\xi}$ can be expressed as the sum of contributions from all mass elements of the lens plane,

$$\hat{\boldsymbol{\alpha}}(\boldsymbol{\xi}) = \frac{4G}{c^2} \int \frac{\boldsymbol{\xi} - \boldsymbol{\xi}'}{|\boldsymbol{\xi} - \boldsymbol{\xi}'|^2} d^2\xi'. \tag{3.8}$$

If the lens is axis-symmetric, we can proceed further and the equation becomes

$$\hat{\boldsymbol{\alpha}}(\xi) = \frac{4GM(\xi)}{c^2\xi}, \tag{3.9}$$

where ξ is the distance from the center of the symmetry and $M(\xi)$ is defined as

$$M(\xi) = \int_0^{\xi} d\xi'\, 2\pi\xi'\Sigma(\xi'). \tag{3.10}$$

Let us consider the system which is composed of the source, the lens, and the observer. Figure 3.2 depicts this situation. The path of ray is deflected by the lens, which is assumed to be the thin sheet. The apparent position of the image is $\boldsymbol{\theta}$ and the true position is $\boldsymbol{\beta}$. And we introduce the reduced deflection angle $\boldsymbol{\alpha}$, which is related with the deflection angle $\hat{\boldsymbol{\alpha}}$ by

$$\boldsymbol{\alpha} = \frac{D_{\rm ds}}{D_{\rm s}}\hat{\boldsymbol{\alpha}}. \tag{3.11}$$

From the figure, the relation between these angular positions is

$$D_{\rm s}\boldsymbol{\theta} = \boldsymbol{\beta}D_{\rm s} - \hat{\boldsymbol{\alpha}}D_{\rm ds}. \tag{3.12}$$

This reduces to

$$\boldsymbol{\beta} = \boldsymbol{\theta} - \boldsymbol{\alpha}, \tag{3.13}$$

which is referred to as *lens equation*. Note that all distances used here $D_{\rm s}, D_{\rm ds}, D_{\rm d}$ are angular diameter distances.

For a special case, suppose that the lens plane has a constant surface density Σ. In this case, the deflection angle is

$$\alpha(\theta) = \frac{D_{\rm ds}}{D_{\rm s}}\frac{4G}{c^2\xi}\Sigma\pi\xi^2. \tag{3.14}$$

Substituting $\xi = D_{\rm d}\theta$, we obtain

$$\alpha(\theta) = \Sigma\frac{4\pi G}{c^2}\frac{D_{\rm d}D_{\rm ds}}{D_{\rm s}}\theta = \frac{\Sigma}{\Sigma_{\rm cr}}\theta, \tag{3.15}$$

where we have defined *critical surface mass density* $\Sigma_{\rm cr}$ as

$$\Sigma_{\rm cr} \equiv \frac{c^2}{4\pi G}\frac{D_{\rm s}}{D_{\rm d}D_{\rm ds}}. \tag{3.16}$$

When the surface density coincides with the critical density, the deflection angle is $\alpha(\theta) = \theta$ and the true position is $\beta = 0$.

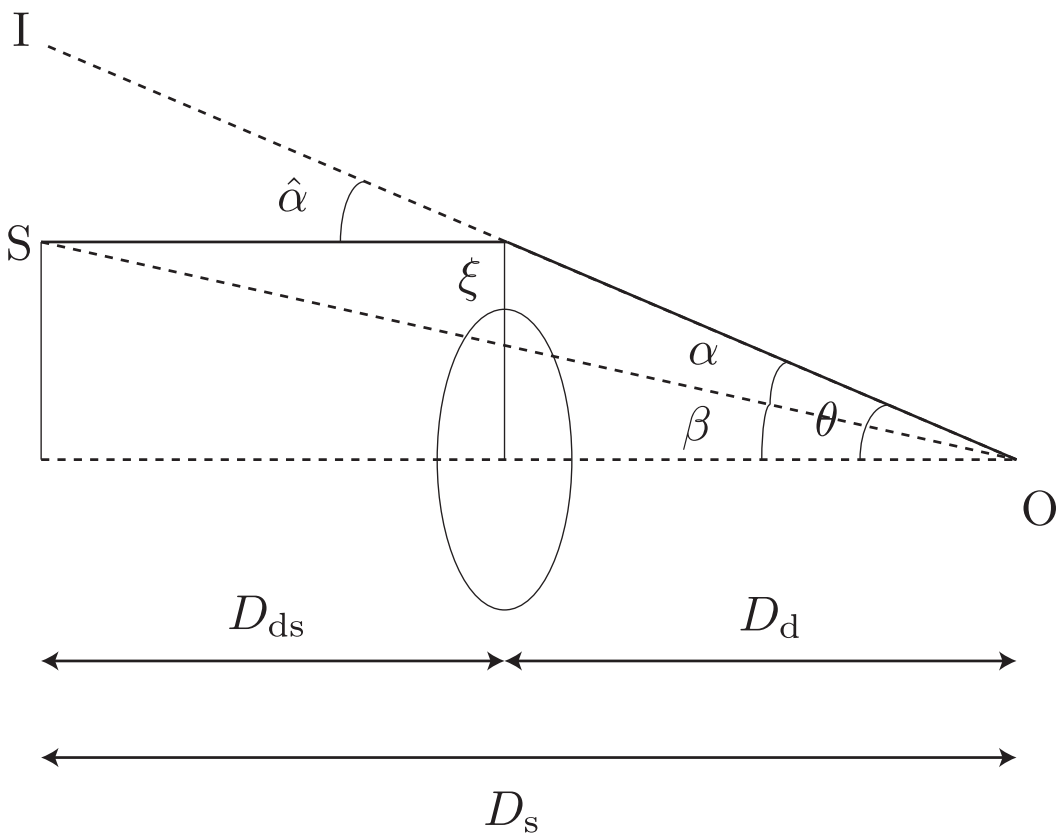

Figure 3.2: Deflection by a plane which has finite surface mass density. The observer at the point O can see a lensed image at the point I, though the true position is the point S. The angular diameter distances between the observer and the source, the observer and the lens, and the lens and the source are $D_{\rm s}$, $D_{\rm d}$, and $D_{\rm ds}$, respectively.

3.2.3 Einstein Radius

Let us consider the axis-symmetric lens again. The lens equation becomes

$$\beta(\theta) = \theta - \frac{D_{\rm d} D_{\rm ds}}{D_{\rm s}} \frac{4GM(\theta)}{c^2\theta}. \tag{3.17}$$

If all of the source, the lens and the observer stand in a straight line ($\beta = 0$), the lensed image looks like a ring. This ring is called as *Einstein ring*. From the lens equation, we can obtain the angular position of the ring, i.e., *Einstein radius* $\theta_{\rm E}$, by solving the following equation,

$$\theta_{\rm E}^2 = \frac{D_{\rm d} D_{\rm ds}}{D_{\rm s}} \frac{4GM(\theta_{\rm E})}{c^2}. \tag{3.18}$$

The Einstein radius corresponds to the characteristic angular scale for strong lensing. If the angular separation between the source and the lens is closer than the Einstein radius, the multiple images are likely to occur.

3.3 Light Propagation in the Inhomogeneous Universe

Here, we discuss weak gravitational lensing due to large-scale structures at cosmological scale, which is commonly referred to as *cosmic shear*. In the previous Section, there is only a single lens object. However, for cosmic shear the lens object is the smooth matter distribution.

3.3.1 Lens Equation in the Inhomogeneous Universe

Again using Fermat's principle, we can obtain the same expression of the deflection angle $\hat{\boldsymbol{\alpha}}$ on the comoving coordinate,

$$\hat{\boldsymbol{\alpha}} = -\frac{2}{c^2} \int \nabla_\perp \Phi d\chi, \tag{3.19}$$

where $\nabla_\perp$ denotes the differentiation in the comoving direction perpendicular to the path of light.

We will relate light deflections with the gravitational potential on a cosmological scale. Let us consider that two close rays. In the homogeneous Universe, the transverse comoving separation of the two light rays at radial comoving distance χ can be written with angular diameter distance $f_K(\chi)$,

$$\boldsymbol{x}_0 = f_K(\chi)\boldsymbol{\theta}. \tag{3.20}$$

But in the inhomogeneous Universe, density fluctuation deflects the path of rays. We employ the differential form of Eq. (3.19),

$$d\hat{\boldsymbol{\alpha}} = -\frac{2}{c^2} \nabla_\perp \Phi(\boldsymbol{x}, \chi') d\chi', \tag{3.21}$$

where $\Phi(\boldsymbol{x}, \chi)$ is the gravitational potential at the transverse and radial comoving distance is $\boldsymbol{x}$ and χ, respectively. For the transverse comoving separation $d\boldsymbol{x}$ is

$$d\boldsymbol{x} = f_K(\chi - \chi')d\hat{\boldsymbol{\alpha}} = -f_K(\chi - \chi')\frac{2}{c^2}\nabla_\perp \Phi(\boldsymbol{x}, \chi')d\chi'. \tag{3.22}$$

We can obtain total deflection between two rays by integrating the above expression,

$$\boldsymbol{x}(\chi) = \int d\boldsymbol{x} = f_K(\chi)\boldsymbol{\theta} - \int_0^\chi d\chi' f_K(\chi - \chi')\frac{2}{c^2}[\nabla_\perp \Phi(\boldsymbol{x}, \chi') - \nabla_\perp \Phi(\boldsymbol{0}, \chi')]. \tag{3.23}$$

If we introduce the apparent position $\boldsymbol{\theta}$ and the true position $\boldsymbol{\beta} = \boldsymbol{x}(\chi)/f_K(\chi)$, we can rewrite Eq. (3.23) as the lens equation,

$$\boldsymbol{\beta} = \boldsymbol{\theta} - \boldsymbol{\alpha}, \tag{3.24}$$

with the scaled deflection angle $\boldsymbol{\alpha}$,

$$\boldsymbol{\alpha} = \int_0^\chi d\chi' \frac{f_K(\chi - \chi')}{f_K(\chi)}\frac{2}{c^2}[\nabla_\perp \Phi(\boldsymbol{x}, \chi') - \nabla_\perp \Phi(\boldsymbol{0}, \chi')]. \tag{3.25}$$

3.3.2 Born Approximation and Jacobian Matrix

The lens equation is an integral equation, and so in general, it is impossible to derive the analytic solution. However, we can approximate the equation by replacing the separation vector in the integral with the zeroth order solution $\boldsymbol{x}_0 = f_K(\chi)\boldsymbol{\theta}$. This approximation corresponds to the integral along the unperturbed ray and called as *Born approximation*. We define a Jacobian matrix A_{ij} as

$$A_{ij} = \frac{\partial \beta_i}{\partial \theta_j} = \delta_{ij} - \frac{\partial \alpha_i}{\partial \theta_j} \tag{3.26}$$

$$= \delta_{ij} - \frac{2}{c^2}\int_0^\chi d\chi' \frac{f_K(\chi - \chi')}{f_K(\chi)f_K(\chi')}\frac{\partial^2}{\partial\theta_i \partial\theta_j}\Phi(f_K(\chi')\boldsymbol{\theta}, \chi'). \tag{3.27}$$

It is useful to introduce *lensing potential* Ψ,

$$\Psi(\boldsymbol{\theta}, \chi) = \frac{2}{c^2}\int_0^\chi d\chi' \frac{f_K(\chi - \chi')}{f_K(\chi)f_K(\chi')}\Phi(f_K(\chi')\boldsymbol{\theta}, \chi'). \tag{3.28}$$

Hence the Jacobian matrix is again expressed with respect to the lensing potential,

$$A_{ij} = \delta_{ij} - \partial_i \partial_j \Psi, \tag{3.29}$$

where $\partial_i \equiv \frac{\partial}{\partial \theta_i}$. The Jacobian matrix is a symmetric matrix, and decomposed into three independent quantities, *convergence* κ and *shear* γ_1, γ_2. The explicit form of the Jacobian matrix is

$$A = \begin{pmatrix} 1 - \kappa - \gamma_1 & -\gamma_2 \\ -\gamma_2 & 1 - \kappa + \gamma_1 \end{pmatrix}. \tag{3.30}$$

Convergence and shear are defined with the Jacobian matrix,

$$\kappa = \frac{1}{2}(\partial_1\partial_1 + \partial_2\partial_2)\Psi,\ \gamma_1 = \frac{1}{2}(\partial_1\partial_1 - \partial_2\partial_2)\Psi,\ \gamma_2 = \partial_1\partial_2\Psi. \tag{3.31}$$

Shear can be treated as a complex quantity,

$$\gamma \equiv \gamma_1 + i\gamma_2 = |\gamma| \exp(2i\phi), \tag{3.32}$$

where ϕ is the polar angle between γ_1 and γ_2. Convergence denotes the isotropic changes of size and brightness, and shear represents stretching the images. The shear transforms as spin-2 field.

3.3.3 Estimation of Shear from Galaxy Shape

Convergence and shear cannot be observed independently in weak lensing surveys. The relation between lensed position $\boldsymbol{x}_l$ and unlensed position $\boldsymbol{x}_u$ is given as

$$\boldsymbol{x}_u = A\boldsymbol{x}_l. \tag{3.33}$$

We can estimate the deformed shape of images but not the size, and the change of the size corresponds to multiplying a constant to the Jacobian matrix. The relation can be rewritten as

$$\begin{pmatrix} x_u \\ y_u \end{pmatrix} = (1-\kappa)\begin{pmatrix} 1-g_1 & -g_2 \\ -g_2 & 1+g_1 \end{pmatrix}\begin{pmatrix} x_l \\ y_l \end{pmatrix}, \tag{3.34}$$

where we have defined *reduced shear* g as

$$g \equiv \frac{\gamma}{1-\kappa}. \tag{3.35}$$

The reduced shear is commonly used as the direct observable in weak lensing surveys. Since weak lensing causes elliptical deformation at the leading order, the second order moment is useful to characterize the distortion,

$$Q_{ij} = \frac{\int d^2x\, I(\boldsymbol{x})W(\boldsymbol{x})x_i x_j}{\int d^2x\, I(\boldsymbol{x})W(\boldsymbol{x})}, \tag{3.36}$$

where $\boldsymbol{x}$ is the angular position from the center of the image, $I(\boldsymbol{x})$ is the light profile of the image, and $W(\boldsymbol{x})$ is the weighting function. Then, one can define the ellipticity of images with Q_{ij}, but there are two commonly used definitions (Bernstein & Jarvis, 2002),

$$e = e_1 + ie_2 = \frac{Q_{11} - Q_{22} + 2iQ_{12}}{Q_{11} + Q_{22}}, \tag{3.37}$$

and

$$\epsilon = \epsilon_1 + i\epsilon_2 = \frac{Q_{11} - Q_{22} + 2iQ_{12}}{Q_{11} + Q_{22} + 2(Q_{11}Q_{22} - Q_{12}^2)^{1/2}}. \tag{3.38}$$

These two definitions have the same numerator, but the absolute value is different. For an elliptical image with axis ratio r, the absolute value becomes

$$|e| = \frac{1-r^2}{1+r^2}, \ |\epsilon| = \frac{1-r}{1+r}. \tag{3.39}$$

For unlensed images, one can also define the second order moment $Q_{ij}^{(\mathrm{s})}$, which is related with Q_{ij} as

$$Q_{ij}^{(\mathrm{s})} = AQA^T. \tag{3.40}$$

Then, one can derive the transformation from lensed ellipticity to instrinsic ellipticity (Schneider & Seitz, 1995; Seitz & Schneider, 1997),

$$e^{(\mathrm{s})} = \frac{e - 2g + g^2 e^*}{1 + |g|^2 - 2\mathrm{Re}(ge^*)}, \tag{3.41}$$

and

$$\epsilon^{(\mathrm{s})} = \begin{cases} \dfrac{\epsilon - g}{1 - g^*\epsilon} & (|g| \leq 1) \\ \dfrac{1 - g\epsilon^*}{\epsilon^* - g^*\epsilon} & (|g| > 1). \end{cases} \tag{3.42}$$

When the intrinsic shape of galaxies is randomly orientated, the mean ellipticity vanishes,

$$\langle e^{(\mathrm{s})} \rangle = \langle \epsilon^{(\mathrm{s})} \rangle = 0. \tag{3.43}$$

In weak lensing limit ($\kappa \ll 1, \ |\gamma| \ll 1$), the ellipticity becomes unbiased estimator of shear,

$$\gamma \approx g \approx \langle \epsilon \rangle \approx \frac{1}{2}\langle e \rangle, \tag{3.44}$$

and the noise for the estimator is dominated by Poisson noise,

$$\sigma_\gamma = \frac{\sigma_\epsilon}{\sqrt{N}} = \frac{\sigma_e/2}{\sqrt{N}}, \tag{3.45}$$

where σ_e and σ_ϵ are intrinsic dispersion of ellipticity, and N is the number of galaxies used to estimate the reduced shear. It is known that the following transformation of convergence does not change the resultant reduced shear,

$$\kappa' = \lambda\kappa + (1 - \lambda), \tag{3.46}$$

where λ is the arbitrary constant. This uncertainty in reduced shear is called as *mass-sheet degeneracy* (Falco et al., 1985). To break the degeneracy, we need additional measurements of magnification.

3.3.4 Inversion from Shear to Convergence

The analysis of shape measurement yields an estimate of shear field. It is also possible to convert the shear field to convergence field, which can be clearly interpreted as the surface mass density. The relation between shear and convergence is given as (Kaiser & Squires, 1993),

$$\gamma(\boldsymbol{\theta}) = \frac{1}{\pi}\int d^2\theta'\,\mathcal{D}(\boldsymbol{\theta}-\boldsymbol{\theta}')\kappa(\boldsymbol{\theta}'), \tag{3.47}$$

$$\mathcal{D}(\boldsymbol{\theta}) \equiv -\frac{\theta_1^2-\theta_2^2+2i\theta_1\theta_2}{\theta^4} = \frac{-1}{(\theta_1-i\theta_2)^2}. \tag{3.48}$$

Thus, convergence can be generated by convoluting shear with the kernel $\mathcal{D}$. In Fourier space, the convolution becomes multiplication,

$$\hat{\gamma}(\boldsymbol{\ell}) = \frac{1}{\pi}\hat{\mathcal{D}}(\boldsymbol{\ell})\hat{\kappa}(\boldsymbol{\ell}), \tag{3.49}$$

where the Fourier transform of the kernel is

$$\hat{\mathcal{D}}(\boldsymbol{\ell}) = \pi\frac{\ell_1^2-\ell_2^2+2i\ell_1\ell_2}{\ell^2}, \tag{3.50}$$

and it satisfies $\hat{\mathcal{D}}(\boldsymbol{\ell})\hat{\mathcal{D}}^*(\boldsymbol{\ell}) = \pi^2$. Note that the Fourier transform of $\hat{\mathcal{D}}(\boldsymbol{\ell})$ at $\boldsymbol{\ell} = \mathbf{0}$ is undefined. Using these relations, we can reconstruct the convergence field,

$$\kappa(\boldsymbol{\theta}) = \kappa_0 + \frac{1}{\pi}\int d^2\theta'\,\hat{\mathcal{D}}^*(\boldsymbol{\theta}-\boldsymbol{\theta}')\gamma(\boldsymbol{\theta}'), \tag{3.51}$$

where κ_0 is undetermined constant term due to unknown $\boldsymbol{\ell} = \mathbf{0}$ mode. The physical meaning of this term is that uniform surface density induces no shear effect. Whereas κ is the real function, the imaginary part arises due to the imperfect inversion.

3.3.5 Systematics for Shape Measurement

Here, we discuss observational challenges for accurate measurements of galaxy shapes. The shapes of galaxies are subject to several observational systematics. Photons emitted from source galaxies are affected by several factors in addition to gravitational lensing. While photons propagate through the atmosphere of the Earth, the photons are scattered by atmospheric molecules, and the images are blurred. In modern measurements, the images are detected by charge coupled device (CCD) in optical telescopes. The pixelization also affects the observed images. Furthermore, various detector noises and statistical fluctuation of photons may change imaging of galaxies. Let us consider the atmospheric effect. In order to correct this effect, we can utilize the observed images of stars. Since the size of stars is quite small, the stars can be approximated as point sources. The observed images is the convolution with point spread function $P_{\rm PSF}$ (PSF),

$$I(\boldsymbol{\theta}) = \int d^2\theta' I(\boldsymbol{\theta}')P_{\rm PSF}(\boldsymbol{\theta}-\boldsymbol{\theta}'). \tag{3.52}$$

The widely used form of PSF is a Gaussian, and its full width at half maximum is called as seeing. For the-state-of-art telescopes, the seeing is around $0''.7$–$0''.8$. The PSF can be estimated from images of stars. Since stars are discretely distributed, we interpolate PSF to the positions of galaxies. As a result, we can remove atmospheric effects by deconvolving the PSF. Note that this discussion is applicable only to ground-based telescopes. For space-based telescopes, the atmospheric effects can be ignored.

Another important systematics in shape measurements is selection bias. The object detection is done by finding the peaks of brightness. If detection criterion would depend on galaxy shapes, the mean shape might not be randomly orientated, and the residual could affect the final cosmological results. Related with selection bias, we need to care about the blended sources, which are overlapping images of two different objects. If the algorithm of shape measurement regards the blended object as a single image, the estimated shape will be biased.

3.3.6 Modeling of Convergence Field

Let us look into the physical meaning of convergence $\kappa(\boldsymbol{\theta})$. Using the lensing potential, convergence becomes

$$\kappa(\boldsymbol{\theta}, \chi) = \frac{1}{2}(\partial_1\partial_1 + \partial_2\partial_2)\Psi \tag{3.53}$$

$$= \frac{1}{c^2}\int_0^\chi d\chi' \frac{f_K(\chi-\chi')f_K(\chi')}{f_K(\chi)}\nabla_\perp^2\Phi(f_K(\chi')\boldsymbol{\theta}, \chi'). \tag{3.54}$$

The gravitational potential follows 3D poisson equation,

$$\nabla^2\Phi = 4\pi G a^2\bar{\rho}\delta. \tag{3.55}$$

The relation between 3D Laplacian ∇^2 and 2D Laplacian $\nabla_\perp^2$ is

$$\nabla^2 = \nabla_\perp^2 + \frac{\partial^2}{\partial\chi'^2}. \tag{3.56}$$

Using this relation, the differential term in Eq. (3.54) becomes

$$\nabla_\perp^2\Phi(f_K(\chi')\boldsymbol{\theta}, \chi') = 4\pi G a^2\bar{\rho}\delta - \frac{\partial^2\Phi}{\partial\chi'^2}. \tag{3.57}$$

The second term vanishes when we integrate in the line-of-sight direction because the positive and negative contributions cancel out. Further, rewriting the mean matter density in terms of the critical density $\bar{\rho} = \rho_{\rm cr}\Omega_{\rm m}a^{-3}$, the expression of convergence can be

$$\kappa(\boldsymbol{\theta}, \chi) = \frac{3}{2}\Omega_{\rm m}\left(\frac{H_0}{c}\right)^2\int_0^\chi d\chi' \frac{f_K(\chi-\chi')f_K(\chi')}{f_K(\chi)a(\chi')}\delta(f_K(\chi')\boldsymbol{\theta}, \chi'). \tag{3.58}$$

From this expression, we can see that convergence corresponds to the projection of density contrast δ with weight function $W(\chi')$,

$$W(\chi') = \frac{f_K(\chi-\chi')f_K(\chi')}{f_K(\chi)}. \tag{3.59}$$

If the Universe is flat, $f_K(\chi) = \chi$ and the weight function is a parabola form $W(\chi') = (\chi - \chi')\chi'/\chi$, which has a maximum at the midpoint between the source and the observer $\chi' = \chi/2$. This means that the convergence is the most sensitive to the structures at the half distance to the source.

In the expressions which we have derived, we have assumed that the source is located at the definite redshift. However, in real observations it is rare to obtain accurate redshifts of sources. In weak lensing surveys, numerous images of distant galaxies are essential. However, a spectroscopic measurement of these galaxies takes a lot of time and some galaxies are too faint to carry out spectroscopy. That is why we have to rely on photometric redshift technique. It enables us to quickly estimate the source redshift only from band magnitudes though the uncertainty of redshift increases. As a result, the source redshift distribution has a broad extent. The observed convergence is the convergence weighted by the source redshift distribution. We denote the source galaxy distribution function as $n(\chi)$ and this function must be normalized as unity,

$$\int_0^{\chi_{\rm H}} d\chi\, n(\chi) = 1, \tag{3.60}$$

where $\chi_{\rm H}$ is the radial comoving distance to the horizon. The observed convergence given a source distribution $n(\chi)$ is

$$\kappa(\boldsymbol{\theta}) = \int_0^{\chi_{\rm H}} d\chi\, q(\chi)\delta(f_K(\chi)\boldsymbol{\theta}, \chi), \tag{3.61}$$

where $q(\chi)$ is the lensing kernel,

$$q(\chi) = \frac{3}{2}\Omega_{\rm m}\left(\frac{H_0}{c}\right)^2 \int_\chi^{\chi_{\rm H}} d\chi'\, n(\chi')\frac{f_K(\chi'-\chi)}{f_K(\chi')}\frac{f_K(\chi)}{a(\chi)}. \tag{3.62}$$

3.4 Statistics of Cosmic Shear

3.4.1 Decomposition of E-mode and B-mode

It is useful to introduce E-mode and B-mode decomposition for a convergence field. There are many equivalent ways of decomposition. One decomposition is the complex surface mass density,

$$\kappa = \kappa_E + i\kappa_B. \tag{3.63}$$

There is another way of decomposition. One can define the following vector,

$$\boldsymbol{u}_\gamma \equiv \begin{pmatrix} \partial_1\gamma_1 + \partial_2\gamma_2 \\ \partial_1\gamma_2 - \partial_2\gamma_1 \end{pmatrix}. \tag{3.64}$$

Its gradient component corresponds to E-mode and its rotational component does to B-mode,

$$\nabla^2\kappa_E = \nabla\cdot\boldsymbol{u}_\gamma,\ \nabla^2\kappa_B = \nabla\times\boldsymbol{u}_\gamma. \tag{3.65}$$

At the linear order, the relation $\nabla\kappa = \boldsymbol{u}_\gamma$ is satisfied, and there is no B-mode. However, non zero B-mode component $\kappa_{\rm B}$ can occur in real observations by following reasons.

1. Higher-order terms beyond Born approximation.
2. Intrinsic alignment of galaxies.
3. Selection bias of lens galaxies or clustering of galaxies.
4. Systematics which arises in image analysis such as PSF corrections.

The B-mode contribution is much smaller than that of E-mode, and so we can use non-detection of B-mode as a null test. On the other hand, in upcoming weak lensing surveys, these factors might be detectable and modeling the B-mode contribution has to be understood.

3.4.2 Convergence Power Spectrum

Next, we will discuss the fundamental statistics of weak lensing. The most basic one is two-point correlation function (2PCF) $\xi(\theta)$ and its Fourier transform, power spectrum $C_\kappa(\ell)$:

$$\xi(\theta) = \langle \kappa(\boldsymbol{\phi})\kappa(\boldsymbol{\phi}+\boldsymbol{\theta})\rangle, \tag{3.66}$$

$$\langle \tilde{\kappa}(\boldsymbol{\ell})\tilde{\kappa}^*(\boldsymbol{\ell}')\rangle = (2\pi)^2\delta_{\rm D}^2(\boldsymbol{\ell}-\boldsymbol{\ell}')C_\kappa(\ell). \tag{3.67}$$

Due to the homogeneity and isotropy of density field, 2PCF and power spectrum depends only on the magnitude of angle and multipole (θ and ℓ), not the direction.

We employ Limber equation (Eq. 2.91) with the weight function,

$$q_1(\chi) = q_2(\chi) = q(\chi). \tag{3.68}$$

The resulting expression of power spectrum $C_\kappa(\ell)$ is

$$C_\kappa(\ell) = \int_0^{\chi_{\rm H}} d\chi \left(\frac{q(\chi)}{f_K(\chi)}\right)^2 P_{\rm m}\left(\frac{\ell+1/2}{f_K(\chi)};\chi\right). \tag{3.69}$$

Though we have applied many assumptions, we can obtain the simple formula for power spectrum. Figure 3.3 shows the spectra based on Eq. (3.69) with linear matter power spectrum and power spectrum with nonlinear correction.

We have worked on convergence power spectra, and we also mention shear power spectra $P_\gamma(\ell)$. The shear power spectra are equal to convergence power spectra. Shear in Fourier space can be written with respect to convergence with Eq. (3.31),

$$\tilde{\gamma}(\boldsymbol{\ell}) = \frac{(\ell_1+i\ell_2)^2}{\ell^2}\tilde{\kappa}(\boldsymbol{\ell}) = e^{2i\beta}\tilde{\kappa}(\boldsymbol{\ell}), \tag{3.70}$$

where β is the polar angle of the wave-vector $\boldsymbol{\ell}$. From this expression, it is clear that shear power spectrum is identical to convergence power spectrum:

$$C_\gamma(\ell) = C_\kappa(\ell). \tag{3.71}$$

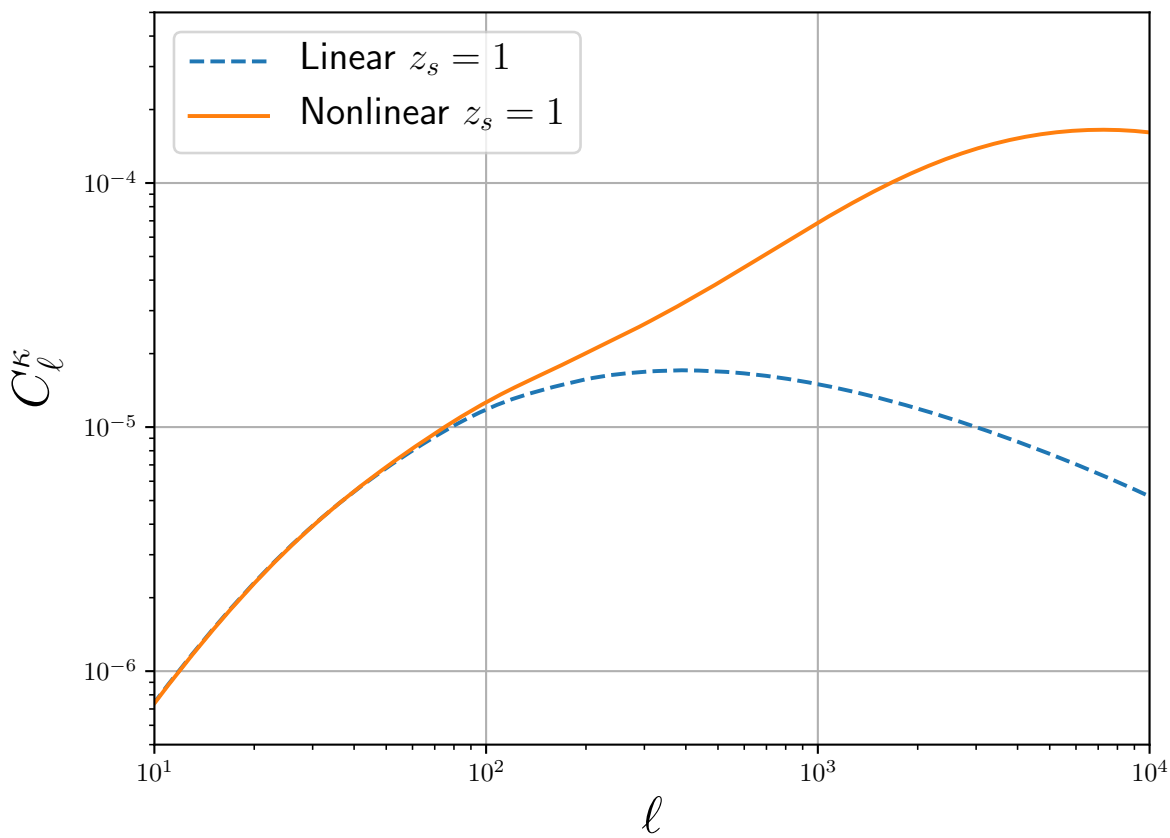

Figure 3.3: Convergence power spectra with the source redshift $z_s = 1$. The solid (dashed) line corresponds to spectrum with nonlinear (linear) matter power spectrum. Nonlinear corrections are based on Takahashi et al. (2012).

So far, we have employed all observed source galaxies to estimate weak lensing signals, which redshift distribution is described by $n(z)$. On the other hand, we have photometric redshift information for each source galaxy, and the whole galaxy sample can be divided according to their photometric redshifts. Thus, we can obtain different weak lensing power spectra with subsamples, which reflect the matter distribution at different epochs. From these spectra, we can trace the evolution of matter growth with weak lensing. This technique is called as *tomography* (Hu, 1999), and is regarded as an efficient method to extract the cosmological information from weak lensing observables. From the whole sample, we can construct the subsamples, which redshift distribution is denoted as

$$n^{(i)}(\chi)\,(i = 1, \ldots, N), \tag{3.72}$$

where N is the number of bins, and i denotes the label of the subsample. Similarly, the lensing kernel $q^{(i)}(\chi)$ is constructed based on $n^{(i)}(\chi)$. Then, we define the auto- and cross-spectra between all pairs of source galaxy samples as

$$C_\kappa^{(ij)}(\ell) = \int_0^{\chi_{\rm H}} d\chi\, \frac{q^{(i)}(\chi) q^{(j)}(\chi)}{f_K^2(\chi)} P_{\rm m}\left(\frac{\ell + 1/2}{f_K(\chi)}; \chi\right). \tag{3.73}$$

Note that the cross-spectra have nonzero amplitudes and convey significant information because weak lensing is sensitive to the foreground structures to the source galaxies.

3.4.3 Shear Correlation Function

Power spectra can be understood straightforward with analytical calculation. On the other hand, in weak lensing surveys, statistics in configuration space is more accessible because the survey geometry and masks can be incorporated in a natural manner. In this Section, we focus on shear 2PCFs, which can be measured directly from shape measurements.

It is useful to decompose shear into two components, tangential shear $\gamma_{\rm t}$ and cross-component $\gamma_\times$:

$$\gamma_{\rm t} = -{\rm Re}[\gamma e^{-2i\phi}],\ \gamma_\times = -{\rm Im}[\gamma e^{-2i\phi}]. \tag{3.74}$$

Here ϕ denotes the polar angle of the position vector $\boldsymbol{\theta}$. If there is a point mass at the center, tangential shear has a positive value $\gamma_{\rm t} > 0$.

The possible combinations of 2PCFs are $\langle\gamma_{\rm t}\gamma_{\rm t}\rangle$, $\langle\gamma_\times\gamma_\times\rangle$, and $\langle\gamma_{\rm t}\gamma_\times\rangle$. The last one vanishes if the Universe is statistically invariant under the mirror transformation. We can define two 2PCFs,

$$\xi_+(\theta) = \langle\gamma\gamma^*\rangle = \langle\gamma_{\rm t}\gamma_{\rm t}\rangle + \langle\gamma_\times\gamma_\times\rangle, \tag{3.75}$$

$$\xi_-(\theta) = {\rm Re}[\langle\gamma\gamma\rangle e^{-4i\phi}] = \langle\gamma_{\rm t}\gamma_{\rm t}\rangle - \langle\gamma_\times\gamma_\times\rangle. \tag{3.76}$$

The estimators of 2PCFs are

$$\hat{\xi}_\pm(\theta) = \frac{\sum_{i,j} w_i w_j (e_{{\rm t},i} e_{{\rm t},j} \pm e_{\times,i} e_{\times,j})}{\sum_{i,j} w_i w_j}. \tag{3.77}$$

The sum is taken over all galaxy pairs, whose separation angular distance belongs to the bin around θ. Shape measurement gives the estimated ellipticity e_i and weight w_i (Miller et al., 2013).

The 2PCFs are related with E/B-mode convergence power spectra $C_\kappa^{\mathrm{E/B}}(\ell)$ via Hankel transformation,

$$\xi_+(\theta) = \frac{1}{2\pi}\int \ell d\ell J_0(\ell\theta)[C_\kappa^{\mathrm{E}}(\ell) + C_\kappa^{\mathrm{B}}(\ell)], \tag{3.78}$$

$$\xi_-(\theta) = \frac{1}{2\pi}\int \ell d\ell J_4(\ell\theta)[C_\kappa^{\mathrm{E}}(\ell) - C_\kappa^{\mathrm{B}}(\ell)], \tag{3.79}$$

where $J_{0,4}$ is the Bessel functions of the first kind. From this integrations, we can compute 2PCFs from analytic power spectra. Figure 3.4 shows measurements of 2PCFs from KiDS survey (Hildebrandt et al., 2017).

3.4.4 Systematics in Modeling of Weak Lensing Statistics

We can model the statistics of weak lensing in a straightforward way, but several systematics affect the results. One of the major systematics is *intrinsic alignment* (IA) (Catelan et al., 2001; Hirata & Seljak, 2004). So far, we have assumed that the intrinsic shape of galaxies are randomly orientated, but galaxy shapes are correlated due to the local tidal field of large-scale structures. Hence, when two galaxies are closely located, they are subject to the same tidal field, and as a result, their shapes become correlated. In addition, the tidal field is caused by massive halos, and they are also source of weak lensing signal. It is known that the lensing and tidal alignment cause distortions at opposite directions, which results in negative correlation between lensed and tidally disrupted shapes. In order to remove the contribution of IA, the power spectrum induced due to IA is simultaneously modeled. Among the analytical modeling, nonlinear linear alignment model (Bridle & King, 2007) is widely used in weak lensing measurements. The total power spectrum is given by

$$C^{(ij)}(\ell) = C_{\mathrm{GG}}^{(ij)}(\ell) + C_{\mathrm{GI}}^{(ij)}(\ell) + C_{\mathrm{II}}^{(ij)}(\ell), \tag{3.80}$$

where the cross-correlation $C_{\mathrm{GI}}^{(ij)}(\ell)$ between intrinsic and lensing contributions and the auto-correlation $C_{\mathrm{II}}^{(ij)}(\ell)$ between intrinsic contributions are written as

$$C_{\mathrm{GI}}^{(ij)}(\ell) = \int_0^{\chi_{\mathrm{H}}} d\chi \frac{q^i(\chi)n^{(j)}(\chi) + n^i(\chi)q^{(j)}(\chi)}{f_K^2(\chi)} P_{\mathrm{GI}}\left(\frac{\ell+1/2}{f_K(\chi)};\chi\right), \tag{3.81}$$

$$C_{\mathrm{II}}^{(ij)}(\ell) = \int_0^{\chi_{\mathrm{H}}} d\chi \frac{n^i(\chi)n^{(j)}(\chi)}{f_K^2(\chi)} P_{\mathrm{II}}\left(\frac{\ell+1/2}{f_K(\chi)};\chi\right), \tag{3.82}$$

The shear-intrinsic power spectrum P_{GI} and intrinsic-intrinsic power spectrum P_{II} are

$$P_{\mathrm{GI}}(k,z) = F(z)P_{\mathrm{m}}(k,z), \tag{3.83}$$

$$P_{\mathrm{II}}(k,z) = F^2(z)P_{\mathrm{m}}(k,z). \tag{3.84}$$

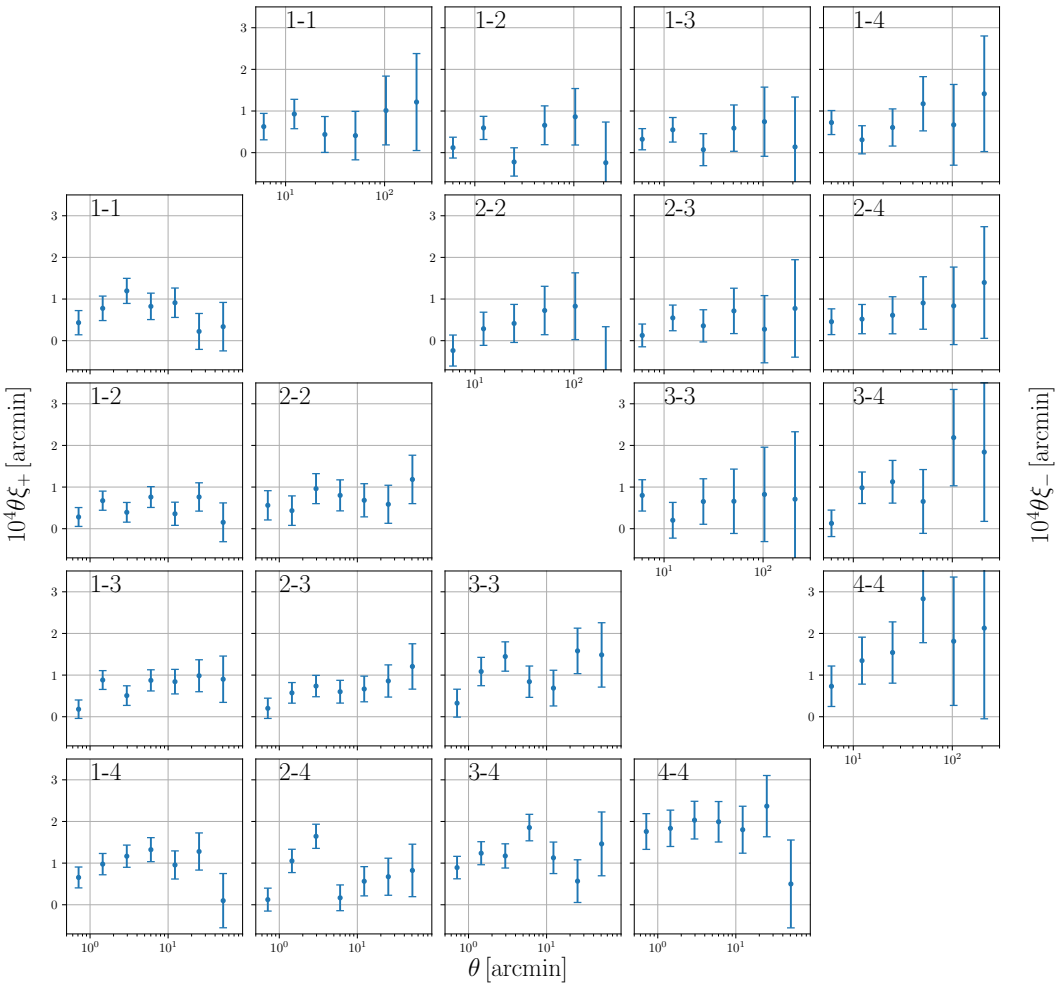

Figure 3.4: Two point correlation functions $\xi_\pm(\theta)$ from measurements in KiDS-450 (Hildebrandt et al., 2017).

The function $F(z)$ is parametrized as

$$F(z) = -A_{\rm IA} C_1 \rho_{\rm cr} \frac{\Omega_{\rm m}}{D(z)} \left(\frac{1+z}{1+z_0}\right)^{\eta} \left(\frac{\bar{L}(z)}{L(z)}\right)^{\beta}, \tag{3.85}$$

where $A_{\rm IA}$ is the normalization constant order of unity, $C_1 = 5 \times 10^{-14}\, h^{-2}\, {\rm M}_{\odot}^{-1}\, {\rm Mpc}^3$ at $z_0 = 0.62$. The redshift and r-band luminosity is assumed to be power-law form with indicis η and β. The index β for luminosity dependence is observed as $\beta = 1.13 \pm 0.27$ for SDSS LOWZ samples (Singh et al., 2015). There is no clear evidence for redshift dependence.

Another notable systematics is feedback effect due to baryonic processes. Hydrodynamical simulations indicate energetic feedback from supernovae and active galactic nuclei dissipate the matter clustering at intermediate scales ($k \sim 0.1\, h\, {\rm Mpc}^{-1}$), and on smaller scales ($k \gtrsim 1\, h\, {\rm Mpc}^{-1}$), gas cools and condensate, and power spectrum is enhanced (Schaye et al., 2015; Springel et al., 2018). That effect results in bias in cosmological parameter estimation for weak lensing (Semboloni et al., 2013; Osato et al., 2015), and can be modeled in the context of halo model (Mead et al., 2015).

3.5 Surveys for Measurements of Weak Gravitaional Lensing

The first detection of weak gravitational lensing at the cosmological scale was reported by several groups in around 2000 (Bacon et al., 2000; Van Waerbeke et al., 2000; Wittman et al., 2000; Rhodes et al., 2001). Sky coverages of these surveys are 0.5–1.5 deg^2. These early results showed that the measured correlation of galaxy ellipticities were larger than expected systematics.

In following years, many wider weak lensing surveys were carried out, including Suprime-Cam survey of the Subaru telescope (Hamana et al., 2003), and Canada-France-Hawaii telescope legacy survey (CFHTLS) (Hoekstra et al., 2006; Heymans et al., 2012). One of critical problems for these surveys was estimation of source redshift distribution $n(z)$. At that time, the observations are performed with a single band and so the photometric redshift was estimated with other multi-band surveys. These surveys had typically small coverage about 1 arcmin^2. For weak lensing, small coverage resulted in large cosmic variance and systematics. But in the following era, this issue was resolved because multi-band imaging surveys had been made available. For example, the deep and multi-band survey of COSMOS field by *Hubble* space telescope enabled one to analyze cosmic shear with high-quality photometric redshifts (Leauthaud et al., 2007).

In the 2010s, we are entering a new era of weak lensing surveys. The state-of-the-art telescopes can take high image quality data and carry out very wide and deep observations. There are several ongoing surveys which aim for precise weak lensing measurements. Such surveys include the Dark Energy Survey (DES: Dark Energy Survey Collaboration, 2016), which has started in 2013 and covers 5000 deg^2 up to the depth $i < 24.5$, the Kilo-Degree Survey (KiDS: de Jong et al., 2013), and Hyper-Suprime Cam

Strategic Survey Program (HSC-SSP: Aihara et al., 2018), which has also been started and will cover 1400 deg^2. The notable point for the HSC survey is its very deep limiting magnitude $i < 26$ with five bands, g, r, i, z, and y.

In the 2020s, larger weak lensing surveys "Stage-IV" are planned to start: *Euclid* (Laureijs et al., 2011; Amendola et al., 2013), Large Synoptic Survey Telescope (LSST: LSST Science Collaboration, 2009), and *WFIRST* (Spergel et al., 2015). When these ongoing and future surveys are available, we have to more care about systematics because wider sky coverage suppresses the statistical errors.

Chapter 4

Astrophysics of Galaxy Clusters

Contents

4.1 Overview

Clusters of galaxies are the most massive bound objects in the Universe. At the center of them, luminous and diffuse galaxies are located, which are classified into cD galaxies. For massive clusters, they have many member galaxies. In reality, only galaxies,

or stellar components, hardly account for mass in clusters. The most part of mass in clusters is made of dark matter. Clusters are encapsulated in dark halos, which extend to broader regions than the distribution of galaxies. In addition, for baryon content, the dominant component is *intra-cluster medium* (ICM), which is mainly composed of hot ($T \sim 10^7$–10^8 K) and ionized plasma and emits intense X-ray from atomic line and free-free emission. We can probe thermodynamic states of hot gas from X-ray observation. However, X-ray is not a unique probe of clusters. From optical observations, we can investigate how many galaxies belong to the clusters. The number of the member galaxies is called as *richness*. The richness is an indicator of the mass of clusters (see, e.g., Murata et al., 2018). In addition, gravitational lensing, i.e., strong lensing or weak lensing, is an important probe for galaxy clusters because, in principle, gravitational lensing can directly probe the matter component regardless of the thermodynamic state of gas.

In this Chapter, we will review basics of galaxy clusters and application of them to cosmology with the particular emphasis on the *Sunyaev–Zel'dovich effect* (SZ). This effect is originally proposed by Sunyaev & Zel'dovich (1972, 1980). As noted above, there are plenty of hot gas in clusters. CMB photons are scattered by hot electrons via inverse Compton scattering, and as a result the spectrum deviates from the blackbody spectrum. In addition to the distortion of the spectrum, the polarization of CMB photons occurs by scattering (Sazonov & Sunyaev, 1999). There are two types of the SZ effect. The first one is the *thermal Sunyeav–Zel'dovich effect* (tSZ). tSZ represents the CMB photons are scattered due to the thermal motion of hot electrons. The other one is the *kinematic Sunyaev–Zel'dovich effect* (kSZ). Instead of thermal motion, the bulk motion of hot gas causes energy transfer between electrons and CMB photons. These two effects appear as CMB temperature anisotropy. Hence, we have to dissect the anisotropy to discriminate other anisotropy. This is observationally quite difficult, but recent progress in CMB measurement has enabled one to measure tSZ on a large scale (Planck Collaboration, 2016d). However, the firm detection of kSZ has not been done yet. By cross-correlating other observables, some groups presented the observational evidence of kSZ (Hand et al., 2012; Schaan et al., 2016). For a review of cosmological application of galaxy clusters, refer to Allen et al. (2011), and for a general review of galaxy cluster formation, refer to Kravtsov & Borgani (2012). For detailed reviews on SZ effects, refer to Birkinshaw (1999); Carlstrom et al. (2002); Kitayama (2014).

4.2 Galaxy Clusters

Galaxy clusters are the most massive and bound objects in the Universe. That is why galaxy clusters work as an ideal laboratory of extreme astrophysics, where energetic X-ray emission is dominant. At the same time, formation of such massive objects are closely related with the initial density peaks. Furthermore, the evolution of dark halos, which host galaxy clusters, is governed by the ambient matter abundance, i.e., density of dark matter, and underlying gravitational physics. Accordingly, galaxy clusters are important objects to probe into cosmology. Here, we will overview the basics of galaxy clusters and theoretical approaches to probe their structures and predict observables, e.g., X-ray

emission from hot gas.

4.2.1 Multi-Wavelength Observations

Since galaxy clusters host energetic gas, they can be observed at wide range of wavelength. The most luminous emission is X-ray from ICM. The primary emission mechanism is collisional: thermal bremsstrahlung (free-free), recombination (free-bound), and line transition (bound-bound). The emissivities of these emissions are proportional to the square of electron number density and inverse of square root of temperature. Hence, the X-ray emission from galaxy clusters is highlighted at central regions. In addition to measurements of bolometric luminosities, modern X-ray satellites make it possible to measure the spatially resolved spectra (see, e.g., Hitomi Collaboration, 2016).

For optical and IR wavelengths, member galaxies are dominant sources at this range. At the core regions, massive and luminous early-type galaxies are likely to be found, and these galaxies show similar color and age distributions, which reflect homogenous nature of galaxy formation. This property is used for optical cluster finding algorithm. As we have already mentioned, SZ effect and weak lensing are also important probes of galaxy clusters. These observables are extensively employed for determination of mass of galaxy clusters.

4.2.2 Equilibrium State of Galaxy Clusters

The onset of formation of halos is initiated by the collapse of surrounding matter. The collisional gas component reaches equilibrium state via dynamical and thermal relaxation. Then, Euler equation can be simplified as the balance between pressure gradient and self-gravity,

$$\frac{1}{\rho_g}\nabla p = -\nabla\phi, \tag{4.1}$$

where ρ_g is the gas density, p is the thermal pressure, and ϕ is the gravitational potential. This state is called as hydrostatic equilibrium (HSE). Then, we proceed with the spherical system, and Euler equation becomes

$$\frac{1}{\rho_g}\frac{dp}{dr} = -\frac{GM(<r)}{r^2}, \tag{4.2}$$

where $M(<r)$ is the enclosed mass within the radius r. The following form is useful with ideal EoS, $p = \rho_g k_{\rm B} T/\mu m_p$, where T is the gas temperature, μ is the mean molecular weight, and m_p is the proton mass,

$$M(<r) = -\frac{r k_{\rm B} T(r)}{G\mu m_p}\left(\frac{d\ln\rho_g(r)}{d\ln r} + \frac{d\ln T(r)}{d\ln r}\right). \tag{4.3}$$

From X-ray observations, we can measure the gas density and temperature profiles, and then, derive hydrostatic mass. So far, we have considered collisional system composed of

gas. On the other hand, collisionless system made of CDM is governed by Jeans equation,

$$M_J(<r) = \frac{r\sigma_r^2(r)}{G}\left(\frac{d\ln\nu(r)}{d\ln r} + \frac{d\ln\sigma_r^2(r)}{d\ln r} + 2\beta(r)\right), \tag{4.4}$$

where $\nu(r)$ is the number density of galaxies, $\beta(r) = 1 - \frac{\sigma_t^2}{2\sigma_r^2}$ is the anisotropy parameter, and σ_t and σ_r are tangential and radial velocity dispersions, respectively. The difference of virialized configurations between collisional (gas) and collisionless (CDM or galaxies) components is that the shape of gas density is rounder than that of collisionless systems because the gas density profile is determined by the gravitational potential (Lau et al., 2011). The gravitational potential is known to be smooth distribution compared with intrinsic dark matter density. In this sense, the shape of galaxy clusters contains information of the formation process (Jing & Suto, 2002; Okabe et al., 2018). Note that HSE does not hold as galaxy clusters continuously undergo merging and accretion of surrounding matter.

4.2.3 Self-Similar Model of Galaxy Clusters

The formation and evolution of galaxy clusters are governed by the gravity. Since the gravitational force has no characteristic scale, the physical properties of galaxy clusters obey scaling relations. Kaiser (1986) developed the baseline model to derive the scaling relations of various quantities related with galaxy clusters, which is referred to as the *self-similar model* (see also Eke et al., 1998). In the self-similar model, all relevant processes are assumed to be scale-free and only gravity drives formation of clusters. In addition, we consider Einstein–de-Sitter Universe ($\Omega_{\rm m} = 1$) and power-law matter power spectrum $P_{\rm m}(k) \propto k^n$. Then, evolution of clusters are controlled by only two parameters: formation redshift z and slope of power spectrum n. It is useful for scaling relations to determine the characteristic mass scale and one commonly used choice is nonlinear mass M_* defined as the mass which makes the mass variance as unity (Eq. 2.102),

$$\sigma(M_*) = \delta_c \simeq 1.686. \tag{4.5}$$

Then, any physical quantities of clusters can be given with respect to the universal variable $\mu \equiv M(z)/M_*(z)$.

Let us proceed with derivation of scaling relations in the self-similar model. First, the mass of halos is arbitrary but the enclosed overdensity Δ for reference density ρ_r, which denotes matter density $\rho_{\rm m}$ or critical density $\rho_{\rm cr}$ in practical cases. The following relation between mass and radius holds,

$$M = \frac{4\pi}{3}R^3\Delta\rho_r. \tag{4.6}$$

In this model, the spherical symmetry and HSE are assumed, and the discussions in Section 4.2.2 hold. The enclosed mass $M(<R)$ should be proportional to $T(R)R$,

$$T \propto \frac{M}{R} \propto (\Delta\rho_r)^{\frac{1}{3}}M^{\frac{2}{3}}. \tag{4.7}$$

The temperature appearing above equation should be measured at the radius R, but if the temperature profile is parameterized as

$$T(r) = T_* \tilde{T}(x = r/R), \tag{4.8}$$

where T_* is the characteristic temperature and $\tilde{T}$ is the scaled temperature profile independent of cluster mass, the observed temperature scales as $\propto T_* \propto T(R)$. In observations, we can measure the spectroscopic temperature $T_{\rm X}$, which is determined from spectrum fitting with single-temperature bremsstrahlung model. In practice, the difference between $T_{\rm X}$ and T_* does not affect the results.

Let us move on scaling relations of gas mass $M_g(< R)$. Similarly to the temperature profile, the gas density profile can be parametrized as, $\rho_g(r) = \rho_{g*}\tilde{\rho}_g(x = r/R)$. Then, the enclosed gas mass can be expressed as

$$M_g(< R) = \int_0^R 4\pi r^2 \rho_g(r) dr = 4\pi \rho_{g*} R^3 \int_0^1 dx\, x^2 \tilde{\rho}_g(x) = 3M \frac{\rho_{g*}}{\Delta\rho_r} \int_0^1 dx\, x^2 \tilde{\rho}_g(x) \propto M, \tag{4.9}$$

where the relation $\rho_{g*} \propto \Delta\rho_r$ is used. Thus, the enclosed gas mass $M_g(< R)$ is proportional to the enclosed total mass $M(< R)$.

With the scaling relations of T and M_g, we can derive scaling relations for interested observables. First, let us consider the X-ray luminosity $L_{\rm X}$. For galaxy clusters, the dominant mechanism of the X-ray emission is free-free emission of ICM. The emissivity of the emission is proportional to $\rho_g^2 T^{1/2}$. Accordingly, the bolometric X-ray luminosity $L_{\rm X}$ scales as

$$L_{\rm X} \propto \rho_g^2 T^{\frac{1}{2}} V \propto \Delta^{\frac{7}{6}} M^{\frac{4}{3}}. \tag{4.10}$$

For other thermodynamic quantities, we can also derive scaling relations. For entropy $K_{\rm X}$,

$$K_{\rm X} \equiv \frac{k_{\rm B} T_{\rm X}}{n_e^{2/3}} \propto \Delta^{-\frac{1}{3}} M^{\frac{2}{3}}, \tag{4.11}$$

and for free electron pressure P_e,

$$P_e = k_{\rm B} n_e T \propto \rho_g T \propto \Delta^{\frac{4}{3}} M^{\frac{2}{3}}. \tag{4.12}$$

Another important quantity $Y_{\rm X}$ has been proposed based on numerical simulations (Kravtsov et al., 2006) and defined as

$$Y_{\rm X} \equiv M_g T_{\rm X} \propto \Delta^{\frac{1}{3}} M^{\frac{5}{3}}. \tag{4.13}$$

It is known that this quantity has smaller scatter than other observables.

4.2.4 Mass-Observable Scaling Relation

The most important parameter to characterize the galaxy cluster is the mass. As we have seen, the analytical model predicts the abundance of galaxy clusters with respect to their masses. However, the direct measurement of mass of galaxy clusters is quite challenging

and only gravitational lensing can measure it only for limited samples. There are more accessible observables of galaxy clusters, e.g., X-ray luminosity or richness. In order to employ galaxy clusters as cosmological probes, we need to convert these observables to mass. From joint measurements with WL and X-ray observations and hydrodynamical simulations, it is found that the mass tightly correlates with the observables, which follows power-law relations in many cases. This relation is called as *mass-observable scaling relation*. We can calibrate the scaling relation with hydrodynamical simulations or measurements with multiple wavelengths, and then estimate the mass of galaxy clusters with limited observables.

In Figure 4.1, we show scaling relations of the luminosity, temperature REXCESS cluster sample (Böhringer et al., 2007; Pratt et al., 2009) observed by *XMM-Newton*. The relation is well fitted with power-law relation with little scatter. This relation can be used to estimate cluster mass from observables, e.g., X-ray luminosities.

4.3 Modeling of Thermodynamic Properties of Intra-Cluster Medium

In this Section, we will present several analytical modeling or fitting formula of profiles of thermodynamic quantities, i.e., number density, temperature, and pressure. For subsequent models, it is common that the density profile of DM follows the NFW profile, but the gas density profile defers from it due to thermal pressure and astrophysical feedback. Utilizing X-ray or SZ observations, we derive analytical, but empirical, treatments. That speeds up predictions of profiles and gives insights into astrophysics of galaxy clusters.

4.3.1 Isothermal β-Model

Here, we introduce empirical gas number density profile, isothermal β-model (Cavaliere & Fusco-Femiano, 1976, 1978), which is known to fit the observed X-ray brightness profile. The number density is given as

$$n_g(r) = \frac{n_{g0}}{[1 + (r/r_c)^2]^{3\beta/2}}. \tag{4.14}$$

This model is empirical one, but here we derive the similar form based on physically motivated discussions (Makino et al., 1998; Suto et al., 1998). Let us consider an isothermal and spherical gas cloud with X-ray temperature $T_{\rm X}$. Then, from Euler equation, gas density satisfies

$$\frac{kT_{\rm X}}{\mu m_p}\frac{d\ln\rho_g(r)}{dr} = -\frac{GM(<r)}{r^2}, \tag{4.15}$$

where μ is the mean molecular weight, and m_p is the proton mass. The enclosed mass $M(<r)$ is given by the NFW profile (Eq. 2.111). Then, the gas density profile can be calculated analytically,

$$\rho_g(r) = \rho_{g0}\exp\left\{-\frac{27}{2}b\left[1 - \frac{\ln(1+r/r_s)}{r/r_s}\right]\right\} = \rho_{g0}e^{-\frac{27}{2}b}\left(1+\frac{r}{r_s}\right)^{\frac{27}{2}b\frac{r_s}{r}}, \tag{4.16}$$

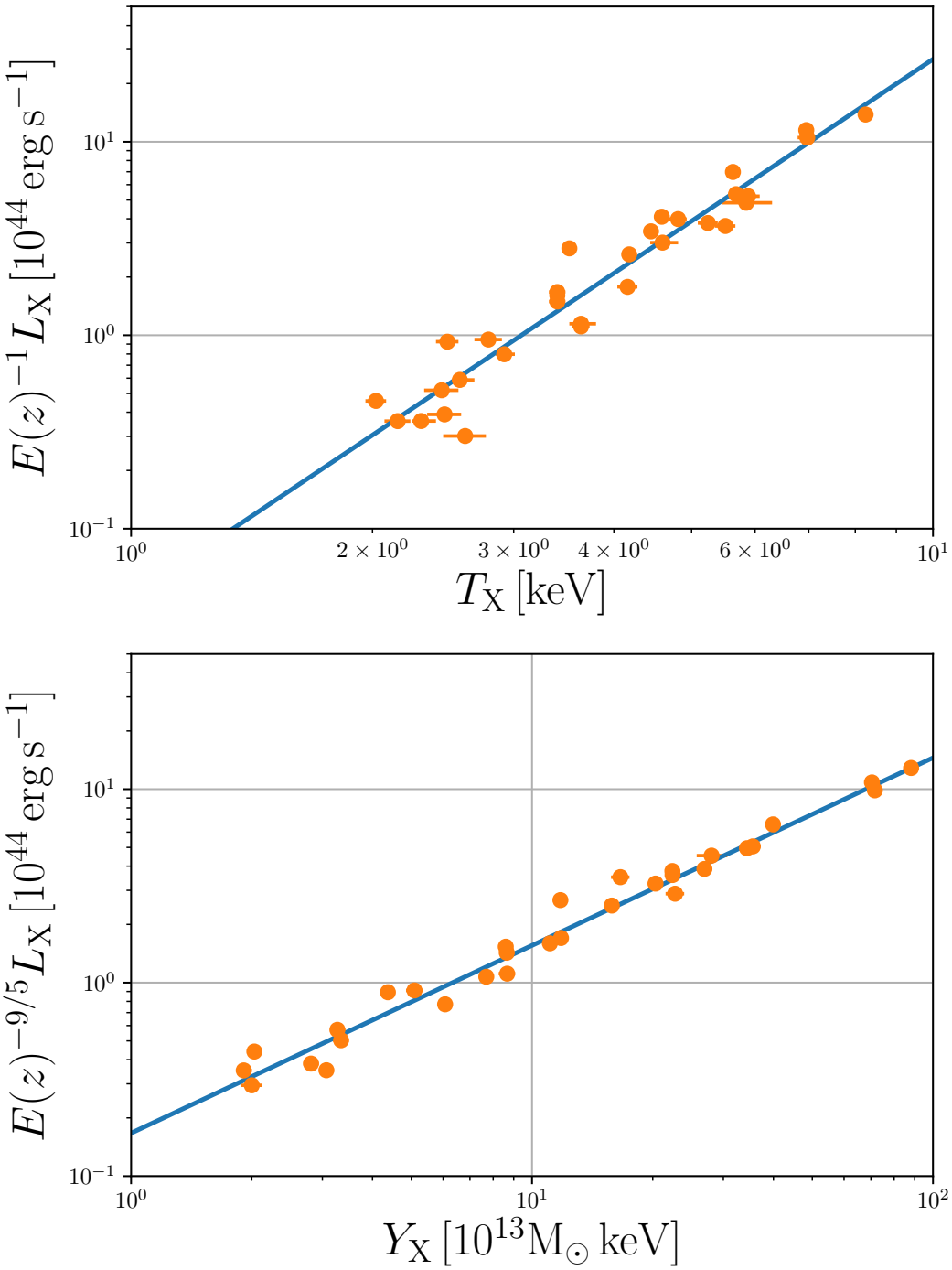

Figure 4.1: Scaling relations between X-ray luminosity, spectroscopic temperature, and integrated Comptonization parameter obtained from REXCESS cluster sample (Pratt et al., 2009). All quantities are measured for core excised regions $0.15 < R/R_{500} < 1$.

with

$$b = \frac{8\pi G\mu m_p \rho_s r_s^2}{27kT_{\rm X}}. \tag{4.17}$$

The X-ray temperature is expected to be close to virial temperature $T_{\rm vir}$ given as

$$kT_{\rm vir} = \gamma \frac{G\mu m_p M(<r)}{3r}, \tag{4.18}$$

where γ is the fudge factor of order of unity which determines the efficiency of shock heating. When $T_{\rm vir}$ is plugged into $T_{\rm X}$, the function b becomes

$$b(r) = \frac{2}{9\gamma}\frac{r}{r_s}\left[\ln\left(1+\frac{r}{r_s}-\frac{r}{r+r_s}\right)\right]^{-1}. \tag{4.19}$$

The functional form looks quite different from the isothermal β-model, but it can well reproduce the behavior.

4.3.2 Komatsu & Seljak Model

Here, we introduce the model developed by Komatsu & Seljak (2002). In this model, the gas density follows dark matter density at the outer part of a halo but at the inner part, gas distribution is assumed to maintain hydrostatic equilibrium (Komatsu & Seljak, 2001). This assumption enables one to determine two free parameters contained in the density and temperature profiles.

First we assume the dark matter density profile follows the NFW profile (Eq. 2.111). Then, we derive the gas density and temperature profiles. In order to obtain these two profiles, we impose three assumptions. The first one is that gas is dynamical equilibrium between gravity and thermal pressure. The second one is that gas density traces dark matter density at $r = r_{\rm vir}$. The last one is that the equation of state is polytropic form $P_g \propto \rho_g^\gamma$. We introduce normalized forms of density and temperature,

$$\rho_g(x) = \rho_g(0) y_g(x), \tag{4.20}$$

$$T_g(x) = T_g(0) y_g^{\gamma-1}(x), \tag{4.21}$$

where $x = r/r_s$. Under three assumptions, one can obtain the explicit expression of $y_g(x)$,

$$y_g(x) \equiv \left\{1 - B\left[1 - \frac{\ln(1+x)}{x}\right]\right\}^{1/(\gamma-1)}, \tag{4.22}$$

where the coefficient B is

$$B \equiv 3\eta^{-1}(0)\frac{\gamma-1}{\gamma}\left[\frac{\ln(1+c)}{c} - \frac{1}{1+c}\right]^{-1}, \tag{4.23}$$

with the concentration parameter c. Analytical expressions of the polytropic index γ and the temperature normalization factor $\eta(0)$ can be obtained by matching density slope

at the virial radius (see appendix of Komatsu & Seljak (2002)). But this expression is complex and hard to compute for each halo. Instead, we use fitting formulae,

$$\gamma = 1.137 + 8.94 \times 10^{-2} \ln(c/5) - 3.68 \times 10^{-3}(c-5), \tag{4.24}$$

$$\eta(0) = 2.235 + 0.202(c-5) - 1.16 \times 10^{-3}(c-5)^2. \tag{4.25}$$

The normalization of $T_g(0)$ is given by

$$T_g(0) = \eta(0) \frac{4}{3+5X} \frac{G m_{\rm p} M}{3 r_{\rm vir}}, \tag{4.26}$$

where $m_{\rm p}$ is the proton mass and $X = 0.76$ is the primordial hydrogen abundance. We require that the gas density traces the dark matter density at $r = r_{\rm vir}$,

$$\rho_g(c) = \rho_g(0) y_g(c) = \frac{\Omega_{\rm b}}{\Omega_{\rm m}} \rho_{\rm dm}(c). \tag{4.27}$$

Thus, we can construct density and temperature profile as a function of a radius, and obtain the gas pressure profile $P_g(x)$ as

$$P_g(x) = \frac{3+5X}{4} \frac{\rho_g(x)}{m_{\rm p}} k_{\rm B} T_g(x). \tag{4.28}$$

4.3.3 Shaw Model

In this Section, we introduce the analytical modeling of thermodynamic profiles of ICM, which we call *Shaw model* in this dissertation. The model goes back to Ostriker et al. (2005); Bode et al. (2009), and has been modified by Shaw et al. (2010), who introduced the concept of radially dependent non-thermal pressure, and Flender et al. (2017), who introduced a method for modeling cool cluster cores.

Some fractions of gas are transformed into stars, which do not contribute the thermal pressure. To determine the stellar mass, we use the observed scaling relations for 91 X-ray selected galaxy groups and clusters in COSMOS field (Giodini et al., 2009),

$$F_*(< R_{\rm 500c}) \equiv \frac{M_*}{M_{\rm 500c}} = f_* \left(\frac{M_{\rm 500c}}{3 \times 10^{14}\,{\rm M}_\odot} \right)^{-S_*}, \tag{4.29}$$

where f_* is the amplitude at the pivot mass $3 \times 10^{14}\,{\rm M}_\odot$, and S_* is the slope with respect to mass. These values are estimated from observations. The amplitude varies from 1% (Budzynski et al., 2014) to 2.58% (Giodini et al., 2009), and the index does from 0 (Leauthaud et al., 2012) to 0.64 (Gonzalez et al., 2007). The stellar mass is estimated within R_{500} but we assume the the stellar mass fraction is the same at $R_{\rm vir}$, i.e., $F_*(< R_{500}) = F_*(< R_{\rm vir})$. The alternative method to estimate stellar mass fraction is the so-called "fossil" model (Nagamine et al., 2006), where the star formation rate is the delay exponential function with decay times of 1.5 Gyr for bulge populations and 4.5 Gyr for disk populations. This model predicts stellar mass fraction smaller ($\lesssim 10\,\%$)

than the empirical relation in Eq. (4.29), but the amplitude is consistent with each other. Hereafter, we use the empirical relation (Eq. 4.29) as the fiducial choice.

Initially, the distributions of density and velocity follow those of dark matter. The initial gas mass is given by

$$M_{g,i} = (f_b - f_*)M_{\rm vir}, \tag{4.30}$$

where the baryon fraction is $f_b = \Omega_{\rm m}/\Omega_{\rm b}$, and the initial total energy of gas is

$$E_{g,i} = 2\pi f_b \int_{r_*}^{R_{\rm vir}} \rho_{\rm DM}(r) 3\sigma_{\rm DM}^2(r) r^2 dr + f_b \int_{r_*}^{R_{\rm vir}} \Phi(r) \frac{dM}{dr} dr, \tag{4.31}$$

where $\sigma_{\rm DM}$ is the velocity dispersion profile of dark matter (see, e.g., Łokas & Mamon, 2001), and Φ is the gravitational potential sourced by dark matter. It is assumed that gas cools into stars within r_*, and the radius r_* determined by the condition $f_b M_{\rm DM} = f_* M_{\rm vir}$. Then, the gas quickly rearranges inside the dark matter NFW profile into HSE with a polytropic equation of state, which is described by the differential equation,

$$\frac{dP_{\rm tot}(r)}{dr} = -\rho_g(r) \frac{d\Phi(r)}{dr}, \tag{4.32}$$

where $P_{\rm tot}$ is the total (thermal + non-thermal) pressure, ρ_g is the gas density. We can write the solution to this equation as

$$P_{\rm tot}(r) = P_0 \theta^{n+1}(r), \tag{4.33}$$

$$\rho_g(r) = \rho_0 \theta^n(r), \tag{4.34}$$

where $\theta(r)$ is the polytropic variable,

$$\theta(r) = 1 + \frac{\Gamma - 1}{\Gamma} \frac{\rho_0}{P_0} (\Phi_0 - \Phi(r)), \tag{4.35}$$

and Φ_0 is the central potential of the cluster. Here, Γ is the polytropic index, for which we adopt the fiducial value $\Gamma = 1.2$, in agreement with hydrodynamical simulations including radiative cooling and stellar feedback (Nagai et al., 2007). Flender et al. (2017) proposed the effect due to radiative cooling by modifying the adiabatic index. Since the cooling becomes effective at the inner core, the adiabatic index is changed within $r_{\rm break}$ as

$$\Gamma'(z) = \tilde{\Gamma}(1+z)^{\gamma}, \tag{4.36}$$

where $\tilde{\Gamma}$ is the amplitude, and γ controls redshift dependence. McDonald et al. (2013) show the strong dependence on redshift of core density.

In order to determine normalization constants, P_0 and ρ_0, we apply two following constraints. First, the condition is based on the total energy budget within $R_{\rm vir}$ during rearrangement,

$$E_{g,f} = E_{g,i} + \epsilon_{\rm DM}|E_{\rm DM}| + \epsilon_{\rm f} M_* c^2 + \Delta E_p, \tag{4.37}$$

where the second term $\epsilon_{\rm DM}|E_{\rm DM}|$ denotes energy transfer due to dynamical friction with dark matter, the third term $\epsilon_{\rm f} M_* c^2$ is released energy due to feedback of SNe and AGN,

and the last term ΔE_p represents work due to expansion by pushing infalling gas. We define the final radius R_f after expansion, within which the gas mass is conserved to $M_{g,i}$. Hence, the work ΔE_p is given as

$$\Delta E_p = \frac{4\pi}{3}(R_{\rm vir}^3 - R_f^3)P_s, \tag{4.38}$$

where the surface pressure P_s at virial radius $R_{\rm vir}$ is assumed to be

$$P_s = f_b P_{\rm DM}(R_{\rm vir}) = f_b \rho_{\rm DM}(R_{\rm vir})\sigma_{\rm DM}^2(R_{\rm vir}). \tag{4.39}$$

The second condition is that the total pressure of the gas at R_f is equal to gas pressure at the virial radius,

$$P_{\rm tot}(R_f) = f_b P_{\rm DM}(R_{\rm vir}). \tag{4.40}$$

Following Shaw et al. (2010), we model the non-thermal pressure fraction as a power law,

$$\frac{P_{\rm nt}}{P_{\rm tot}}(r) = \alpha(z)\left(\frac{r}{R_{500}}\right)^{n_{\rm nt}}, \tag{4.41}$$

where r is the distance from the center of halo, and the power law index $n_{\rm nt}$ is a free parameter. Since non-thermal pressure cannot exceed total pressure, at the outermost radius ($R_{\rm max}$), the inequality $\alpha(z) \leq (R_{\rm max}/R_{500})^{-n_{\rm nt}}$ should be satisfied. Following Shaw et al. (2010), we take the outermost radius as $4R_{500}$, and then it leads to $\alpha(z) \leq 4^{-n_{\rm nt}}$. We parametrize the redshift dependent part as

$$\alpha(z) = \alpha_0 \times \min[(1+z)^\beta, (f_{\rm max} - 1)\tanh(\beta z) + 1], \tag{4.42}$$

where α_0 and β are free parameters and $f_{\rm max} = 4^{-n_{\rm nt}}/\alpha_0$. Based on this functional form, at low redshift, the redshift dependence is power law, but at high redshift, $f(z)$ asymptotes to the maximum value $4^{-n_{\rm nt}}$. Shi & Komatsu (2014) presented the analytical modeling of non-thermal pressure based on assumptions that non-thermal pressure is sourced by growth of cluster mass via merges and accretion, and turbulent motion dissipates with a time-scale determined from dynamical time (see also, Shi et al., 2015, 2016).

4.3.4 Universal Pressure Profile

So far, we have introduced analytical modeling of thermodynamic quantities. Alternatively, we can also employ the fitting formula based on the universal pressure profile proposed by Nagai et al. (2007), which functional form is similar to the NFW profile,

$$\frac{P_{\rm e}(r)}{P_{500}} = p(x)\left[\frac{M_{500c}}{3\times 10^{14} h_{70}^{-1}{\rm M}_\odot}\right]^{0.12}, \tag{4.43}$$

$$p(x) \equiv \frac{P_0}{(c_{500}x)^\gamma[1+(c_{500}x)^\alpha]^{(\beta-\gamma)/\alpha}}, \tag{4.44}$$

$$P_{500} = 1.65\times 10^{-3} E(z)^{8/3}\left[\frac{M_{500c}}{3\times 10^{14} h_{70}^{-1}{\rm M}_\odot}\right]^{2/3} h_{70}^2\,{\rm keV\,cm^{-3}}, \tag{4.45}$$

where $x = r/R_{500}$ and $h_{70} = h/0.7$. We need to introduce several free parameters, which are directly fitted with X-ray or SZ observations.

With the measurements of SZ selected clusters (Planck Collaboration, 2013), we can obtain the universal pressure profile as

$$(P_0, c_{500}, \gamma, \alpha, \beta) = (6.41, 1.81, 0.31, 1.33, 4.13). \tag{4.46}$$

Note that the sample used in calibration consists of clusters of which the mass range is from 0.9 to $15\times10^{14}\,\mathrm{M}_\odot$ and the redshift is less than 0.5. In the case of X-ray observations, we can also fit the parameters with REXCESS cluster sample (Arnaud et al., 2010), and resultant parameters are

$$(P_0, c_{500}, \gamma, \alpha, \beta) = (8.403, 1.117, 0.3081, 1.0510, 5.4905). \tag{4.47}$$

While Eq. (4.43) can reproduce the pressure profile for halos at this range, the pressure profile of group size halos and high redshift halos still remain uncertain. The above fitting formula assumes hydrostatic equilibrium, which leads to the bias of the mass estimate. In order to incorporate the non-thermal pressure support, the hydrostatic bias parameter $b_{\rm HSE}$ is commonly introduced. We rescale $M_{500c} \to M_{500c}(1 - b_{\rm HSE})$ and $R_{500} \to R_{500}(1 - b_{\rm HSE})^{1/3}$. Typically, $b_{\rm HSE} = 0.2$–0.4 can fit the observed results well and is suggested by hydrodynamical simulations.

4.3.5 Hydrodynamical Simulations

The last method we explain is hydrodynamical simulations. Compared with the analytical modeling, we can take various baryonic physics into account, though we need some model parameters. Furthermore, we can investigate clusters with the wide range of redshifts in contrast to observations, where only nearby clusters can be detected. In this method, however, there is a critical disadvantage in cosmological studies. Running cosmological hydrodynamical simulations is computationally expensive and cover small volumes, which leads to lack of number of simulated clusters. Nevertheless, hydrodynamical simulations are still useful and can calibrate fitting formula, e.g., the universal pressure profile. Battaglia et al. (2012) presented the following fitting formula based on simulations including baryonic processes,

$$\frac{P_{\rm th}}{P_{500}} = P_0 \left(\frac{x}{x_c}\right)^{-0.3} \left[1 + \frac{x}{x_c}\right]^{\beta}, \tag{4.48}$$

$$x \equiv \frac{r}{R_{500}}, \tag{4.49}$$

$$P_{500} = f_b \frac{G M_{500} 500 \rho_{\rm cr}(z)}{2 R_{500}}, \tag{4.50}$$

where

$$(P_0, x_c, \beta) = (7.49, 0.710, 4.19). \tag{4.51}$$

This fitting formula provides another way to compute pressure profile and is useful for scrutinizing whether baryonic processes are critical in modeling of ICM.

Figure 4.2 shows the pressure profile of Coma cluster based on methods described so far.

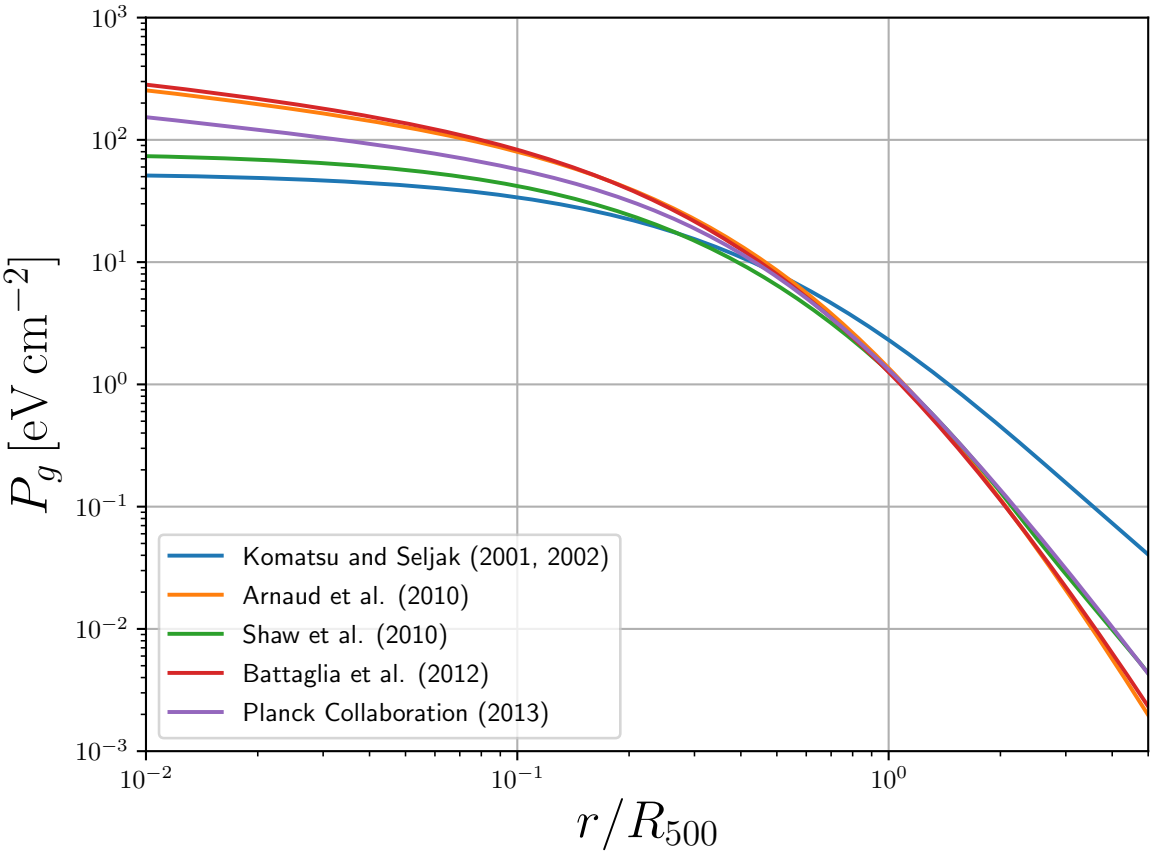

Figure 4.2: Pressure profiles of Coma cluster ($M_{500} = 6.61 \times 10^{14}\, h^{-1}\, \mathrm{M}_\odot$) based on Komatsu & Seljak model (Komatsu & Seljak, 2001, 2002), Shaw model (Shaw et al., 2010), universal pressure profile (Arnaud et al., 2010; Planck Collaboration, 2013), and fitting formula from hydrodynamical simulations (Battaglia et al., 2012).

4.4 The Sunyaev–Zel'dovich Effect

Here, we review the formulation of SZ effects and derive frequency dependence of variation of flux or brightness temperature.

4.4.1 Kompaneets Equation

Hereafter, we adopt the natural unit $c = \hbar = k_{\rm B} = 1$. We begin with the relativistic Boltzmann equation,

$$P^\mu \frac{\partial f}{\partial x^\mu} - \Gamma^\mu_{\nu\lambda} P^\nu P^\lambda \frac{\partial f}{\partial P^\mu} = \mathcal{C}[f], \tag{4.52}$$

where the right hand side is the collision term. In the homogeneous and isotropic Universe, the distribution function depends only on time t and the magnitude of the momentum $|\boldsymbol{P}|$. Equivalently, we can replace $|\boldsymbol{P}|$ with the energy E,

$$E^2 = |\boldsymbol{P}|^2 c^2 + m^2 c^4, \ |\boldsymbol{P}| = \sqrt{g_{ij} P^i P^j}. \tag{4.53}$$

Substituting Christoffel symbols of the homogeneous Universe in Eq. (4.52), the Boltzmann equation in the homogenous and isotropic Universe is

$$\frac{\partial f}{\partial t} - \frac{\dot{a}}{a} \frac{E^2 - m^2}{E} \frac{\partial f}{\partial E} = \frac{1}{E} \mathcal{C}[f]. \tag{4.54}$$

Let us consider the situation that there are photons and free electrons and they are interacting via Compton scatterings,

$$\gamma + e \longleftrightarrow \gamma + e \tag{4.55}$$

The distribution functions of photons and electrons are denoted as f_γ and f_e, respectively. The collision term of photons can be expressed as

$$\begin{aligned} \mathcal{C}[f_\gamma(\boldsymbol{P}_\gamma)] \ = \ & \frac{1}{2} \int \frac{2d^3 P_e}{(2\pi)^3 2E_e} \frac{2d^3 P'_e}{(2\pi)^3 2E'_e} \frac{2d^3 P'_\gamma}{(2\pi)^3 2E'_\gamma} (2\pi)^4 \delta^4_{\rm D}(P_\gamma + P_e - P'_\gamma - P'_e) \\ & \times |\mathcal{M}|^2 \{ f_\gamma(\boldsymbol{P}'_\gamma) f_e(\boldsymbol{P}'_e)[1 - f_e(\boldsymbol{P}_e)][1 + f_\gamma(\boldsymbol{P}_\gamma)] \\ & - f_\gamma(\boldsymbol{P}_\gamma) f_e(\boldsymbol{P}_e)[1 - f_e(\boldsymbol{P}'_e)][1 + f_\gamma(\boldsymbol{P}'_\gamma)] \}, \end{aligned} \tag{4.56}$$

where $E_e = \sqrt{|\boldsymbol{P}_e|^2 + m_e^2}$, $E'_e = \sqrt{|\boldsymbol{P}'_e|^2 + m_e^2}$, and $E_\gamma = |\boldsymbol{P}_\gamma|$. From Klein–Nishina formula and under the assumption of soft photons $E_\gamma \ll m_e$, the square of the scattering amplitude averaged over spin is

$$|\mathcal{M}|^2 = 3\pi m_e^2 \sigma_{\rm T} (1 + \cos^2\theta), \tag{4.57}$$

where $\cos\theta = \boldsymbol{P}_\gamma \cdot \boldsymbol{P}'_\gamma / |\boldsymbol{P}_\gamma||\boldsymbol{P}'_\gamma|$. We are considering non-relativistic electrons and so the 4-momenta of photons and electrons can be

$$P_\gamma = (p, |\boldsymbol{p}|), \ P_e = \left(m_e + \frac{q^2}{2m_e}, \boldsymbol{q} \right), \ P'_\gamma = (p', \boldsymbol{p}'), \ P'_e = \left(m_e + \frac{q'^2}{2m_e}, \boldsymbol{q}' \right), \tag{4.58}$$

where $p = |\boldsymbol{p}|$, $p' = |\boldsymbol{p}'|$, $q = |\boldsymbol{q}|$, and $q' = |\boldsymbol{q}'|$. For the distribution of electrons, they follow Maxwell–Boltzmann distribution and so we can approximate $1 - f_e \simeq 1$. In the case of an isotropic system, the distribution functions depends only on the magnitude of momenta. The collision term becomes

$$\begin{aligned}\mathcal{C}[f_\gamma(p)] &= 3\pi^3\sigma_{\rm T}\int\frac{d^3q}{(2\pi)^3}\frac{d^3q'}{(2\pi)^3}\frac{d^3p'}{(2\pi)^3}\frac{1}{p'}\left[1+\left(\frac{\boldsymbol{p}\cdot\boldsymbol{p}'}{pp'}\right)\right]\\ &\quad\times\delta_{\rm D}\left(p-p'+\frac{q^2-q'^2}{2m_e}\right)(2\pi)^3\delta^3_{\rm D}(\boldsymbol{p}-\boldsymbol{p}'+\boldsymbol{q}-\boldsymbol{q}')\\ &\quad\times\{f_\gamma(p')f_e(q')[1+f_\gamma(p)]-f_\gamma(p)f_e(q)[1+f_\gamma(p')]\}. \end{aligned}\tag{4.59}$$

We are considering Thomson limit and the energy of photons are much smaller than the rest mass of electrons, i.e., $p \ll m_e$ and $p' \ll m_e$. If the scattering occurs efficiently, the magnitudes of photon energy and kinetic energy of electrons are comparable,

$$p \sim p' \sim \frac{q^2}{2m_e} \sim \frac{q'^2}{2m_e}. \tag{4.60}$$

From the inequalities $p \ll m_e$ and $p' \ll m_e$,

$$q \sim q' \gg p \sim p'. \tag{4.61}$$

Typically, $|\boldsymbol{p}-\boldsymbol{p}'| \ll |\boldsymbol{q}-\boldsymbol{q}'|$. We approximate the second delta function in Eq. (4.59) by Taylor expansion,

$$\begin{aligned}\delta^3_{\rm D}(\boldsymbol{p}-\boldsymbol{p}'+\boldsymbol{q}-\boldsymbol{q}') &\simeq \delta^3_{\rm D}(\boldsymbol{q}-\boldsymbol{q}')+(p_i-p'_i)\cdot\frac{\partial}{\partial q_i}\delta^3_{\rm D}(\boldsymbol{q}-\boldsymbol{q}')\\ &\quad+\frac{1}{2}(p_i-p'_i)(p_j-p'_j)\frac{\partial^2}{\partial q_i\partial q_j}\delta^3_{\rm D}(\boldsymbol{q}-\boldsymbol{q}'). \end{aligned}\tag{4.62}$$

Substituting the first term of Eq. (4.62) to Eq. (4.59), this leads to $p = p'$ and $q = q'$, and the integral vanishes. For the second term, the integrand is odd for momenta and this term also vanishes because the distribution is an even function due to the isotropy. The third term yields non-vanishing contribution. First, we integrate angular part of $\boldsymbol{p}'$. Furthermore, the integral is irrelevant to the direction of $\boldsymbol{p}$, and so we average over all directions. Employing the following formula,

$$\int\frac{d\Omega}{4\pi}\frac{d\Omega'}{4\pi}\left[1+\left(\frac{\boldsymbol{p}\cdot\boldsymbol{p}'}{pp'}\right)\right](p_i-p'_i)(p_j-p'_j)=\frac{4}{9}(p^2+p'^2)\delta_{ij}, \tag{4.63}$$

we can simplify the collision term,

$$\begin{aligned}\mathcal{C}[f_\gamma(p)] &= \frac{\sigma_{\rm T}}{3}\int\frac{d^3q}{(2\pi)^3}d^3q'dp'\,p'(p'^2+p^2)\\ &\quad\times\delta_{\rm D}\left(p-p'+\frac{q^2-q'^2}{2m_e}\right)\nabla^2_{\boldsymbol{q}}\delta^3_{\rm D}(\boldsymbol{q}-\boldsymbol{q}')\\ &\quad\times\{f_\gamma(p')f_e(q')[1+f_\gamma(p)]-f_\gamma(p)f_e(q)[1+f_\gamma(p')]\}. \end{aligned}\tag{4.64}$$

In order to proceed, we perform partial integration twice and the result is

$$\begin{aligned}\mathcal{C}[f_\gamma(p)] &= \frac{\sigma_{\rm T}}{3}\int\frac{d^3q}{(2\pi)^3}dp'\,p'(p'^2+p^2)\\ &\times\left\{\left[\frac{q^2}{m_e^2}\delta''_{\rm D}(p-p')\right]f_e(q)[f_\gamma(p')-f_\gamma(p)]\right.\\ &\left.-\left[\frac{2q}{m_e}\delta'_{\rm D}(p-p')+\delta'_{\rm D}\frac{1}{q^2}\frac{d(q^2f'_e)}{dq}\right]f_\gamma(p)[1+f_\gamma(p')]\right\}. \qquad (4.65)\end{aligned}$$

The electron density is

$$n_e = 2\int\frac{d^3q}{(2\pi)^3}f_e(q). \qquad (4.66)$$

The partial integration of this expression gives

$$\int\frac{d^3q}{(2\pi^3)}qf'_e(q) = -\frac{3}{2}n_e. \qquad (4.67)$$

The electrons are not generally in thermal equilibrium, we can define generalized temperature T_e,

$$2\int\frac{d^3q}{(2\pi)^3}\frac{q^2}{2m_e}f_e(q) = \frac{3}{2}n_eT_e. \qquad (4.68)$$

From these definitions, we can rewrite Eq. (4.65) as

$$\begin{aligned}\mathcal{C}[f_\gamma(p)] &= \frac{n_e\sigma_{\rm T}}{2m_e}\int_0^\infty dp'\;p'(p'^2+p^2)\,\{T_e\delta''_{\rm D}(p-p')[f_\gamma(p')-f_\gamma(p)]\\ &+\delta'_{\rm D}(p-p')[f_\gamma(p')+f_\gamma(p)+2f_\gamma(p')f_\gamma(p)]\}\,. \qquad (4.69)\end{aligned}$$

Finally, we perform p' integration and obtain the simplest form,

$$\mathcal{C}[f_\gamma(p)] = \frac{n_e\sigma_{\rm T}}{m_e}\frac{1}{p}\frac{\partial}{\partial p}\left\{p^4\left[T_e\frac{\partial f_\gamma}{\partial p}+f_\gamma(1+f_\gamma)\right]\right\}. \qquad (4.70)$$

Substituting Eq. (4.70) to the Boltzmann equation (Eq. 4.54) and from $f = f_\gamma$ and $E = p$, we get

$$\frac{\partial f}{\partial t}-\frac{\dot a}{a}\frac{E^2-m^2}{E}\frac{\partial f}{\partial E} = \frac{n_e\sigma_{\rm T}}{m_e}\frac{1}{E^2}\frac{\partial}{\partial E}\left\{E^4\left[T_e\frac{\partial f}{\partial E}+f(1+f)\right]\right\}. \qquad (4.71)$$

Given the distribution function of electrons, we can compute the density from Eq. (4.66) and the temperature from Eq. (4.68), and subsequently time evolution of the distribution function of photons from Eq. (4.71).

When the expansion is negligible, we can drop the second term on the right hand side of Eq. (4.71). We convert the independent variables E and t to x and y defined as

$$E\to x = \frac{E}{T_e},\;\; t\to y = \frac{\sigma_{\rm T}}{m_e}\int^t n_eT_edt. \qquad (4.72)$$

Using these variables Eq. (4.71) becomes

$$\frac{\partial f}{\partial y} = \frac{1}{x^2}\frac{\partial}{\partial x}\left[x^4\left(\frac{\partial f}{\partial x} + f(1+f)\right)\right]. \tag{4.73}$$

This equation is referred to as *Kompaneets equation*. The introduced quantity y is called as *Compton-y*. Let us consider the physical meaning of y. The differential form of y is

$$dy = \frac{T_e}{m_e} n_e \sigma_{\mathrm{T}} dt. \tag{4.74}$$

The first term T_e/m_e corresponds to the variation of wavelength in Thomson scattering. The residual term denotes the optical depth $d\tau = n_e\sigma_{\mathrm{T}}dt$, which corresponds to the fraction of the number of scattered photons. The Compton-y is the mean variation of wavelength while light travels are scattered until t.

4.4.2 Spectral Distortion of CMB by the Sunyaev–Zel'dovich Effect

In this Section, we will discuss how the spectrum of CMB is affected by tSZ, i.e., scattering by hot plasma of clusters. The Compton-y in the ordinary unit is

$$y = \frac{\sigma_{\mathrm{T}} k_{\mathrm{B}}}{m_e c^2}\int T_e(r) n_e(r) dr. \tag{4.75}$$

In Kompaneets equation (Eq. 4.73), since the temperature T_e in hot plasma is high, we can ignore terms which do not contain T_e. As a result, Kompaneets equation can be simplified as

$$\frac{\partial f}{\partial y} = \frac{1}{x^2}\frac{\partial}{\partial x}\left(x^4\frac{\partial f}{\partial x}\right). \tag{4.76}$$

In order to solve this equation, we introduce a new variable ξ and a corresponding function

$$\xi \equiv \ln x + 3y,\ \ F(\xi, y) \equiv f(x, y) = f(e^{\xi - 3y}, y). \tag{4.77}$$

Eq. (4.76) becomes

$$\frac{\partial F}{\partial y} = \frac{\partial^2 F}{\partial \xi^2}. \tag{4.78}$$

This differential equation takes a form of a diffusion equation. We can solve it with Fourier transform and the general solution is

$$F(\xi, y) = \frac{1}{\sqrt{4\pi y}}\int_{-\infty}^{\infty} d\xi' e^{-(\xi-\xi')^2/4y} F(\xi', 0). \tag{4.79}$$

In the case where the photons come from CMB, the unperturbed distribution function should be the Planck function. The explicit form is

$$f(x, 0) = \frac{1}{e^x - 1} \equiv f_0(x). \tag{4.80}$$

The typical size of clusters L is Mpc and the electron density n_e and the temperature T_e are $n_e \sim 10^{-3}\,\mathrm{cm}^3$ and $k_\mathrm{B}T_e \sim 10\,\mathrm{keV}$. From this estimation, Compton-y in the direction of clusters has a typical value $y \sim 10^{-4}$. In such a case, where Compton-y is much smaller than unity, we can approximate the distribution function at the linear order in Eq. (4.76) as

$$f(x,y) \simeq f_0(x) + \frac{y}{x^2}\frac{\partial}{\partial x}\left(x^4\frac{\partial f_0}{\partial x}\right). \tag{4.81}$$

The relative variation of the distribution function is

$$\frac{\Delta f}{f} \equiv \frac{f(x,y)-f_0(x)}{f_0(x)} \simeq \frac{y}{x^2 f_0}\frac{\partial}{\partial x}\left(x^4\frac{\partial f_0}{\partial x}\right) = \frac{xy}{1-e^{-x}}\left(x\coth\frac{x}{2}-4\right). \tag{4.82}$$

This quantity is equal to the variation of the brightness $I_\nu = 4\pi\nu^3 f$. The variation of brightness temperature is related with the variation of brightness and so we can obtain the formula for the temperature variation,

$$\begin{aligned}\frac{\Delta T}{T} &= \frac{1-e^{-x}}{x}\frac{\Delta I_\nu}{I_\nu} = \frac{1-e^{-x}}{x}\frac{\Delta f}{f} \\ &= y\left(x\coth\frac{x}{2}-4\right) \to \begin{cases} -2y & (x \ll 1) \\ x(x-4) & (x \gg 1). \end{cases}\end{aligned} \tag{4.83}$$

For massive clusters, relativistic corrections become important (Itoh et al., 1998; Nozawa et al., 1998). However, in our interested range, the expression (Eq. 4.83) is correct within a few percent. Figure 4.3 shows the variance of flux and brightness temperature for unit Compton-y parameter. This equation implies photons with lower frequency are scattered by hot electrons and there are less photons in that range, and this results in temperature decrement. On the other hand, for higher frequency there are more high energy photons and the brightness temperature gets higher. This variation of the temperature is the observable from CMB experiments. The most characteristic point is that that expression does not contain redshift dependent factors, i.e., the selection function is flat. For X-ray observations, the observable flux contains the luminosity distance, which increases with redshift. That is why X-ray flux limited samples suffer from selection bias. On the other hand, tSZ has an advantage to find clusters at high redshift, though observations of tSZ are demanding.

4.5 Cosmology with the Sunyaev–Zel'dovich Effect

In this Section, we extend our scope to cosmological scale. The large-scale maps ($\gtrsim \mathrm{deg}^2$) of Compton-y reflects gas distribution in the Universe. Furthermore, tSZ maps are made available by several groups. For example, we show all-sky tSZ maps measured by the *Planck* satellite in Figure 4.4. In general, tSZ is sensitive to high density regions and as a result provides independent information from other cosmological probes, e.g., cosmic shear or galaxy clustering. However, the issue is that tSZ comes from the baryon component and so we have to model dynamics of gas, which has been discussed in Section 4.3.

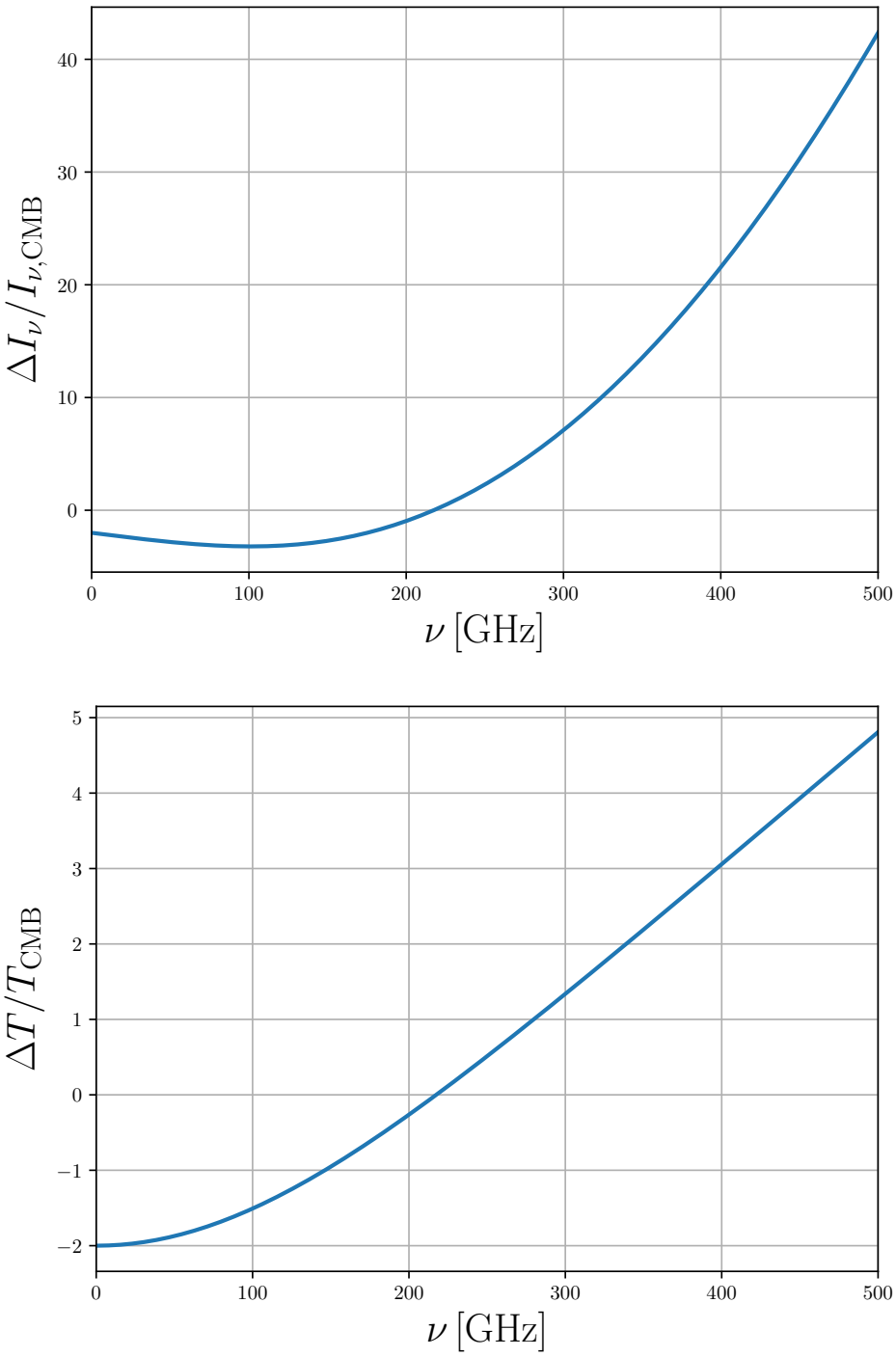

Figure 4.3: Variations of intensity and temperature for unit Compton-y parameter with respect to CMB intensity and temperature.

Here, we explain how we can describe properties of gas and employ tSZ as a cosmological probe.

4.5.1 Analytical Calculation Based on Halo Model

Since Compton-y is the integration of the product of density and temperature, the main contribution of tSZ comes from clusters, i.e., halos, and the contribution from filaments should be subdominant. In order to model gas dynamics, we employ halo model, in which all matter is associated with halos.

Let us consider the power spectrum of Compton-y parameter C_ℓ^{yy}. The power spectrum can be decomposed into 1-halo and 2-halo terms (Makino & Suto, 1993; Komatsu & Kitayama, 1999),

$$C_\ell^{yy} = C_\ell^{1\mathrm{h}} + C_\ell^{2\mathrm{h}}. \tag{4.84}$$

The 1-halo term is expressed as

$$C_\ell^{1\mathrm{h}} = \int_0^{z_{\max}} dz \frac{dV}{dz d\Omega} \int_{M_{\min}}^{M_{\max}} dM \frac{dn(M,z)}{dM} |\tilde{y}_\ell(M,z)|^2, \tag{4.85}$$

where $dV/dzd\Omega$ is the comoving volume per redshift and solid angle, $dn(M,z)/dM$ is the halo mass function, and $\tilde{y}_\ell(M,z)$ is the 2D Fourier transform of 3D Compton-y profile,

$$\tilde{y}_\ell(M,z) = \frac{4\pi r_s}{\ell_s^2} \left(\frac{\sigma_\mathrm{T}}{m_e c^2}\right) \int_0^\infty dx\, x^2 P_e(M,z,x) \frac{\sin(\ell x/\ell_s)}{\ell x/\ell_s}, \tag{4.86}$$

where $P_e(M,z,x)$ is the electron pressure, $\ell_s = D_A(z)/r_s$, and $D_A(z)$ is the angular diameter distance. Supposed that the gas is fully ionized, the electron pressure can be written with respect to gas pressure,

$$P_e(M,z,x) = \frac{2+2X}{3+5X} P_{\mathrm{gas}}(M,z,x), \tag{4.87}$$

where $X = 0.76$ is the primordial hydrogen abundance. Next, the 2-halo term can be given by

$$C_\ell^{2\mathrm{h}} = \int_0^{z_{\max}} dz \frac{dV}{dz d\Omega} P_\mathrm{m}\left(k = \frac{\ell + 1/2}{D_A(z)}, z\right) \left[\int_{M_{\min}}^{M_{\max}} dM \frac{dn(M,z)}{dM} \tilde{y}_\ell(M,z) b(M,z)\right]^2, \tag{4.88}$$

where $b(M,z)$ is the halo bias (see Section 2.4.2) and $P_\mathrm{m}(k,z)$ is the 3D matter power spectrum. Finally, we can compute the power spectrum of Compton-y, if halo mass function, bias, cosmological parameters, and pressure profile are specified.

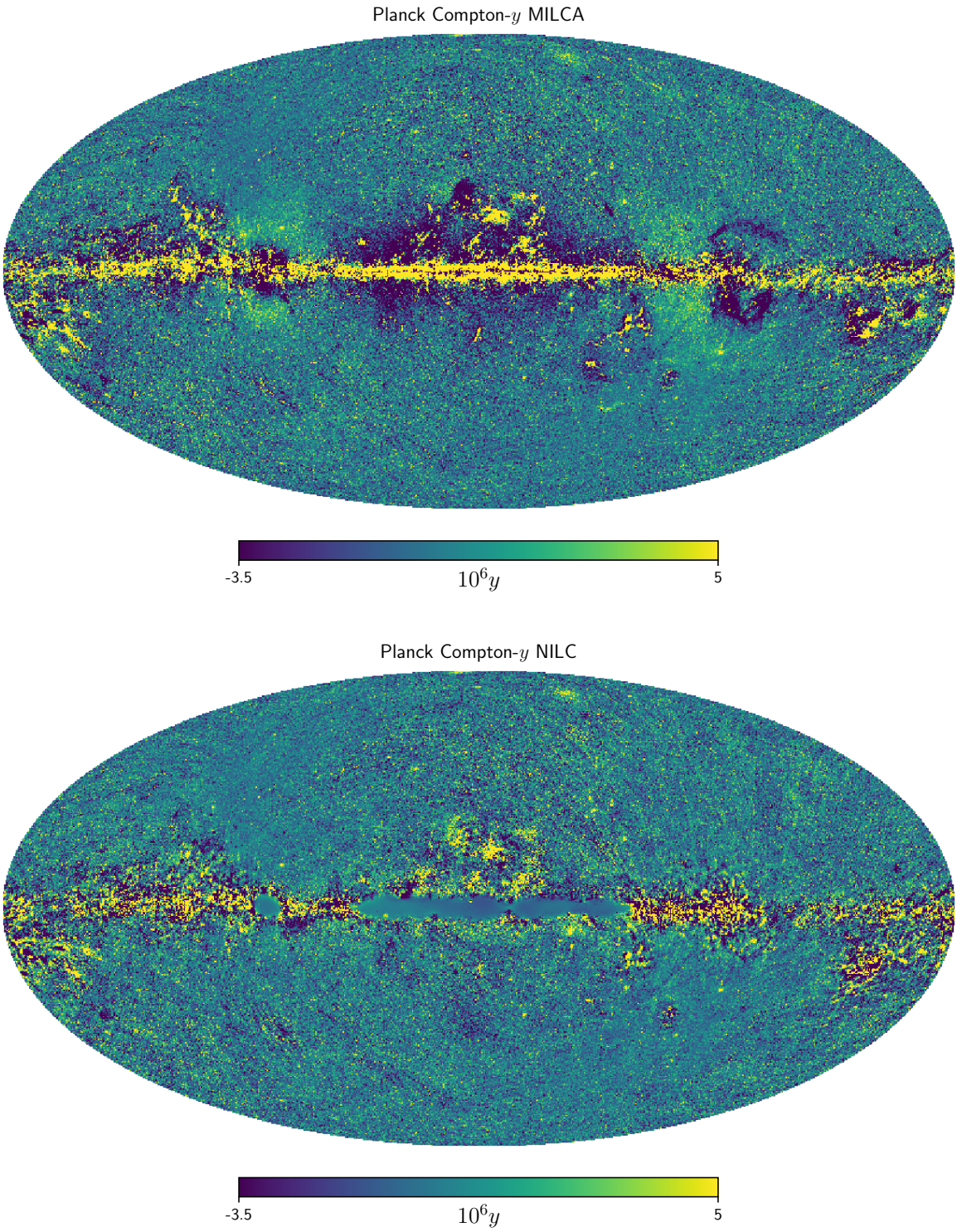

Figure 4.4: All-sky tSZ maps reconstructed from the observations of the *Planck* mission with MILCA and NILC algorithms (Planck Collaboration, 2016d).

Chapter 5

Numerical Simulations

Contents

In this Chapter, we will discuss numerical methods used in cosmology and astrophysics. The nonlinearity of gravity makes it intractable to analytically solve the evolution of density and velocity distribution. On the other hand, the nonlinear evolution plays a critical role to drive a tiny fluctuation into collapsed objects, i.e., dark halos. How can we tackle on this problem? One of the solution is the perturbative expansion. This method is fast (typically, $\mathcal{O}(1)$ sec for calculation of matter power spectrum) but the applicable range is limited to mildly nonlinear scales. Numerical simulations enable one to trace the nonlinear evolution down to the resolution, though this method adopts many approximations. Observational facts, e.g., abundance of halos, can remarkably be reproduced. The key approximation is that the smooth matter distribution is discretized as many particles which have no spatial size[1]. On this aspect, this type of simulations is referred to as *N-body simulations*. In N-body simulations for cosmological volume, the basic equation can be reduced to Newtonian equation in the expanding space-time.

We review the history of N-body simulations briefly. The application of N-body simulations in astrophysics has emerged in 1970s. The main target was to follow the evolution of clusters and groups of galaxies. In 1980s, N-body simulations were applied to

[1] In realistic simulations, particles have finite size called as smoothing length by a technical reason, which will be discussed later in this Chapter.

cosmology, which deal with structures on Mpc scales. The studies focus on the large-scale structures using statistical methods. Since more powerful computers become available, N-body simulations play a more important role. One of the great discoveries by N-body simulations is that dark matter is *cold*, i.e., the velocity dispersion of dark matter particles is negligible. If dark matter is hot, e.g., massive neutrinos, even relatively large structures like galaxies are smeared out and cannot be observed today. Thus, numerical simulations have become an essential tool for observational cosmology. In this Chapter, we describe the numerical methods on various aspects.

5.1 Cosmological N-body Simulation

5.1.1 Basic Equations

First, let us consider the self-gravitating system under Newtonian gravity, which is composed of N particles. In this situation, only gravity is assumed to work as an interaction between particles. Note that in cosmological simulations, this particle has no counterpart in a real system[2]. Generally, the number of particle is much less than the number of true physical particles (atoms or molecules), which is the order of Avogadro number. The particles in the simulations can be regarded as an assembly of unit particles and have much more mass.

The basic equations of gravity are equation of motion and Poisson equation,

$$\ddot{\boldsymbol{r}}_i = -\nabla_i \Phi(\boldsymbol{r}_i), \tag{5.1}$$

$$\Phi(\boldsymbol{r}) = -G \sum_{j=1}^{N} \frac{m_j}{[(\boldsymbol{r}-\boldsymbol{r}_j)^2+\epsilon^2]^{1/2}}, \tag{5.2}$$

where m_i is the particle mass, Φ is a gravitational potential, and ϵ is a softening length. The softening length is introduced for several reasons. One is that if two particles approach too close, the gravitational force becomes too large and the time step becomes too short. Without the softening length, we cannot proceed the simulation any more in a realistic time scale. The second reason is that we want to prevent a bound state of a two particles pair, which clearly contradicts the collisionless picture. The softening length can be regarded as a force resolution.

In cosmological simulations, the space is no longer static but expanding. It is useful to work on the comoving coordinate configuration. Suppose a periodic and expanding box in which there are N particles, the equations can be written as

$$\frac{d}{dt}(a^2\dot{\boldsymbol{x}}) = -\frac{1}{a}\nabla_i \phi(\boldsymbol{x}_i), \tag{5.3}$$

$$\nabla^2 \phi(\boldsymbol{x}) = 4\pi G \sum_{i=1}^{N} m_i \left[-\frac{1}{L^3} + \sum_{\boldsymbol{n}} \delta(\boldsymbol{x}-\boldsymbol{x}_i-\boldsymbol{n}L) \right]. \tag{5.4}$$

[2]This is not the case in other fields. For example, in the simulations of globular clusters, each particle corresponds to single star.

Here, ϕ is a peculiar gravitational potential. It differs from the Newtonian gravitational potential Φ in that ϕ corresponds to the difference from the mean background potential. Note that the sum is taken over the all of periodic images with the integer vector $\boldsymbol{n} = (n_1, n_2, n_3)$. The term $-1/L^3$ is needed to ensure that the contribution from the mean density vanishes.

5.1.2 Algorithms for Calculation of Gravitational Force

The most expensive part in N-body simulations is force calculation. Naively, we need to compute the distance of all pairs of particles, and the computational cost scales as $\mathcal{O}(N^2)$. For small N, e.g., $N \sim 100$, it is possible to directly calculate all distances at each time step. However, for large N or to obtain high resolution, we cannot proceed with the simulation, because the computational time dramatically increases. This is the major difficulty in cosmological N-body simulations. Several methods to resolve this problem have been developed in previous works. One is to invent a computer specialized only for gravity calculation. For example, Sugimoto et al. (1990) developed the pipeline for many-body gravity calculation `GRAPE`. This computer is designed and optimized only for computing mutual interactions of all particles pairs.

The other solution is a new algorithm to approximate the gravity force calculation. Since cosmological simulations in which we are interested are collisionless simulations, we do not need much accuracy for gravity from distant particles. Based on this fact, we can use a faster method to compute gravity. First, we introduce the particle-mesh (PM) method. In this method, we convert the particle distribution into density field in a mesh grid. Now, we will solve the Poisson equation for this grid with Fourier transform. Here, we can make use of the fast Fourier transform (FFT). The algorithm is highly optimized, and the calculation cost scales as $\mathcal{O}(N \log N)$. This greatly reduces the computational time and enables N-body simulations with large N. However, the resolution which PM method can reach is limited to the grid size. Due to the nature of attractive force, particles gather toward the dense region. Generally, we are interested in such dense regions in which halos or galaxies form, and we need high resolution for it. Thus, a practical way is to combine the direct calculation for short-range force and the PM method for long-range force. This adaptive method is called as particle-particle-particle-mesh ($\mathrm{P^3M}$) method. With this method we can obtain high resolution in dense regions but more computation time is needed. The last method which we introduce is the Tree-PM algorithm (see, e.g., Ishiyama et al., 2009). Tree algorithm is a grouping method of particles. Each group in which particles are close is called as branch. Particles which belong to other branch is regarded as one particle and so the number of force calculation decreases. Figure 5.1 shows a schematic picture of gravity calculation based on tree algorithm. In the Tree-PM algorithm, we continue to use PM method for distant particles but we make use of tree algorithm for close particles.

This Tree-PM algorithm is implemented in various codes, e.g., `GADGET` (Springel et al., 2001; Springel, 2005) and `GreeM` (Ishiyama et al., 2009). Although we do not discuss here, there are more methods to efficiently calculate gravitational force in many-body systems, e.g., adaptive refinement tree (`ART`: Kravtsov et al. (1997)) and moving mesh algorithm

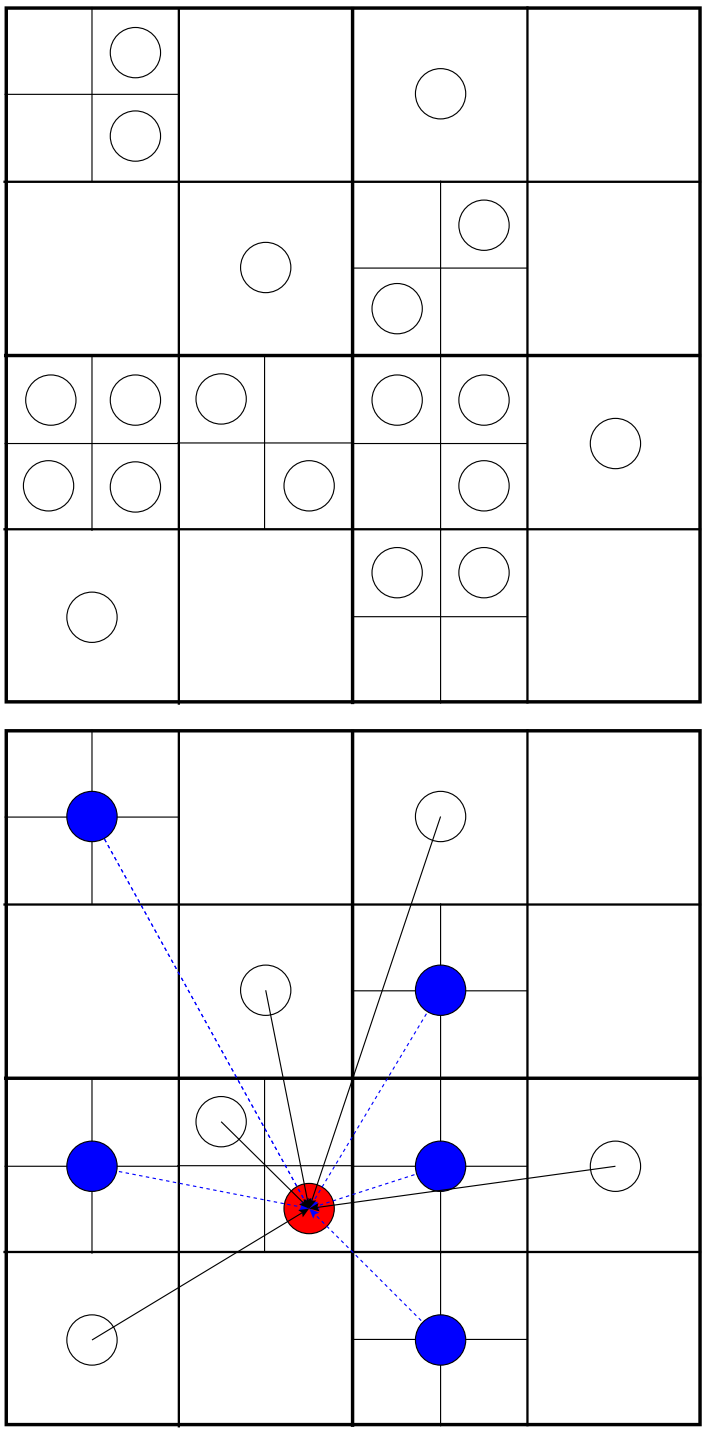

Figure 5.1: A schematic picture of the tree algorithm (Ishiyama et al., 2009). The upper panel shows the configuration of particles. In the lower panel, the gravity exerted to the red particle can be calculated as the force from white particles, each of which corresponds to distinct particle, and blue particles, which are grouped based on tree algorithm. This algorithm reduces the calculation of distance evaluation.

(AREPO: Springel (2010)).

5.1.3 Initial Condition

We have discussed the algorithms of N-body simulations. The remaining task is to generate initial conditions for the simulations. Ideally, we have to run a simulation from big-bang $t = 0$. But at that time, the Universe is so hot that the situation is totally different, and force other than gravity efficiently cannot be ignored. In practice, we start a simulation after recombination, typically $z \approx 100$. Then, we generate the distribution of particles and velocity field at the initial redshift. In such early Universe, the density distribution follows almost Gaussian. Hence, linear power spectrum has sufficient information to generate the initial conditions. The straightforward way is to generate GRF so that it reproduces the power spectrum. The distribution of Fourier mode of the initial density perturbation $\delta(\boldsymbol{k}) = |\delta(\boldsymbol{k})|e^{i\theta(\boldsymbol{k})}$ follows Rayleigh distribution for the amplitude and uniform distribution for the phase[3],

$$P(|\delta(\boldsymbol{k})|) = \exp\left[-\frac{|\delta(\boldsymbol{k})|^2}{P(k)}\right]\frac{2|\delta(\boldsymbol{k})|^2}{P(k)}, \tag{5.5}$$

$$P(\theta(\boldsymbol{k})) = \frac{1}{2\pi}. \tag{5.6}$$

However, if we simply generate GRF in a straightforward way, the resultant initial condition suffers from large shot noise, and the power spectrum of the initial condition could be incorrect.

To resolve these problems, we make use of *Lagrangian perturbation theory* (LPT: Matsubara, 2008). In Lagrangian picture, the evolution of the density is described in the rest frame of the fluid. The Eulerian position $\boldsymbol{x}$ with the initial position $\boldsymbol{q}$ can be given by Lagrangian position, or displacement vector $\boldsymbol{\Psi}$,

$$\boldsymbol{x} = \boldsymbol{q} + \boldsymbol{\Psi}(\boldsymbol{q}, t). \tag{5.7}$$

Now we work on the equations for the displacement vector $\boldsymbol{\Psi}(\boldsymbol{q}, t)$ instead of Eulerian coordinates $\boldsymbol{x}$. The basic procedure to create initial conditions is that first we generate uniform particle distributions, for which *glass* distribution is often used (White, 1994), and then move particles according to the displacement vector. This distribution has minimal shot noise. The full description of basic equations is found in Scoccimarro (1998). We can expand these equations perturbatively with respect to the density. The lowest order solution is called as *Zel'dovich approximation* (Zel'dovich, 1970),

$$\nabla_q \cdot \boldsymbol{\Psi}^{(1)} = -D_1\delta(\boldsymbol{q}), \tag{5.8}$$

where $\delta(\boldsymbol{q})$ is the density field and D_1 is the linear growth factor. The density field can be obtained from power spectrum using FFT (for details, see Scoccimarro, 1998; Hahn

[3]Recently, Angulo & Pontzen (2016) propose that two initial conditions, where the amplitude is identical to the square root of the power spectrum but the phases are opposite, greatly reduce the sample variance of the statistics.

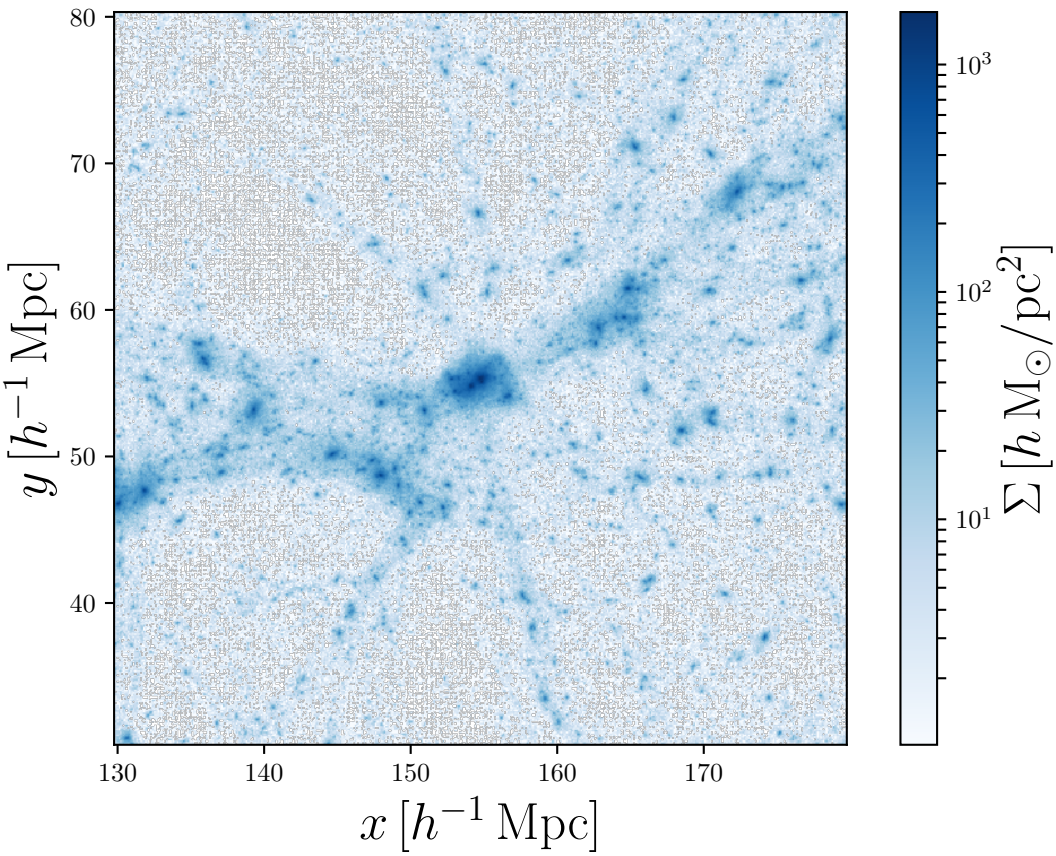

Figure 5.2: An example of N-body simulation run at the redshift $z = 0.26771$ by `L-Gadget2` code (Springel, 2005) with the massive halo $M_{\mathrm{vir}} = 1.89 \times 10^{15}\,h^{-1}\,\mathrm{M}_\odot$ centered. The surface mass density is shown for the slice of $50\,h^{-1}\,\mathrm{Mpc} \times 50\,h^{-1}\,\mathrm{Mpc} \times 50\,h^{-1}\,\mathrm{Mpc}$. There are various types of structures: dark halos, filaments, and voids.

& Abel, 2011). The second order solution, called 2LPT, can be obtained similarly,

$$\nabla_q \cdot \mathbf{\Psi}^{(2)} = \frac{1}{2} D_2 \sum_{i \neq j} [\mathbf{\Psi}^{(1)}_{i,i} \mathbf{\Psi}^{(1)}_{j,j} - \mathbf{\Psi}^{(1)}_{i,j} \mathbf{\Psi}^{(1)}_{j,i}], \tag{5.9}$$

where $\mathbf{\Psi}^{(1)}_{i,j} = \partial \mathbf{\Psi}^{(1)}_i / \partial \boldsymbol{q}_j$ and D_2 is the second-order growth factor. It is convenient to define Lagrangian potentials $\phi^{(1)}$ and $\phi^{(2)}$. They obey following Poisson equations,

$$\nabla^2_q \phi^{(1)}(\boldsymbol{q}) = \delta(\boldsymbol{q}), \tag{5.10}$$

$$\nabla^2_q \phi^{(2)}(\boldsymbol{q}) = \sum_{i>j} \{\phi^{(1)}_{,ii}(\boldsymbol{q}) \phi^{(1)}_{,jj}(\boldsymbol{q}) - [\phi^{(1)}(\boldsymbol{q})]^2\}. \tag{5.11}$$

The Eulerian position and velocity field can be

$$\boldsymbol{x} = \boldsymbol{q} - D_1 \nabla_q \phi^{(1)} + D_2 \nabla_q \phi^{(2)}, \tag{5.12}$$

$$\boldsymbol{v} = \frac{d\boldsymbol{x}}{dt} = -D_1 f_1 H \nabla_q \phi^{(1)} + D_2 f_2 H \nabla_q \phi^{(2)}, \tag{5.13}$$

where f_i is the logarithmic derivatives of growth factors and H is the Hubble parameter. In practice, 2LPT is commonly used to generate initial density and velocity fields. According to the obtained fields, we can generate initial conditions for N-body simulations.

5.2 Linking Simulations to Observations

Here, we explain numerical methods to link simulations to realistic observations. Since, for hydrodynamical simulations, thermodynamic quantities for gas particles or magnitude for stellar particles are automatically obtained, it is straightforward to carry out mock observations. On the other hand, as we have already noted, the particle distribution which is the output of N-body simulations corresponds to matter distribution, and for mock observations, it should be converted into observables.

5.2.1 Ray-Tracing Simulation

For weak lensing surveys, we simulate how light propagates in the inhomogeneous Universe. The equation which governs path of rays is the geodesic equation derived from general relativity. However, it is not practical to rigorously solve the path in the simulated Universe. We employ the multiple-planes method (White & Hu, 2000; Jain et al., 2000; Hamana & Mellier, 2001) to solve this geodesic equation approximately. The basic scheme is that we project particle distribution onto several planes in each snapshot and assume that the path of ray bends only when crossing those planes. This approximation is valid especially for weak lensing because the path of ray is curved weakly.

We introduce the implementation proposed by Hilbert et al. (2009), which requires less memory for ray-tracing simulations. The setup is depicted in Figure 5.3. First, we adopt flat-sky approximation, which is valid for small opening angles of the light-cone.

What we want to obtain is the true position as a function of the image position and the source distance $\boldsymbol{\beta}(\boldsymbol{\theta},\chi)$ and the Jacobian matrix $A_{ij}(\boldsymbol{\theta},\chi)$. The basic equations which we have to solve are the lens equation (Eqs. 3.24 and 3.25), and the definition of Jacobian matrix (Eq. 3.26). Again, we rewrite these equations with the notation used here,

$$\begin{aligned}
\boldsymbol{\beta}(\boldsymbol{\theta},\chi) &= \boldsymbol{\theta} - \frac{2}{c^2}\int_0^{\chi} d\chi' \frac{f_K(\chi-\chi')}{f_K(\chi)f_K(\chi')}\nabla_{\boldsymbol{\beta}}\Phi(f_K(\chi')\boldsymbol{\beta},\chi), && (5.14)\\
A_{ij}(\boldsymbol{\theta},\chi) &= \frac{\partial\beta_i(\boldsymbol{\theta},\chi)}{\partial\theta_j} \\
&= \delta_{ij} - \frac{2}{c^2}\int_0^{\chi} d\chi' \frac{f_K(\chi-\chi')}{f_K(\chi)f_K(\chi')}\frac{\partial^2\Phi(f_K(\chi')\boldsymbol{\beta},\chi)}{\partial\beta_i\partial\beta_k}A_{kj}(\boldsymbol{\theta},\chi'). && (5.15)
\end{aligned}$$

This expression differs from the one in Born approximation in that the product of matrix appears. Because of this term, the Jacobian matrix is no longer symmetric. We can parametrize the Jacobian matrix with convergence, shear, and rotation which angle is denoted as ω:

$$\begin{aligned}
A_{ij}(\boldsymbol{\theta},\chi) &\equiv \begin{pmatrix} \cos\omega & \sin\omega \\ -\sin\omega & \cos\omega \end{pmatrix}\begin{pmatrix} 1-\kappa-\gamma_1 & -\gamma_2 \\ -\gamma_2 & 1-\kappa+\gamma_1 \end{pmatrix} && (5.16)\\
&\simeq \begin{pmatrix} 1-\kappa-\gamma_1 & -\gamma_2+\omega \\ -\gamma_2-\omega & 1-\kappa+\gamma_1 \end{pmatrix}, && (5.17)
\end{aligned}$$

where in weak lensing regime, the rotation angle ω is very close to zero.

From here, we work on solving Eqs. (5.14) and (5.15). It is sufficient to consider the deflection at each plane. At k-th plane[4], the deflection $\boldsymbol{\alpha}^{(k)}(\boldsymbol{\beta}^{(k)})$ at the position $\boldsymbol{\beta}^{(k)}$ can be given by the gradient of the lensing potential $\psi^{(k)}(\boldsymbol{\beta}^{(k)})$,

$$\boldsymbol{\alpha}^{(k)}(\boldsymbol{\beta}^{(k)}) = \nabla_{\boldsymbol{\beta}^{(k)}}\psi^{(k)}(\boldsymbol{\beta}^{(k)}). \tag{5.18}$$

For the Jacobian matrix, we need the second derivatives and define the following matrix,

$$U_{ij}^{(k)} \equiv \frac{\partial^2\psi^{(k)}(\boldsymbol{\beta}^{(k)})}{\partial\beta_i^{(k)}\partial\beta_j^{(k)}} = \frac{\partial\alpha_i^{(k)}(\boldsymbol{\beta}^{(k)})}{\partial\beta_j^{(k)}}. \tag{5.19}$$

The lensing potential can be obtained from the Poisson equation as

$$\frac{1}{2}\nabla^2_{\boldsymbol{\beta}^{(k)}}\psi^{(k)}(\boldsymbol{\beta}^{(k)}) = \sigma^{(k)}(\boldsymbol{\beta}^{(k)}). \tag{5.20}$$

The dimensionless surface mass density $\sigma^{(k)}$ is defined as the projection of matter between planes,

$$\sigma^{(k)}(\boldsymbol{\beta}^{(k)}) = \frac{3H_0^2\Omega_{\rm m}}{2c^2}\frac{f_K^{(k)}}{a^{(k)}}\int_{\chi_{\rm L}^{(k)}}^{\chi_{\rm U}^{(k)}} d\chi'\,\delta(f_K(\chi')\boldsymbol{\beta}^{(k)},\chi'), \tag{5.21}$$

[4]We count planes from the observer to the source.

where δ is matter density contrast. In N-body simulations, we construct a mesh of the density contrast for each plane. Using Fourier transform, we can solve Poisson equation (Eq. 5.20). From obtained the lensing potential, derivatives can be estimated with finite difference. However, in general, we cannot find a cell of the mesh, whose position is identical to $\boldsymbol{\beta}^{(k)}$. To evaluate the lensing potential at $\boldsymbol{\beta}^{(k)}$, the linear interpolation is usually used.

If the deflection angle at each plane can be obtained, the total deflection angle also can be derived as the sum of the deflection angle with weights from foreground planes,

$$\boldsymbol{\beta}^{(k)}(\boldsymbol{\theta}) = \boldsymbol{\theta} - \sum_{i=1}^{k-1} \frac{f_K^{(i,k)}}{f_K^{(k)}} \boldsymbol{\alpha}^{(k)}(\boldsymbol{\beta}^{(k)}), \tag{5.22}$$

where $f_K^{(i,k)} = f_K(\chi^{(k)} - \chi^{(i)})$. This expression is not necessarily appropriate for numerical simulations because we have to store deflection angles at all planes. We can modify this expression in the memory efficient way. First, the position $\boldsymbol{\beta}^{(k)}$ can be written using two previous positions, $\boldsymbol{\beta}^{(k-1)}$ and $\boldsymbol{\beta}^{(k-2)}$,

$$f_K^{(k)}(\boldsymbol{\beta}^{(k)}) = f_K^{(k)}(\boldsymbol{\beta}^{(k-2)}) + f_K^{(k-2,k)}\boldsymbol{\epsilon} - f_K^{(k-1,k)}\boldsymbol{\alpha}^{(k-1)}(\boldsymbol{\beta}^{(k-1)}), \tag{5.23}$$

where $\boldsymbol{\epsilon} = \dfrac{f_K^{(k-1)}}{f_K^{(k-2,k-1)}}(\boldsymbol{\beta}^{(k-1)} - \boldsymbol{\beta}^{(k-2)})$. Thus,

$$\boldsymbol{\beta}^{(k)} = \left(1 - \frac{f_K^{(k-1)}}{f_K^{(k)}} \frac{f_K^{(k-2,k)}}{f_K^{(k-2,k-1)}}\right) \boldsymbol{\beta}^{(k-2)} + \frac{f_K^{(k-1)}}{f_K^{(k)}} \frac{f_K^{(k-2,k)}}{f_K^{(k-2,k-1)}} \boldsymbol{\beta}^{(k-1)} - \frac{f_K^{(k-1,k)}}{f_K^{(k)}} \boldsymbol{\alpha}^{(k-1)}(\boldsymbol{\beta}^{(k-1)}). \tag{5.24}$$

What we have to store in order to estimate the position $\boldsymbol{\beta}^{(k)}$ can be reduced to the deflection angle only at $(k-1)$-th and $(k-2)$-th planes. In addition, the computational cost is also reduced. As an initial condition, we have to specify the initial position as the unperturbed path,

$$\boldsymbol{\beta}^{(0)} = \boldsymbol{\beta}^{(1)} = \boldsymbol{\theta}. \tag{5.25}$$

In order to obtain the recursive relation for the Jacobian matrix, we differentiate Eq. (5.24). The result is

$$A_{ij}^{(k)} = \left(1 - \frac{f_K^{(k-1)}}{f_K^{(k)}} \frac{f_K^{(k-2,k)}}{f_K^{(k-2,k-1)}}\right) A_{ij}^{(k-2)} + \frac{f_K^{(k-1)}}{f_K^{(k)}} \frac{f_K^{(k-2,k)}}{f_K^{(k-2,k-1)}} A_{ij}^{(k-1)} - \frac{f_K^{(k-1,k)}}{f_K^{(k)}} U_{il}^{(k-1)} A_{lj}^{(k-1)}. \tag{5.26}$$

Given the configuration of planes and snapshots of N-body simulations, we can obtain deflection angles, convergence and shear at any plane. We show an example of convergence map calculated with the ray-tracing method in Figure 5.4.

5.2.2 Simulations of the Sunyaev–Zel'dovich Effect

As we have already discussed in Chapter 4, we need electron pressure field for tSZ and velocity field for kSZ. Here, we explain how to generate mock SZ maps from simulations especially for tSZ.

5.2.2.1 Creating Mock Maps from Hydrodynamical Simulations

For simulating tSZ effect, we need electron pressure field, which is easily accessible once we run a hydrodynamical simulation. The basic procedure to create mock tSZ maps is similar to ray-tracing simulations. However, since the distortion of ray affects only small scale structures, which are not important due to limited resolution, we simply project these fields in the line-of-sight direction. There is one caveat that gas particle has a spatial extent and it should be incorporated in an appropriate way. Here, we follow the procedure proposed by Roncarelli et al. (2007); Ursino et al. (2010). A single gas particle has a contribution to Compton-y denoted as y_i,

$$y_i = \frac{k_{\rm B}\sigma_{\rm T}}{m_e c^2}\frac{n_{e,i}m_i}{\rho_i}\frac{T_i}{L_{{\rm pix},i}^2}, \tag{5.27}$$

where $n_{e,i}$ is electron density, m_i is gas particle mass, ρ_i is the gas density, and T_i is the temperature. And $L_{{\rm pix},i}$ is a physical pixel size at the particle position. Then, we distribute y_i to each pixel according to a spatial extent of SPH particle. We assign Compton-y to each pixel with the following procedure. The kernel function of SPH is given as,

$$w(r) \propto \begin{cases} 1-6r^2+6r^3 & (0 \le r \le 1/2) \\ 2(1-r)^3 & (1/2 \le r \le 1) \\ 0 & (1 \le r), \end{cases} \tag{5.28}$$

where h is the smoothing length. Let $r = \Delta\theta/\alpha_h$, where $\Delta\theta$ is an angular distance between the centers of the particle and of the pixel, and α_h is a subtended angle of smoothing length of the gas particle. However, we have to fix the normalization of the kernel function. It is straightforward to calculate contributions to all pixels and fix the normalization as the sum of the contributions is unity. However, the computational cost to carry out this operation is so large that it is not realistic to determine the normalization for all gas particles. Instead, we make use of integrability of the kernel function. The kernel function can be approximated as the product of the one of the two directions, $w(r) \simeq w(x) \times w(y)$. Then, we make use of the integral $W(x) \equiv \int_{-1}^{x'} w(x')dx'$, where the normalization is $W(1) = 1$. We can compute the weight at each pixel f as

$$f = [W(x_1) - W(x_0)] \times [W(y_1) - W(y_0)], \tag{5.29}$$

where (x_0, x_1) and (y_0, y_1) is the corresponding angular edge of the pixel. Thus we can calculate weight without summing up many contributions.

In Figure 5.5, the simulated tSZ and kSZ maps from Magneticum simulations (Soergel et al., 2018) are shown. For tSZ, we plot Compton-y, and for kSZ, the quantity,

$$b = \int \frac{v_{\rm los}}{c}\sigma_T n_e dl, \tag{5.30}$$

where $v_{\rm los}$ is the line-of-sight velocity and n_e is the free electron density, is plotted. The temperature variation due to kSZ is

$$\frac{\Delta T}{T} = -b. \tag{5.31}$$

5.2.2.2 Pasting Pressure Profile onto Dark Matter Distribution

Though hydrodynamical simulations incorporate various baryonic processes, there are several disadvantages for using them to create tSZ maps. For instance, it is quite challenging to run a hydrodynamical simulation with large simulation box. The volume of the largest cosmological hydrodynamical simulations is around $(500\,h^{-1}\,\mathrm{Mpc})^3$, which is not sufficient for generating mock maps for all-sky surveys. One of solutions to this problem is using N-body simulations instead of hydrodynamical simulations. Running N-body simulations is computationally efficient even for large simulation box of $(1\,h^{-1}\,\mathrm{Gpc})^3$. Furthermore, we can run N-body simulations many times, and the multiple realizations are useful to estimate the covariance matrix of statistics.

For this purpose, we develop a pasting method, which creates pressure field from outputs of N-body simulations for simulating tSZ. We rely on the halo model approach, where we assign thermal pressure only to particles which belong to halos, and compute thermal pressure from models of ICM (Shaw model in Section 4.3.3 or universal pressure profile in Section 4.3.4) given halo mass and redshift. First, we explain *particle-based pasting*, where we assign pressure to each particle and can incorporate the effects due to asphericity and substructures. Once we run N-body simulations and apply halo finding algorithm, we compute the pressure profile of each halo based on the ICM model. Then, we assign pressure to each particle so that the total energy should be conserved. Let us consider the halo with N particles and the pressure profile $P(r; M, z)$. The total thermal energy of this halo is given as

$$E = \int 4\pi r^2 P(r; M, z) dr. \tag{5.32}$$

If we simply assign the pressure according to the radius, i.e., $P_i = P(r_i; M, z)$, the total thermal energy of particles is given as

$$E_p = \sum_i^N P_i \frac{m_i}{\rho_i}, \tag{5.33}$$

where m_i is the particle mass and ρ_i is the density estimated from NFW profile. However, the total energy for particles will be less than the total energy E directly computed from pressure profile because in outskirt region, there are less particles and thus the sparse sampling depresses the estimate of total thermal pressure. In order to avoid this anomaly, we assign pressure to maintain the total thermal energy, i.e., $E = E_p$. Next, we sort the particles according to radii in ascending order. We impose on the condition that each particle contains pressure P_i which has the contribution from the shell between the particle and the next one,

$$\int_{r_{i-1}}^{r_i} 4\pi r^2 P(r; M, z) dr = P_i \frac{4\pi}{3}(r_i^3 - r_{i-1}^3), \tag{5.34}$$

where $r_0 = 0$. By summing contributions for all particles, the energy conservation $E = E_p$ is automatically satisfied. Once the pressure P_i is obtained, we create pixelized Compton-y map based on the assignment scheme presented in Section 5.2.2. In Figure 5.6, we show the mock tSZ map based on the particle-based pasting method with the Shaw model.

We also develop simpler pasting method: *halo-based pasting*. Instead of using particle distributions, we use only halo catalog to apply the ICM model for each halo according to halo mass and redshift. After the computation, we simply project the pressure field to generate mock tSZ map. In contrast to particle-based pasting, we do not need to care about the extent of particles and energy conservation, but some details, e.g., substructures and asphericity, might be missed.

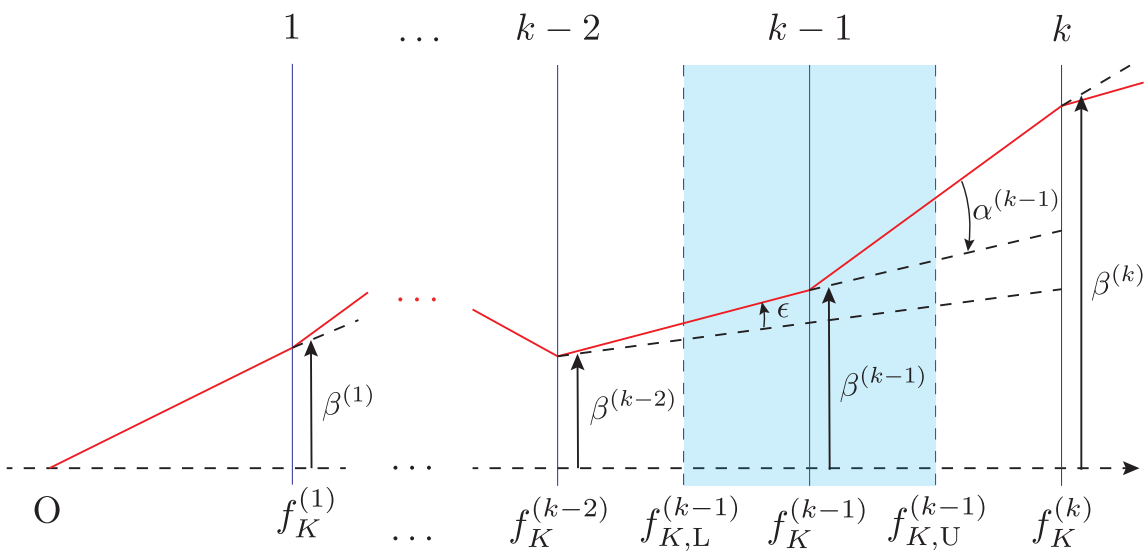

Figure 5.3: Schematic view of ray-tracing simulations. The blue solid lines correspond to projected planes, and the red solid line shows the simulated path of ray.

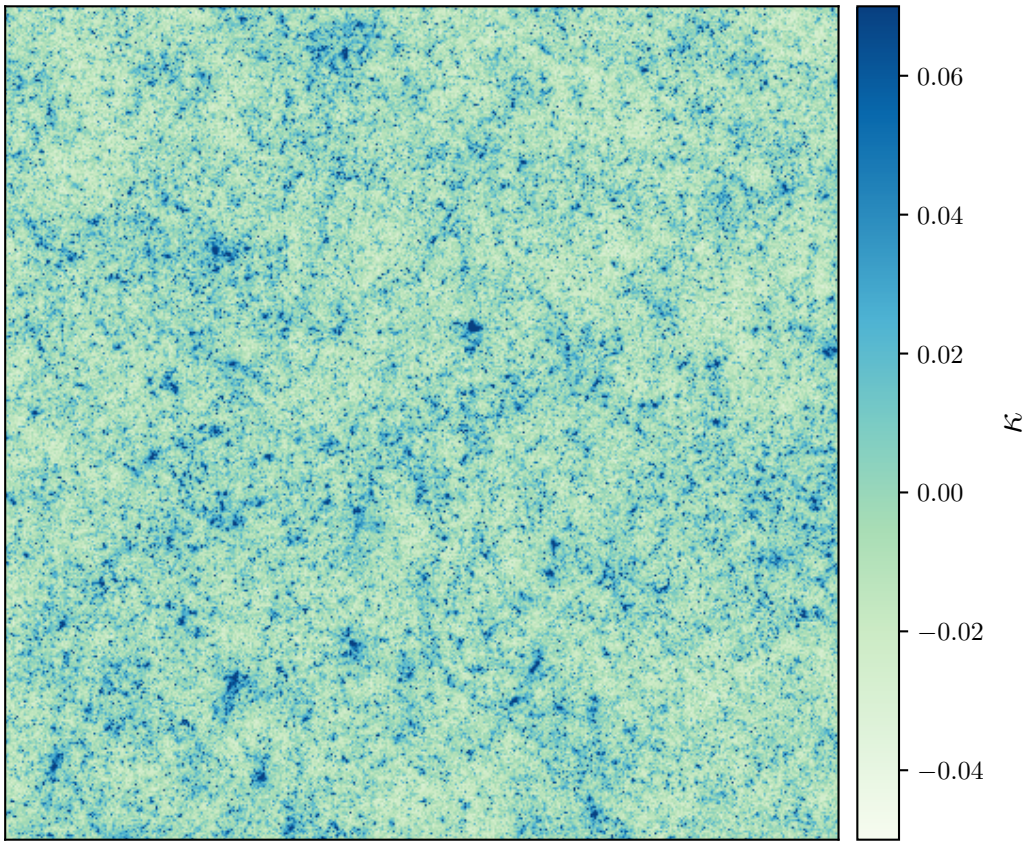

Figure 5.4: Convergence map generated with the ray-tracing method. The redshift distribution of source galaxies is the one in the Subaru Hyper Suprime-Cam survey and the size of the map is $10 \times 10\,\mathrm{deg}^2$.

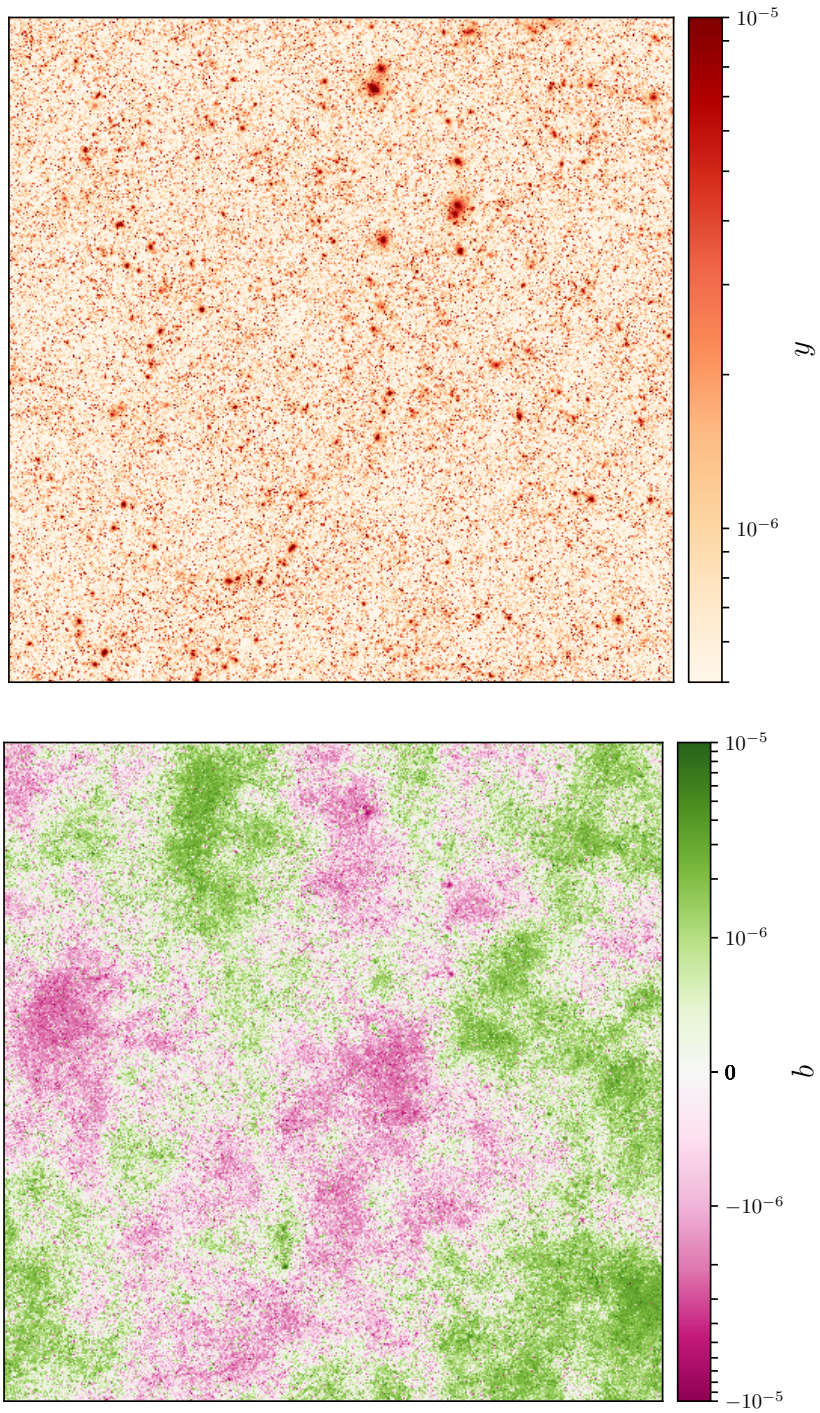

Figure 5.5: Compton-y (upper panel) and kSZ (lower panel) maps generated from hydrodynamical simulations (Magneticum: Soergel et al., 2018). The map size is $35 \times 35\,\mathrm{deg}^2$.

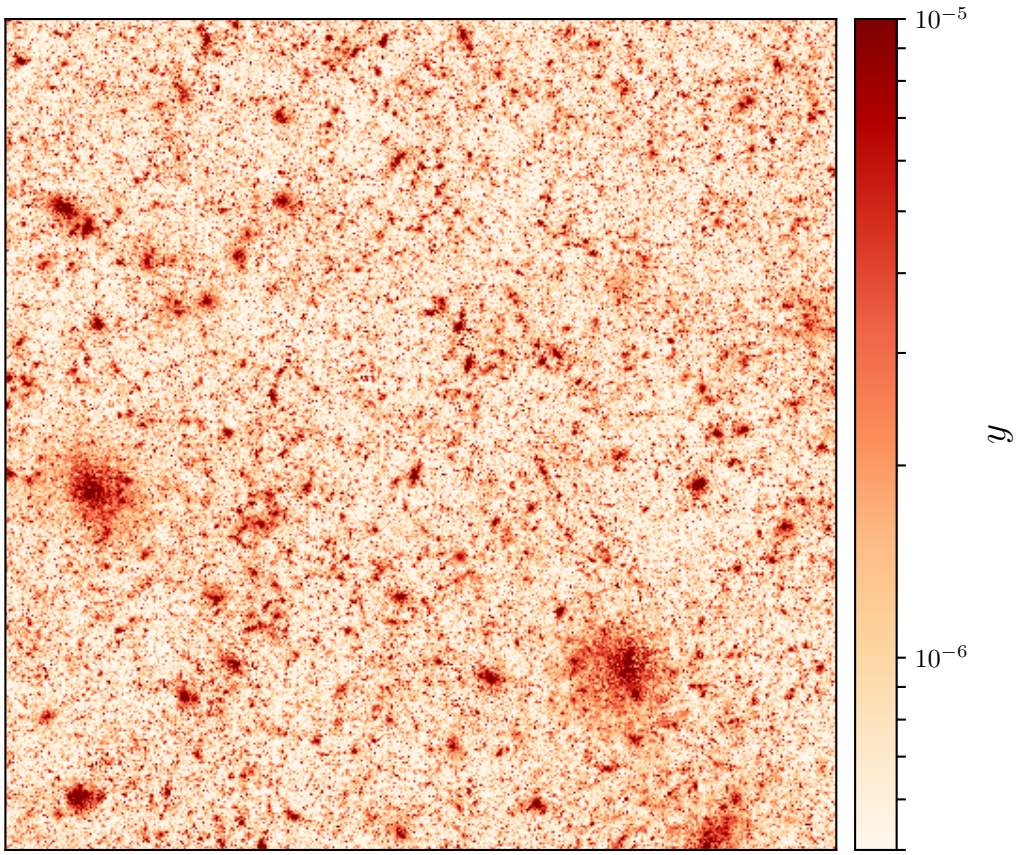

Figure 5.6: Compton-y map generated from N-body simulation based on particle-based pasting method. The size of the map is $10 \times 10\,\mathrm{deg}^2$.

Chapter 6

Cross-Correlation of WL and tSZ from RCSLenS and *Planck* and Its Implications for Cluster Astrophysics and Cosmology

Contents

In this Chapter, we present the analysis of the measurements of the cross-correlation of WL and tSZ from *Planck* and the Red Cluster Sequence Lensing Survey (RCSLenS) to constrain the amplitude of the non-thermal pressure fraction in galaxy clusters and the amplitude of the matter power spectrum σ_8.

6.1 Introduction

As we have seen so far, both of WL and tSZ are important probes into the large-scale structures in the Universe. However, the information that can be extracted either from WL or tSZ is limited; WL suffers from degeneracies between cosmological parameters, while tSZ suffers from astrophysical uncertainties. Thus, a combination of WL and tSZ can arguably be more efficient in extracting cosmological parameters. For this purpose, we focus on cross-correlation of WL and tSZ in addition to the auto-power spectrum of the tSZ. The cross-correlation analysis has a possibility to enable us to place more stringent constraints on cosmological parameters evading the astrophysical uncertainties and implications to physics of ICM (Munshi et al., 2014; Ma et al., 2015; Hojjati et al., 2015; Battaglia et al., 2015). Although the cross-correlation has already been detected by several groups (Van Waerbeke et al., 2014; Hill & Spergel, 2014; Hojjati et al., 2017, note that their Compton-y maps are based on *Planck* data but constructed in different ways.), the analysis of parameter constraints with the cross-correlations has not been done yet. In this Chapter, we conduct the detailed analysis and obtain quantitative results of the parameter constraints.

In cross-correlating, there are two approaches for the measurement. One is that first we identify massive clusters, where most of signal is thought to come from, and then cross-correlate the WL signal at the regions where clusters are located. However, we can identify only massive and nearby clusters, and in this case, it is better to study the profiles of SZ and WL for each detected source. The other approach, which we focus on in this Chapter, is the cross-correlation of the Compton-y *map*, which has vast sky coverage (in case of *Planck*, the half of the sky is covered) and has the advantange over the cluster-wise approach. Almost half of signals come from group-size halos ($M_{500} \sim 10^{14}\,\mathrm{M}_\odot$), and these halos are rarely included in SZ detected cluster catalog due to the low signal-to-noise-ratio. Although we cannot identify each of them, the Compton-y map contains such halos. Other candidate which can contribute to the SZ signal is gas in filaments. However, it is found that such gas has low temperature and is not fully ionized (McCarthy et al., 2014). As a result, the contribution can be negligible.

It is timely to investigate the ability of the cross-correlation with numerical simulations. We combine the output from an N-body simulation with a semi-analytic model for the pressure, in order to create mock tSZ and WL maps. Using these maps, we estimate the covariance matrix of the tSZ power spectrum and the tSZ-WL cross-correlation. The main results of this analysis are the constrains on σ_8 and the amount of non-thermal pressure in the ICM, derived from recent measurements from *Planck* (Planck Collaboration, 2016d) and the Red Cluster Sequence Lensing Survey (RCSLenS) (Hildebrandt et al., 2016; Hojjati et al., 2017). Recently, it is reported that there is a tension of inferred

σ_8 between the measurements of CMB temperature anisotropy and large-scale structure, e.g., power spectrum of WL (Battye et al., 2015; Leauthaud et al., 2017). Furthermore, tSZ power spectra measured from SPT and ACT are lower than the prediction based on *Planck* best-fit cosmological parameters (Planck Collaboration, 2016c). This fact also may be related to the σ_8 tension, though there is a possibility that the incomplete separation of foreground contamination causes the low amplitude of the power spectrum. The tSZ-WL cross-correlation along with tSZ power spectrum is one of promising probes into this problem.

This Chapter is organized as follows. In Section 6.2, we review the basics of tSZ and WL, and the analytic halo model for power spectra and cross-correlation. We describe our semi-analytic model and simulations in Section 6.3. In Section 6.4, we present measured spectra and cross-correlation obtained from our model and constraints on the property of non-thermal pressure and σ_8. We conclude in Section 6.5.

We assume the Universe is spatially flat and follows the ΛCDM model. We adopt cosmological parameters inferred from temperature and polarization data set of CMB (TT,TE,EE+lowP) from the *Planck* mission (Planck Collaboration, 2016d). The relative energy density of matter, baryons, and cosmological constant at the present Universe are $\Omega_{\rm m} = 0.3156$, $\Omega_{\rm b} = 0.04917$, $\Omega_\Lambda = 0.6844$. The Hubble parameter is $h = 0.6727$ with $H_0 = 100h\,{\rm km\,s^{-1}\,Mpc^{-1}}$. The slope and amplitude of the scalar pertubation are $n_{\rm s} = 0.9645$ and $A_{\rm s} = 2.2065 \times 10^{-9}$ with the pivot scale $k_{\rm pivot} = 0.05\,{\rm Mpc^{-1}}$. Though we will constrain the amplitude later, the fiducial value of the amplitude at the scale of $8\,h^{-1}\,{\rm Mpc}$ is $\sigma_8 = 0.831$.

6.2 Formalism

6.2.1 The Thermal Sunyaev–Zel'dovich Effect

Here, we briefly review essential equations related to the tSZ effect. For further details, refer to Section 4.4. The variation of temperature due to tSZ scales as the line-of-sight integration of the free electron pressure P_e,

$$\frac{\Delta T}{T_{\rm CMB}} = g_\nu(x) y = g_\nu(x) \frac{\sigma_{\rm T}}{m_e c^2} \int P_e \, dl, \tag{6.1}$$

where y is the Compton-y parameter, $T_{\rm CMB} = 2.726\,{\rm K}$ is the CMB temperature, $\sigma_{\rm T}$ is the Thomson scattering cross-section, m_e is the electron mass, and $g_\nu(x)$ is the frequency dependent function given by

$$g_\nu(x) = x \frac{e^x - 1}{e^x + 1} - 4, \left(x = \frac{h\nu}{k_{\rm B} T_{\rm CMB}} \right). \tag{6.2}$$

We do not include relativistic corrections for $g_\nu(x)$ (Itoh et al., 1998; Nozawa et al., 1998) because this effect is important only at the most massive clusters and we basically focus on the Compton-y parameter. For fully ionized primordial gas, the electron pressure P_e

is related with thermal pressure $P_{\rm th}$ as

$$P_e = \frac{2X+2}{5X+3} P_{\rm th}, \tag{6.3}$$

where $X = 0.76$ is the hydrogen mass fraction.

The observable of tSZ is Compton-y parameter and the power spectrum of Compton-y is the fundamental and widely used statistic in studies of tSZ. Here, let us consider the method of computing the power spectrum based on the halo model prescription. Following the halo model formalism in Cole & Kaiser (1988); Komatsu & Kitayama (1999), we can derive the expression for the angular power spectrum of Compton-y as the sum of 1-halo and 2-halo contributions:

$$C^{yy}(\ell) = C^{yy(\rm 1h)}(\ell) + C^{yy(\rm 2h)}(\ell), \tag{6.4}$$

$$C^{yy(\rm 1h)}(\ell) = \int_0^{z_{\rm dec}} dz \frac{d^2V}{dzd\Omega} \int_{M_{\rm min}}^{M_{\rm max}} dM \frac{dn(M,z)}{dM} |y_\ell(M,z)|^2, \tag{6.5}$$

$$C^{yy(\rm 2h)}(\ell) = \int_0^{z_{\rm dec}} dz \frac{d^2V}{dzd\Omega} P_{\rm m}(k_\ell, z) \left[\int_{M_{\rm min}}^{M_{\rm max}} dM \frac{dn(M,z)}{dM} b(M,z) y_\ell(M,z) \right]^2, \tag{6.6}$$

where $k_\ell = \ell/\{(1+z)d_A(z)\}$, $z_{\rm dec}$ is the redshift of last scattering, $d_A(z)$ is the angular diameter distance, $d^2V/dzd\Omega = (1+z)^2 d_A^2/H(z)$ is the comoving volume element per redshift and solid angle, $y_\ell(M,z)$ is the Fourier transform of Compton-y from a single halo and $P_{\rm m}(k,z)$ is the linear matter power spectrum. The explicit formula of $y_\ell(M,z)$ is

$$y_\ell = \frac{4\pi R_s}{\ell_s^2} \frac{\sigma_{\rm T}}{m_e c^2} \int dx\, x^2 P_e(x) \frac{\sin(\ell x/\ell_s)}{\ell x/\ell_s}, \tag{6.7}$$

where $x = r/R_s$, $\ell_s = d_A/R_s$, and R_s is the arbitrary scale radius. We use two definitions of the halo mass M: virial mass $M_{\rm vir}$ and the enclosed mass $M_{\rm 200b}$. The latter mass definition denotes the enclosed mass within the overdensity of 200 times the mean background density. For $M_{\rm 200b}$, the corresponding overdensity with respect to the critical density is $\Delta = 200\rho_{\rm m}(z)/\rho_{\rm cr}(z) = 200\Omega_{\rm m}(z)$. The range of integration for halo mass in Eqs. (6.5) and (6.6) is set as $M_{\rm min} = 10^{12}\, h^{-1}\,{\rm M}_\odot$ and $M_{\rm max} = 10^{16}\, h^{-1}\,{\rm M}_\odot$. For halo mass function $dn(M,z)/dM$ and halo bias $b(M,z)$, we adopt fitting formulae from Bocquet et al. (2016) and Tinker et al. (2010), respectively (see also Sections 2.4.1 and 2.4.2). For convenience, we also define $M_{\rm 500c}$ as the halo mass with the mean density of $\Delta = 500$ times the critical density.

6.2.2 Cross-Correlation of tSZ and WL

In this Section, we consider the cross-correlation of tSZ and WL. The observable in WL observations that we focus on is convergence field $\kappa(\boldsymbol{\theta})$, which roughly corresponds to the projected density convolved with the lensing kernel. The cross-power spectrum of Compton-y and convergence can also be computed from the halo model prescription. We

can obtain the expression by replacing one of y_ℓ in Eqs. (6.5) and (6.6) with κ_ℓ, which is the Fourier transform of the convergence signal from a single halo:

$$C^{y\kappa}(\ell) = C^{y\kappa(1\mathrm{h})}(\ell) + C^{y\kappa(2\mathrm{h})}(\ell), \tag{6.8}$$

$$C^{y\kappa(1\mathrm{h})}(\ell) = \int_0^{z_{\mathrm{dec}}} dz \frac{d^2V}{dzd\Omega} \int_{M_{\mathrm{min}}}^{M_{\mathrm{max}}} dM \frac{dn}{dM} y_\ell(M,z)\kappa_\ell(M,z), \tag{6.9}$$

$$\begin{aligned} C^{y\kappa(2\mathrm{h})}(\ell) = & \int_0^{z_{\mathrm{dec}}} dz \frac{d^2V}{dzd\Omega} P_{\mathrm{m}}(k_\ell, z) \\ & \times \int_{M_{\mathrm{min}}}^{M_{\mathrm{max}}} dM \frac{dn}{dM} b(M,z)\kappa_\ell(M,z) \\ & \times \int_{M_{\mathrm{min}}}^{M_{\mathrm{max}}} dM \frac{dn}{dM} b(M,z) y_\ell(M,z). \end{aligned} \tag{6.10}$$

Next, we review how to compute the lensing signal from a single halo. For density profile, we adopt the NFW profile (Section 2.4.3). The halo model calculation necessitates the Fourier transform of the projected density, i.e., convergence, denoted as $\kappa_\ell(M,z)$,

$$\kappa_\ell(M,z) = \int 2\pi\theta\kappa(\theta) J_0(\ell\theta)\, d\theta = \frac{M\tilde{u}_M(k_\ell, z)}{d_A^2 \Sigma_{\mathrm{crit}}(z)}, \tag{6.11}$$

where $\kappa(\theta)$ is the convergence from a single halo, $J_0(x)$ is the zeroth-order Bessel function, $\tilde{u}_M(k)$ is the Fourier transform of the scaled density $u_M(r) = \rho(r)/M$, and $\Sigma_{\mathrm{crit}}(z)$ is the critical surface mass density. The analytical expressions of $\tilde{u}_M(k)$ and $\Sigma_{\mathrm{crit}}(z)$ are found in Oguri & Takada (2011). For the calculation of $\Sigma_{\mathrm{crit}}(z)$ we need the redshift distribution of source galaxies. For RCSLenS, we adopt the following fitting function (Harnois-Déraps et al., 2016):

$$\begin{aligned} n_{\mathrm{RCSLenS}}(z) = & \; az\exp[-(z-b)^2/c^2] + dz\exp[-(z-e)^2/f^2] + \\ & gz\exp[-(z-h)^2/i^2], \end{aligned} \tag{6.12}$$

where

$$(a,b,c,d,e,f,g,h,i) = (2.94, -0.44, 1.03, 1.58, 0.40, 0.25, 0.38, 0.81, 0.12). \tag{6.13}$$

In practice, two-point correlation function $\xi^{y\kappa}(\theta)$ is commonly used in observations. We can transform the cross-power spectrum into the cross-correlation via Hankel transformation:

$$\xi^{y\kappa}(\theta) = \int \frac{\ell d\ell}{2\pi} C^{y\kappa}(\ell) J_0(\ell\theta). \tag{6.14}$$

6.3 Methods

6.3.1 Modeling of the ICM Pressure Profile

In order to compute pressure profile of halos, we employ Shaw model and the universal pressure profile calibrated by *Planck* SZ observation (Planck Collaboration, 2013). The

details on the ICM modeling can be found in Sections 4.3.3 and 4.3.4. For the universal pressure profile, following the prescription in Dolag et al. (2016), the halo mass and halo radius are rescaled as $M_{500c} \to M_{500c}/1.2$ and $R_{500} \to R_{500}/(1.2)^{1/3}$. In Section 6.4.2, we incorporate these pressure profiles into the halo model scheme to compute the power spectrum and cross-correlations in order to constrain σ_8 and non-thermal pressure amplitude.

6.3.2 Numerical Simulations and Map Making Procedure

To estimate the covariance matrix, we create realistic mock maps for WL and tSZ with N-body simulations. First, we run a simulation to obtain the spatial matter distribution. We utilize the Tree-PM code `Gadget-2` (Springel, 2005). The set up of the simulations is as follows; the number of particles is $N = 2048^3$, the volume of the simulation box is $(1\,h^{-1}\,\mathrm{Gpc})^3$, and the particle mass is $m_\mathrm{p} = 1.02 \times 10^{10}\,h^{-1}\,\mathrm{M}_\odot$. The initial condition is generated at the redshift $z_\mathrm{ini} = 59$ with a parallelized code developed by Nishimichi et al. (2009, 2010); Valageas & Nishimichi (2011), which calculates displacement and velocity field based on the second order Lagrangian perturbation theory. We store 10 snapshots to construct a light-cone output from $z = 4.13$ to $z = 0.0$. The redshifts at which snapshots are stored are determined to satisfy $\chi(z_{i+1}) - \chi(z_i) = 500\,h^{-1}\,\mathrm{Mpc}$ $(i = 1, \ldots, 9)$ and $\chi(z_1) = 250\,h^{-1}\,\mathrm{Mpc}$ (see Figure 6.1).

For halo finder, we employ the `Rockstar` halo finder (Behroozi et al., 2013). We assign gas pressure to each particle which belongs to a halo according to the radius from the center with the Shaw model or the universal pressure profile based on the particle-based pasting (see Section 5.2.2.2). If a particle does not belong to any halos, it does not contribute to tSZ signal, i.e., the thermal pressure is zero. Since the code automatically provides the concentration parameter by fitting the density profile with the NFW profile, we use this estimated concentration parameter instead of the one computed from the fitting formula of concentration parameter. Thus, by projecting the obtained pressure field, one can construct mock Compton-y maps.

In order to create mock convergence field, we employ the multiple-plane ray-tracing method (see also Section 5.2.1). First, we place snapshots to create the light-cone which fills the volume from $z = 0$ to $z = 4.13$ (see Figure 6.1). For each snapshot, we extract $500\,h^{-1}\,\mathrm{Mpc}$ slice, i.e., half of the simulation box, in the line-of-sight direction and then randomly rotate and translate particles keeping periodic boundary condition so that the same structure does not appear multiple times on the same angular position. The angular extent of each map is $10^\circ \times 10^\circ$ and the number of grids on a side is 8192, which corresponds to the pixel size of $10^\circ/8192 \simeq 0.073\,\mathrm{arcmin}$. Finally, by repeating the random rotation and translation 100 times, we generate 100 mock $10^\circ \times 10^\circ$ convergence maps in total, applying weights derived from the source redshift distribution (Eq. 6.12).

Figure 6.2 shows examples of convergence and Compton-y maps. For the Compton-y map, we do not include ray deflection effect because the effect is negligible at the scales where measurements are available (Tröster & Van Waerbeke, 2014). For sanity check, we measure the average Compton-y parameter $\langle y \rangle$. For the Shaw model profile, $\langle y \rangle = (1.47 \pm 0.10) \times 10^{-6}$ and for the universal pressure profile, $\langle y \rangle = (1.07 \pm 0.10) \times 10^{-6}$. The

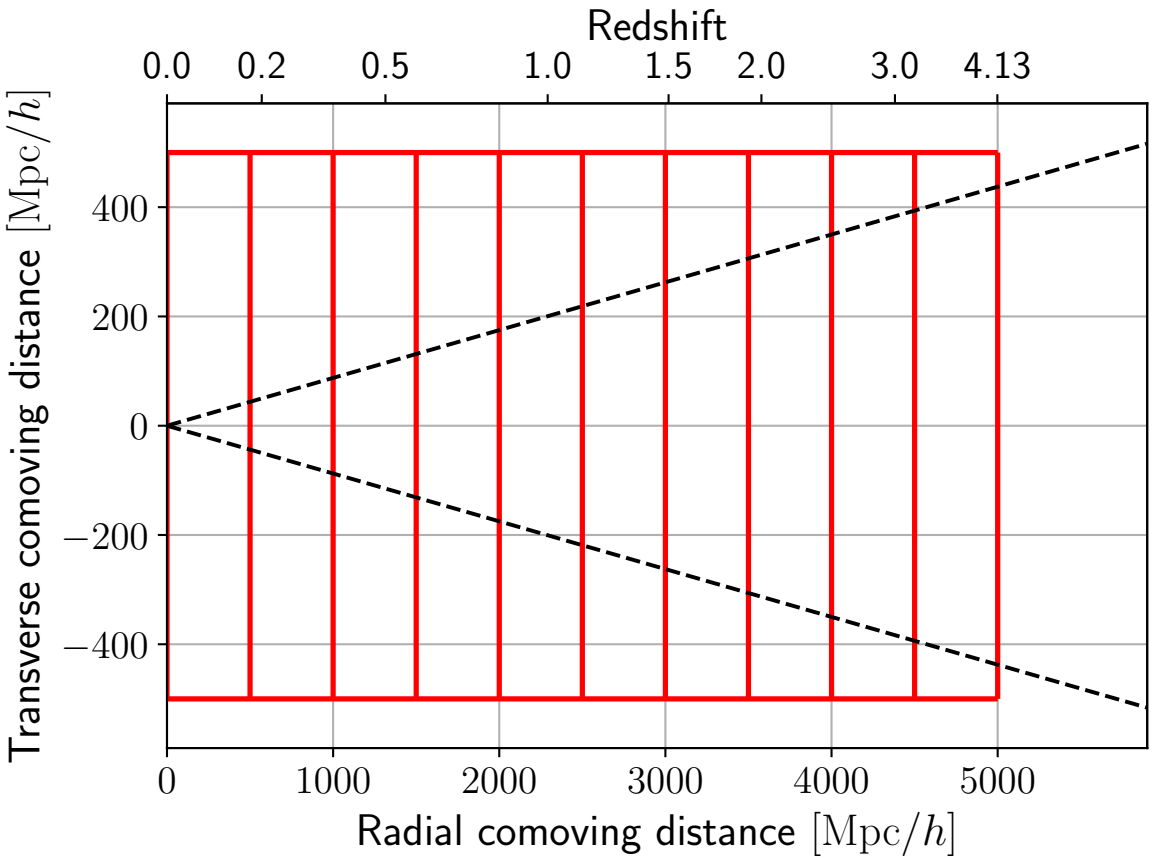

Figure 6.1: Configuration of snapshots. Each red rectangle corresponds to a single snapshot and the dashed lines show the extended angle of the light-cone. The length in the line-of-sight direction is $500\,h^{-1}$ Mpc. We randomly rotate and translate simulation box based on periodic boundary condition, and then extract the corresponding region from the original snapshot, which has $1000\,h^{-1}$ Mpc on a side. When creating mock Compton-y map, the redshift of each particle is computed according to the distance from the observer. The dashed lines show the opening angle of 10 deg.

error corresponds to the standard deviation over 100 mock maps. The results are close to that of the previous study (Dolag et al., 2016) based on hydrodynamics simulations, $\langle y \rangle = 1.18 \times 10^{-6}$. Note that they adopted the different hydrodynamics model and cosmological parameters, which may lead to the difference of the values. For reference, Khatri & Sunyaev (2015) presented bounds of the average Compton-y from which they subtracted the contribution from resolved galaxy clusters as $5.4 \times 10^{-8} < \langle y \rangle < 2.2 \times 10^{-6}$.

In order to make our simulated maps more realistic, we add the detector noise to convergence and Compton-y maps, and then smooth them with the Gaussian filter. For tSZ maps, following Dolag et al. (2016), we add the Gaussian noise so that the standard deviation of the noise map is $\sigma = 1.5 \times 10^{-6}$ with the FWHM window scale $\theta_{\rm FWHM} = 10\,\text{arcmin}$. For WL, the dominant source of the noise is the shape noise and the noise can be modeled as Gaussian (Van Waerbeke, 2000). The variance of the noise is given as

$$\sigma^2 = \frac{\sigma_\epsilon^2}{\theta_{\rm pix}^2 n_{\rm gal}}, \tag{6.15}$$

where σ_ϵ is the standard deviation of the intrinsic ellipticity, $\theta_{\rm pix}$ is the pixel size of the map, and $n_{\rm gal}$ is the mean surface number density of source galaxies. For RCSLenS, we adopt $\sigma_\epsilon = 0.277$ and $n_{\rm gal} = 5.8\,\text{arcmin}^{-2}$ (Hojjati et al., 2017). After adding the noise, both of the maps are smoothed with the Gaussian filter with $\theta_{\rm FWHM} = 10\,\text{arcmin}$ which is the same smoothing scale in reconstructing the Compton-y map in *Planck* (Planck Collaboration, 2016c).

6.3.3 Estimation of the Covariance Matrix

We present how the covariance matrix is measured from the mock maps from simulations. In our analysis, the data vector $\boldsymbol{N}$ for the joint analysis of auto-power spectrum of tSZ and cross-correlations of tSZ-WL is defined as

$$\boldsymbol{N} = (C^{yy}(\ell_1), \ldots, C^{yy}(\ell_{n_C}), \xi^{y\kappa}(\theta_1), \ldots, \xi^{y\kappa}(\theta_{n_\xi}))^{\rm T}, \tag{6.16}$$

where the dimensions of the data vectors are $n_C = 13$ and $n_\xi = 8$. The binning of angular separation is equally spaced in the range of $2.55' \leq \theta \leq 160'$. Table 6.1 shows the data for the auto-power spectrum of tSZ measured by *Planck*, and we use the power spectrum in the multipole range of $52.5 \leq \ell \leq 1247.5$. Though in *Planck* data, there are more available data points for lower multipoles, we do not use these data points due to the size of mock maps. We have 100 mock maps and as a result $R = 100$ measurement of the data vector $\boldsymbol{N}^r$ $(r = 1, \ldots, R)$. The area of mock maps is $100\,\text{deg}^2$, but we will apply this covariance matrix to the measurements by *Planck* and RCSLenS, both of which have larger survey areas. Since the covariance matrix scales as the inverse square of the survey area, we multiply a scaling factor to adjust the survey area. The estimated covariance matrix is expressed as

$$\text{Cov}_{ij} = f_{ij}^s \frac{1}{R-1} \sum_{r=1}^{R} (N_i^r - \bar{N}_i)(N_j^r - \bar{N}_j), \tag{6.17}$$

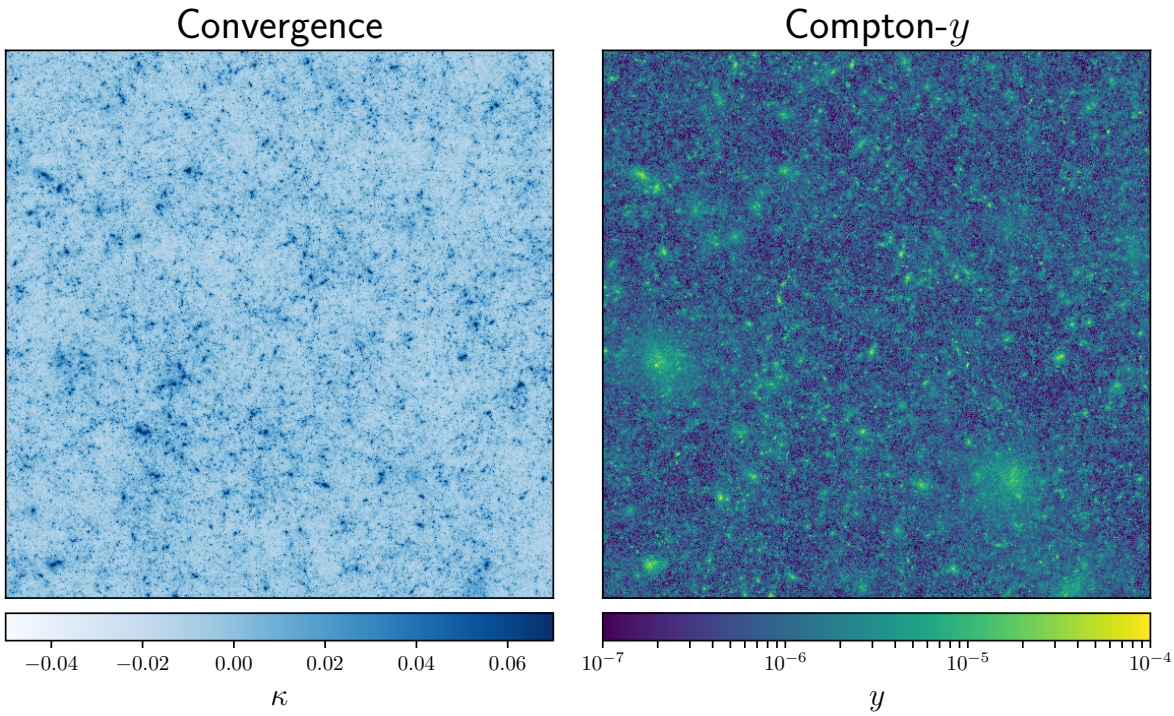

Figure 6.2: Convergence and Compton-y maps obtained from N-body simulations. For Compton-y map, we adopt Shaw model to compute the pressure profile of halos. The length on a side corresponds to $10\,^{\circ}$.

where $\bar{N}$ is the mean over the R realizations:

$$\bar{\boldsymbol{N}} = \frac{1}{R}\sum_{r=1}^{R}\boldsymbol{N}^r, \tag{6.18}$$

and f_{ij}^s is the scaling factor of the survey area:

$$f_{ij}^s = \begin{cases} A_{\rm sim}/A_{Planck} & \text{(between the power spectrum)} \\ A_{\rm sim}/A_{\rm RCSLenS} & \text{(between the cross-correlation).} \end{cases} \tag{6.19}$$

The survey areas are taken as $A_{\rm sim} = 100\,{\rm deg}^2$, $A_{Planck} = 20626\,{\rm deg}^2$ and $A_{\rm RCSLenS} = 560\,{\rm deg}^2$. For covariance between the power spectrum and the cross-correlation, there is no appropriate scaling factor because the sizes of the survey areas of *Planck* and RCSLenS are different. In order to estimate the cross-covariance, we generate 100 Gaussian maps of Compton-y and convergence which reproduce the power spectrum $C^{yy}(\ell)$ and cross-spectra $C^{y\kappa}(\ell)$ computed from the halo model with the fiducial parameters. The size of Gaussian maps is matched with the survey area of *Planck* (RCSLenS) for Compton-y (convergence) maps. Then, we compute the power spectra and the cross-correlations based on these maps, and estimate the cross-covariance as the variance over 100 Gaussian maps. For the power spectrum of tSZ, we take into account the variance $\sigma_{\rm fg}$ (see Table 6.1), which arises from incomplete separation between the signal of tSZ and contaminants, e.g., cosmic infrared background. In Figure 6.3, the covariance matrices measured from our simulations and Gaussian maps are shown. For the power spectrum part, though the diagonal components are dominated, there are substantial off-diagonal correlations caused by the connected trispectrum term (Horowitz & Seljak, 2017).

6.4 Results

6.4.1 Power Spectrum and Cross-Correlation

We show power spectra of Compton-y for different models in Figure 6.4. The results of the analytic model (Shaw et al., 2010) and the simulation based pasting model are not consistent at smaller scales ($\ell \gtrsim 2000$) possibly due to the lack of resolution in N-body simulations. In addition, the effects of the asphericity and substructures can explain part of the differences (Battaglia et al., 2012). However, at scales which can be accessible by *Planck* data ($100 \lesssim \ell \lesssim 1000$), both models give consistent results. For even larger scales ($\ell \lesssim 100$), the power spectra of the Shaw model is suppressed and the variance is quite large affected by the size of mock maps. Overall, all of the results overestimate the power spectrum compared with the measurement of *Planck*. One of the possible reasons is that our input parameter $\sigma_8 = 0.831$ is high. We will address this point in the following Section. The covariance matrix estimated from mock simulations gives similar amplitudes to those in Planck Collaboration (2016d). However, our covariance matrix includes the off-diagonal terms, which are not considered in Planck Collaboration (2016d).

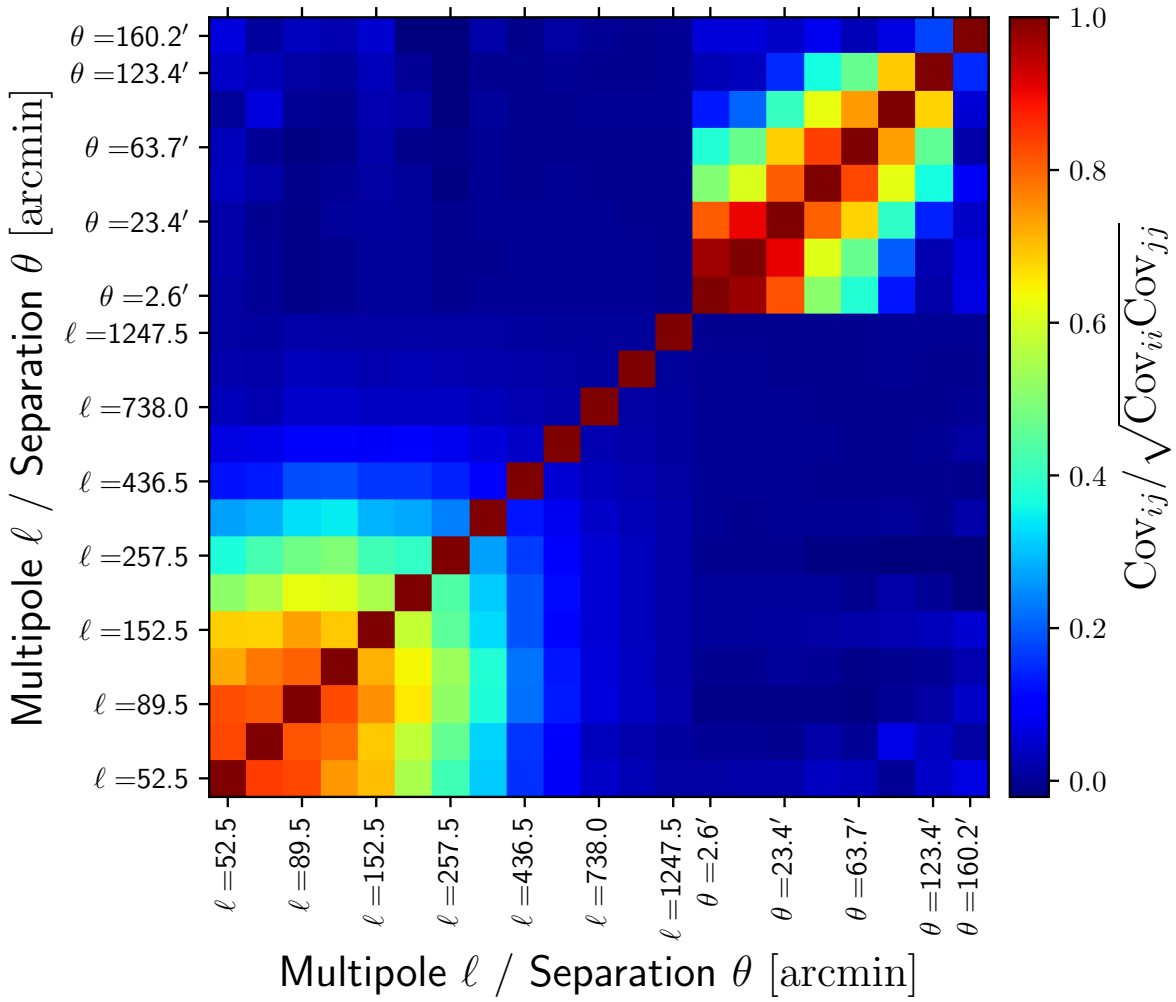

Figure 6.3: Covariance matrices measured from simulations and Gaussian maps. From 1st to 13th rows and columns correspond to the power spectra, and from 14th to 21st rows and columns do to cross-correlations. The upper left (lower left) part corresponds to the covariance with pressure profile based on Shaw model (universal pressure profile). The scaling factor due to the size of areas has already been applied.

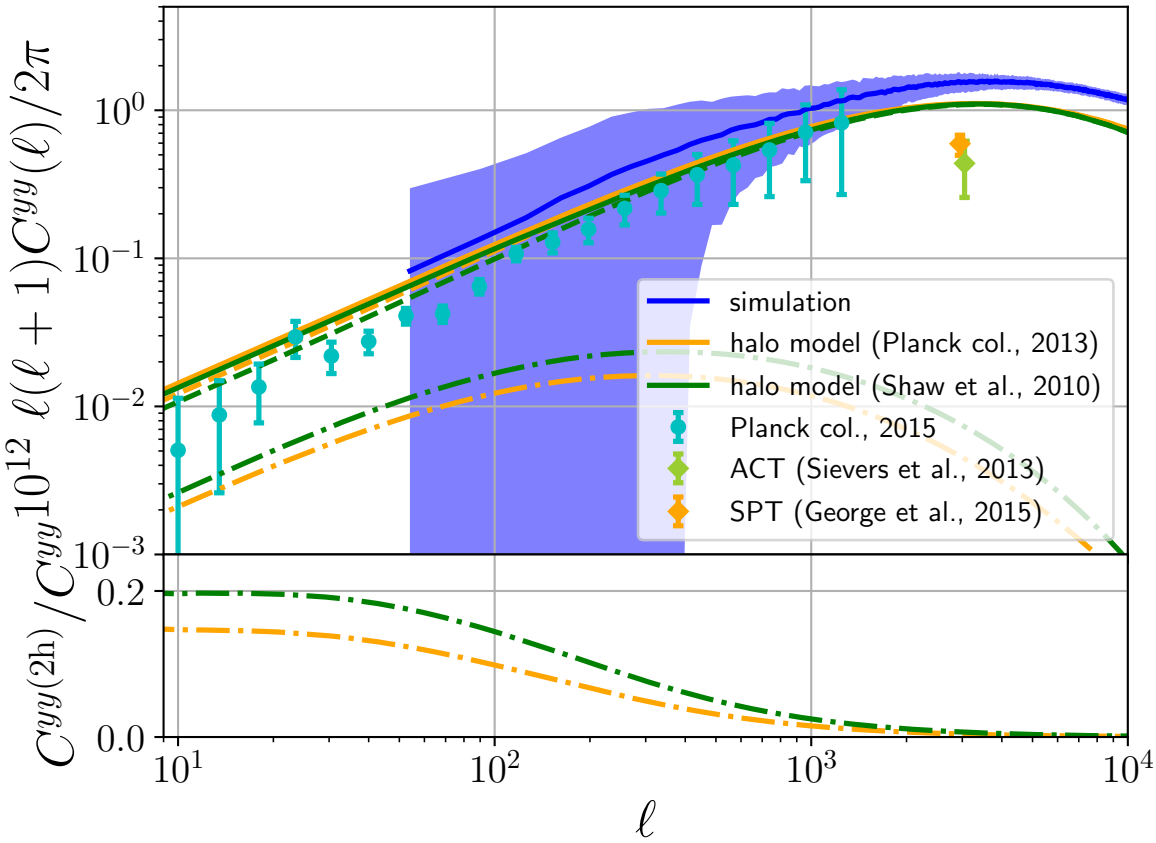

Figure 6.4: Power spectra of Compton-y from simulations, the halo model prediction of two different pressure profile. The dashed (dot-dashed) line shows 1-halo (2-halo) contribution. The lower panel shows the ratio of 2-halo term to the total spectrum. For comparison, the observational estimates from *Planck* (Planck Collaboration, 2016c), ACT (Sievers et al., 2013), and SPT (George et al., 2015). are also shown. The shaded region corresponds to the standard deviation over 100 mock maps which cover 100 square degrees.

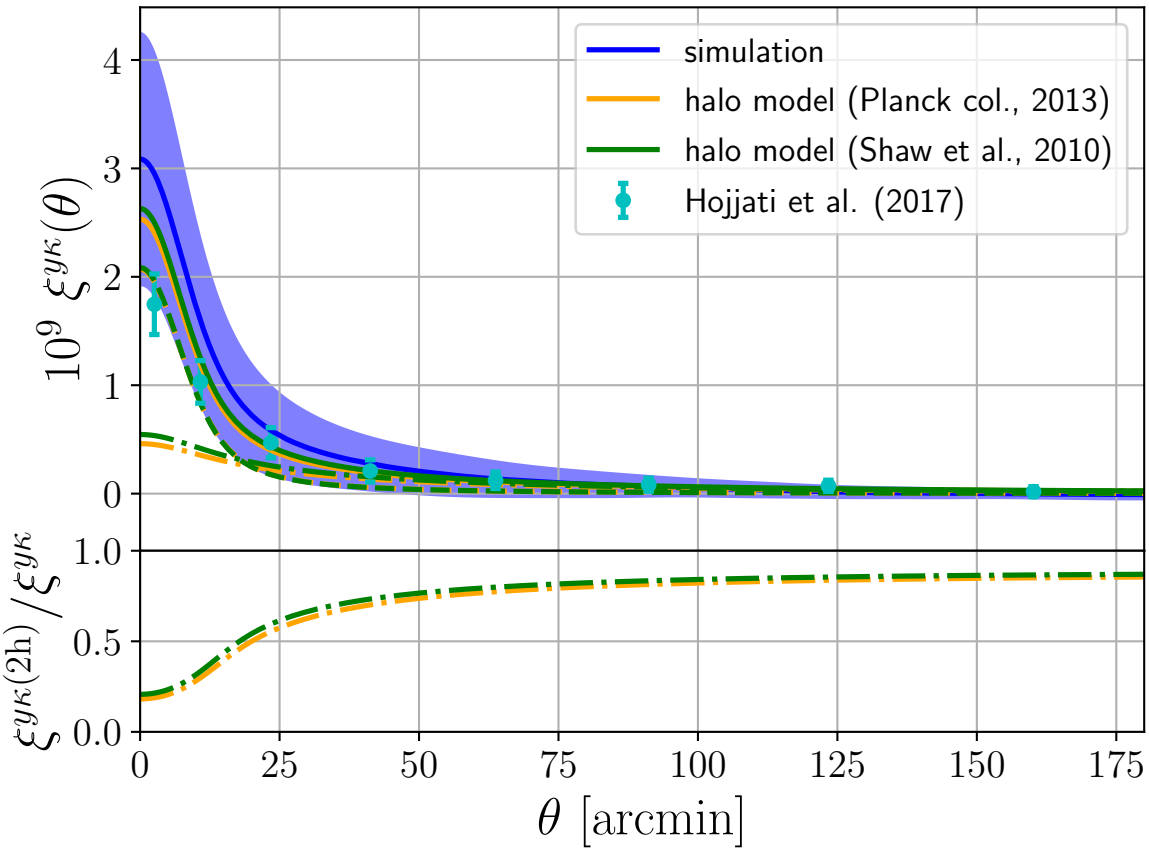

Figure 6.5: Cross-correlation function of tSZ and WL from our simulation and halo model calculations. The dashed (dot-dashed) line shows 1-halo (2-halo) contribution. The lower panel shows the ratio of 2-halo term to the total cross-correlation. The shaded region corresponds to the standard deviation over 100 mock maps which cover 100 square degrees.

Figure 6.5 shows the cross-correlation of tSZ and WL from our simulation based pasting model and halo model calculations. Although the excess of the cross-correlations at small scales ($\theta < 10\,\mathrm{arcmin}$) can be seen as a possible tension, the results are consistent with each other on larger scales. This difference also can be induced by the high value of σ_8.

6.4.2 Constraints on Non-Thermal Pressure and σ_8

With the power spectrum and the cross-correlation measured by *Planck* and RCSLenS, we can constrain the amplitude α_0 of the non-thermal pressure and the amplitude of the matter power spectrum, i.e., σ_8. Other model parameters and cosmological parameters are fixed at the fiducial values. The posterior distribution when both of the power spectrum and the cross-correlation are used is given as

$$\log L(\alpha_0, \sigma_8 | \boldsymbol{N}_{\mathrm{data}}) = -\frac{1}{2}(\boldsymbol{N}_{\mathrm{data}} - \boldsymbol{N}_{\mathrm{model}})^{\mathrm{T}}(\mathrm{Cov})^{-1}(\boldsymbol{N}_{\mathrm{data}} - \boldsymbol{N}_{\mathrm{model}}) + \mathrm{const.}, \quad (6.20)$$

where $\boldsymbol{N}_{\mathrm{data}} = (\boldsymbol{C}^{yy}_{Planck}, \boldsymbol{\xi}^{y\kappa}_{\mathrm{RCSLenS}})$ and $\boldsymbol{N}_{\mathrm{model}}$ is the halo model prediction given α_0 and σ_8. When we use either the power spectrum or the cross-correlation, we simply use a submatrix of the covariance and a subvector of the model vector.

We estimate the probability contours by computing the posterior probability at regular grids. The posterior distribution is shown in Figure 6.6 with different data sets, power spectrum only, cross-correlation only, both of them. The red, blue, and green solid lines correspond to the confidence regions with the data sets of both of power spectra and cross-correlations, power spectra only, and cross-correlations only, respectively. With all data sets, the clear degeneracy between σ_8 and α_0 can be seen. If only the power spectra are employed, moderate $\sigma_8 \sim 0.85$ are preferred but the estimated α_0 is clearly larger than the fiducial value 0.18. On the other hand, the results with cross-correlations (red and green lines) prefer low $\sigma_8 \sim 0.6$ and low $\alpha_0 \sim 0.05$. The low non-thermal pressure amplitude α_0 is strongly inconsistent with the predictions based on hydrodynamical cosmological simulations (Shaw et al., 2010; Nelson et al., 2014). The estimated value of σ_8 is quite smaller than the result from CMB measurements of *Planck*, $\sigma_8 = 0.831 \pm 0.013$ (TT,TE,EE+lowP, Planck Collaboration, 2016d). However, recent analysis of KiDS weak lensing survey (Köhlinger et al., 2017) reports $\sigma_8(\Omega_{\mathrm{m}}/0.3)^{0.5} = 0.651 \pm 0.058$, i.e. $\sigma_8 = 0.635 \pm 0.057$ for $\Omega_{\mathrm{m}} = 0.3156$, which is consistent with our result within 1-σ level.

In addition, we investigate how the small scale (less than 10 arcmin, which is the smoothing scale) cross-correlations affect the results. Figure 6.7 shows the confidence regions with small scale cross-correlations excluded. In these cases, all of results become consistent with each other. This result indicates that the tension originates from the small scales.

In Figure 6.8, we show the tSZ power spectrum and tSZ-WL cross-correlation, together with the best-fit model parameters estimated with the data sets of power spectrum only, cross-correlation only, and both. Remarkably, when we include cross-correlations, the best-fit power spectrum can reproduce ACT and SPT data points, though these data points are not used in the analysis.

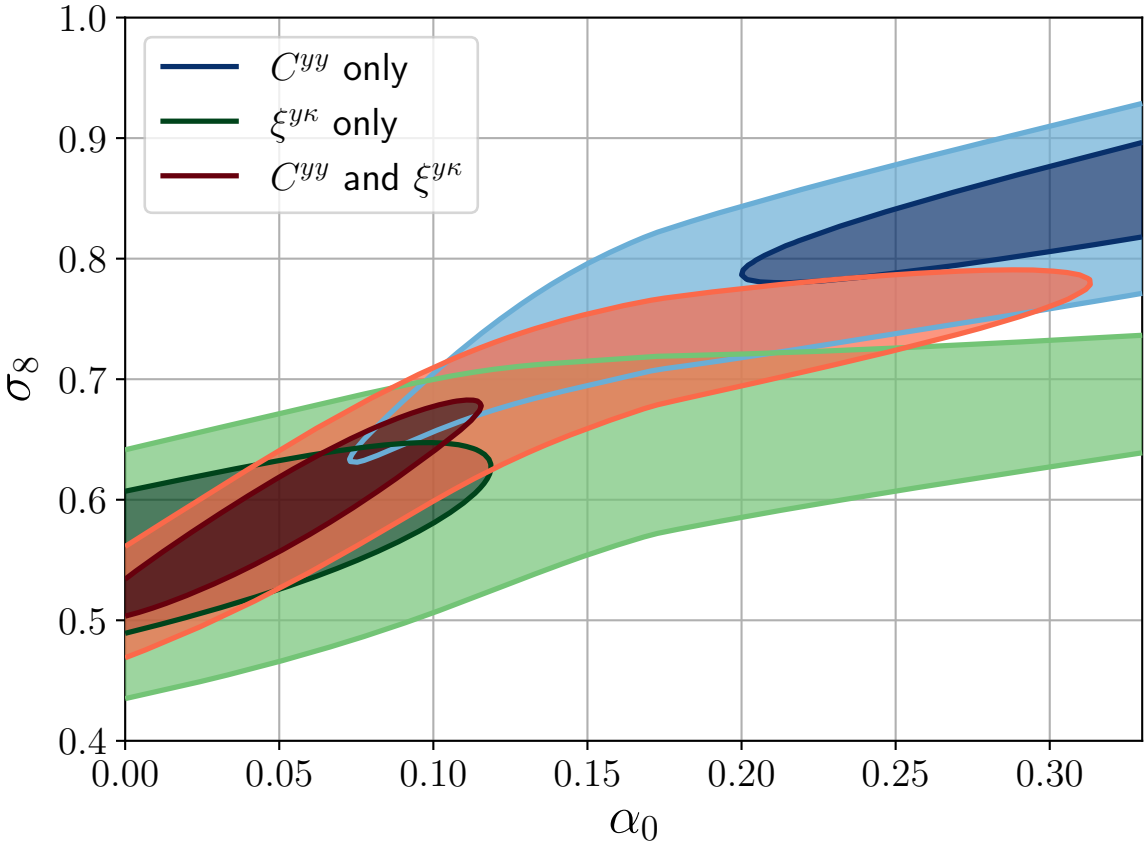

Figure 6.6: Posterior distributions of non-thermal pressure parameters α_0 and σ_8. The inner (outer) colored region corresponds to 1-σ (2-σ) confidence level. The results with data sets of power spectra and cross-correlations, power spectra only, and cross-correlations are shown in solid red, blue, and green regions, respectively.

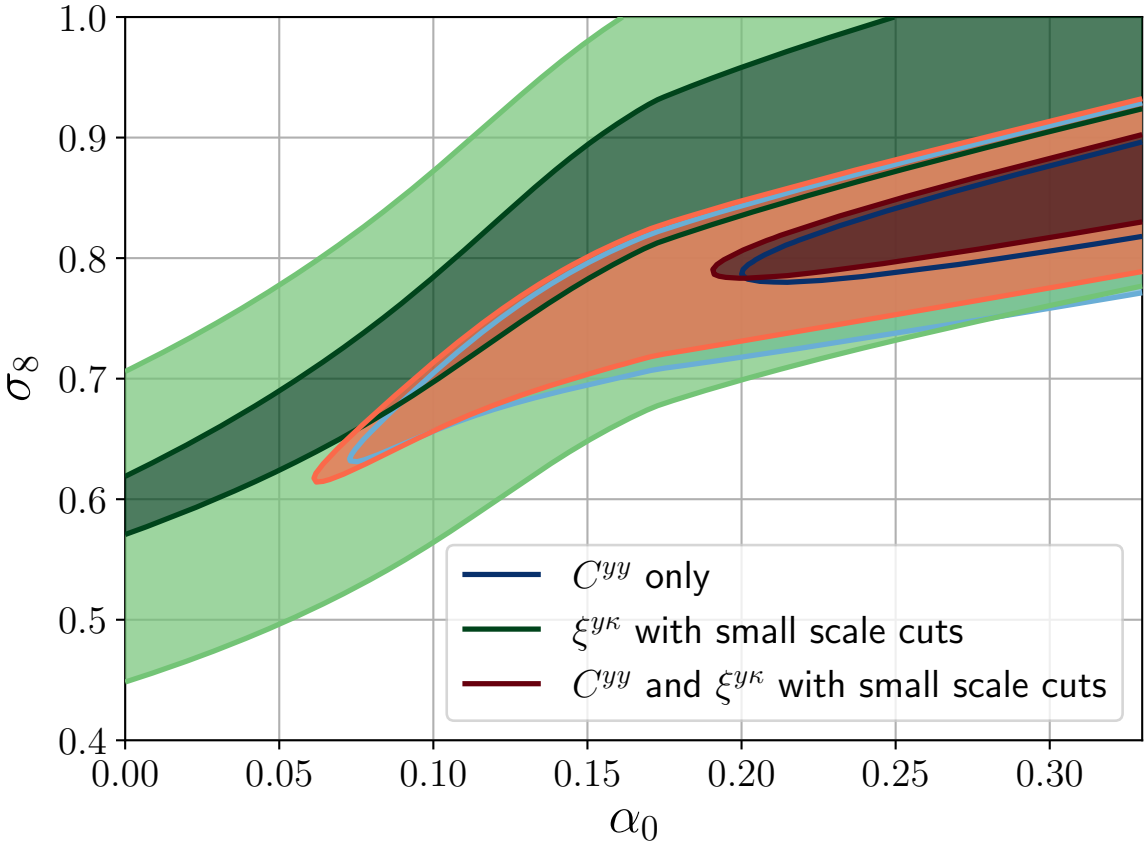

Figure 6.7: Posterior distributions of non-thermal pressure parameters α_0 and σ_8 with small scale ($<$ 10 arcmin) cuts in cross-correlations. The inner (outer) colored region corresponds to 1-σ (2-σ) confidence level. The results with data sets of power spectra and cross-correlations, power spectra only, and cross-correlations only are shown in solid red, blue, and green regions, respectively. Note that the blue regions are identical in Figure 6.6 because this data set does not include cross-correlations.

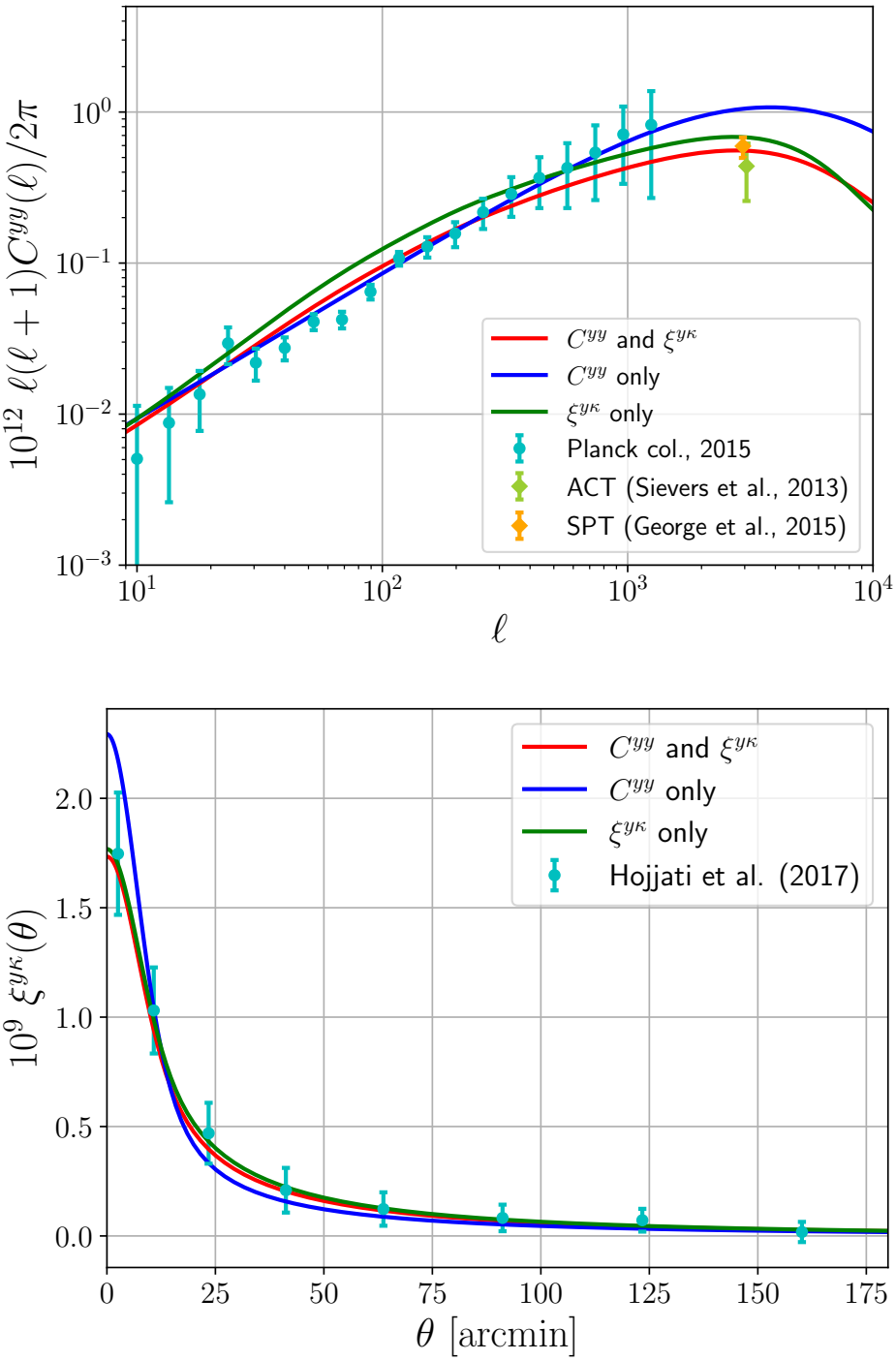

Figure 6.8: Power spectra and cross-correlations with best-fit parameters. The results using data sets of power spectra only, cross-correlations only, and both are shown as blue, green, and red lines, respectively.

We next derive constraints on σ_8 using the universal pressure profile with parameters calibrated against *Planck* data (Eq. 4.43). Note that we apply the pressure profile to less massive and/or high redshift halos, which are not calibrated in this pressure profile. Using only the tSZ power spectrum data, we find $\sigma_8 = 0.785^{+0.029}_{-0.043}$, consistent with Planck Collaboration (2016c), who find $\sigma_8(\Omega_\mathrm{m}/0.28)^{3/8} = 0.80^{+0.01}_{-0.03}$, i.e., $\sigma_8 = 0.76^{+0.01}_{-0.03}$ for $\Omega_\mathrm{m} = 0.3156$, from a similar analysis. The tSZ-WL cross-correlation on the other hand prefers a lower value of $\sigma_8 = 0.677^{+0.046}_{-0.077}$. Combining the two data sets, we find $\sigma_8 = 0.746^{+0.026}_{-0.038}$. The posterior distributions derived from tSZ and the tSZ-WL cross-correlation show a clear tension (see Figure 6.9).

6.4.3 Mitigating the Tension between the Data Sets

As seen above, the constraints on σ_8 and α_0 from the tSZ power spectrum and the tSZ-WL cross-correlation are inconsistent. The tension seems to originate from the small scales, as we have seen in Figure 6.7. Here, we investigate if modifications to the gas model can help mitigate the tension. The analytic pressure profile is calibrated against X-ray observations of massive clusters over a wide range of redshift, and low redshift galaxy groups (Flender et al., 2017). Therefore, the gas profile of galaxy groups at high redshift is not calibrated in the current framework.

High-redshift, low-mass groups and clusters contribute a considerable fraction to the total tSZ power spectrum and tSZ-WL cross-correlation, as shown in Figure 6.10, where we show the contribution from objects with $z > 0.2$ and $M_{500\mathrm{c}} < 4 \times 10^{14}\, h^{-1}\,\mathrm{M}_\odot$. These objects contribute around 50% to the measured tSZ-WL cross-correlation, and 50%–100% to the tSZ power spectrum at $1000 < \ell < 10000$. At multipoles probed by *Planck* ($50 \lesssim \ell \lesssim 1000$), they contribute still $\sim$ 10%–50%.

In order to mitigate the tension between data sets, we consider the case of varying a parameter, S_*, which is the power index of the stellar-to-halo-mass relation defined in Eq. (4.29). When we take high S_*, the gas fraction reduces especially for group size halos, and then the resultant power spectra and cross-correlations are suppressed. To demonstrate that the high S_* model has a possibility to alleviate the tension, we repeat our analysis with $S_* = 0.7$. In this case, we find that the tension between the two data sets, the tSZ power spectrum and tSZ-WL cross-correlation, is mitigated (see Figure 6.11). Both data sets are consistent with the fiducial value $\alpha_0 = 0.18$.

We note that the high value for the slope in the stellar fraction, $S_* = 0.7$, is inconsistent with the results from Flender et al. (2017), who find $S_* = 0.12 \pm 0.1$. On the other hand, the steep slope is consistent with the results from Gonzalez et al. (2007), who analyze the stellar content of groups and clusters over a wide range of masses, 6×10^{13}–$10^{15}\,\mathrm{M}_\odot$, and find $S_* = 0.64 \pm 0.13$.

We have also tried other modification to the gas model in order to mitigate the tension, varying f_*, ϵ_f, or introducing an additional redshift dependence to the tSZ signal, but found that enhanced star formation due to high S_* works best, since it has the most impact on small scales, where the tension originates.

$\ell_{\rm min}$	$\ell_{\rm max}$	$\ell_{\rm eff}$	$10^{12} D_\ell^{yy}$	$10^{12}\ell(\ell+1)/(2\pi)\sigma_{\rm fg}$
46	60	52.5	0.04093	0.00172
60	78	68.5	0.04227	0.00320
78	102	89.5	0.06463	0.00567
102	133	117.0	0.10738	0.00969
133	173	152.5	0.12858	0.01889
173	224	198.0	0.15696	0.02895
224	292	257.5	0.21738	0.04879
292	380	335.5	0.28652	0.08374
380	494	436.5	0.36682	0.13524
494	642	567.5	0.42666	0.19500
642	835	738.0	0.53891	0.27718
835	1085	959.5	0.71103	0.37576
1085	1411	1247.5	0.82294	0.55162

Table 6.1: The tSZ auto-power spectrum measured in the *Planck* mission (Planck Collaboration, 2016d). The first three columns show the minimum, maximum, and medium, or effective, of multipole bins. The fourth column shows the power spectrum amplitudes and the fifth one shows uncertainty due to foreground separation. The power spectrum amplitude D_ℓ^{yy} is defined as $\ell(\ell+1)/(2\pi)C_\ell^{yy}$.

Data sets	Constraints on σ_8
C^{yy} and $\xi^{y\kappa}$	$0.746^{+0.026}_{-0.038}$
C^{yy} only	$0.785^{+0.029}_{-0.043}$
$\xi^{y\kappa}$ only	$0.677^{+0.046}_{-0.077}$

Table 6.2: Summary of constraints on σ_8. The best-fit value and 16% and 84% percentile values are shown.

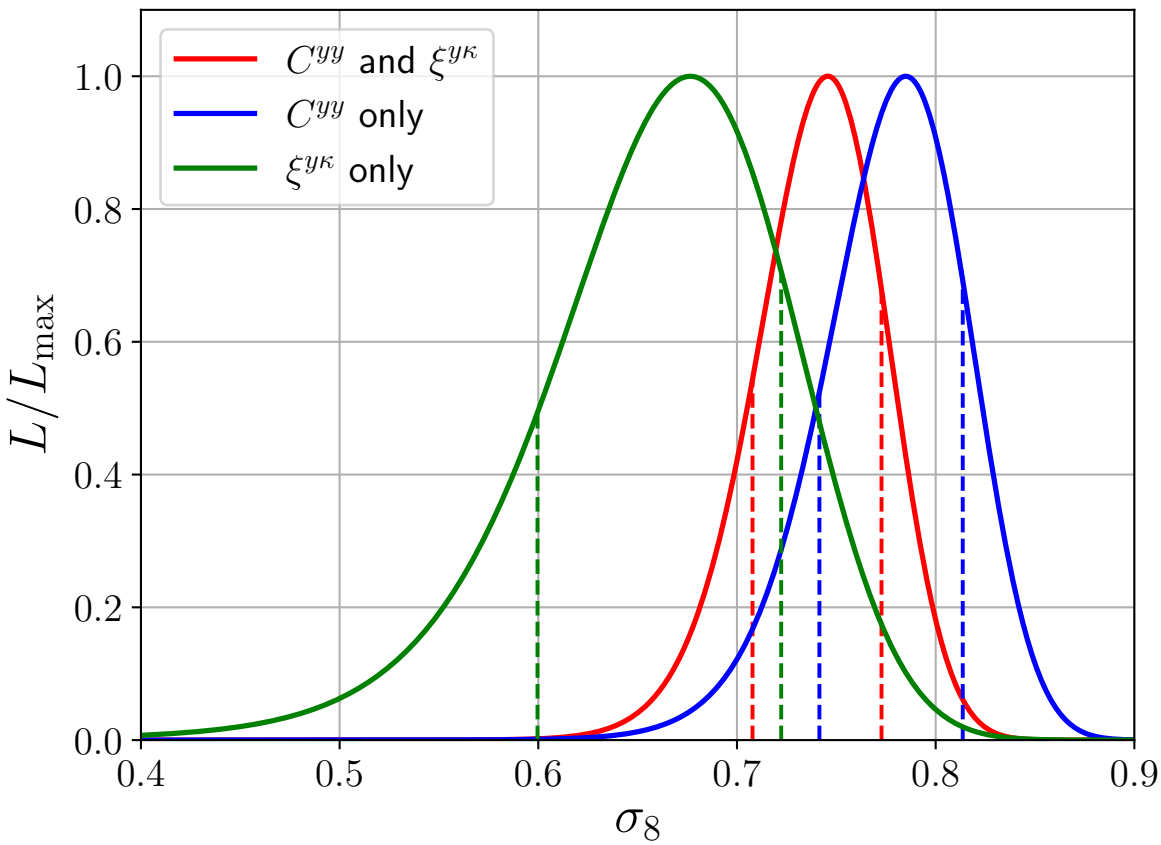

Figure 6.9: Posterior distributions of σ_8 with the power spectrum and the cross-correlation using the observationally calibrated universal pressure profile. The dashed lines show the 16% and 84% percentile.

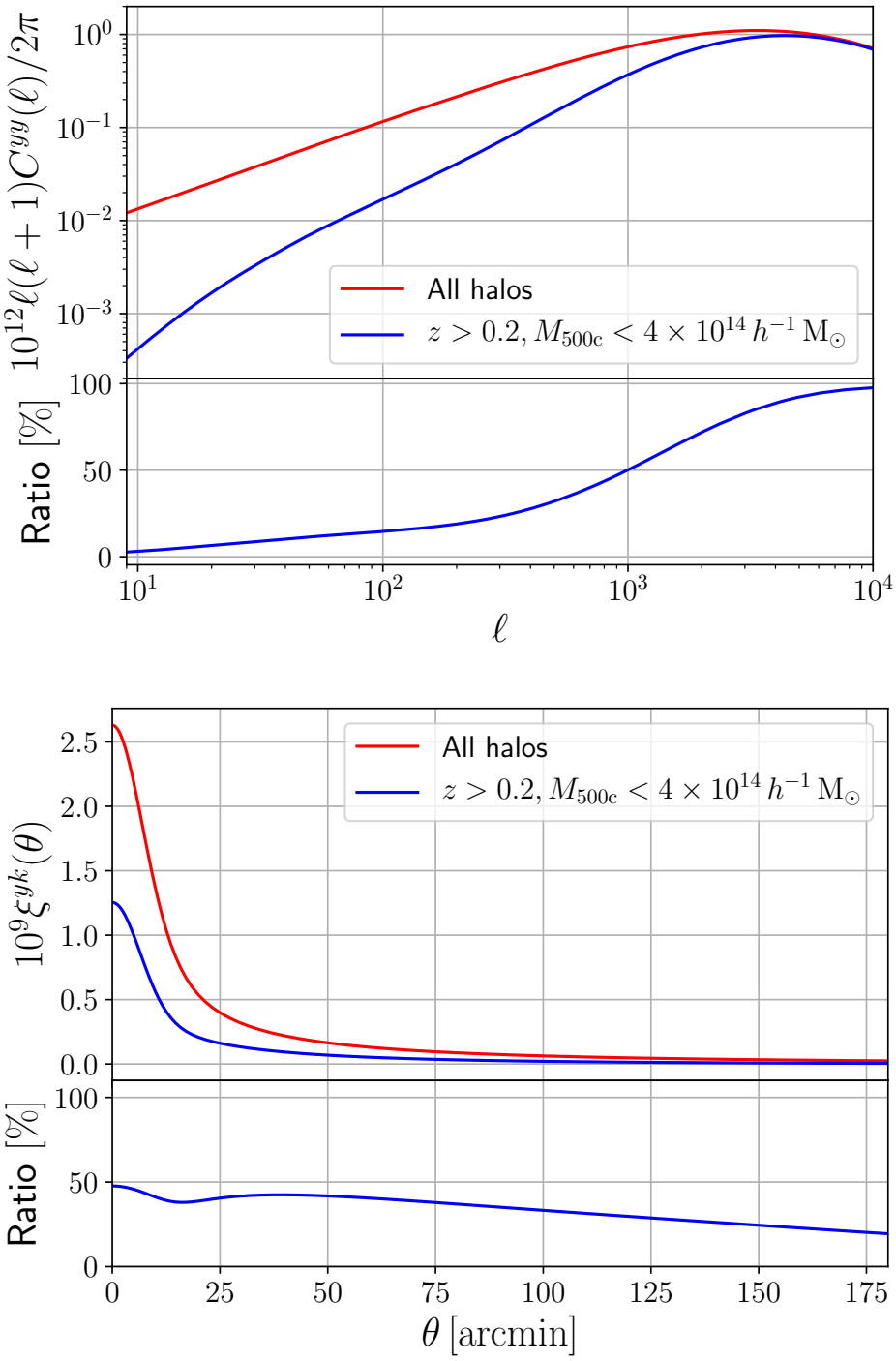

Figure 6.10: Contributions of the power spectrum and cross-correlation from high redshift groups ($z > 0.2$ and $M_{500c} < 4 \times 10^{14}\, h^{-1}\, \mathrm{M}_\odot$). The lower panels show the fraction with respect to contributions from all halos

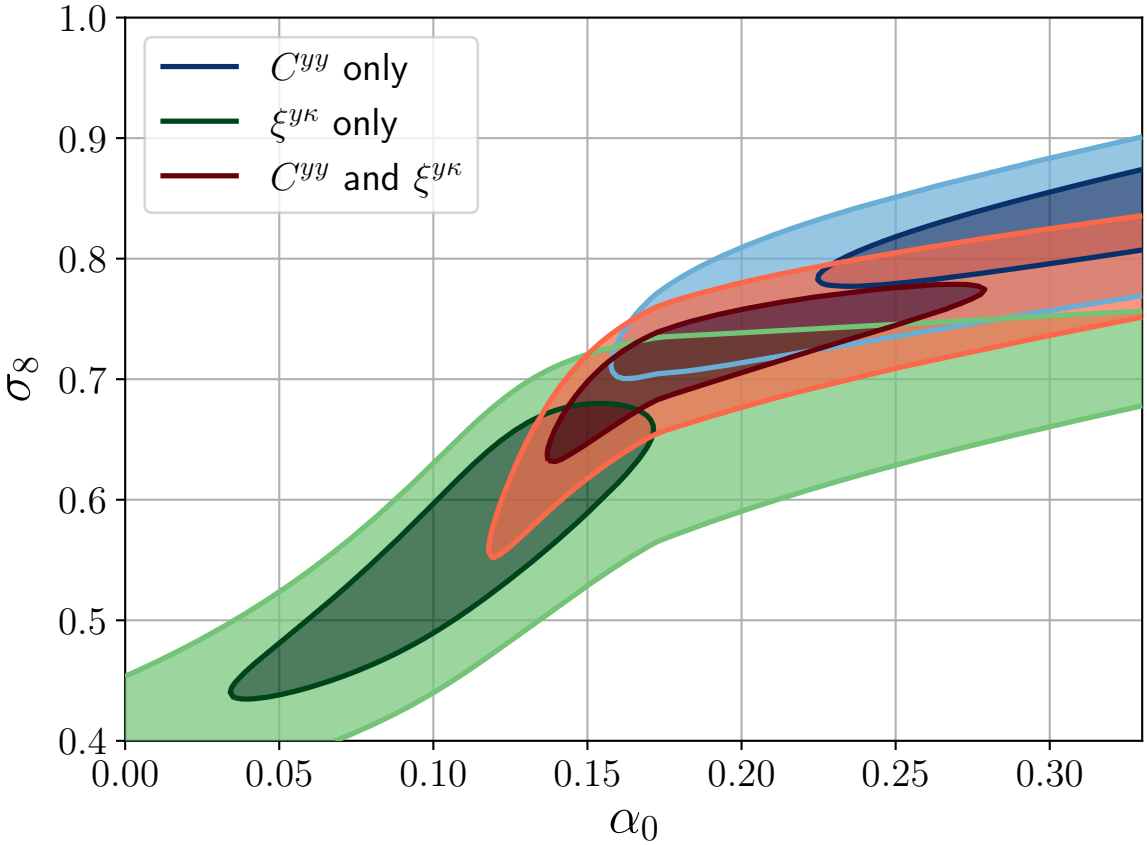

Figure 6.11: Posterior distributions of non-thermal pressure parameters α_0 and σ_8 with $S_* = 0.7$. The inner (outer) colored region correponds to 1-σ (2-σ) confidence region. The results with data sets of power spectra and cross-correlations, power spectra only, and cross-correlations only are shown in solid red, blue, and green regions, respectively.

6.5 Conclusions

The tSZ effect probes the thermal properties of the hot, ionized gas in the Universe, while the WL signal reflects mostly the dark matter distribution, and is thus less affected by baryonic physics. Current and future CMB and galaxy redshift surveys enable measurements of these observables, which can be used to infer astrophysical and cosmological information. The first detections of the tSZ-WL cross-correlation have been recently reported in Van Waerbeke et al. (2014); Hill & Spergel (2014); Hojjati et al. (2017). The cross-correlation can be a valuable probe in addition to tSZ and WL alone, as it can help break parameter degeneracies.

In this work, we have modeled the tSZ-WL cross-correlation using the halo model approach. We have modeled the pressure profile following the semi-analytic ICM model (Shaw model) from Flender et al. (2017), as well as the universal pressure profile calibrated against observations (Planck Collaboration, 2013). In order to estimate the covariance matrix, we have produced mock tSZ and WL maps. For WL, we employ the ray-tracing technique to generate mock maps of the convergence field. For tSZ, we follow the approach from Roncarelli et al. (2007), painting the signal into the halos in the simulation.

We constrain the free parameters in our model, taking into account measurements of the tSZ power spectrum from *Planck* (Planck Collaboration, 2016c), as well as measurements of the tSZ-WL cross-correlation from RCSLenS and *Planck* (Hojjati et al., 2017). With the observationally calibrated universal pressure profile from Planck Collaboration (2013), and leaving σ_8 as the only free parameter, we find that the tSZ data alone prefers $\sigma_8 = 0.785^{+0.029}_{-0.043}$, consistent with the value of 0.76 found in Planck Collaboration (2016c). However, the value for σ_8 becomes lower when taking into account the tSZ-WL cross-correlation. With the cross-correlation alone we find $\sigma_8 = 0.677^{+0.046}_{-0.077}$, and with the combined data $\sigma_8 = 0.746^{+0.026}_{-0.038}$.

We repeat the analysis using the pressure profile from the Shaw model from Flender et al. (2017), leaving the amplitude of non-thermal pressure, α_0, and σ_8 as free parameters. Here, we find that the tSZ power spectrum prefers $\alpha_0 \sim 0.3$ and $\sigma_8 \sim 0.85$, while the tSZ-WL cross-correlation prefers a significantly lower α_0 of ~ 0.05 and $\sigma_8 \sim 0.6$ (see Figure 6.6). Ignoring the small scales (< 10 arcmin) in the analysis seems to alleviate the tension (see Figure 6.7).

Another way to alleviate the tension between the two data sets is to consider modifications in the gas model. We find that allowing for a steep slope in the stellar-to-halo-mass relation, $S_* = 0.7$, results in posterior distributions from the two data sets that are less in tension (see Figure 6.11), pointing towards enhanced star formation in low-mass halos. With the combined data, we find that a model with $\sigma_8 \sim 0.7$ and $\alpha_0 \sim 0.2$ is preferred.

The tSZ power spectrum and the tSZ-WL cross-correlation are exciting new probes of cluster astrophysics and cosmology. Upcoming imaging surveys, such as *Euclid* and LSST, and CMB experiments, such as ACTPol, SPT-3G, and CMB-Stage IV, will enable more precise measurements of these observables, especially at smaller scales than the ~ 10 arcmin size of the *Planck* beam, which currently limits the resolution of our analysis. If future data confirm the tension seen here with higher significance, we might derive interesting conclusions about the gas physics of groups and clusters, such as enhanced

star formation, i.e., reduced gas content in low-mass halos. Another possibility would be to derive constraints on the shape of the pressure profile (see, Battaglia et al., 2017).

Chapter 7

Measurements of Cross-Correlations of WL and tSZ with Subaru Hyper Suprime-Cam and *Planck*

Contents

Here, we present measurements of the cross-correlation function of convergence and Compton-y with WL measurement of first year data of the Hyper Suprime-Cam (HSC) survey and *Planck* tSZ result. With this cross-correlation measurement, deep observations by the HSC survey realize high source galaxy density and enable us to probe into structures at high redshifts ($z \gtrsim 1$). For predictions of cross-correlations and power spectra, we employ the halo model prescription with the universal pressure profile. For better estimation of the covariance matrix beyond Gaussian approximation, we utilize the all-sky mock simulations and develop the method to reproduce the gas distribution from the simulations to create realistic mock WL and tSZ maps. We can incorporate the systematic effects due to survey geometry and discrete distributions of WL source galaxies. With Markov Chain Monte-Carlo (MCMC) technique, we constrain the cosmological parameters along with hydrostatic bias parameter, which reflects the fraction of non-thermal pressure support in galaxy clusters. In addition to the cross-correlation, we make use of the analysis of the tSZ auto-power spectra by *Planck* (Planck Collaboration, 2016d; Bolliet et al., 2018) and impose priors on cosmological parameters from HSC cosmic shear analysis (Hikage et al., 2018) or *Planck* CMB results (Planck Collaboration, 2018a). Thus, we can address the tension of σ_8 and the non-thermal pressure contribution at high redshifts, which is complementary to the analysis with RCSLenS and *Planck*.

7.1 Introduction

In the previous Chapter, we presented the analysis of the cross-correlations with RCSLenS and *Planck*. There, constraints on the two parameters are considered: the amplitude of the matter power spectrum σ_8 and the amplitude of the non-thermal pressure support α_0 in the Shaw model. Here, for non-thermal pressure, we focus on the hydrostatic bias parameter in the universal pressure profile, which determines the ratio between the total mass and the mass supported only by the thermal pressure, because the physical meaning is simple and fundamental. Furthermore, the hydrostatic bias is measured for nearby massive clusters in WL mass calibration measurements (see, e.g., Miyatake et al., 2018), where the mass is estimated both from WL and SZ measurements, and it is assumed that WL measurements give unbiased estimate of the total mass. Both of the mass calibration measurements and hydrodynamical simulations suggest that the fraction of the non-thermal pressure support is 10–30%. However, the results of SZ cluster count (Planck Collaboration, 2016e) and the tSZ power spectrum (Planck Collaboration, 2016d) imply higher non-thermal pressure support around 40%. This discrepancy may come from the different range of probed scales of mass or redshift. Though only nearby massive clusters are detected in mass calibration measurements, less massive and distant halos can contribute in tSZ power spectrum. The HSC survey has the advantage of the low limiting magnitude, and can probe structures at high redshifts ($z \gtrsim 1$), which are not well studied in previous studies.

We also extend the cosmological parameter space from only σ_8 to full standard pa-

rameters: baryon and CDM densities, Hubble parameter, the tilt and amplitude of power spectrum of the scalar perturbation. Since the CDM density and Hubble parameter also affects the power spectrum and cross-correlations, these parameters should be taken into account. However, only with power spectrum and cross-correlations, constraining power on cosmological parameters is weak. Therefore, we include priors on cosmological parameters from HSC cosmic shear analysis (Hikage et al., 2018) or *Planck* CMB results (Planck Collaboration, 2018a) to obtain reasonable and converged results.

This Chapter is organized as follows. In Section 7.2, we review the basics of WL analysis from shape catalog in the HSC survey. We present the measurement and analysis of the tSZ effect with *Planck* data in Section 7.3. In Section 7.4, we present the mock simulations of WL and tSZ created from all-sky N-body simulations. In Section 7.5, the measurement of the cross-correlations from HSC and *Planck* is presented. We show results of the constraints on cosmological parameters and hydrostatic bias parameter in Section 7.6, and discuss the results in Section 7.7. We conclude in Section 7.8.

7.2 Weak Lensing Analysis with HSC S16A Data

Here, we overview the WL analysis with the HSC survey.

7.2.1 Weak Lensing Shape Catalog

The HSC survey is the ongoing optical imaging survey (Aihara et al., 2018). Here, we use the internal data release of the first year observation, which is labelled as S16A. The HSC S16A survey region is split into six patches: GAMA15H, WIDE12H, GAMA09H, VVDS, XMM, and HECTOMAP, and the total area coverage is $136.9\,\mathrm{deg}^2$ with a mean i-band seeing of $0.58''$. The galaxy shapes are estimated from the co-added i-band images with the re-Gaussianization method (Hirata & Seljak, 2003) and calibrated with image simulations in Mandelbaum et al. (2018b). The shape catalog contains > 12 million galaxies after conservative source selection, e.g., $S/N \geq 10$ and $i \leq 24.5$, and the mean number density is $n_g = 24.6\,\mathrm{arcmin}^{-2}$.

7.2.2 Reconstruction of the Convergence Field

Here, we present analysis of the weak lensing shape catalog (Mandelbaum et al., 2018a). We employ the reconstruction method of Kaiser & Squires (1993) and follow the analysis for HSC S16A shape catalog in Oguri et al. (2018). The shear is estimated from shape catalogs as

$$\hat{\gamma}_\alpha(\boldsymbol{\theta}) = \frac{\sum_i w_i(\gamma_\alpha(\boldsymbol{\theta}_i) - c_{\alpha,i})W(|\boldsymbol{\theta} - \boldsymbol{\theta}_i|)}{\sum_i w_i(1+m_i)W(|\boldsymbol{\theta} - \boldsymbol{\theta}_i|)}, \tag{7.1}$$

where w_i is the lens weight, $\gamma_\alpha(\boldsymbol{\theta}_i)$ is the local shear estimated as $\gamma_\alpha(\boldsymbol{\theta}_i) = e_{\alpha,i}/2\mathcal{R}$ with the galaxy shape ellipticity $e_{\alpha,i}$ and shear responsivity $\mathcal{R}$, and $W(\boldsymbol{\theta})$ is the Gaussian

smoothing function:

$$W(\theta) = \frac{1}{\pi\theta_s^2} \exp\left(-\frac{\theta^2}{\theta_s^2}\right), \tag{7.2}$$

and $c_{\alpha,i}$ and m_i is the additive and multiplicative biases, which are calibrated in Mandelbaum et al. (2018b). For smoothing scale θ_s, we adopt $\theta_s = 0.2'$ following Oguri et al. (2018). Then, we convert the shear field to the convergence field as

$$\hat{\kappa}(\boldsymbol{\theta}) = \frac{1}{\pi} \int d^2\theta' \frac{\gamma_{\rm t}(\boldsymbol{\theta}|\boldsymbol{\theta}')}{|\boldsymbol{\theta} - \boldsymbol{\theta}'|^2}, \tag{7.3}$$

where $\gamma_{\rm t}(\boldsymbol{\theta}|\boldsymbol{\theta}')$ is the tangential shear at the position $\boldsymbol{\theta}$ with respect to $\boldsymbol{\theta}'$.

In the practical analysis, we adopt the flat-sky approximation. First, we compute the pixelized shear field on the regular grid with the pixel size of $0.5'$ for each patch of the survey regions. Then, we apply fast Fourier transform (FFT) to the shear field and compute the Fourier transform of convergence field as

$$\hat{\kappa}(\boldsymbol{\ell}) = \frac{(\ell_1 + i\ell_2)^2}{\ell^2} \hat{\gamma}(\boldsymbol{\ell}). \tag{7.4}$$

Then, the convergence field is obtained by the inverse FFT. Though the convergence field should be the real function, the resultant field may have imaginary part (see Section 3.4.1). The real and imaginary parts are called as E-mode and B-mode convergence, respectively. In the subsequent analysis, we use only E-mode convergence, which we simply call convergence field, and the B-mode will be used for null tests.

We also compute smoothed number density field:

$$n(\boldsymbol{\theta}) = \sum_i W(|\boldsymbol{\theta} - \boldsymbol{\theta}_i|). \tag{7.5}$$

In order to remove the effects due to boundary and low density pixels, we mask the pixel where the number density is less than the half of the mean number density. We show resultant convergence maps in Figure 7.1.

7.2.3 Source Redshift Distributions

For predictions of cross-correlations, we need information of redshifts of source galaxies. Since HSC can detect faint galaxies due to high sensitivity, the resultant galaxy sample has higher redshifts compared with existing optical surveys. There are a number of algorithms to estimate the photometric redshifts of source galaxies (for details, see Tanaka et al., 2018). We use the `Ephor_AB` code reweighted with COSMOS 30-band observations as the fiducial model, but the different algorithms give consistent results within a few per cent for calculations of cross-correlations.

7.3 The All-Sky Compton-y Map from *Planck*

The Compton-y map is constructed from 30 to 857 GHz channel maps of *Planck* full mission data with component separation algorithm (Planck Collaboration, 2016d). The

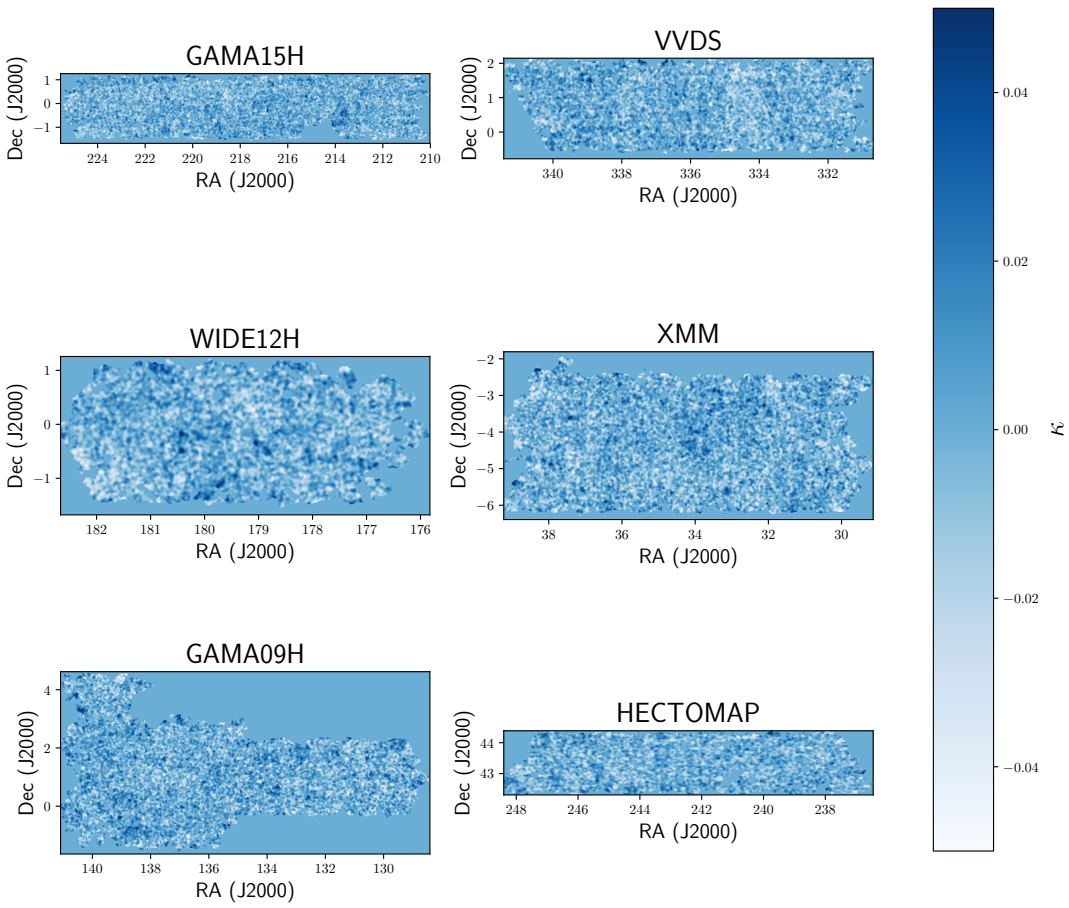

Figure 7.1: The convergence maps from the HSC S16A shape catalog. The survey regions are split into six patches:GAMA15H, WIDE12H, GAMA09H, VVDS, XMM, and HECTOMAP.

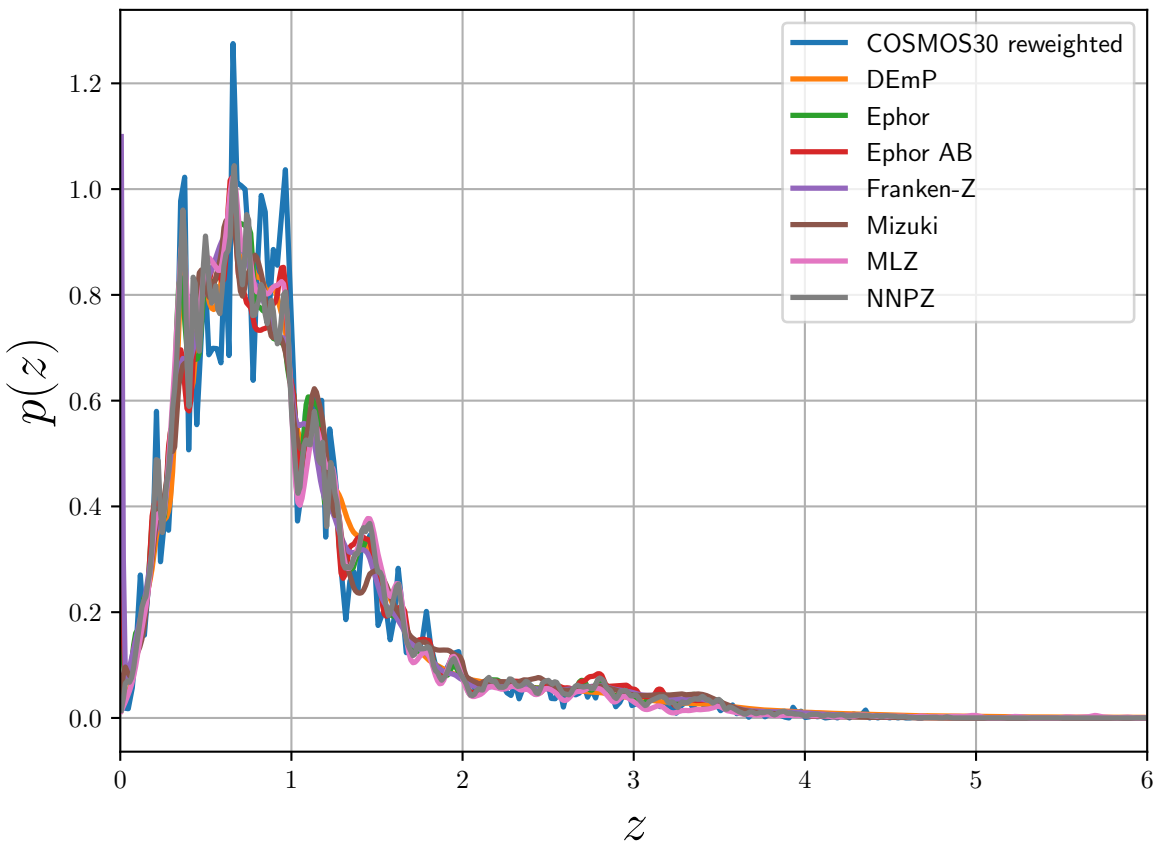

Figure 7.2: The stacked redshift distributions of source galaxies for different methods: `Ephor_AB` reweighted with COSMOS 30-band observations, `DEmP`, `Ephor`, `Ephor_AB`, `Franken-Z`, `Mizuki`, `MLZ`, and `NNPZ`.

map is pixelized in `Healpix` (Górski et al., 2005) format with $N_{\rm side} = 2048$. The *Planck* team provides maps with two different component separation algorithm: MILCA (Modified Internal Linear Combination Algorithm) and NILC (Needlet Independent Linear Combination), which basically try to find the linear combination of several components so that the variance of the reconstructed map is minimized. Hereafter, we use the map constructed with MILCA as the fiducial map because it has lower noise contribution at large scales. We show the MILCA Compton-y map in Figure 7.3.

In this study, we also utilize the measurement of tSZ auto-power spectrum. In order to avoid contaminations originating from systematics, the full mission data are separated by half, and the cross-power spectrum between the separated first and last maps is used as a baseline power spectrum.

In order to incorporate the foreground effects, we adopt the model proposed in Bolliet et al. (2018). The total power spectrum is given as

$$C_{yy} = C_{\rm tSZ} + A_{\rm CIB}C_{\rm CIB} + A_{\rm RS}C_{\rm RS} + A_{\rm IR}C_{\rm IR} + A_{\rm CN}C_{\rm CN}, \tag{7.6}$$

where $C_{\rm tSZ}$ is the contribution from tSZ, which can be computed from the halo model, and the rest of terms are templates for foreground: cosmic infrared background (CIB), radio sources (RS), infrared point sources (IR), and correlated noise (CN). Here, we introduce the nuisance parameters $A_{\rm CIB}$, $A_{\rm RS}$, $A_{\rm IR}$, and $A_{\rm CN}$ to vary the amplitudes of foreground contributions. Since the power at the highest multipole $\ell = 2472$ is dominated by the CN term, the amplitude is determined as $A_{\rm CN} = C_{yy}(\ell = 2472)/C_{\rm CN}(\ell = 2472) = 0.903$. Table 6.1 shows the total power spectrum, contribution from resolved clusters, and foreground templates (Bolliet et al., 2018). We also impose the physical upper bound with the power spectrum from resolved clusters $C_{\rm RC}$; the foreground contribution should not exceed the residual contribution, i.e.,

$$A_{\rm CIB}C_{\rm CIB} + A_{\rm RS}C_{\rm RS} + A_{\rm IR}C_{\rm IR} + A_{\rm CN}C_{\rm CN} < C_{yy} - C_{\rm RC}. \tag{7.7}$$

At each step of MCMC, the amplitudes should satisfy this relation.

7.4 Mock Simulations

In this Section, we present mock simulations used to estimate the covariance matrix of cross-correlations and auto-power spectrum of tSZ.

7.4.1 All-Sky Mock Compton-y Map

We generate mock tSZ map from the all-sky halo catalog of Takahashi et al. (2017). In the simulations, cosmological parameters are adopted from *WMAP* 9 years results (Hinshaw et al., 2013): the CDM density parameter $\Omega_{\rm CDM} = 0.233$, the baryon density parameter $\Omega_{\rm b} = 0.046$, the matter density parameter $\Omega_{\rm m} = \Omega_{\rm CDM} + \Omega_{\rm b} = 0.279$, the cosmological constant density $\Omega_\Lambda = 0.721$, the scaled Hubble constant $h = 0.7$, the amplitude of the matter power spectrum $\sigma_8 = 0.82$, and the spectral index of the scalar perturbation $n_{\rm s} =$

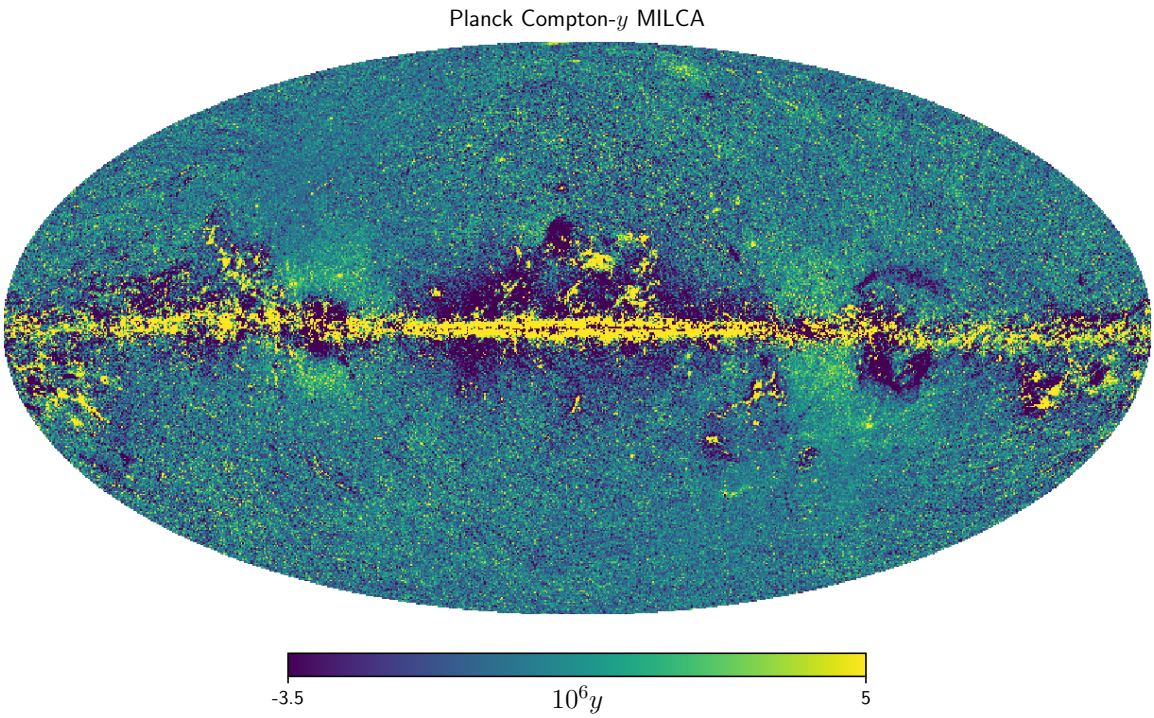

Figure 7.3: Compton-y map reconstructed from the *Planck* data with MILCA method (Planck Collaboration, 2016d).

$\ell_{\rm min}$	$\ell_{\rm max}$	$\ell_{\rm eff}$	$10^{12}D_{yy}$	$10^{12}D_{\rm RC}$	$10^{12}D_{\rm CIB}$	$10^{12}D_{\rm RS}$	$10^{12}D_{\rm IR}$	$10^{12}D_{\rm CN}$
9	12	10.0	0.00508	0.000421	0.000000	0.000043	0.000007	0.000001
12	16	13.5	0.00881	0.000710	0.000000	0.000142	0.000024	0.000001
16	21	18.0	0.01363	0.001251	0.000000	0.000296	0.000048	0.000002
21	27	23.5	0.02961	0.002837	0.000000	0.000400	0.000073	0.000004
27	35	30.5	0.02241	0.003933	0.000902	0.000541	0.000111	0.000006
35	46	40.0	0.02849	0.005969	0.002010	0.001056	0.000224	0.000010
46	60	52.5	0.04276	0.010318	0.003119	0.001647	0.000449	0.000018
60	78	68.5	0.04580	0.014045	0.006278	0.002787	0.000837	0.000030
78	102	89.5	0.07104	0.024061	0.012242	0.004306	0.001400	0.000052
102	133	117.0	0.11914	0.032976	0.021584	0.006842	0.002701	0.000089
133	173	152.5	0.15150	0.047100	0.045915	0.011264	0.004721	0.000153
173	224	198.0	0.19390	0.062380	0.070582	0.016744	0.008115	0.000262
224	292	257.5	0.28175	0.081730	0.119786	0.027345	0.014618	0.000456
292	380	335.5	0.39837	0.101911	0.211686	0.043275	0.024893	0.000815
380	494	436.5	0.56743	0.117412	0.332863	0.070587	0.051570	0.001503
494	642	567.5	0.76866	0.132234	0.434931	0.115356	0.107293	0.002934
642	835	738.0	1.11010	0.143214	0.602030	0.154926	0.197053	0.006334
835	1085	959.5	1.66140	0.156202	0.754733	0.207200	0.361713	0.016171

Table 7.1: The tSZ auto-power spectrum measured in the *Planck* mission (Planck Collaboration, 2016d) and reanalyzed in Bolliet et al. (2018). The first three columns show the minimum, maximum, and medium, or effective, of multipole bins. D_{yy}, $D_{\rm RC}$, $D_{\rm CIB}$, $D_{\rm RS}$, $D_{\rm IR}$, and $D_{\rm CN}$ correspond to the amplitudes of power spectrum of total contributions, resolved clusters, cosmic infrared background, radio source, infrared source, and correlated noise, respectively. The power spectrum amplitude D_ℓ is defined as $\ell(\ell+1)/(2\pi)C_\ell$.

0.97. From the halo catalog, we construct the all-sky tSZ map based on the halo-based pasting method (see Section 5.2.2.2) with the universal pressure profile with $b_{\rm HSE} = 0.42$, which is the best-fit value in the reanalysis of the *Planck* tSZ measurement (Bolliet et al., 2018). First, we create 108 mock tSZ maps from the halo catalog. Then, we add the detector noise, which is assumed to be white noise. After adding the noise, we smooth the tSZ map with the circular Gaussian window function with the full-width half-mean $\theta_{\rm FWHM} = 10'$, which corresponds to the Gaussian window scale $\theta_s = \theta_{\rm FWHM}/(2\sqrt{\log 2}) = 6.0'$. The noise power spectrum is given as

$$N_\ell = 2\pi\theta_s^2\sigma_y^2, \tag{7.8}$$

where $\sigma_y = 1.5 \times 10^{-6}$ is the variance of the noise distribution estimated from 1D PDF analysis (Khatri & Sunyaev, 2015; Dolag et al., 2016). Finally, we apply the galactic and radio point source masks provided by the *Planck* mission (Planck Collaboration, 2016d). The sky coverage fraction after masking is $f_{\rm sky} = 0.49$. Figure 7.4 shows one of the mock all-sky tSZ maps.

We deconvolve mask spectrum from the pseudo-spectrum with `MASTER` algorithm (Hivon et al., 2002). The relation between psuedo-power spectrum and true power spectrum can be given as

$$\tilde{C}_\ell = \sum_{\ell'} M_{\ell\ell'} B_{\ell'}^2 C_{\ell'} + \tilde{N}_{\ell'}, \tag{7.9}$$

where $\tilde{C}_\ell$ denotes the pseudo-power spectrum directly measured from tSZ map, $\tilde{N}_\ell$ is the noise pseudo-power spectrum, $M_{\ell\ell'}$ is the mode-coupling matrix, and B_ℓ is the window function describing smoothing effects of the beam and finite pixelization. The noise pseudo-power spectrum is

$$\tilde{N}_\ell = \frac{N_\ell}{4\pi} \sum_{\ell=0} \mathcal{W}_\ell (2\ell+1), \tag{7.10}$$

and the mode-coupling matrix is

$$M_{\ell_1\ell_2} = \frac{2\ell_2+1}{4\pi} \sum_{\ell_3} (2\ell_3+1)\mathcal{W}_{\ell_3} \begin{pmatrix} \ell_1 & \ell_2 & \ell_3 \\ 0 & 0 & 0 \end{pmatrix}^2, \tag{7.11}$$

where the last term is the Wigner-3j symbol. Then, we invert Eq. (7.9) to obtain the true power spectrum from the psuedo-power spectrum.

Figure 7.5 shows auto-power spectra of Compton-y from 108 mock all-sky Compton-y maps. The mock spectrum can reproduce the halo model results, but the discrepancy can be seen at small scales ($\ell \gtrsim 800$) because the simulations cannot resolve halos $\sim 10^{13}\,{\rm M}_\odot$ which contribute to the signal at this scale. However, at such scales, the errors due to incomplete separation dominate, and the discrepancy does not affect covariance estimation.

7.4.2 HSC Mock Shape Catalog

In order to create mock convergence maps for the HSC survey, we employ the mock HSC shape catalog (Shirasaki et al., 2019). The mock catalog is prepared for the HSC

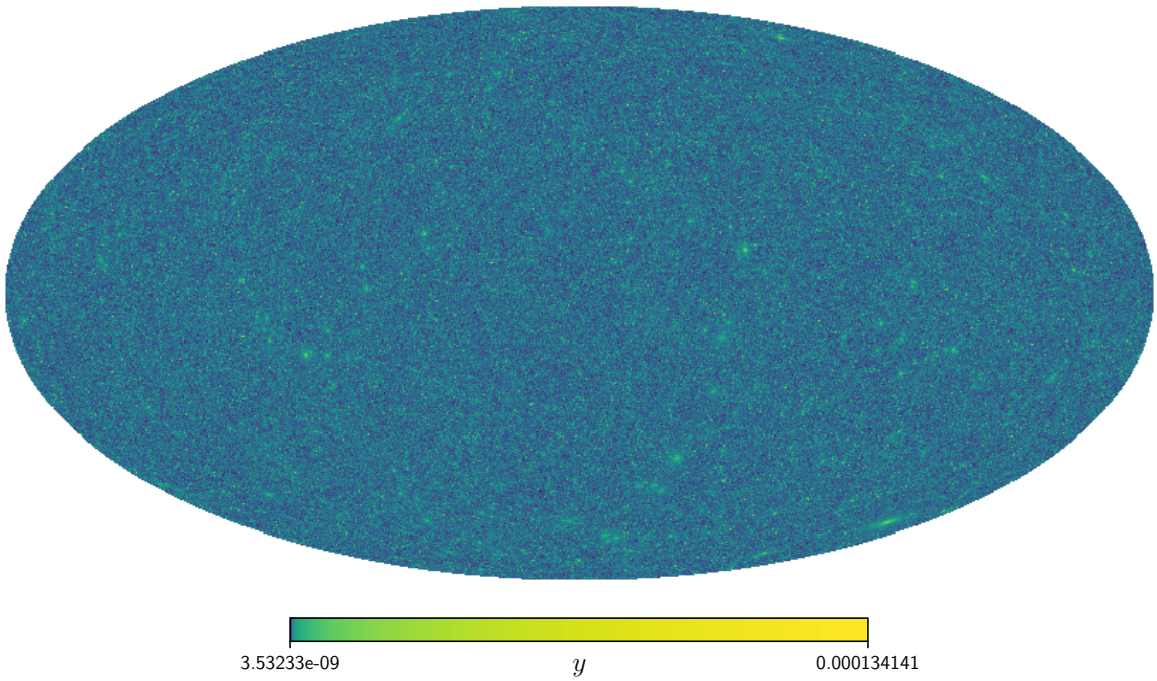

Figure 7.4: The mock Compton-y map reconstructed from all-sky halo catalogs based on halo-based pasting method with universal pressure profile with $b_{\rm HSE} = 0.42$.

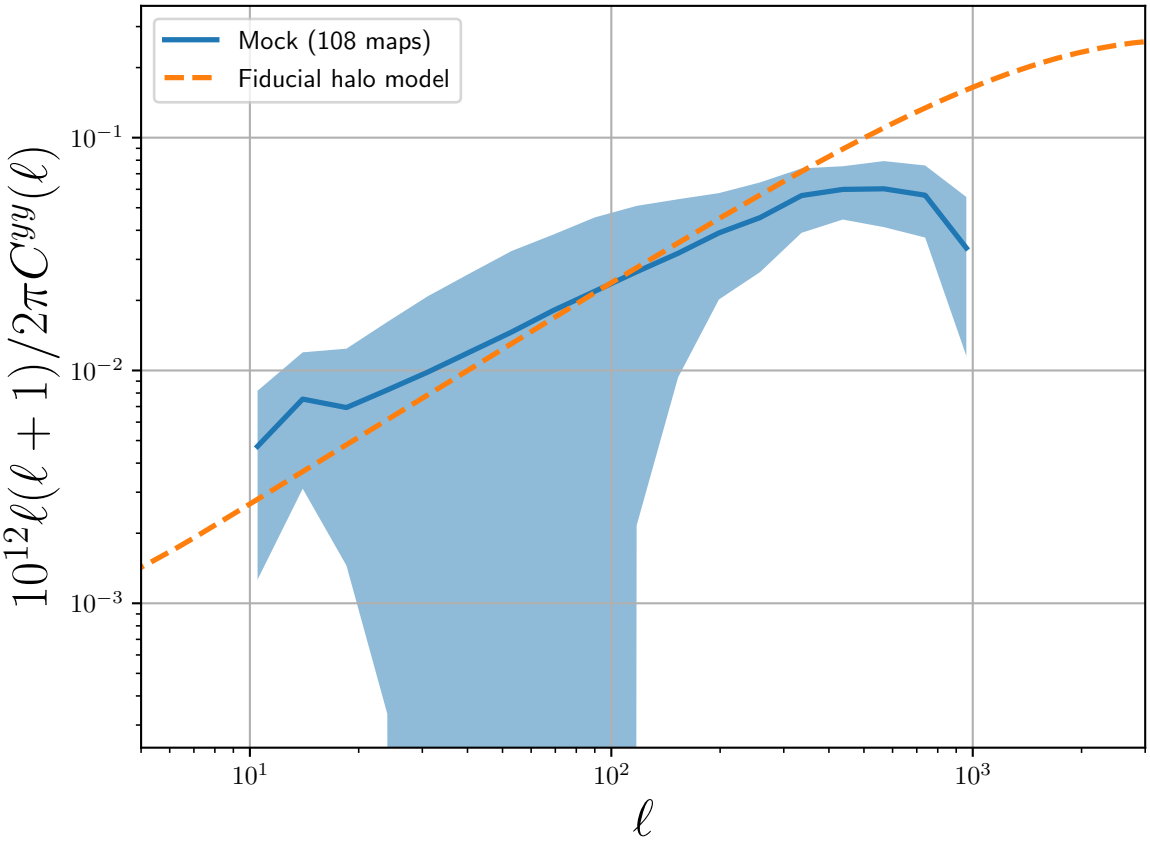

Figure 7.5: The power spectra measured from 108 mock tSZ maps. The shaded region corresponds to the standard deviation among 108 maps. The dashed line corresponds to the result based on halo model with universal pressure profile.

survey and constructed directly from the S16A shape catalog, and the same cosmological parameters in all-sky simulations presented in the previous Section are adopted. First, we randomly rotate the shapes of all galaxies in the catalog to remove the lensing signal. Then, we take the all-sky lensing map (Takahashi et al., 2017), and deform the shape again according to the shear and convergence at the position of each galaxy. As a result, we can obtain the mock catalogs which contain the lensing signal and systematic effects, e.g., discrete distribution of source galaxies and photometric redshift distribution.

The HSC S16A survey region is divided into 6 patches, which cover $136.9\,\mathrm{deg}^2$ in total, and Figure 7.6 shows convergence maps created from mock shape catalogs. Then, we can extract 21 HSC regions from one realization of the all-sky map, and we compute the cross-correlation from these maps for $108 \times 21 = 2268$ realizations. Figure 7.7 shows cross-correlations obtained from 2268 mock maps.

7.5 Measurements of the Cross-Correlations of tSZ and WL

7.5.1 Measurements with HSC and *Planck* Data

We measure the cross-correlation signal with the estimator,

$$\hat{\xi}(\theta) = \frac{\sum_{i,j} \kappa(\boldsymbol{\theta}_i) y(\boldsymbol{\theta}_j) B(|\boldsymbol{\theta}_i - \boldsymbol{\theta}_j|, \theta_b)}{\sum_{i,j} B(|\boldsymbol{\theta}_i - \boldsymbol{\theta}_j|; \theta_b)}. \tag{7.12}$$

The function B denotes the binning scheme:

$$B(\theta; \theta_b) = \begin{cases} 1 & (\theta_b - \Delta\theta/2 < \theta < \theta_b + \Delta\theta/2) \\ 0 & (\text{otherwise}), \end{cases} \tag{7.13}$$

where the range of bins is $0' < \theta_b < 40'$ with equally spaced bins and the number of bins is $N_b = 8$, i.e., $\Delta\theta = 5'$. Instead of cross-power spectrum, we employ the cross-correlations because we can incorporate the masking effect in a straightforward way. In Figure 7.8, the measurement of the cross-correlation function for each patch in HSC S16A is shown. The chi-square with respect to the null detection is $\chi^2 = 48.1$.

7.5.2 Null Tests

In order to confirm the cross-correlation signal is significant and is not spurious due to systematic effects, we measure the cross-correlation of Compton-y map and auxiliary maps of B-mode, PSF, and stars. The systematic error on the shape measurement is

$$e_{\mathrm{sys}} = \tilde{\alpha} e_{\mathrm{p}} + \tilde{\beta} e_{\mathrm{q}}, \tag{7.14}$$

where e_{p} is the PSF shape, and e_{q} is residual PSF at the positions of reserved stars, i.e., $e_{\mathrm{q}} \equiv e_{\mathrm{p}} - e_{\mathrm{star}}$. Then, we reconstruct the convergence fields from e_{p} and e_{q}, and compute

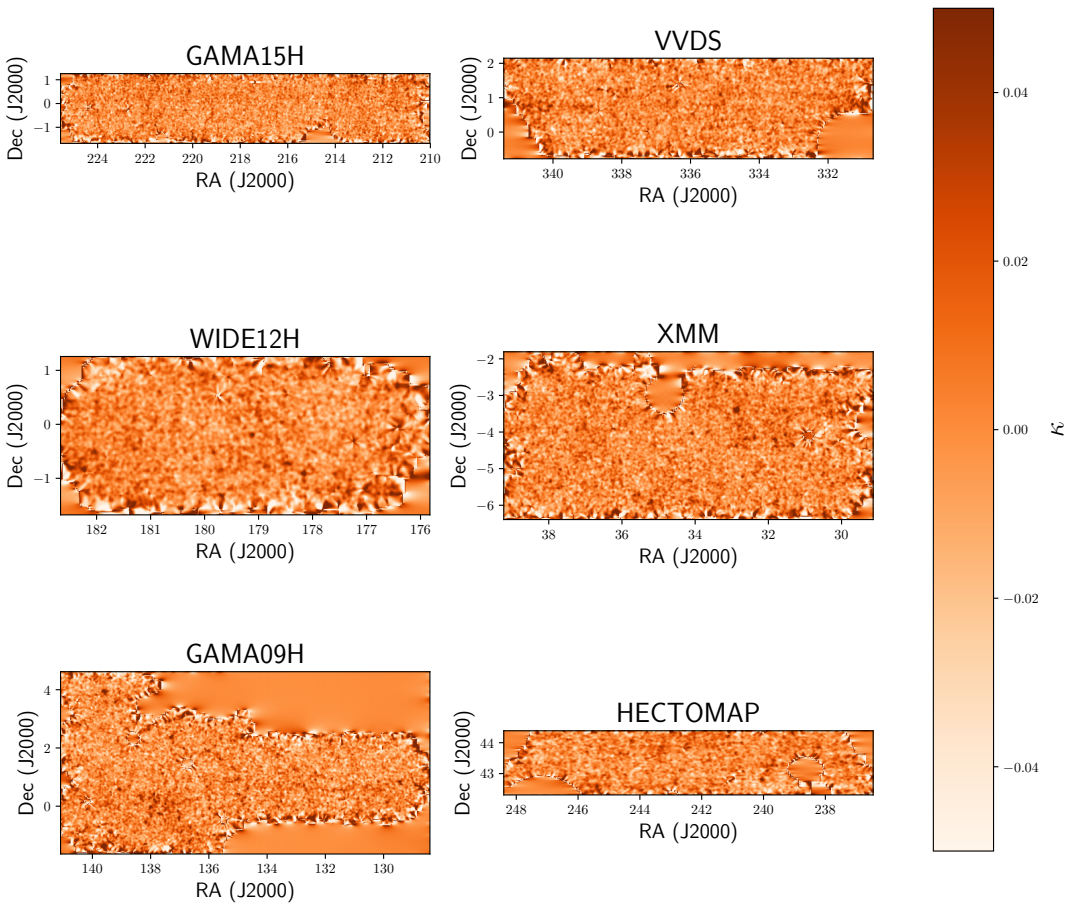

Figure 7.6: The convergence maps from the mock shape catalog. The survey regions are split into six patches:GAMA15H, WIDE12H, GAMA09H, VVDS, XMM, and HECTOMAP.

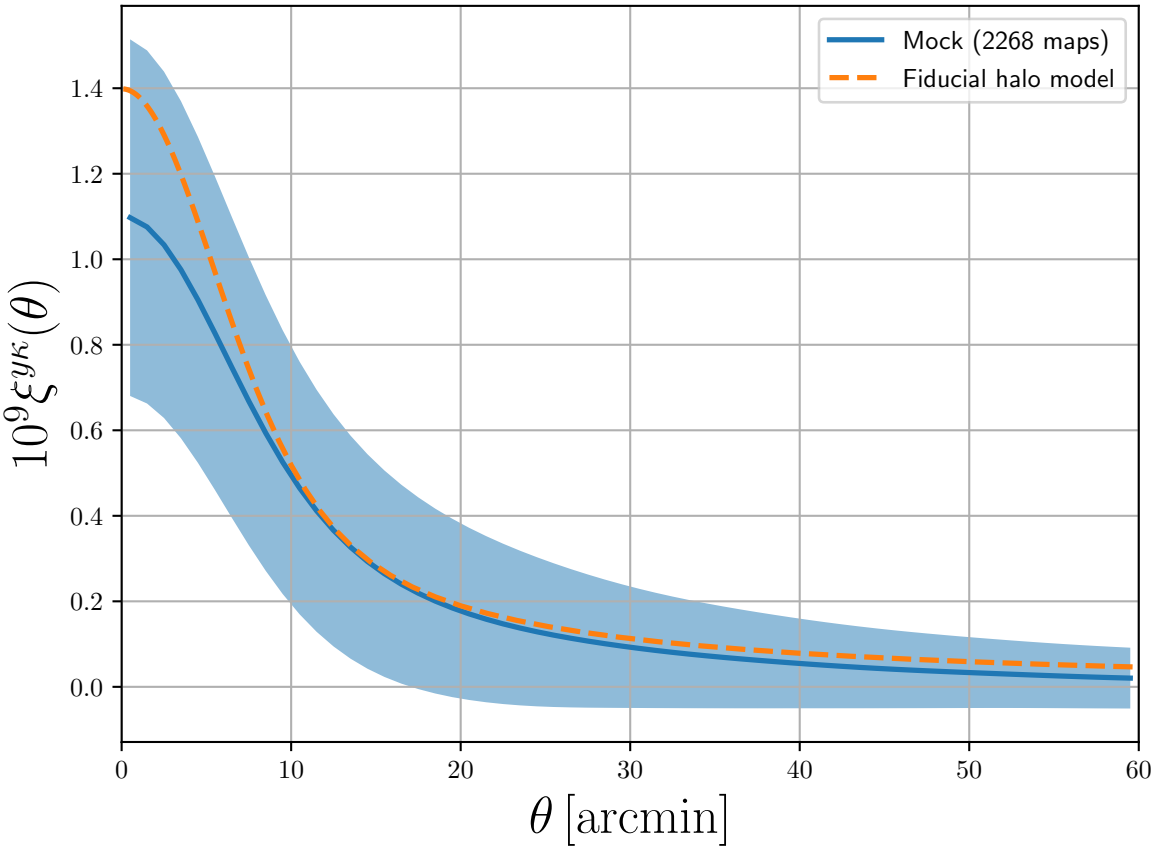

Figure 7.7: The cross-correlations of WL and tSZ measured from 2268 mock maps. The shaded region corresponds to the standard deviation among 2268 maps. The dashed line corresponds to the result based on halo model with universal pressure profile.

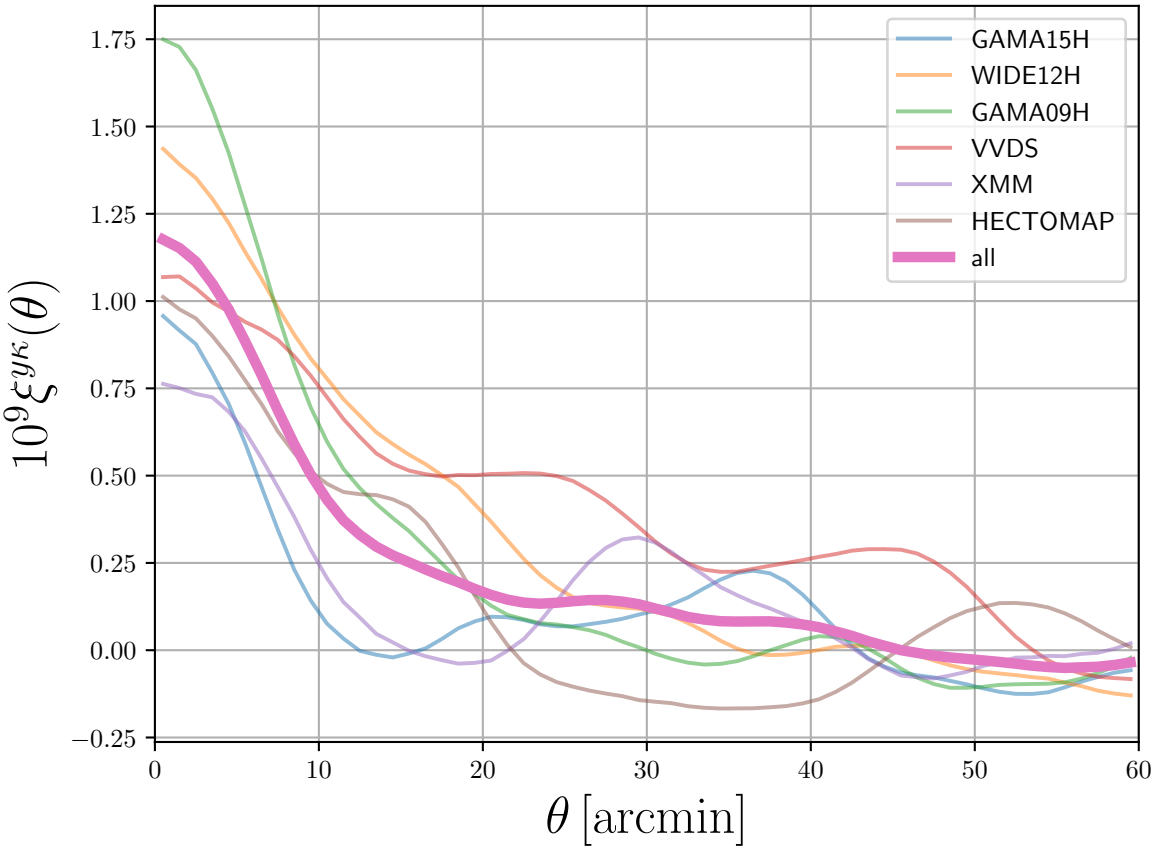

Figure 7.8: The cross-correlation function with HSC and *Planck* measurements. The each thin line corresponds to the result for each patch in the HSC survey. For all patches, the positive correlation can be observed.

corresponding cross-correlation functions $\xi^{y\mathrm{p}}$ and $\xi^{y\mathrm{q}}$. For amplitudes for PSF leakage and PSF residual, we adopt the best-fit value in Hikage et al. (2018),

$$\tilde{\alpha} = 0.057, \ \tilde{\beta} = -1.22. \tag{7.15}$$

We show the cross-correlation measurements between Compton-y and convergence fields from B-mode, PSF leakage, and PSF residual in Figure 7.9. It is clear that E-mode convergence is correlated with Compton-y map but no coherent signals can be seen for other maps.

7.5.3 Contributions from Resolved Clusters

In order to estimate the contributions from clusters which have already been detected in HSC S16A footprints, we repeat the measurement with the additional mask covering the detected clusters. We use the cluster catalog in Medezinski et al. (2018), which contains 5 clusters located within the HSC footprints and the SZ signals have already been detected by *Planck*. The locations, redshifts, and masses which are inferred by fitting the WL signal with the NFW profile are shown in Table 7.2. We mask the regions within the angular extent $\theta_{200} = R_{200}/D_A(z)$ for each cluster, where $D_A(z)$ is the angular diameter distance. In Figure 7.10, we show the cross-correations with and without the mask of cluster regions. The difference between two signals corresponds to the contribution from massive clusters which are detected by *Planck*. Accordingly, the massive clusters can contribute to the signal by at most $\sim 20\%$, and thus the rest of signal comes from the unresolved, i.e., low-mass, halos. Hence, the cross-correlations contain the information from low-mass halos, which are not easily accessible from other observables.

7.6 Constraints on Cosmological Parameters and Hydrostatic Bias

Here, we present the analysis for constraining cosmological parameters and hydrostatic bias parameter b_{HSE} with MCMC technique.

7.6.1 Posterior Distribution of Parameters

In this analysis, we use the measurements of cross-correlations with HSC and *Planck* and tSZ auto-power spectrum from *Planck* in order to constrain cosmological parameters and hydrostatic bias parameter b_{HSE}. Only with these two statistics, the constraining power in the high dimensional parameter space is so weak that it is not practical to obtain converged MCMC chains. Hence, we add priors on cosmological parameters from HSC cosmic shear analysis (Hikage et al., 2018) or *Planck* CMB results (Planck Collaboration, 2018b).

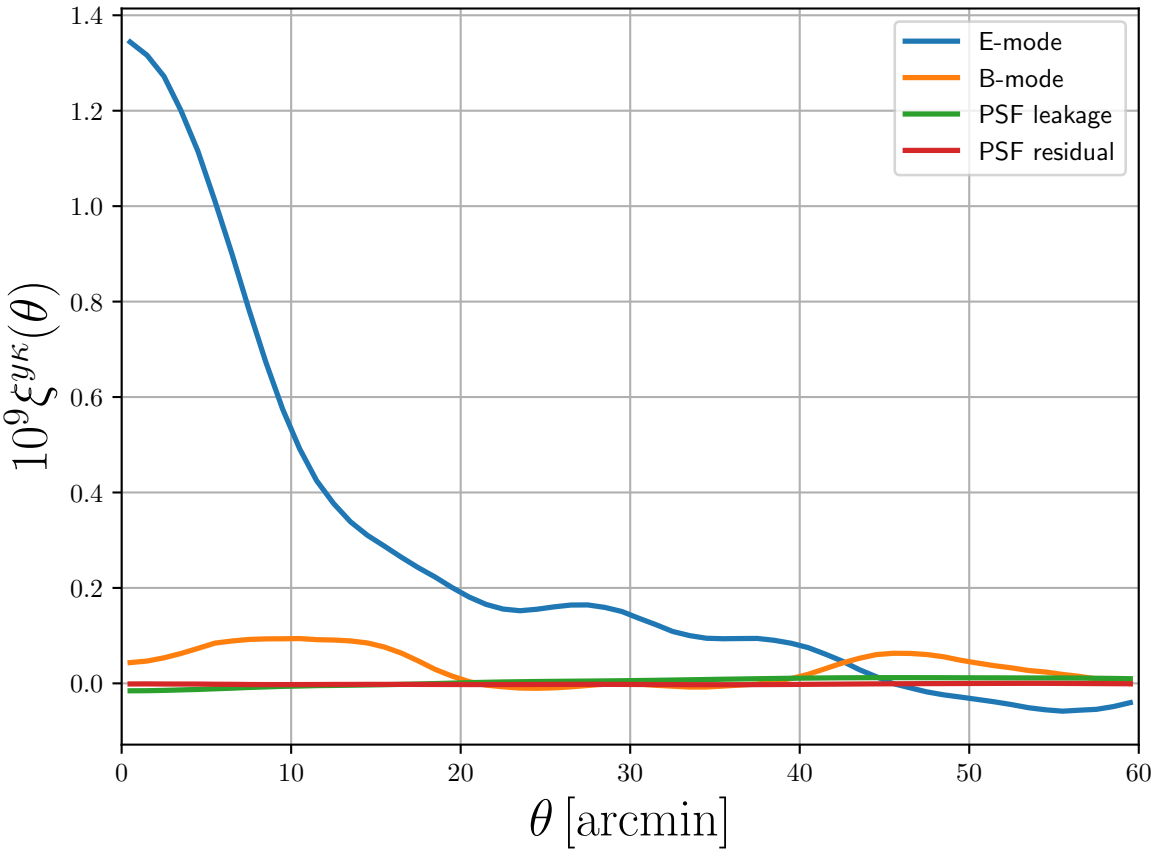

Figure 7.9: The null tests for cross-correlation measurements. For E-mode convergence, significant signals can be detected, but for B-mode covergence and reconstructed fields from PSF leakage $e_{\rm p}$ and PSF residual $e_{\rm q}$, there are almost no signals at all scales.

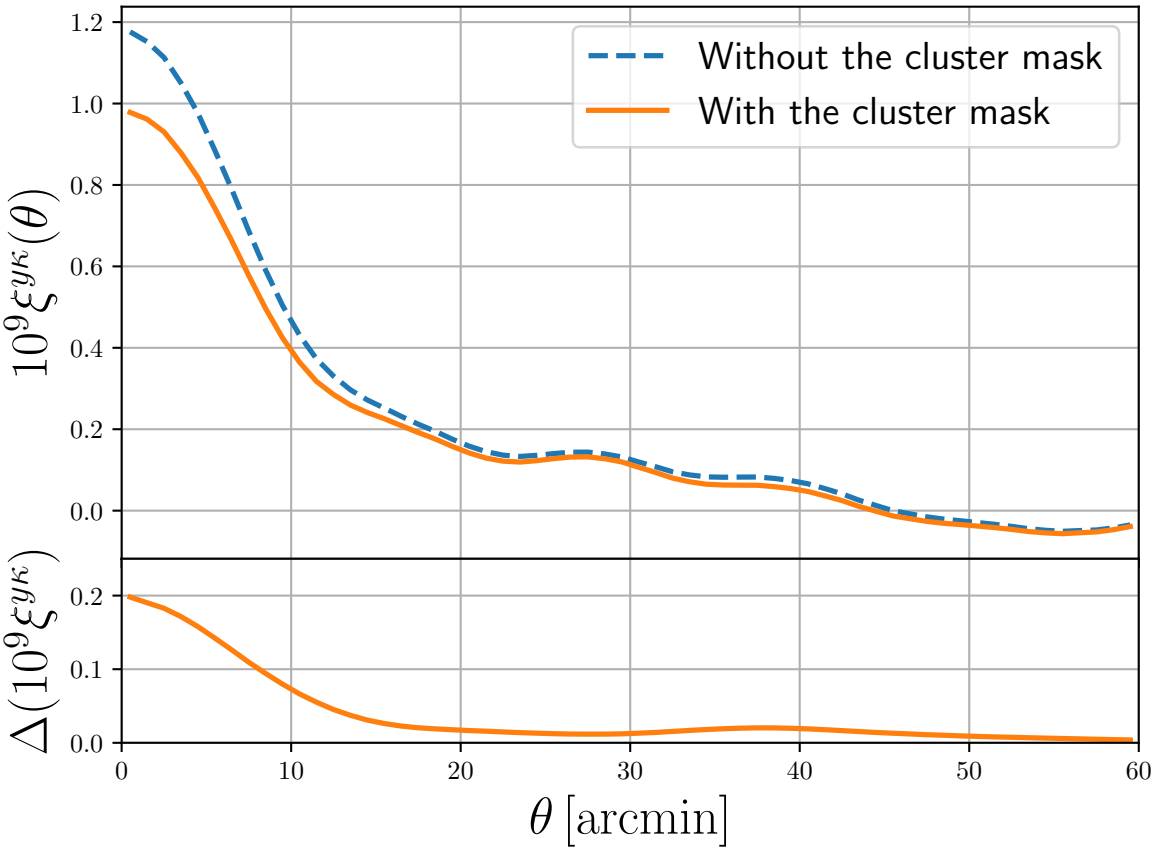

Figure 7.10: The cross-correlation function with (solid line) and without (dashed line) the additional mask of 5 *Planck*-SZ selected clusters (Medezinski et al., 2018). The lower panel shows the difference between the two signals, which corresponds to the contribution from the clusters.

First, we define the data vector as

$$N_C = (C^{yy}(\ell_1), \ldots, C^{yy}(\ell_{n_C})), \tag{7.16}$$
$$N_\xi = (\xi^{y\kappa}(\theta_1), \ldots, \xi^{y\kappa}(\theta_{n_\xi})), \tag{7.17}$$
$$N = (N_C, N_\xi), \tag{7.18}$$

where $n_C = 18$ and $n_\xi = 8$ are the number of bins in auto-power spectrum and cross-correlation, respectively. The bins for angular separation is equally spaced and its range is

$$0' \leq \theta \leq 40'. \tag{7.19}$$

For multipole, the binning is shown in Table 7.1, and we use the power spectrum in the range of

$$10.0 \leq \ell \leq 959.5, \tag{7.20}$$

where we do not use the largest multipole bin $\ell_{\rm eff} = 1247.5$ in auto-power spectrum because the mock simulations are not accurate at this scale due to the resolution. From the mock measurements, we estimate covariance matrix,

$$\mathrm{Cov}_{ij} = \frac{1}{R-1}\sum_{r=1}^{R}(N_i^r - \bar{N}_i)(N_j^r - \bar{N}_j), \tag{7.21}$$

where R is the number of realizations, $\bar{N}$ is the sample mean of R measurements, and $r = 1, \ldots, R$ denotes the label of the realization. There are $R = 108$ maps for mock Compton-y, and $R = 2268$ maps for mock convergence. As a result, we have 108 and 2268 measurements of auto-power spectrum and cross-correlations, respectively. For estimation of cross-covariance between auto-power spectrum and cross-correlation, we additionally generate 2268 maps for Compton-y by rotating the coordinates to adjust the one in mock convergence map. These additional mock Compton-y maps are used solely for cross-covariance estimation.

The likelihood $\mathcal{L}$ is assumed to be multivariate Gaussian as

$$\log \mathcal{L}(\boldsymbol{p}) = -\frac{1}{2}\sum_{i,j}(\hat{N}_i - N_i(\boldsymbol{p}))\mathrm{Cov}_{ij}^{-1}(\hat{N}_j - N_j(\boldsymbol{p})) + \mathrm{const.}, \tag{7.22}$$

where $\hat{N}$ is the measurement, $N(\boldsymbol{p})$ is the prediction based on the halo model, and $\boldsymbol{p}$ is the parameter vector, which includes cosmological parameters and hydrostatic bias. The parameter vector is composed of physical baryon density $\omega_{\rm b} \equiv \Omega_{\rm b}h^2$, physical CDM density $\omega_{\rm c} \equiv \Omega_{\rm c}h^2$, scaled Hubble parameter h, tilt and amplitude of the scalar perturbation $n_{\rm s}$ and $\ln(10^{10}A_{\rm s})$, and the hydrostatic mass bias parameter $b_{\rm HSE}$. Only with auto-power spectrum and cross-correlations, the constraining power is weak, and it is hard to obtain converged results. Therefore, we add priors on cosmological parameters from external measurements. Such data include the results of *Planck* of TT,TE,EE+lowE dataset (Planck Collaboration, 2018a), TT,TE,EE+lowE+lensing dataset (Planck Collaboration, 2018b), and HSC cosmic shear analysis (Hikage et al., 2018). Hence, the posterior distribution $\mathcal{P}$ is given as

$$\log \mathcal{P}(\boldsymbol{p}) = \log \mathcal{L}(\boldsymbol{p}) + \log P(\boldsymbol{p}) + \mathrm{const.} \tag{7.23}$$

For priors on cosmological parameters, we assume the Gaussian form as

$$\log P(\boldsymbol{p}) = -\frac{1}{2}\sum_{\alpha,\beta}(p_\alpha - \bar{p}_\alpha)C^{-1}(p_\alpha, p_\beta)(p_\beta - \bar{p}_\beta) + \text{const.}, \tag{7.24}$$

where the mean $\bar{\boldsymbol{p}}$ and the covariance matrix $C(p_\alpha, p_\beta)$ are estimated from MCMC chains. For the prior on hydrostatic bias, we adopt a flat prior with the range of 0 and 1. We utilize the Affine invariant Markov chain Monte-Carlo code `emcee` (Foreman-Mackey et al., 2013) to obtain chains for the posterior distribution.

7.6.2 Constraints on Cosmological Parameters and Hydrostatic Mass Bias

We show constraints of parameters with tSZ auto-power spectrum and WL-tSZ cross-correlations for different priors in Figures 7.11, 7.12, and 7.13. The constraints on cosmological parameters become tighter than those only from priors because additional information is provided by the auto-power spectrum and cross-correlation, and these statistics help to break the parameter degeneracy. On the other hand, hydrostatic bias is not determined by the prior information, and it is necessary to employ statistics related with tSZ. We can obtain the lower value < 0.1 for the bias with the HSC prior and higher value ≈ 0.4 for the *Planck* priors, because the bias parameter is degenerate with matter density and the amplitude of matter power spectrum. For the HSC prior, the inferred value of matter density is lower than that from *Planck* priors. As a result, the difference propagates to the estimation of the bias parameter in this analysis.

In Figure 7.14, the constraints on the matter density $\Omega_{\rm m}$ and the amplitude of matter power spectrum σ_8 are shown. There is a clear tension between the results with HSC and *Planck* priors, which corresponds to the σ_8 tension between low-redshift and high-redshift observations (see, e.g., Battye et al., 2015). It is still difficult to completely mitigate the tension even if the current statistics are considered.

7.7 Discussions

Here, we discuss the implications of the results, especially the constraints on the hydrostatic bias. As we have seen in the previous Section, the constraints on the bias parameter strongly depend on priors, or the value of $\Omega_{\rm m}$. Here, we focus on the result with *Planck* prior because previous works of mass calibration measurements and hydrodynamical simulations also adopt *Planck* cosmology or similar one. We compare the results of constraints on the hydrostatic bias from mass calibration measurements of galaxy clusters in Figure 7.15. Though the error bars are quite large, mass calibration measurements show hydrostatic bias 10–30% for detected clusters. These values are consistent with the results from hydrodynamical simulations (Suto et al., 2013; Shi et al., 2016). On the other hand, the analysis of the power spectrum of tSZ (Bolliet et al., 2018) shows higher hydrostatic bias $\sim 40\%$, which corresponds to the large fraction of non-thermal pressure.

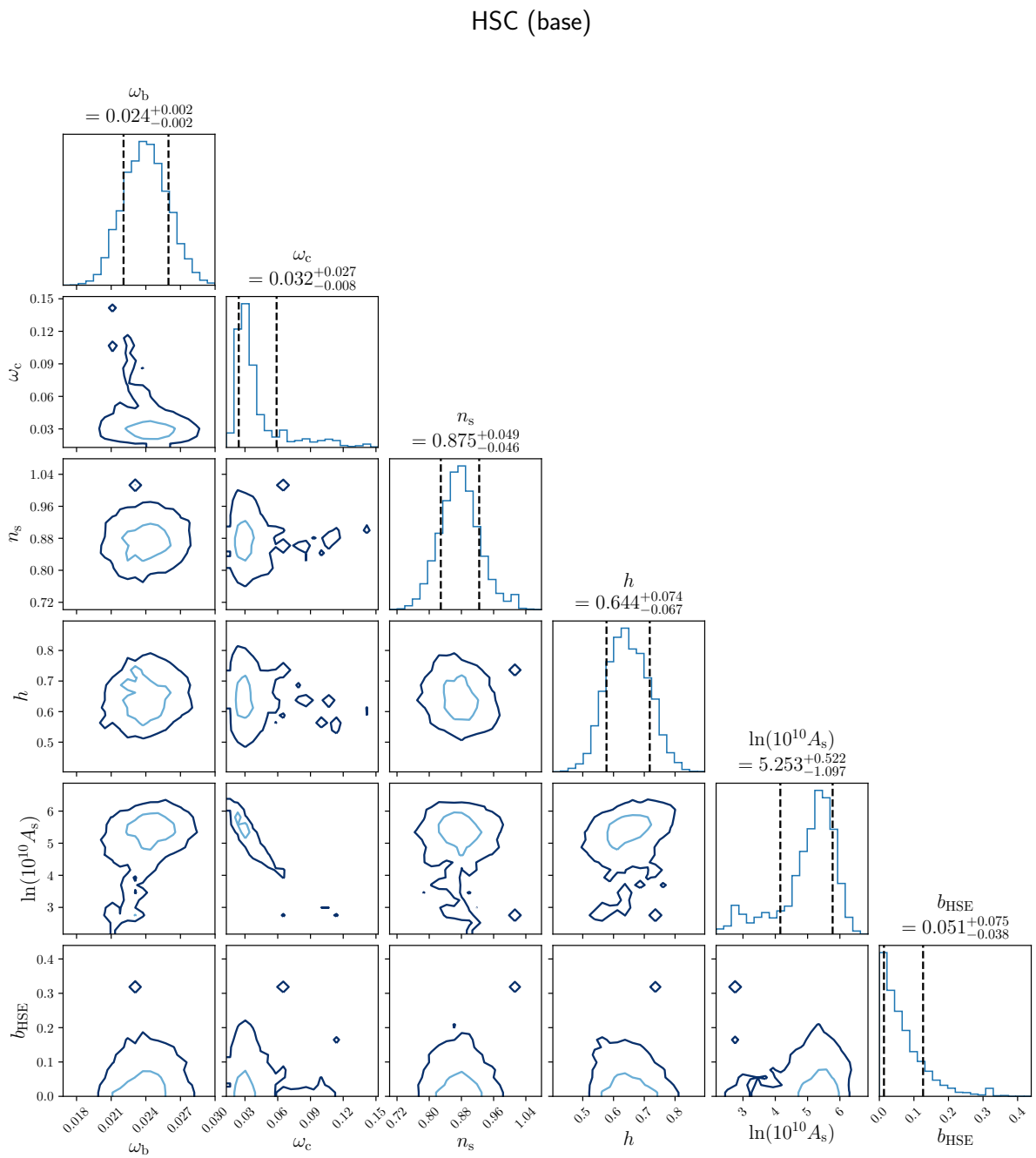

Figure 7.11: Constraints on parameters from tSZ auto-power spectrum and WL-tSZ cross-correlation with priors from HSC cosmic shear (Hikage et al., 2018). The light (dark) solid line corresponds to the 1-σ (2-σ) confidence level.

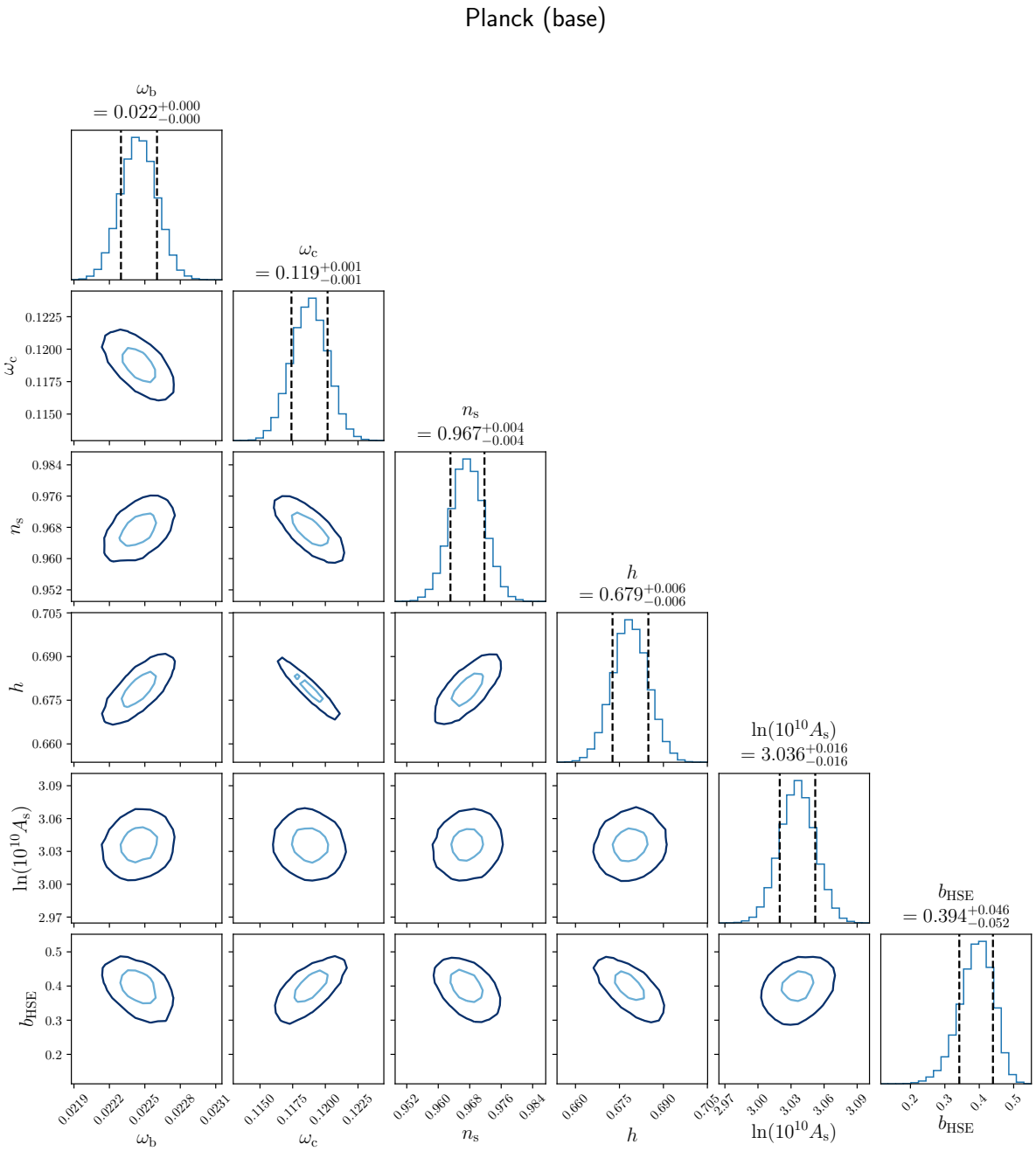

Figure 7.12: Constraints on parameters from tSZ auto-power spectrum and WL-tSZ cross-correlation with priors from *Planck* TT,TE,EE+lowE dataset (Planck Collaboration, 2018a). The light (dark) solid line corresponds to the 1-σ (2-σ) confidence level.

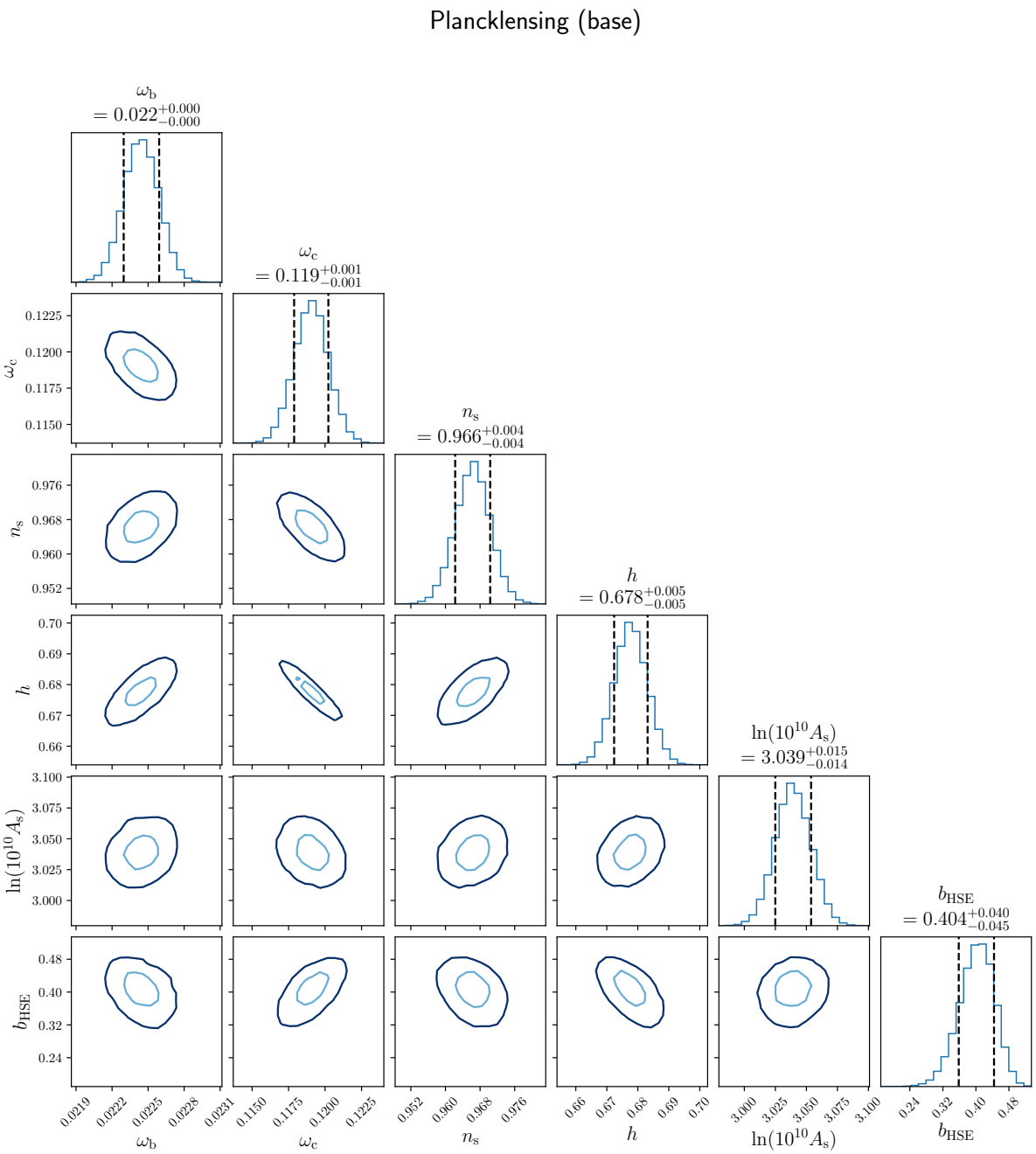

Figure 7.13: Constraints on parameters from tSZ auto-power spectrum and WL-tSZ cross-correlation with priors from *Planck* TT,TE,EE+lowE+lensing dataset (Planck Collaboration, 2018b). The light (dark) solid line corresponds to the 1-σ (2-σ) confidence level.

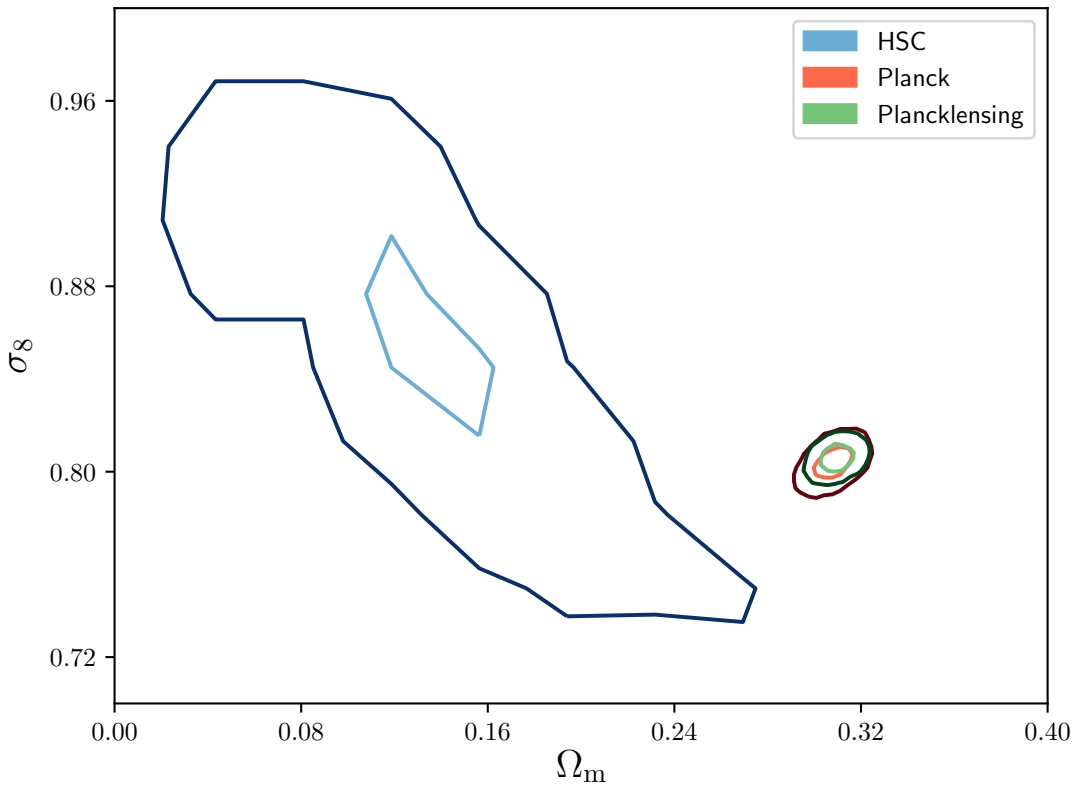

Figure 7.14: Constraints on the matter density Ω_m and the amplitude of the matter power spectrum σ_8. The blue, red, and green contours show the results with priors from HSC cosmic shear, *Planck* TT,TE,EE+lowE, and *Planck* TT,TE,EE+lowE+lensing datasets, respectively.

One of the possibilities to explain the discrepancy is the difference of sensitivity on mass and redshift scale for each measurement. Although the signal of tSZ power spectrum comes from halos of the wide range of mass (see, e.g., Makiya et al., 2018), mass calibration measurements probe only into massive clusters. Thus, our results imply higher non-thermal pressure support for less massive galaxy clusters or galaxy groups, instead of redshift evolution of the hydrostatic mass bias.

Another possibility to mitigate the discrepancy between our results and mass calibration measurements is the incomplete separation in constructing Compton-y map, although there is large uncertainty on the contribution. When constructing Compton-y map from raw temperature map, various contaminants, e.g., CIB or radio sources, can distort the true signal. In the analysis of the power spectrum, we have already incorporated the systematic effects due to auto-power spectra of CIB, radio sources, etc. based on Bolliet et al. (2018). However, it has been reported that the cross-power spectrum between CIB and tSZ also contributes to the total power spectrum (Addison et al., 2012). Furthermore, Shirasaki (2019) argues that the cross-corelation of tSZ and emission from CIB or radio sources can be a negative contribution. The dominant terms of these effects are almost scale independent and lead to significant changes of the amplitude of the cross-correlations. Hence, the negative correlation leads to the lower value of hydrostatic bias, and the contribution alleviates the discrepancy. The accurate modeling of the radio sources and CIB will be addressed in future works.

7.8 Conclusions

We present measurements of cross-correlations of WL and tSZ from HSC S16A and *Planck* data. For WL, we reconstruct the convergence field from HSC S16A shape catalog (Mandelbaum et al., 2018a), which covers $136.9\,\mathrm{deg}^2$ with the mean number density $n_g = 24.6\,\mathrm{arcmin}^{-2}$. For tSZ, we make use of the Compton-y map based on MILCA algorithm from 30 to 857 GHz channel maps of *Planck* data. For accurate estimation of covariance matrix, we develop a method to create mock all-sky WL and tSZ maps from N-body simulations (Takahashi et al., 2017). The various systematic effects, e.g., survey masks and discrete distribution of source galaxies, are incorporated in a natural way. For predictions of auto-power spectrum and cross-correlation, we use the halo model prescription with the universal pressure profile. For calibration of the universal pressure profile, the clusters are assumed to be in HSE, and thus the true mass may be larger than the estimated mass under HSE because the turbulent motion can also support the self-gravity of galaxy clusters. In order to take into account the non-thermal pressure support, we introduce the hydrostatic mass bias parameter b_{HSE}, and rescale the mass in the universal pressure profile. We also develop a method to create mock all-sky tSZ maps from halo catalogs of N-body simulations. We also add the detector noise and apply Gaussian smoothing and the survey mask. Thus, the realistic mock tSZ maps are obtained and used for estimation of covariance matrix. In addition to mock tSZ maps, we also utilize the mock shape catalog, which is created from the HSC S16A shape catalog. Using the N-body simulations, which are also used for creating mock tSZ maps,

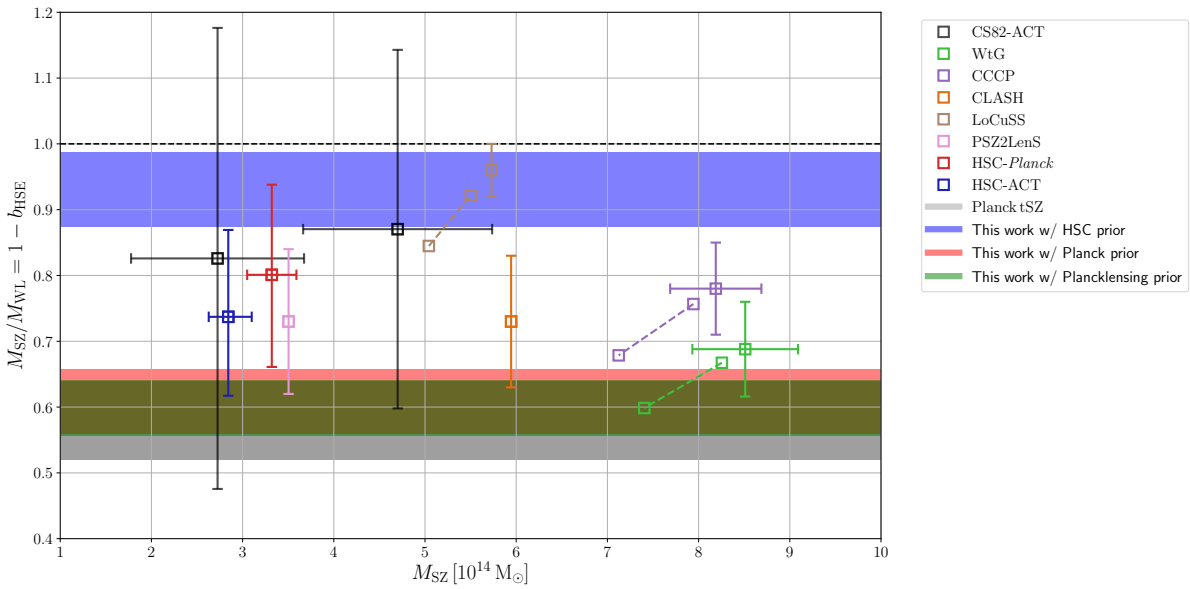

Figure 7.15: Constraints on the hydrostatic mass bias parameter $b_{\rm HSE}$ from the analysis of auto-power spectrum and cross-correlations and cluster mass calibration measurements. Since all halos regardless of their mass contribute to the auto-power spectrum and cross-correlations, results from these statistics are shown as belts. The mass calibration measurements are HSC-ACT (Miyatake et al., 2018), CS82-ACT (Battaglia et al., 2016), LoCuSS (Smith et al., 2016), CLASH (Penna-Lima et al., 2017), PSZ2LenS (Sereno et al., 2017), HSC-*Planck* (Medezinski et al., 2018), WtG (von der Linden et al., 2014), and CCCP (Hoekstra et al., 2015). The squares connected with dashed lines represent the values corrected by Eddington bias in the range of 3–15% calculated in Battaglia et al. (2016). The result of the re-analysis of tSZ power spectrum from *Planck* (Bolliet et al., 2018) is also shown.

the mock weak lensing signal is put on each galaxy shape. It enables one to take into account complex systematics specific to the observation. Then, we compute the auto-power spectrum and cross-correlation from the suite of mock maps, and estimate the covariance matrix.

With the measurement and the covariance matrix estimated from mock simulations, we perform the analysis to constrain the cosmological parameters and the hydrostatic bias parameter with tSZ auto-power spectrum and WL-tSZ cross-correlation. Only with the auto-power spectrum and cross-correlation, it is not practical to obtain the converged results due to weak constraining power. Hence, we add priors on cosmological parameters from HSC cosmic shear analysis (Hikage et al., 2018) and *Planck* CMB results (Planck Collaboration, 2018a,b). The constraints on the hydrostatic bias depend on the priors on cosmological parameters, especially dark matter density. In the case of *Planck* prior, which is adopted in most of previous works, we find high value of the hydrostatic bias parameter $\sim 40\%$. This result is consistent with tSZ power spectrum analysis (Bolliet et al., 2018), though our cross-correlation of tSZ and WL is sensitive to nearby structures compared with the case of tSZ power spectrum. Thus, it implies no redshift evolution for hydrostatic bias parameter. On the other hand, the discrepancy between mass calibration measurements might be explained by the mass dependence of the hydrostatic bias. Because both of tSZ power spectrum and tSZ-WL cross-correlations can probe into less massive halos ($M \lesssim 10^{14}\,\mathrm{M}_\odot$), which are not accessible both for mass calibration measurements and hydrodynamical simulations, the higher value of the hydrostatic bias can be realized by high non-thermal pressure support in such less massive halos. Since the HSC regions are limited to small sky coverage of $\sim 100\,\mathrm{deg}^2$, the constraint is not so tight, but for full sky coverage $\sim 1000\,\mathrm{deg}^2$, tighter constraints can be obtained, and it will be possible to probe into the redshift evolution of non-thermal pressure support via inference of hydrostatic bias by tomography technique.

Name in *Planck* SZ catalog	NED name	RA [deg]	Dec [deg]
PSZ2 G068.61-46.60	Abell 2457	338.91999	1.48489
PSZ2 G167.98-59.95	Abell 0329	33.67122	−4.56735
PSZ2 G174.40-57.33	Abell 0362	37.92156	−4.88258
PSZ2 G228.50+34.95	MaxBCG J140.53188+03.76632	140.54565	3.77820
PSZ2 G231.79+31.48	MACS J0916.1-0023/Abell 0776	139.03851	−0.40453

Redshift z	Mass M_{200} [$10^{14}\,h^{-1}\,\mathrm{M}_\odot$]	Angular extent θ_{200} [arcmin]
0.0594	2.02	19.43
0.1393	2.21	9.12
0.1843	4.12	8.79
0.2701	31.03	12.48
0.3324	8.10	6.75

Table 7.2: The catalog of SZ detected clusters by *Planck* which are located in HSC S16A footprints (Medezinski et al., 2018). The mass of clusters is inferred by fitting WL signal assuming the NFW profile. The positions of clusters are defined as those of brightest central galaxies.

Chapter 8

Conclusions

In modern observational cosmology, the concordance model, so-called ΛCDM model, which can remarkably explain the observational facts, has been established in the last decade. In Chapter 2, we presented reviews on the current picture of the Universe based on observational cosmology. The foundation of the current understanding of the Universe is owed to various cosmological observations. Among such observations, the anisotropy and polarization measurements of CMB, spectroscopic observations of galaxies, and weak gravitational lensing have played a central role in observational cosmology. In addition to these observables, the recent developments in telescopes and observational technique enable one to detect cosmological observables of which signal-to-noise-ratio is not high. For example, the thermal Sunyaev–Zel'dolvich effect and the Lyman-α forest can be detected. Since these observables trace the large-scale structures and can add independent information, we can place tighter constraints on cosmological parameters and test general relativity on a cosmological scale.

In this dissertation, we have focused on two major cosmological observables: weak gravitation lensing (WL) and the thermal Sunyaev–Zel'dovich effect (tSZ). First, the basics of gravitational lensing is presented in Chapter 3. WL probes into the large-scale structures in an unbiased way, and thus, WL is regarded as one of main science targets in ongoing and future imaging surveys. The statistics of WL have widely been used for constraining cosmological parameters. Among them, the amplitude of the matter power spectrum can be precisely determined due to the unbiased nature of WL. In Chapter 4, astrophysics of galaxy clusters with particular emphasis on the tSZ effect is reviewed. Since galaxy clusters are the most massive and bound objects in the Universe, they are ideal laboratories for energetic and violent dynamics, and the abundance is sensitive to the underlying cosmological models. One of the major advantages of tSZ is that since Compton-y parameter, which is the observable of tSZ effect, is the projected pressure field, it directly connects the fundamental thermodynamic quantities, e.g., thermal pressure or number density, to the observed quantity. The gas distribution, which can be traced with tSZ, reflects the large-scale structures, and we can use statistics of tSZ, e.g., power spectrum, to constrain cosmological parameters. It is found that the power spectrum of tSZ strongly depends on the amplitude of matter power spectrum. Though the signal-to-

noise-ratio of the measurements of tSZ is not so high compared with WL, it can provide additional information on cosmology, and can be a unique probe into astrophysics of galaxy clusters at high redshifts.

So far, cosmological analysis with WL and tSZ are well studied separately. However, since both WL and tSZ trace the large-scale structures, significant cross-correlations between them can be expected. The cross-correlation between WL and tSZ has been first reported by Van Waerbeke et al. (2014) using data from CFHTLenS and *Planck*. The power spectrum and cross-correlation can be well reproduced with the halo model prescription. For estimation of the covariance matrix, we develop a numerical method to create mock maps from N-body simulations. We presented the methodology to generate mock tSZ and WL maps from N-body simulations in Chapter 5. In Chapter 6, we apply our theoretical prediciton based on halo model and covariance matrix estimated from simulations to the cross-correlation measurement with the data of RCSLenS and *Planck* (Hojjati et al., 2017). We find that the amplitude of matter power spectrum and the amplitude of the non-thermal pressure support can be constrained with these statistics (Osato et al., 2018). There is a tension between tSZ auto-power spectrum and WL-tSZ cross-correlation. We show that this tension can be mitigated by modifying the pressure profile for group-size halos at high redshifts, which are not used for calibration of the parameters included in the modeling of pressure profile. Thus, the tension can be caused by the uncertainty for such unresolved halos. In order to probe the structures at high redshifts with the cross-correlations, we employ the data from Subaru Hyper Suprime-Cam (HSC) WL survey and the *Planck* mission and present the analysis of the measurement in Chapter 7. The HSC survey covers $136.9\,\mathrm{deg}^2$ in the first year data, and deeper observations are made possible due to high limiting magnitude. Thus, the obtained source galaxies have higher redshifts than those with other imaging surveys. With this data, we reconstruct the WL convergence field and measure the cross-correlations with the Compton-y parameter from the *Planck* measurement. For the analysis of this measurement, we apply the scheme to create mock observations to the all-sky N-body simulations. Hence, we can generate large sky coverage mock maps and incorporate the survey geometry and the discrete distribution of source galaxies. With the measurement and the covariance matrix, we constrain cosmological parameters and the hydrostatic mass bias parameter, which is the ratio between true mass and mass supported by the thermal pressure. It is known that the some fraction of mass of galaxy clusters is supported by turbulent and bulk motions. Accordingly, the hydrostatic mass is underestimated compared with the true mass. With the priors on cosmological parameters from HSC cosmic shear analysis or *Planck* CMB results, we place constraints on the hydrostatic mass bias parameter. The constraints on the bias depend on the priors, i.e., cosmological parameters. However, we find that the appreciable fraction of mass can be supported by the non-thermal pressure even at high redshifts and the resultant constraints are consistent with WL mass calibration measurements.

Our findings from the analysis of tSZ-WL cross-correlations can be summarized as follows.

- From the analysis of cross-correlation from RCSLenS and *Planck*, we find that the

tSZ power spectrum prefers $\alpha_0 \sim 0.3$, the non-thermal pressure fraction in the Shaw model, and $\sigma_8 \sim 0.85$, the amplitude of the matter power spectrum, while the tSZ-WL cross-correlation prefers a significantly lower α_0 of ~ 0.05 and $\sigma_8 \sim 0.6$.

- The tension above can be mitigated by allowing for a steep slope in the stellar-to-halo-mass relation, which corresponds to enhanced star formation in low-mass halos. This fact indicates that the tension is possibly caused by the uncertainty on the calibration against low-mass halos at high redshifts.

- We employ the WL measurement by the HSC survey, which enables deeper observations than RCSLenS. That is why we can probe into structures at higher redshifts with high precision. With the halo model prescription with the universal pressure profile and the covariance matrix estimated from all-sky N-body simulations, we constrain cosmological parameters and hydrostatic bias parameter with tSZ auto-power spectrum from *Planck* and tSZ-WL cross-correlations from *Planck* and HSC.

- In the case of *Planck* prior, the estimated hydrostatic bias parameter is consistent with tSZ auto-power spectrum analysis, though the cross-correlation and auto-power spectrum are sensitive to halos at different redshifts. This fact indicates the no redshift evolution in hydrostatic bias parameter.

- However, the estimated hydrostatic bias is higher than the values from WL mass calibration measurements. The discrepancy might be due to the difference of the probed mass scale. Only massive clusters are investigated in the mass calibration measurements. On the other hand, the appreciable fraction of tSZ auto-power spectrum and tSZ-WL cross-correlations come from low-mass halos. The higher value of the hydrostatic bias implies that non-thermal pressure support is more predominant in low-mass halos than massive halos.

The current constraints are limited by the small coverage of the HSC survey. However, the survey is still ongoing, and more data will be released in short timescale. For full sky coverage $\sim 1000\,\mathrm{deg}^2$, tighter constraints can be obtained. Furthermore, the high source galaxy number density in the HSC survey enables one to carry out the tomographic measurement of the cross-correlations. With this measurement, we can address redshift evolution of the hydrostatic mass bias parameter in more details. For the tSZ side, we are planning to employ the data with Atacama Cosmology Telescope (ACT), which angular resolutions is 1 arcmin. In the current analysis, we are restricted to constraints on simplified model parameters α_0 and b_{HSE} due to the large beam size 10 arcmin in *Planck*. The high resolution of ACT enables one to probe the fine structure of ICM, e.g., radial profile of non-thermal pressure. By refining the model of ICM, we can improve the constraints on cosmological parameters and investigate the mass and redshift evolution of the non-thermal pressure. In addition, previous works suggest that the cross-power or cross-correlation which arise from contaminants in Compton-y map reconstruction, e.g., cosmic infrared background or radio point sources, can contribute to the signal. That might distort the amplitude of the power spectrum or cross-correlation, and result in

bias in the estimated parameters. The further modeling of these contaminants will be addressed in future works.

Bibliography

Addison G. E., Dunkley J., Spergel D. N., 2012, Monthly Notices of the Royal Astronomical Society, 427, 1741

Aihara H., et al., 2018, Publications of the Astronomical Society of Japan, 70, S4

Allen S. W., Evrard A. E., Mantz A. B., 2011, Annual Review of Astronomy and Astrophysics, 49, 409

Amendola L., et al., 2013, Living Reviews in Relativity, 16, 6

Anderson L., et al., 2014, Monthly Notices of the Royal Astronomical Society, 441, 24

Angulo R. E., Pontzen A., 2016, Monthly Notices of the Royal Astronomical Society, 462, L1

Arnaud M., Pratt G. W., Piffaretti R., Böhringer H., Croston J. H., Pointecouteau E., 2010, Astronomy & Astrophysics, 517, A92

BOSS Collaboration 2015, Physical Review D, 92, 123516

Bacon D. J., Refregier A. R., Ellis R. S., 2000, Monthly Notices of the Royal Astronomical Society, 318, 625

Baltz E. A., Marshall P., Oguri M., 2009, Journal of Cosmology and Astro-Particle Physics, 2009, 015

Bardeen J. M., Bond J. R., Kaiser N., Szalay A. S., 1986, The Astrophysical Journal, 304, 15

Bartelmann M., Schneider P., 2001, Physics Reports, 340, 291

Battaglia N., Bond J. R., Pfrommer C., Sievers J. L., 2012, The Astrophysical Journal, 758, 75

Battaglia N., Hill J. C., Murray N., 2015, The Astrophysical Journal, 812, 154

Battaglia N., et al., 2016, Journal of Cosmology and Astro-Particle Physics, 2016, 013

Battaglia N., Ferraro S., Schaan E., Spergel D. N., 2017, Journal of Cosmology and Astroparticle Physics, 11, 040

Battye R. A., Charnock T., Moss A., 2015, Physical Review D, 91, 103508

Behroozi P. S., Wechsler R. H., Wu H.-Y., 2013, The Astrophysical Journal, 762, 109

Bennett C. L., et al., 2003, The Astrophysical Journal Supplement Series, 148, 1

Bernstein G. M., Jarvis M., 2002, The Astronomical Journal, 123, 583

Bhattacharya S., Heitmann K., White M., Lukić Z., Wagner C., Habib S., 2011, The Astrophysical Journal, 732, 122

Birkinshaw M., 1999, Physics Reports, 310, 97

Bocquet S., Saro A., Dolag K., Mohr J. J., 2016, Monthly Notices of the Royal Astronomical Society, 456, 2361

Bode P., Ostriker J. P., Vikhlinin A., 2009, The Astrophysical Journal, 700, 989

Boggess N. W., et al., 1992, The Astrophysical Journal, 397, 420

Böhringer H., et al., 2007, Astronomy & Astrophysics, 469, 363

Bolliet B., Comis B., Komatsu E., Macías-Pérez J. F., 2018, Monthly Notices of the Royal Astronomical Society, 477, 4957

Bridle S., King L., 2007, New Journal of Physics, 9, 444

Bryan G. L., Norman M. L., 1998, The Astrophysical Journal, 495, 80

Budzynski J. M., Koposov S. E., McCarthy I. G., Belokurov V., 2014, Monthly Notices of the Royal Astronomical Society, 437, 1362

Bullock J. S., Kolatt T. S., Sigad Y., Somerville R. S., Kravtsov A. V., Klypin A. A., Primack J. R., Dekel A., 2001, Monthly Notices of the Royal Astronomical Society, 321, 559

Carlstrom J. E., Holder G. P., Reese E. D., 2002, Annual Review of Astronomy and Astrophysics, 40, 643

Catelan P., Kamionkowski M., Blandford R. D., 2001, Monthly Notices of the Royal Astronomical Society, 320, L7

Cavaliere A., Fusco-Femiano R., 1976, Astronomy & Astrophysics, 500, 95

Cavaliere A., Fusco-Femiano R., 1978, Astronomy & Astrophysics, 70, 677

Cole S., Kaiser N., 1988, Monthly Notices of the Royal Astronomical Society, 233, 637

Cole S., Kaiser N., 1989, Monthly Notices of the Royal Astronomical Society, 237, 1127

Comparat J., Prada F., Yepes G., Klypin A., 2017, Monthly Notices of the Royal Astronomical Society, 469, 4157

DES Collaboration 2017, arXiv e-prints,

Dark Energy Survey Collaboration 2016, Monthly Notices of the Royal Astronomical Society, 460, 1270

Davis M., Huchra J., 1982, The Astrophysical Journal, 254, 437

Davis M., Huchra J., Latham D. W., Tonry J., 1982, The Astrophysical Journal, 253, 423

Dawson K. S., et al., 2013, The Astronomical Journal, 145, 10

Despali G., Giocoli C., Angulo R. E., Tormen G., Sheth R. K., Baso G., Moscardini L., 2016, Monthly Notices of the Royal Astronomical Society, 456, 2486

Diemer B., 2018, The Astrophysical Journal Supplement Series, 239, 35

Diemer B., Kravtsov A. V., 2014, The Astrophysical Journal, 789, 1

Diemer B., Kravtsov A. V., 2015, The Astrophysical Journal, 799, 108

Dodelson S., 2003, Modern cosmology

Dolag K., Komatsu E., Sunyaev R., 2016, Monthly Notices of the Royal Astronomical Society, 463, 1797

Duffy A. R., Schaye J., Kay S. T., Dalla Vecchia C., 2008, Monthly Notices of the Royal Astronomical Society, 390, L64

Dutton A. A., Macciò A. V., 2014, Monthly Notices of the Royal Astronomical Society, 441, 3359

Einasto J., 1965, Trudy Astrofizicheskogo Instituta Alma-Ata, 5, 87

Einstein A., 1916, Annalen der Physik, 354, 769

Eisenstein D. J., et al., 2005, The Astrophysical Journal, 633, 560

Eke V. R., Navarro J. F., Frenk C. S., 1998, The Astrophysical Journal, 503, 569

Falco E. E., Gorenstein M. V., Shapiro I. I., 1985, The Astrophysical Journal, 289, L1

Flender S., Nagai D., McDonald M., 2017, The Astrophysical Journal, 837, 124

Font-Ribera A., McDonald P., Slosar A., 2018, Journal of Cosmology and Astro-Particle Physics, 2018, 003

Foreman-Mackey D., Hogg D. W., Lang D., Goodman J., 2013, Publications of the Astronomical Society of the Pacific, 125, 306

Friedmann A., 1922, Zeitschrift fur Physik, 10, 377

Friedmann A., 1924, Zeitschrift fur Physik, 21, 326

Gao L., Navarro J. F., Cole S., Frenk C. S., White S. D. M., Springel V., Jenkins A., Neto A. F., 2008, Monthly Notices of the Royal Astronomical Society, 387, 536

George E. M., et al., 2015, The Astrophysical Journal, 799, 177

Giodini S., et al., 2009, The Astrophysical Journal, 703, 982

Gonzalez A. H., Zaritsky D., Zabludoff A. I., 2007, The Astrophysical Journal, 666, 147

Górski K. M., Hivon E., Banday A. J., Wandelt B. D., Hansen F. K., Reinecke M., Bartelmann M., 2005, The Astrophysical Journal, 622, 759

Gunn J. E., Gott J. Richard I., 1972, The Astrophysical Journal, 176, 1

Gunn J. E., Peterson B. A., 1965, The Astrophysical Journal, 142, 1633

Guth A. H., 1981, Physical Review D, 23, 347

Hahn O., Abel T., 2011, Monthly Notices of the Royal Astronomical Society, 415, 2101

Hamana T., Mellier Y., 2001, Monthly Notices of the Royal Astronomical Society, 327, 169

Hamana T., et al., 2003, The Astrophysical Journal, 597, 98

Hand N., et al., 2012, Physical Review Letters, 109, 041101

Harnois-Déraps J., et al., 2016, Monthly Notices of the Royal Astronomical Society, 460, 434

Harrison E. R., 1970, Physical Review D, 1, 2726

Heymans C., et al., 2012, Monthly Notices of the Royal Astronomical Society, 427, 146

Hikage C., et al., 2018, arXiv e-prints, p. arXiv:1809.09148

Hilbert S., Hartlap J., White S. D. M., Schneider P., 2009, Astronomy & Astrophysics, 499, 31

Hildebrandt H., et al., 2016, Monthly Notices of the Royal Astronomical Society, 463, 635

Hildebrandt H., et al., 2017, Monthly Notices of the Royal Astronomical Society, 465, 1454

Hill J. C., Spergel D. N., 2014, Journal of Cosmology and Astroparticle Physics, 2, 030

Hinshaw G., et al., 2013, The Astrophysical Journal Supplement Series, 208, 19

Hirata C., Seljak U., 2003, Monthly Notices of the Royal Astronomical Society, 343, 459

Hirata C. M., Seljak U., 2004, Physical Review D, 70, 063526

Hitomi Collaboration 2016, Nature, 535, 117

Hivon E., Górski K. M., Netterfield C. B., Crill B. P., Prunet S., Hansen F., 2002, The Astrophysical Journal, 567, 2

Hoekstra H., et al., 2006, The Astrophysical Journal, 647, 116

Hoekstra H., Herbonnet R., Muzzin A., Babul A., Mahdavi A., Viola M., Cacciato M., 2015, Monthly Notices of the Royal Astronomical Society, 449, 685

Hogg D. W., 1999, preprint, pp astro–ph/9905116 (`arXiv:astro-ph/9905116`)

Hojjati A., McCarthy I. G., Harnois-Deraps J., Ma Y.-Z., Van Waerbeke L., Hinshaw G., Le Brun A. M. C., 2015, Journal of Cosmology and Astroparticle Physics, 10, 047

Hojjati A., et al., 2017, Monthly Notices of the Royal Astronomical Society, 471, 1565

Horowitz B., Seljak U., 2017, Monthly Notices of the Royal Astronomical Society, 469, 394

Hu W., 1999, The Astrophysical Journal, 522, L21

Hubble E., 1929, Proceedings of the National Academy of Science, 15, 168

Huchra J. P., et al., 2012, The Astrophysical Journal Supplement Series, 199, 26

Ishiyama T., Fukushige T., Makino J., 2009, Publications of the Astronomical Society of Japan, 61, 1319

Itoh N., Kohyama Y., Nozawa S., 1998, The Astrophysical Journal, 502, 7

Jain B., Seljak U., White S., 2000, The Astrophysical Journal, 530, 547

Jing Y. P., 1998, The Astrophysical Journal Letters, 503, L9

Jing Y. P., Suto Y., 2002, The Astrophysical Journal, 574, 538

Jones D. H., et al., 2009, Monthly Notices of the Royal Astronomical Society, 399, 683

Kaiser N., 1986, Monthly Notices of the Royal Astronomical Society, 222, 323

Kaiser N., 1992, The Astrophysical Journal, 388, 272

Kaiser N., 1998, The Astrophysical Journal, 498, 26

Kaiser N., Squires G., 1993, The Astrophysical Journal, 404, 441

Khatri R., Sunyaev R., 2015, Journal of Cosmology and Astroparticle Physics, 8, 013

Kilbinger M., 2015, Reports on Progress in Physics, 78, 086901

Kitayama T., 2014, Progress of Theoretical and Experimental Physics, 2014, 06B111

Klypin A. A., Trujillo-Gomez S., Primack J., 2011, The Astrophysical Journal, 740, 102

Köhlinger F., et al., 2017, Monthly Notices of the Royal Astronomical Society, 471, 4412

Komatsu E., Kitayama T., 1999, The Astrophysical Journal Letters, 526, L1

Komatsu E., Seljak U., 2001, Monthly Notices of the Royal Astronomical Society, 327, 1353

Komatsu E., Seljak U., 2002, Monthly Notices of the Royal Astronomical Society, 336, 1256

Kravtsov A. V., Borgani S., 2012, Annual Review of Astronomy and Astrophysics, 50, 353

Kravtsov A. V., Klypin A. A., Khokhlov A. M., 1997, The Astrophysical Journal Supplement Series, 111, 73

Kravtsov A. V., Vikhlinin A., Nagai D., 2006, The Astrophysical Journal, 650, 128

LSST Science Collaboration 2009, preprint, p. arXiv:0912.0201 (`arXiv:0912.0201`)

Lau E. T., Nagai D., Kravtsov A. V., Zentner A. R., 2011, The Astrophysical Journal, 734, 93

Laureijs R., et al., 2011, preprint, p. arXiv:1110.3193 (`arXiv:1110.3193`)

Leauthaud A., et al., 2007, The Astrophysical Journal Supplement Series, 172, 219

Leauthaud A., et al., 2012, The Astrophysical Journal, 744, 159

Leauthaud A., et al., 2017, Monthly Notices of the Royal Astronomical Society, 467, 3024

Limber D. N., 1953, The Astrophysical Journal, 117, 134

LoVerde M., Afshordi N., 2008, Physical Review D, 78, 123506

Łokas E. L., Mamon G. A., 2001, Monthly Notices of the Royal Astronomical Society, 321, 155

Ma Y.-Z., Van Waerbeke L., Hinshaw G., Hojjati A., Scott D., Zuntz J., 2015, Journal of Cosmology and Astroparticle Physics, 9, 046

Makino N., Suto Y., 1993, The Astrophysical Journal, 405, 1

Makino N., Sasaki S., Suto Y., 1998, The Astrophysical Journal, 497, 555

Makiya R., Ando S., Komatsu E., 2018, Monthly Notices of the Royal Astronomical Society, 480, 3928

Mandelbaum R., 2018, Annual Review of Astronomy and Astrophysics, 56, 393

Mandelbaum R., et al., 2018a, Publications of the Astronomical Society of Japan, 70, S25

Mandelbaum R., et al., 2018b, Monthly Notices of the Royal Astronomical Society, 481, 3170

Matsubara T., 2008, Physical Review D, 77, 063530

McCarthy I. G., Le Brun A. M. C., Schaye J., Holder G. P., 2014, Monthly Notices of the Royal Astronomical Society, 440, 3645

McDonald M., et al., 2013, The Astrophysical Journal, 774, 23

McQuinn M., White M., 2011, Monthly Notices of the Royal Astronomical Society, 415, 2257

Mead A. J., Peacock J. A., Heymans C., Joudaki S., Heavens A. F., 2015, Monthly Notices of the Royal Astronomical Society, 454, 1958

Medezinski E., et al., 2018, Publications of the Astronomical Society of Japan, 70, S28

Miller L., et al., 2013, Monthly Notices of the Royal Astronomical Society, 429, 2858

Miyatake H., et al., 2015, The Astrophysical Journal, 806, 1

Miyatake H., et al., 2018, arXiv e-prints, p. arXiv:1804.05873

Mo H. J., White S. D. M., 1996, Monthly Notices of the Royal Astronomical Society, 282, 347

More S., Miyatake H., Mandelbaum R., Takada M., Spergel D. N., Brownstein J. R., Schneider D. P., 2015, The Astrophysical Journal, 806, 2

Munshi D., Valageas P., van Waerbeke L., Heavens A., 2008, Physics Reports, 462, 67

Munshi D., Joudaki S., Coles P., Smidt J., Kay S. T., 2014, Monthly Notices of the Royal Astronomical Society, 442, 69

Murata R., Nishimichi T., Takada M., Miyatake H., Shirasaki M., More S., Takahashi R., Osato K., 2018, The Astrophysical Journal, 854, 120

Murray S. G., Power C., Robotham A. S. G., 2013, Astronomy and Computing, 3, 23

Nagai D., Kravtsov A. V., Vikhlinin A., 2007, The Astrophysical Journal, 668, 1

Nagamine K., Ostriker J. P., Fukugita M., Cen R., 2006, The Astrophysical Journal, 653, 881

Navarro J. F., Frenk C. S., White S. D. M., 1996, The Astrophysical Journal, 462, 563

Navarro J. F., Frenk C. S., White S. D. M., 1997, The Astrophysical Journal, 490, 493

Nelson K., Lau E. T., Nagai D., 2014, The Astrophysical Journal, 792, 25

Nishimichi T., et al., 2009, Publications of the Astronomical Society of Japan, 61, 321

Nishimichi T., Taruya A., Koyama K., Sabiu C., 2010, Journal of Cosmology and Astroparticle Physics, 7, 002

Nozawa S., Itoh N., Kohyama Y., 1998, The Astrophysical Journal, 508, 17

Oguri M., Hamana T., 2011, Monthly Notices of the Royal Astronomical Society, 414, 1851

Oguri M., Takada M., 2011, Physical Review D, 83, 023008

Oguri M., Lee J., Suto Y., 2003, The Astrophysical Journal, 599, 7

Oguri M., Takada M., Okabe N., Smith G. P., 2010, Monthly Notices of the Royal Astronomical Society, 405, 2215

Oguri M., Bayliss M. B., Dahle H., Sharon K., Gladders M. D., Natarajan P., Hennawi J. F., Koester B. P., 2012, Monthly Notices of the Royal Astronomical Society, 420, 3213

Oguri M., et al., 2018, Publications of the Astronomical Society of Japan, 70, S26

Okabe T., Nishimichi T., Oguri M., Peirani S., Kitayama T., Sasaki S., Suto Y., 2018, Monthly Notices of the Royal Astronomical Society, 478, 1141

Osato K., Shirasaki M., Yoshida N., 2015, The Astrophysical Journal, 806, 186

Osato K., Flender S., Nagai D., Shirasaki M., Yoshida N., 2018, Monthly Notices of the Royal Astronomical Society, 475, 532

Ostriker J. P., Bode P., Babul A., 2005, The Astrophysical Journal, 634, 964

Paczynski B., 1986, The Astrophysical Journal, 304, 1

Peebles P. J. E., 1980, The large-scale structure of the universe

Peebles P. J. E., 1993, Principles of Physical Cosmology

Penna-Lima M., Bartlett J. G., Rozo E., Melin J. B., Merten J., Evrard A. E., Postman M., Rykoff E., 2017, Astronomy & Astrophysics, 604, A89

Penzias A. A., Wilson R. W., 1965, The Astrophysical Journal, 142, 419

Phillips M. M., 1993, The Astrophysical Journal Letters, 413, L105

Pillepich A., Porciani C., Hahn O., 2010, Monthly Notices of the Royal Astronomical Society, 402, 191

Planck Collaboration 2013, Astronomy & Astrophysics, 550, A131

Planck Collaboration 2016a, Astronomy & Astrophysics, 594, A1

Planck Collaboration 2016b, Astronomy & Astrophysics, 594, A11

Planck Collaboration 2016c, Astronomy & Astrophysics, 594, A13

Planck Collaboration 2016d, Astronomy & Astrophysics, 594, A22

Planck Collaboration 2016e, Astronomy & Astrophysics, 594, A24

Planck Collaboration 2018a, arXiv e-prints, p. arXiv:1807.06209

Planck Collaboration 2018b, arXiv e-prints, p. arXiv:1807.06210

Pratt G. W., Croston J. H., Arnaud M., Böhringer H., 2009, Astronomy & Astrophysics, 498, 361

Press W. H., Schechter P., 1974, The Astrophysical Journal, 187, 425

Rhodes J., Refregier A., Groth E. J., 2001, The Astrophysical Journal, 552, L85

Riess A. G., et al., 2011, The Astrophysical Journal, 730, 119

Roncarelli M., Moscardini L., Borgani S., Dolag K., 2007, Monthly Notices of the Royal Astronomical Society, 378, 1259

Rubin V. C., Ford W. Kent J., 1970, The Astrophysical Journal, 159, 379

Rubin V. C., Ford W. K. J., Thonnard N., 1980, The Astrophysical Journal, 238, 471

SDSS Collaboration 2000, The Astronomical Journal, 120, 1579

Sato K., 1981, Monthly Notices of the Royal Astronomical Society, 195, 467

Sazonov S. Y., Sunyaev R. A., 1999, Monthly Notices of the Royal Astronomical Society, 310, 765

Schaan E., et al., 2016, Physical Review D, 93, 082002

Schaye J., et al., 2015, Monthly Notices of the Royal Astronomical Society, 446, 521

Schneider P., Seitz C., 1995, Astronomy & Astrophysics, 294, 411

Schneider P., Ehlers J., Falco E. E., 1992, Gravitational Lenses, doi:10.1007/978-3-662-03758-4.

Scoccimarro R., 1998, Monthly Notices of the Royal Astronomical Society, 299, 1097

Seitz C., Schneider P., 1997, Astronomy & Astrophysics, 318, 687

Seljak U., Warren M. S., 2004, Monthly Notices of the Royal Astronomical Society, 355, 129

Semboloni E., Hoekstra H., Schaye J., 2013, Monthly Notices of the Royal Astronomical Society, 434, 148

Sereno M., Covone G., Izzo L., Ettori S., Coupon J., Lieu M., 2017, Monthly Notices of the Royal Astronomical Society, 472, 1946

Shaw L. D., Nagai D., Bhattacharya S., Lau E. T., 2010, The Astrophysical Journal, 725, 1452

Sheth R. K., Tormen G., 1999, Monthly Notices of the Royal Astronomical Society, 308, 119

Sheth R. K., Mo H. J., Tormen G., 2001, Monthly Notices of the Royal Astronomical Society, 323, 1

Shi X., Komatsu E., 2014, Monthly Notices of the Royal Astronomical Society, 442, 521

Shi X., Komatsu E., Nelson K., Nagai D., 2015, Monthly Notices of the Royal Astronomical Society, 448, 1020

Shi X., Komatsu E., Nagai D., Lau E. T., 2016, Monthly Notices of the Royal Astronomical Society, 455, 2936

Shirasaki M., 2019, Monthly Notices of the Royal Astronomical Society, 483, 342

Shirasaki M., Hamana T., Takada M., Takahashi R., Miyatake H., 2019, arXiv e-prints, p. arXiv:1901.09488

Sievers J. L., et al., 2013, Journal of Cosmology and Astroparticle Physics, 10, 060

Singh S., Mandelbaum R., More S., 2015, Monthly Notices of the Royal Astronomical Society, 450, 2195

Slosar A., et al., 2011, Journal of Cosmology and Astro-Particle Physics, 2011, 001

Smith G. P., et al., 2016, Monthly Notices of the Royal Astronomical Society, 456, L74

Soergel B., Saro A., Giannantonio T., Efstathiou G., Dolag K., 2018, Monthly Notices of the Royal Astronomical Society, 478, 5320

Spergel D., et al., 2015, preprint, p. arXiv:1503.03757 (`arXiv:1503.03757`)

Springel V., 2005, Monthly Notices of the Royal Astronomical Society, 364, 1105

Springel V., 2010, Monthly Notices of the Royal Astronomical Society, 401, 791

Springel V., Yoshida N., White S. D. M., 2001, New Astronomy, 6, 79

Springel V., et al., 2018, Monthly Notices of the Royal Astronomical Society, 475, 676

Starobinsky A. A., 1980, Physics Letters B, 91, 99

Sugimoto D., Chikada Y., Makino J., Ito T., Ebisuzaki T., Umemura M., 1990, Nature, 345, 33

Sunyaev R. A., Zel'dovich Y. B., 1972, Comments on Astrophysics and Space Physics, 4, 173

Sunyaev R. A., Zel'dovich Y. B., 1980, Monthly Notices of the Royal Astronomical Society, 190, 413

Suto Y., Sasaki S., Makino N., 1998, The Astrophysical Journal, 509, 544

Suto D., Kawahara H., Kitayama T., Sasaki S., Suto Y., Cen R., 2013, The Astrophysical Journal, 767, 79

Takada M., Jain B., 2003a, Monthly Notices of the Royal Astronomical Society, 340, 580

Takada M., Jain B., 2003b, Monthly Notices of the Royal Astronomical Society, 344, 857

Takada M., Komatsu E., Futamase T., 2006, Physical Review D, 73, 083520

Takahashi R., Sato M., Nishimichi T., Taruya A., Oguri M., 2012, The Astrophysical Journal, 761, 152

Takahashi R., Hamana T., Shirasaki M., Namikawa T., Nishimichi T., Osato K., Shiroyama K., 2017, The Astrophysical Journal, 850, 24

Tanaka M., et al., 2018, Publications of the Astronomical Society of Japan, 70, S9

Tinker J., Kravtsov A. V., Klypin A., Abazajian K., Warren M., Yepes G., Gottlöber S., Holz D. E., 2008, The Astrophysical Journal, 688, 709

Tinker J. L., Robertson B. E., Kravtsov A. V., Klypin A., Warren M. S., Yepes G., Gottlöber S., 2010, The Astrophysical Journal, 724, 878

Tonry J., Davis M., 1979, The Astronomical Journal, 84, 1511

Treu T., 2010, Annual Review of Astronomy and Astrophysics, 48, 87

Tröster T., Van Waerbeke L., 2014, Journal of Cosmology and Astroparticle Physics, 11, 008

Tsujikawa S., 2013, Classical and Quantum Gravity, 30, 214003

Ursino E., Galeazzi M., Roncarelli M., 2010, The Astrophysical Journal, 721, 46

Valageas P., Nishimichi T., 2011, Astronomy & Astrophysics, 527, A87

Van Waerbeke L., 2000, Monthly Notices of the Royal Astronomical Society, 313, 524

Van Waerbeke L., et al., 2000, Astronomy & Astrophysics, 358, 30

Van Waerbeke L., Hinshaw G., Murray N., 2014, Physical Review D, 89, 023508

Viel M., Becker G. D., Bolton J. S., Haehnelt M. G., 2013, Physical Review D, 88, 043502

Walsh D., Carswell R. F., Weymann R. J., 1979, Nature, 279, 381

Watson W. A., Iliev I. T., D'Aloisio A., Knebe A., Shapiro P. R., Yepes G., 2013, Monthly Notices of the Royal Astronomical Society, 433, 1230

Weinberg S., 1972, Gravitation and Cosmology: Principles and Applications of the General Theory of Relativity

Weinberg S., 2008, Cosmology

Weinberg D. H., Mortonson M. J., Eisenstein D. J., Hirata C., Riess A. G., Rozo E., 2013, Physics Reports, 530, 87

White S. D. M., 1994, arXiv e-prints, pp astro–ph/9410043

White M., Hu W., 2000, The Astrophysical Journal, 537, 1

Wittman D. M., Tyson J. A., Kirkman D., Dell'Antonio I., Bernstein G., 2000, Nature, 405, 143

Yèche C., Palanque-Delabrouille N., Baur J., du Mas des Bourboux H., 2017, Journal of Cosmology and Astro-Particle Physics, 2017, 047

Zel'dovich Y. B., 1970, Astronomy & Astrophysics, 500, 13

Zel'dovich Y. B., 1972, Monthly Notices of the Royal Astronomical Society, 160, 1P

Zwicky F., 1933, Helvetica Physica Acta, 6, 110

de Jong J. T. A., et al., 2013, The Messenger, 154, 44

von der Linden A., et al., 2014, Monthly Notices of the Royal Astronomical Society, 443, 1973